RADIATION AND SNOWMELT DYNAMICS IN MOUNTAIN FORESTS

A Thesis Submitted to the College of
Graduate Studies and Research
in Partial Fulfilment of the Requirements
for the Degree of Doctorate of Philosophy
in the Department of
Geography and Planning
(Centre for Hydrology)
University of Saskatchewan
Saskatoon

by

Chad Ronald Ellis

March 2011

PERMISSION TO USE

In presenting this thesis in partial fulfilment of the requirements for a Postgraduate degree from the University of Saskatchewan, I agree that the Libraries of this University may make it freely available for inspection. I further agree that permission for copying of this thesis in any manner, in whole or in part, for scholarly purposes may be granted by the professor or professors who supervised my thesis work or, in their absence, by the Head of the Department or the Dean of the College in which my thesis work was done. It is understood that any copying or publication or use of this thesis or parts thereof for financial gain shall not be allowed without my written permission. It is also understood that due recognition will be given to me and to the University of Saskatchewan in any scholarly use which may be made of any material in this thesis.

Requests for permission to copy or to make other use of material in this thesis in whole or in part should be addressed to:

Head of the Department of Geography and Planning
University of Saskatchewan
117 Science Place
Saskatoon, Saskatchewan, Canada
S7N 5C8

ABSTRACT

Utilising extensive field observations and physically-based simulations of forest-snow processes, the impacts of needleleaf forest-cover on radiation and snowmelt dynamics were investigated in an eastern Rocky Mountain headwater catchment. At low-elevation pine forest sites, the sparse canopy-cover allowed for substantial shortwave transmittance to snow, giving topography-influenced snow radiation balances and snowmelt timing. By comparison, the denser high-elevation spruce cover minimised shortwave radiation to snow, resulting in snowmelt dominated by longwave radiation gains, and close synchronisation in melt timing across opposing mountain slopes.

Field observations were used to direct and evaluate physically-based simulation models describing radiation-snow exchanges in needleleaf forests. This included the estimation of shortwave irradiance transfer through sparse needleleaf canopies with explicit account for differing shortwave transmittance properties of trunks, crowns, and gaps within highly structured mountain pine stands. Improved representation of sub-canopy longwave irradiance to mountain snow was also made through the determination of added longwave emissions from shortwave heated canopies.

From model simulations, forest-cover effects on radiation to snow were found to vary substantially with both topography and seasonal meteorological conditions. In general, forest-cover increased radiation during the mid-winter by reducing longwave losses from snow. However, with greater shortwave irradiance into the spring, forest-cover effects on radiation to snow became increasing influenced by topography, with greater radiation under more open canopies on south-facing slopes and under more closed canopies on north-facing slopes.

Drawing upon past field investigations and modelling exercises, a physically-based simulation model was constructed to represent snow accumulation and melt processes in needleleaf forest environments. By means of an objective evaluation, the model well represented differences in snow accumulation and melt in paired forest and clearing sites of varying location and climate. The model was subsequently applied to examine forest-cover impacts on mountain snowmelt, revealing that forest-cover removal substantially increased total snowmelt and sizeably expanded the spring melt period through a de-synchronisation of melt contributions from south-facing and north-facing landscapes. These results demonstrate the potential for altering the magnitude and timing of mountain snowmelt through topographic-specific changes in mountain forest-cover.

ACKNOWLEDGEMENTS

First I wish to express my appreciation to my supervisor, Dr. J. Pomeroy, for his encouragement, mentoring, and commitment to my research and scientific development. I am also very grateful to Mr. M. Solohub for his invaluable assistance in preparing and set-up of field equipment and assistance with field work. Also appreciated is the help in field work from my fellow grad students, and especially A. Sabourin of Ècole Polytechnique, Paris for her many hours of hard work. A special thank you to Mr. T. Brown for his assistance in implementing the forest routines within CRHM, as well as to X. Fang for the insight provided in our many discussions. Much gratitude is also due to Dr. R. Essery for his supervision and hospitality during my studies at the University of Edinburgh.

To my academic committee, Drs. X. Guo, D. de Boer, and C. Maule, I am very appreciative of the feedback and confidence you have shown in me, and am grateful to Dr. D. Lettenmaier of the University of Washington for serving as my external examiner. I also thank Dr. Guo for the lending of her portable spectroradiometer. I am very fortunate to have the experience of working throughout my graduate training with Dr. T. Link, University of Idaho, who has provided much support to my research. Much appreciation is also given to Dr. D. Marks (USDA-ARS) and Dr. J. Hardy (USACE) for their role in providing the radiometer array instrumentation, the data from which has proven critical to this work. Thank you to the School of Geosciences, University of Edinburgh, for the access to office space and resources during my stay. Funding and support involved in my research was provided by the Centre for Hydrology, the Department of Geography and Planning, the University of Saskatchewan, the Natural Sciences and Engineering Research Council of Canada (Alexander Graham Bell Doctoral Student Scholarship, Discovery Grants and Instrument Grants, Michael Smith Foreign Student Supplement (CGS-MSFSS)), the Canada Research Chairs Program, the Improved Processes, Parameterisation for Prediction in Cold Regions (IP3) network as funded by the Canadian Foundation for Climate and Atmospheric Studies (CFCAS), the Province of Saskatchewan Science and Technology Innovation Fund, the Canada Foundation for Innovation (CFI), the Natural Environment Research Council (UK) the GEWEX Americas Prediction Project (GAPP), and the Biogeosciences Institute, University of Calgary.

For my father Ron, my mother Judy, and my sister Crystal

TABLE OF CONTENTS

LIST OF SYMBOLS

a	minor (horizontal) axis through a representative prolate crown shape []
A	aspect (azimuth) [° or radians]
b	major (vertical) axis through a representative prolate crown shape []
b_{d}	active biomass layer depth [m]
B	fraction of ice in wet snow []
c_{o}	crown overlap factor []
c_{p}	specific heat capacity of air [MJ kg^{-1} K^{-1}]
C_{area}	apparent area of a single representative crown [m^{2}]
C_{volm}	volume a single representative crown []
C	Celsius [°]
C_{c}	fraction of horizontal canopy coverage []
C_{e}	intercepted snow exposure coefficient []
C_{f}	transmitting crown forest-cover fraction []
$C_{f(\mathrm{o})}$	calculated crown fraction prior to adjustment by (1–T_f) []
C_{l}	‘canopy-leaf contact area’ per unit ground []
C_{R}	canopy intercepted rainload [kg m^{-2}]
CRHM	Cold Regions Hydrological Model []
d	day(s) []
d	diametre [m]
d_{v}	forest mensuration data value [m]
d/h	ratio of forest (gap) clearing diameter to height []
$d/h(R^*_{\mathrm{max}})$	forest (gap) clearing dimension of maximum net radiation to snow []
DOY	day of year []
e_{a}	vapour pressure [kPa]
ea_{mean}	mean daily vapour pressure [kPa]
e_{s}	saturation vapour pressure [kPa]
E	evaporation from a partially wetted canopy [kg m^{-2} t^{-1}]
E_{p}	evaporation from a fully wetted canopy [kg m^{-2} t^{-1}]
E^*_{f}	net latent heat flux to canopy layer [MJ m^{-2} t^{-1} or W m^{-2}]
f_{C}	fraction of crown foliage to total forest foliage []

f_{T}	fraction of trunk foliage to total forest foliage []
F	exponent value []
g_f	fraction of green foliage to total forest foliage []
G_f	fully-transmitting gap forest-cover fraction []
h	forest height [m]
hr	hour []
H	defined horizontal area [m^{2}]
H^*_f	net sensible heat flux to canopy layer [MJ m^{-2} or W m^{-2}]
H_{in}	incoming horizontal snow transport rate [kg m^{-2} t^{-1}]
H_{out}	outgoing horizontal snow transport rate [kg m^{-2} t^{-1}]
hr	hour []
$\overline{h}_{\mathrm{s}}$	mean snow depth [m]
I_{in}	shortwave or longwave irradiance [MJ m^{-2} t^{-1} or W m^{-2}]
I^*_{s}	species-specific maximum intercepted snowload [kg m^{-2}]
I_{o}	solar constant [4.921 MJ m^{-2} h^{-1}]
I_{r}	canopy rainfall interception rate [kg m^{-2} t^{-1}]
$I_{\mathrm{r,o}}$	canopy intercepted rainload [kg m^{-2}]
I_{s}	canopy snowfall interception rate [kg m^{-2} t^{-1}]
$I_{\mathrm{s,o}}$	canopy intercepted snowload [kg m^{-2}]
k	forest shortwave extinction coefficient [m^{-1}]
k	intercepted snow shape coefficient (Chapter 6) []
k_{d}	diffuse fraction of shortwave irradiance []
k_{t}	atmosphere transmittance index []
K	degrees Kelvin []
K_{b}	direct-beam shortwave irradiance [MJ m^{-2} t^{-1} or W m^{-2}]
K_{d}	diffuse shortwave irradiance [MJ m^{-2} t^{-1} or W m^{-2}]
K_{ex}	exo-atmospheric shortwave irradiance [MJ m^{-2} t^{-1} or W m^{-2}]
K_{in}	shortwave irradiance [MJ m^{-2} t^{-1} or W m^{-2}]
K_{o}	above-canopy shortwave irradiance [MJ m^{-2} t^{-1} or W m^{-2}]
K_{o}(L)	shortwave irradiance to a level surface [MJ m^{-2} t^{-1} or W m^{-2}]
K_{o}(S)	shortwave irradiance to a sloped surface [MJ m^{-2} t^{-1} or W m^{-2}]

K_{out}	outgoing (reflected) shortwave irradiance [MJ m^{-2}]
K^*	net shortwave radiation [MJ m^{-2} t^{-1} or W m^{-2}]
K^*_f	sub-canopy net shortwave radiation [MJ m^{-2} t^{-1} or W m^{-2}]
K^*_f	net shortwave radiation to canopy layer (Chapter 5) [MJ m^{-2} or W m^{-2}]
l	forest shortwave irradiance extinction pathlength [m]
$l_{\mathrm{c}(i)}$	pathlength through a single representative crown [m]
LAI	leaf area index [m^{2} m^{-2}]
$LAI`$	effective leaf area index [m^{2} m^{-2}]
L_{d}	leaf area density [m^{2} m^{-3}]
L_{in}	longwave irradiance [MJ m^{-2}]
L_{out}	longwave exitance [MJ m^{-2}]
LPC	Level Pine Clearing observation site []
LPF	Level Pine Forest observation site []
LG	hypothetical level forest clearing *gap* site []
LS	hypothetical level site []
LSC	Level Spruce Clearing observation site []
LU	landscape unit []
$L`$	optical forest depth [m]
L^*	net longwave radiation [MJ m^{-2} t^{-1} or W m^{-2}]
m_{canopy}	canopy snow mass balance [kg m^{-2}]
$m_{\mathrm{sub\text{-}canopy}}$	sub-canopy snow mass balance [kg m^{-2}]
m.a.s.l.	metres above sea level [m]
M	snowmelt [kg m^{-2}], or snowmelt rate [kg m^{-2} t^{-1}]
$\mathrm{M}_{\mathrm{DOY}}$	day of median value of total snowmelt []
MB	model (or mean) bias index []
MCRB	Marmot Creek Research Basin []
ME	model efficiency index []
MJ	mega Joules [1e^{6} N m]
n	number []
nm	nanometre [1×10^{-9} m]
NPC	North-facing Pine Clearing observation site []

NPF	North-facing Pine Forest observation site []
NG	hypothetical 30° north-facing forest clearing *gap* site []
NS	hypothetical 30° north-facing slope site []
NSC	North-facing Spruce Clearing observation site []
NSF	North-facing Spruce Forest observation site []
p	probability []
p_f	canopy longwave transfer (probability) function []
$p_f(f_{\mathrm{C}})$	probability of longwave emission transfer from f_{C} to sub-canopy []
$p_f(f_{\mathrm{T}})$	probability of longwave emission transfer from f_{T} to sub-canopy []
P	precipitation rate [kg m^{-2} t^{-1}]
P_{r}	rainfall rate [kg m^{-2} t^{-1}]
P_{s}	snowfall rate [kg m^{-2} t^{-1}]
q_{e}	canopy sublimation rate [kg m^{-2} s^{-1}]
Q_{E}	net latent heat flux (energy for snowmelt in Chapter 7) [MJ m^{-2} t^{-1} or W m^{-2}]
Q_{G}	net ground heat flux (energy for snowmelt in Chapter 7) [MJ m^{-2} t^{-1} or W m^{-2}]
Q_{H}	net sensible heat flux (energy for snowmelt in Chapter 7) [MJ m^{-2} t^{-1} or W m^{-2}]
Q_{K}	net shortwave radiation snowmelt energy [MJ m^{-2} t^{-1} or W m^{-2}]
Q_{L}	net longwave radiation snowmelt energy [MJ m^{-2} t^{-1} or W m^{-2}]
Q_{M}	snowmelt energy [MJ m^{-2} t^{-1} or W m^{-2}]
Q_{P}	rainfall advection energy (snowmelt energy in Chapter 7) [MJ m^{-2} t^{-1} or W m^{-2}]
Q^*	net energy to snow [MJ m^{-2} t^{-1} or W m^{-2}]
Q^*_f	net energy to canopy layer [MJ m^{-2} t^{-1} or W m^{-2}]
r_a	aerodynamic resistance [s m^{-1}]
rh	relative humidity [%]
R	fraction of shortwave irradiance reflected from canopy cover []
R_{d}	canopy rain drip rate [kg m^{-2} t^{-1}]
R_{d}	representative crown or trunk dimension (Chapter 4) [m]
$R(i)$	rank of mensuration value i []
R_{in}	all-wave irradiance [MJ m^{-2} or W m^{-2}]
$R_{\mathrm{in},f}$	sub-canopy all-wave irradiance [MJ m^{-2} or W m^{-2}]
$R_{\mathrm{in},g}$	forest gap all-wave irradiance [MJ m^{-2} or W m^{-2}]

RMSE	root mean square error [units variable]
R^2	correlation coefficient []
R^*	net all-wave radiation [MJ m^{-2}]
R^*_{max}	maximum net radiation to snow [MJ m^{-2} or W m^{-2}]
sd	standard deviation [units variable]
S	hypothetical sloped surface site []
S	sublimation loss rate (Chapter 6) [kg m^{-2} t^{-1}]
$\overline{S}$	mean maximum snowload per unit area of branch [kg m^{-2}]
SnoMIP2	(second) snow model inter-comparison project []
S_{max}	maximum canopy rainload storage [kg m^{-2}]
SPC	Southeast-facing Pine Clearing observation site []
SPF	Southeast-facing Pine Forest observation site []
SG	hypothetical 30° south-facing forest clearing *gap* site []
SS	hypothetical 30° south-facing slope site []
SSC	Southeast-facing Spruce Clearing observation site []
SSF	Southeast-facing Spruce Forest observation site []
SWE	snow water equivalent [kg m^{-2} or mm]
$\mathrm{SWE}_{\mathrm{o}}$	antecedent snow water equivalent [kg m^{-2}]
$\overline{\mathrm{SWE}}$	spatially-representative snow water equivalent of site [kg m^{-2}]
t	timestep [variable]
T_{a}	air temperature [°C or K]
T_{b}	threshold ice-bulb temperature for canopy snow unloading [°C]
T_{crown}	crown surface temperature [°C or K]
T_f	forest temperature or forest foliage surface temperature [°C or K]
T_f	non-transmitting trunk forest-cover fraction (Chapter 4) []
T_{max}	maximum daily air temperature [°C]
T_{r}	rainfall temperature [°C]
T_{s}	snow surface temperature [°C or K]
T_{trunk}	trunk surface temperature [°C or K]
U	internal (stored) snow energy [MJ m^{-2} t^{-1}]
U_{l}	canopy snow unloading rate [kg m^{-2} t^{-1}]

v	(forest) sky view factor []
$v(R^*_{\mathrm{max}})$	forest sky view factor giving maximum net radiation to snow []
V_{gap}	fraction of the overlying forest-cover opened by the forest gap []
V_{i}	sublimation rate of intercepted snow [s^{-1}]
V_{s}	determined sublimation flux for a 500 μm radius ice-sphere [s^{-1}]
vwc	volumetric water content []
W	watt [J s^{-1}]
x	non-transmitting component of infinitesimally small canopy layer []
x_{no}	non-overlapping forest shadow component []
x_{o}	overlapping forest shadow component []
x_{avg}	average observed value []
x_{obs}	observed value []
x_{sim}	simulated value []
X	infinitesimally small canopy layer []
z_{d}	vertical penetration depth into the canopy []
^	operator denoting angle between two vectors []
∞	infinity []

Greek Symbols

α_{s}	snow albedo []
β	fraction of ice in wet snow []
γ	forest gap extinction pathlength adjustment factor []
δ	solar declination (or change) [radians]
Δ	slope of saturation vapour pressure curve [kPa K^{-1}]
ε	thermal emissivity []
$\varepsilon_{\mathrm{atm}}$	thermal emissivity of atmosphere []
ε_f	thermal emissivity of forest-cover []
ε_{s}	thermal emissivity of snow []
θ	elevation angle above horizon [radians]
θ_{s}	solar elevation angle [° or radians]
Λ	slope gradient angle [° or radians]

Θ	directional vector of irradiance [° or radians]
κ	fraction of shortwave irradiance absorbed by canopy cover []
λ_f	latent heat of fusion [MJ kg^{-1}]
λ_s	latent heat of sublimation [MJ kg^{-1}]
u	wind speed [m s^{-1}]
u_forest	forest wind speed [m s^{-1}]
u_open	wind speed at open site [m s^{-1}]
u_h	wind speed at canopy top [m s^{-1}]
μm	micrometre [1 × 10^{-6} m]
u_mean	mean daily wind speed [m s^{-1}]
u_ξ	within-canopy wind speed at depth ξ from canopy top [m s^{-1}]
ξ	depth from canopy top (as a fraction of forest height) []
ξ_s	effective forest shortwave extinction pathlength (ratio to forest height) []
ρ_a	density of air [kg m^{-3}]
ρ_s	density of snowfall [kg m^{-3}]
ρ_w	density of water [kg m^{-3}]
$\overline{\rho_\mathrm{s}}$	mean snow density [kg m^{-3}]
σ	Stefan-Boltzmann constant [W m^{-2} K^{-4}]
$\sum$	summation notation []
τ	forest shortwave transmittance []
τ_b	forest transmittance of direct-beam shortwave irradiance []
$\tau_\mathrm{b,g}$	forest gap transmittance of direct-beam shortwave irradiance []
τ_d	forest transmittance of diffuse shortwave irradiance []
τ_f	forest transmittance of vertical shortwave irradiance []
φ	slope aspect (azimuth) [° or radians]
Φ	latitude [° or radians]
ψ	canopy wind speed extinction coefficient []
ω	geometric slope correction factor for shortwave irradiance []
ω_a	specific mixing ratio of air []
ω_s	saturation mixing ratio of air []

LIST OF FIGURES

LIST OF TABLES

1. INTRODUCTION AND OBJECTIVES

1.1. Introduction

In Western North America, the bulk of river flows are generated from mountain snowmelt (Eschner et al., 1969; Gray and Landine, 1988; Mote et al., 2005), providing a vital water supply to the Mackenzie, Saskatchewan, and Mississippi drainage basins (Marks and Winstral, 2001). Much of mountain regions are covered by evergreen needleleaf forest-cover, which strongly influences snowmelt runoff due to impacts both on snow accumulation (Jeffery, 1965; Lundberg and Halldin, 1994; Pomeroy et al., 2002) and the timing of snowmelt (Metcalfe and Buttle, 1995; Davis et al., 1997; Hardy et al., 1998). Presently however, these flows are under ever-increasing demand to satisfy the rapidly expanding agricultural, industrial and municipal water needs of Western North America (Martz et al., 2007). As such, more effective use of mountain river flows gained through forest management practices are expected to benefit from an enhanced understanding of snow processes in mountain needleleaf forest environments.

Snow accumulation under needleleaf forest-cover may differ substantially to that in nearby open environments. The structure and density of needleleaf canopies provide for high snow interception efficiencies, and the ability to support heavy snowloads over extended periods (Schmidt and Gluns, 1991; Hedstrom and Pomeroy, 1998). Here, the exposure of canopy intercepted snow to increased shortwave irradiance and wind ventilation promotes its sublimation to the atmosphere (Troendle and King, 1985; Schmidt et al., 1988; Pomeroy and Schmidt, 1993; Lundberg and Halldin, 1994). Subsequently, canopy sublimation represents a loss in winter snow accumulations under the canopy, decreasing the amount of snowmelt available for soil moisture recharge (e.g. Grant et al., 2004), vegetation growth (e.g. Cooper et al., 2006) and ecosystem productivity (e.g. Arp et al., 2006). However, the degree to which snow accumulation is reduced in needleleaf forests is highly variable, ranging from 30 – 50 % to that of adjacent clearings in cold Canadian and Russian mountain and boreal forests (Hedstrom and Pomeroy, 1998; Pomeroy et al., 2002; Gelfan et al., 2004), to nearly even accumulations reported in temperate Finnish forests (Koivusalo and Kokkonen, 2002). Such differences are largely attributed to varying combinations of: (i) canopy interception capacity, as controlled by the density and structure of the forest canopy and amount of snow unloading (MacDonald, 2010), as well as (ii) the potential for sublimation from the canopy, as influenced by meteorological conditions of radiation, humidity, and wind speed (Thorpe and Mason, 1966; Schmidt, 1991; Parviainen and Pomeroy, 2000).

Formally defined, the change in the total mass balance of snow ($\mathrm{d}m/\mathrm{d}t$) within a defined forest area may be described explicitly through separate accounting of canopy snow accumulations ($m_{(\mathrm{canopy})}$) and ground snow accumulations ($m_{(\mathrm{sub\text{-}canopy})}$) by

$$\frac{\mathrm{d}m}{\mathrm{d}t} = \frac{\mathrm{d}m_{(\mathrm{canopy})}}{\mathrm{d}t} + \frac{\mathrm{d}m_{(\mathrm{sub\text{-}canopy})}}{\mathrm{d}t} \tag{1.1}$$

Here, the canopy and sub-canopy snow mass balances may be stated in terms of the individual mass fluxes respective to each, i.e.

$$\frac{\mathrm{d}m}{\mathrm{d}t} = \frac{\mathrm{d}(I_\mathrm{s} - S - U_\mathrm{l})}{\mathrm{d}t} + \frac{\mathrm{d}((P_\mathrm{s} - I_\mathrm{s}) + U_\mathrm{l} - M)}{\mathrm{d}t} \tag{1.2}$$

where P_s is the snowfall, I_s is the canopy snow interception, S is the sublimation loss from the canopy, U_l is the canopy snow unloading, and M is snowmelt [all units in kg m^{-2}]. However, from a strict water resource perspective, focus is placed on the sub-canopy snow mass balance (m_{canopy}), as it upon melt represents the main water source satisfying many hydrological and ecological functions. Consequently, this simplifies the forest snow mass balance to

$$\frac{\mathrm{d}m_{(\mathrm{sub\text{-}canopy})}}{\mathrm{d}t} = \frac{\mathrm{d}((P_\mathrm{s} - I_\mathrm{s}) + U_\mathrm{l} - M)}{\mathrm{d}t} \tag{1.3}$$

A schematic representation of the snow mass fluxes defined in Eq. 1.3 is given in Figure 1.1.

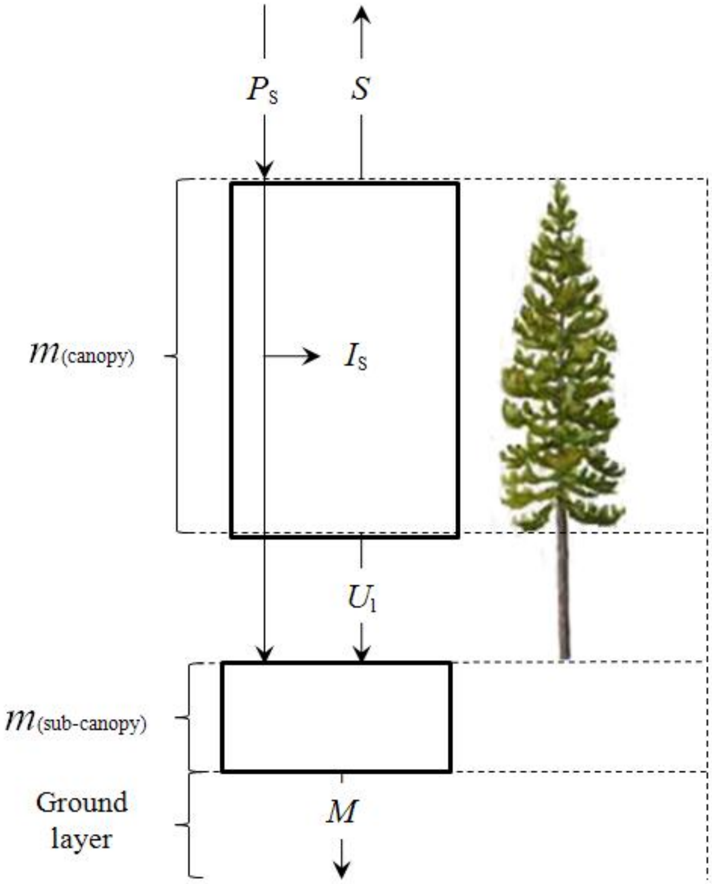

Figure 1. 1. Schematic of needleleaf forest snow mass balance depicting separate canopy snow mass balance ($m_{(canopy)}$) and sub-canopy snow mass balances ($m_{(sub\text{-}canopy)}$), showing the mass fluxes of snowfall (P_s), canopy interception (I_s), canopy sublimation (S), canopy snow unloading (U_l), and snowmelt (M).

Along with snow accumulation effects, forest-cover also may influence the timing of snowmelt by altering the energy available for snowpack warming and melt. The total amount of energy to snow (Q^*) is given by the sum of radiative, turbulent, advective and conductive energy fluxes, i.e.

$$K^* + L^* + Q_H + Q_E + Q_G + Q_P = \frac{dU}{dt} + Q_M = Q^* \qquad \textbf{(1.4)}$$

where Q_M is the energy for snowmelt, dU/dt is the change in internal (stored) energy of the snowpack, K^* and L^* are respective net shortwave and longwave radiations, Q_H and Q_E are the respective net sensible and latent heat turbulent fluxes, Q_P is the energy from rainfall advection, and Q_G is the net ground heat flux [all terms stated in MJ m^{-2} or W m^{-2}], which are shown for an abstracted forest scene in Figure 1.2.

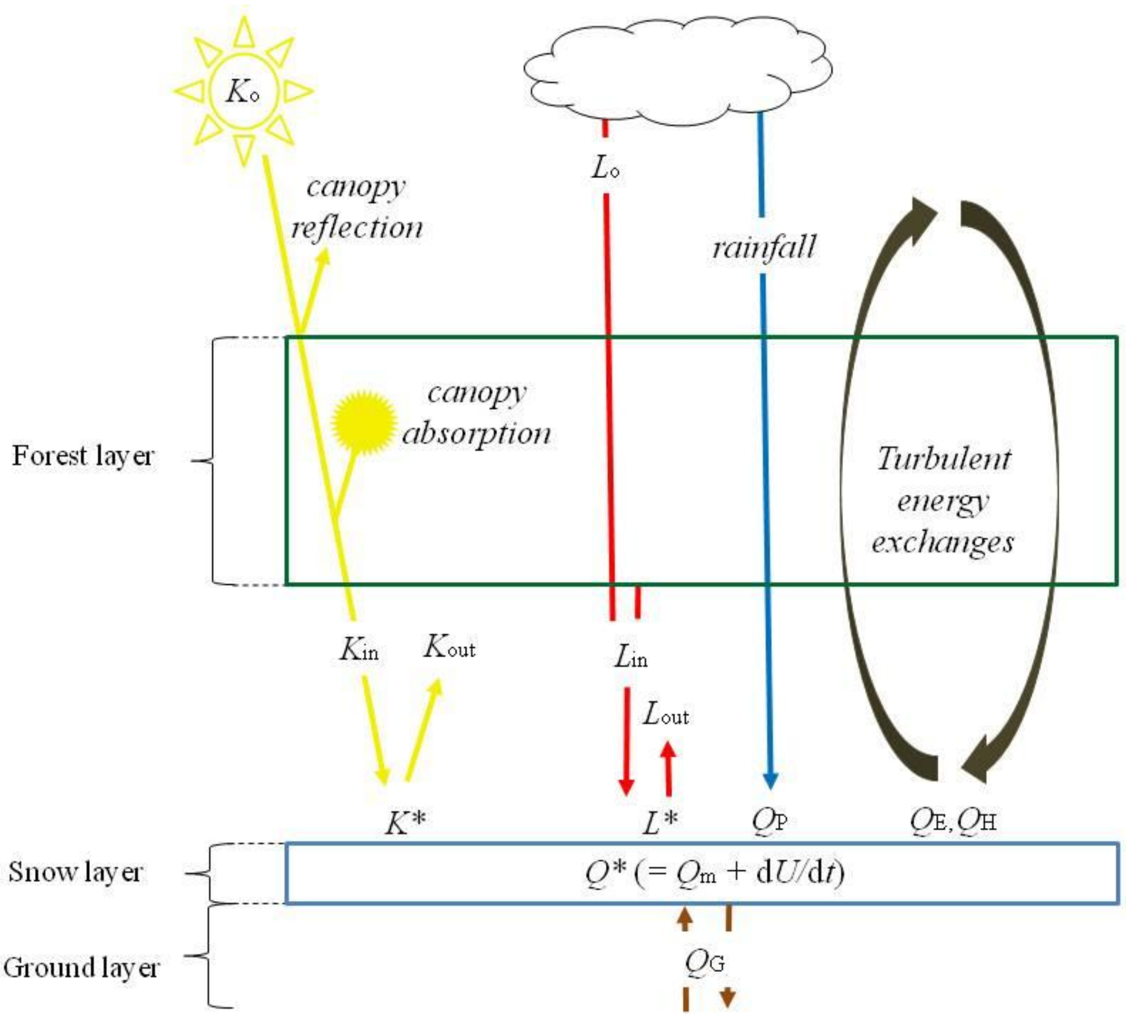

Figure 1. 2. Schematic of a generalized needleleaf forest snow energy balance showing total energy to snow (Q^*), energy for snowmelt (Q_M), change in internal snow energy (dU/dt), above-canopy shortwave irradiance (K_o), sub-canopy shortwave irradiance (K_{in}), net shortwave radiation to snow (K^*), above-canopy longwave irradiance (L_o), sub-canopy longwave irradiance (L_{in}), net longwave radiation to snow (L^*), rainfall advection energy (Q_P), turbulent latent heat flux (Q_E), turbulent sensible heat flux (Q_H), and ground heat flux (Q_G).

In forest environments, Q^* contributions from Q_G are typically small (Pomeroy et al., 1997), as well are those from Q_E and Q_G due to the large suppression of turbulent exchanges by the canopy (Harding and Pomeroy, 1996). Alternatively, rainfall may deliver substantial amounts of energy to snow, able in producing rapid melt (Marks et al., 1998) particularly in coastal environments where rain-on-snow events are more frequent. However, forest snowmelt is typically dominated by radiation (Link and Marks, 1999), itself altered by forest-cover through the extinction of shortwave irradiance and added longwave radiation from canopy emissions. As such, particular focus within this work is placed upon describing sub-canopy radiation fluxes to snow and their contribution to melt, for which a brief overview of the snow radiation balance is given in the following section.

1.2. Definition of radiation fluxes

Investigations of radiation dynamics in snow hydrology typically focus on two spectra ranges: (i) shortwave (solar) radiation (spectral wavelength range: 305 – 2800 nm), and longwave (thermal) radiation (spectral wavelength range: 5 – 50 μm), which combine to give the total all-wave radiation flux. Within the contents of this work, shortwave, longwave, and total radiation are denoted respectively by K, L, and R. Following this convention, the net shortwave (K^*), net longwave (L^*), and total net all-wave radiation (R^*) terms are given by the sum of their respective incoming and outgoing fluxes, i.e.

$$\begin{aligned} R^* &= R_{\mathrm{in}} - R_{\mathrm{out}} \\ &= K^* + L^* = K_{\mathrm{in}} - K_{\mathrm{out}} + L_{\mathrm{in}} - L_{\mathrm{out}} \end{aligned} \tag{1.5}$$

Here, all radiation terms are stated in MJ m^{-2} or W m^{-2}. As stated regarding the effect on total energy to snow (Q^*), forest-cover also strongly influences R^* by its extinction of above-canopy shortwave irradiance (K_o) via canopy reflection and absorption, while increasing L_{in} to snow by longwave emissions from canopy foliage. However, the effect of forest-cover on total radiation to snow is highly variable, capable of either increasing or decreasing R^* relative to that of open snowcovers. Consequently, the effect of forest-cover upon R^* may be described in terms of a special case of Ambach's (1974) 'radiation paradox', in which maximum R^* may be realised under varying canopy-cover densities, depending on factors such as meteorological conditions, above-canopy irradiance, the radiating temperature of canopy, and snow albedo. Yet, despite numerous studies into the canopy effects on radiation to snow in level environments (e.g. Bohren and Thorud, 1973; Sicart et al., 2004), much less is known in mountain environments, where the complex topography is expected to strongly influence forest-cover impacts on snow radiation. It is this uncertainty that provides the motivation for this research to better understand how forest-cover effects radiation and snowmelt dynamics in mountain environments.

1.3. Study objectives

In examining the effects of needleleaf forest-cover on radiation to snow and snowmelt dynamics in the Canadian Rocky Mountains, the following research questions will be addressed:

1. How does needleleaf forest-cover influence shortwave and longwave radiation exchanges to mountain snowcovers? How are these effects influenced by topography (i.e. slope and aspect) and meteorological conditions?
2. How are changes in forest-cover expected to impact the timing and magnitude of mountain snowmelt?
3. What improvements can be made in simulating radiation and snow processes in mountain forest systems?

These questions will be addressed by analysis of meteorological observations collected at field sites of varying forest-cover, elevation, and topographic orientation in an eastern Canadian Rocky Mountain headwater basin. Field observations will be further employed in the development and improvement of physically-based simulation models, the application of which will provide an extension of field-based results over a larger range of spatial and temporal scales. Within this thesis, analysis and discussion of results are presented throughout Chapters 3 – 7, with major findings of the work summarized in Chapter 8. The following provides an outline of the subject matter and objectives of Chapters 3 – 7:

Chapter 3: Observations of forest-cover effects on radiation and snowmelt (pursuant to research questions 1 and 2)

Utilising multi-year field observations collected in low elevation pine forests and high elevation spruce forests, an assessment of needleleaf forest-cover effects on radiation dynamics and snowmelt within a headwater basin is performed. Analysis focuses on how combinations of varying topography and forest-cover density influence shortwave and longwave radiation exchanges to mountain snowcovers, and impact the timing of snowmelt. Results will illustrate how radiation and snowmelt dynamics differ between low-elevation pine, and high-elevation spruce forest stands.

Chapter 4: Simulation of shortwave radiation to snow in mountain needleleaf forests (pursuant to research questions 1, 2, and 3)

A physically-based approach is outlined and evaluated for simulating shortwave radiation to snow in needleleaf forests of varying canopy density/structure and meteorological conditions. A particular aim of the model is to provide a more realistic account of shortwave transfers in sparse conifer stands consisting of non-transmitting trunks, partially-transmitting crowns, and fully transmitting canopy gaps. Subsequent application of the model examines how changes in needleleaf forest-cover affect shortwave radiation fluxes to snow at sites of differing topographical orientation.

Chapter 5: Sensitivity of radiation to mountain snowcover with varying forest-cover and meteorology (pursuant to research questions 1, 2, and 3)

Using a simplified modelling approach to describe forest-radiation transfers, an assessment is performed investigating the influence of meteorological conditions on radiation to mountain snow. A particular advantage of the approach lies in the description of forest-cover density using a single, intuitive metric: the forest sky view factor. Application of the model illustrates how forest-cover affects radiation to snow on slopes of opposing topography in an eastern Canadian Rocky Mountain location over winter-spring meteorological conditions. Based on observations of canopy temperature and sub-canopy longwave irradiance in forest stands of differing canopy density and topographic orientation, a procedure for approximating forest longwave enhancements from shortwave heating of the canopy is outlined and evaluated. Further representation of the meteorological influences on longwave fluxes to snow is made by accounting for snow surface cooling effects on longwave exitance from snow. The improved approximation of longwave radiation to sub-canopy snow by these approaches is used to investigate forest-cover effects on radiation to mountain snowcover under observed winter-spring meteorological conditions.

Chapter 6: Simulation of forest snow accumulation and melt in needleleaf forest environments (pursuant to research question 3)

A model developed from investigations of forest-snow processes in cold regions is described and evaluated for estimating snow accumulation and melt in needleleaf forest environments of varying canopy density and climate. With incorporation into the Cold Regions Hydrological Model (CRHM), model evaluation is completed by comparison of snow accumulation and melt simulations to observations at five paired forest-clearing sites located in Canada, Switzerland, Finland, and the United States. Further demonstration of the physical approach taken by the model in describing snowmelt is made via comparison of simulated energy fluxes to snow to detailed observations collected at forest and clearing sites within an eastern Canadian Rocky Mountain basin.

Chapter 7: Impacts of forest-cover change upon radiation and snowmelt in the eastern Canadian Rocky Mountains (pursuant to research questions 1 and 2)

Drawing upon the physically-based modelling procedures developed and tested within the previous chapters of this work, the impact of forest-cover changes on the magnitude and timing of mountain snowmelt are examined in the context of forest harvesting treatments performed in an eastern Rocky Mountain headwater basin. The influence of forest clear-cut size on radiation to snowcovers of opposing topography is examined using a geometrically-based model describing radiation dynamics in forest clearings. By coupling corrected radiation fluxes to the appropriate snow process modules within CRHM, forest-cover impacts on snowmelt are assessed by application of the model under observed mountain meteorological conditions. Model results illustrate the potential impacts needleleaf forest-cover changes may have on the magnitude and timing of snowmelt in a mountain headwater basin.

2. METHODOLOGY

2.1. Study area

All field studies were conducted at or near the Marmot Creek Research Basin (MCRB), located in the Kananaskis River Valley of Alberta, Canada (50°57`N, 115°09`W) (Figure 2.1). The MCRB encompasses approximately 9.4 km^2, and is divided in nearly equal parts by the Cabin Creek (2.12 km^2), Middle Creek (2.85 km^2), and Twin Creek (2.64 km^2) sub-basins, from which all flows merge into the Marmot Creek mainstem. Elevation of the MCRB ranges from 1550 – 2750 m.a.s.l., of which the higher elevation needleleaf forests are dominated by Engelmann spruce (*Picea engelmannii* Parry ex Engelm.), subalpine fir (*Abies lasiocarpa* (Hook.) Nutt.) and subalpine larch (*Larix lyallii* Parl.), and lower elevation forests by lodgepole pine (*Pinus contorta* var. *latifolia* Engelm. ex S. Wats.) (Kirby and Ogilvy, 1969). The ground surface consists mostly of poorly developed mountain soils containing glaciofluvial and till surficial deposits (Beke, 1969). However, exposed bedrock is present at higher elevations and along creek channels at lower elevations (Stevenson, 1967).

2.2. Study sites

For the winters of 2005 – 2007 inclusive, near-surface meteorological observations were collected at the following sites: a Level Pine Clearing (LPC), a Level Pine Forest (LPF), a North-facing Pine Forest (NPF), a Southeast-facing Pine Clearing (SPC), and a Southeast-facing Pine Forest (SPF). Similar observations were made during the spring of 2008 at a Level Spruce Clearing (LSC), a North-facing Spruce Forest (NSF) and a South-facing Spruce Forest (SSF). Snow surveys were conducted at all pine and spruce sites during their respective meteorological observation periods, as well as at North-facing Spruce Clearing (NSC) and South-facing Spruce Clearing (SSC) sites located adjacent to the NSF and SSF sites, respectively. Note that unlike the sloped pine forest sites, meteorological observations at the LPF were continued after the spring of 2007. The locations of all the MCRB observation sites and pictures of the meteorological observation installations at each are shown in Figure 2.1, with descriptions of the topography and forest-cover of all sites provided in Table 2.1.

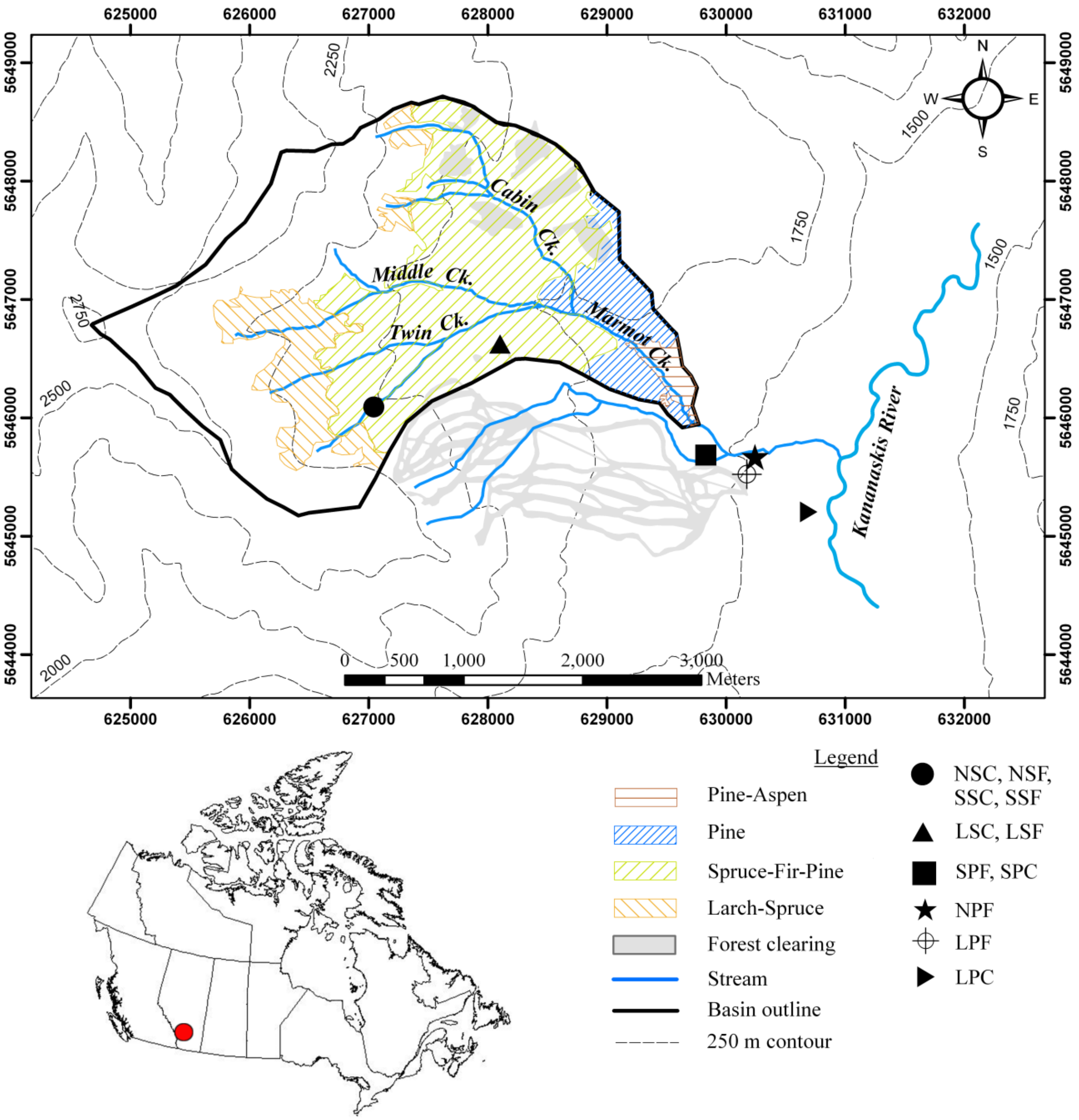

Figure 2.1. Map of the Marmot Creek Research Basin (MCRB) (see complete figure caption below).

Level Pine Clearing (LPC) Level Pine Forest (LPF)

North-facing Pine Forest (NPF) Southeast-facing Pine Forest (SPF)

Southeast-facing Pine Clearing (SPC)

Figure 2.1. Pine forest and clearing observation sites (see complete figure caption below).

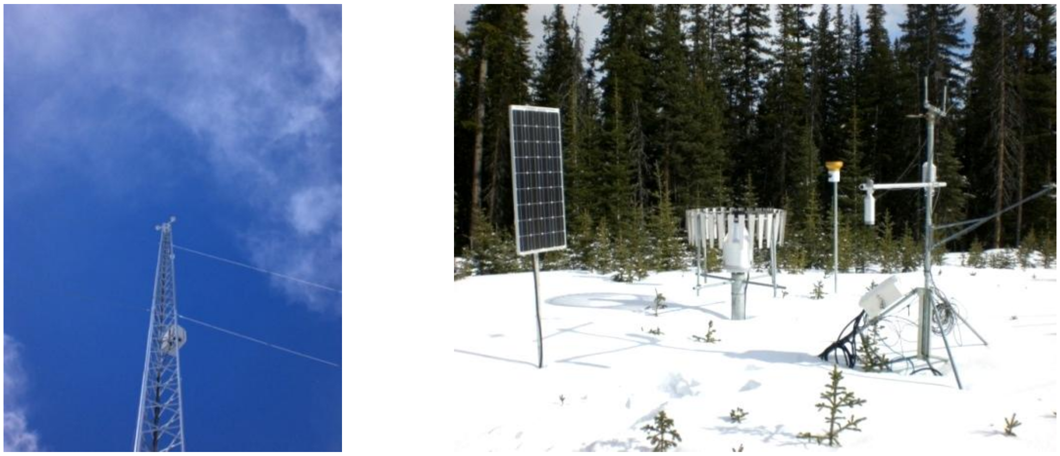

Level Spruce Clearing site (LSC) showing tower for observations reference radiation (left) and near-surface meteorological observation installation (right).

Level Spruce Forest (LSF)

North-facing Spruce Forest (NSC)

South-facing Spruce Forest (SSC)

Figure 2.1. Spruce forest and clearing observation sites (see complete figure caption below).

North-facing Spruce Clearing (NSC) South-facing Spruce Clearing (SSC)

Figure 2. 1. Top: Map of the Marmot Creek Research Basin (MCRB) showing the locations of the following observation sites: the Level Pine Clearing (LPC), Level Pine Forest (LPF), North-facing Pine Forest (NPF), Southeast-facing Pine Forest (SPF), Southeast-facing Pine Clearing (SPC), Level Spruce Clearing (LSC), Level Spruce Forest (LSF), North-facing Spruce Forest (NSF), South-facing Spruce Forest (SSF), North-facing Spruce Clearing (SSC), and South-facing Spruce Clearing (NSC). Inset indicates the general location of the MCRB. Bottom: pictures of the observation sites, showing the main meteorological installations at each.

Table 2. 1. Topographic and forest-cover descriptions of the Level Pine Clearing (LPC), Level Pine Forest (LPF), North-facing Pine Forest (NPF), Southeast-facing Pine Forest (SPF), Level Spruce Clearing (LSC), North-facing Spruce Clearing (NSC), North-facing Spruce Forest (NSF), South-facing Spruce Clearing (SSC), and South-facing Spruce Forest (SSF).

Site:	***Abbreviation***	***Observation Period***	***Elevation* [m.a.s.l.]**	***Slope/ Aspect* [º]**	***Forest height* [m]**	***LAI`* $[m^2\ m^{-2}]$**	***Sky view* []**
Level Pine Clearing	LPC	Jan 05 – present	1457	0/0	0	0	0.94
Level Pine Forest	LPF	Mar 05 – present	1528	0/0	~15	1.4	0.22
North-facing Pine Forest	NPF	Mar 05 – May 07	1480	29/351	~15	1.5	0.19
Southeast-facing Pine Clearing	SPC	Mar – Jun 05, Mar – Apr 06	1566	28/150	0	0	0.92
Southeast-facing Pine Forest	SPF	Mar 05 – May 07	1563	26/146	~16	1.3	0.33
Level Spruce Clearing	LSC	Jun 05 – present	1850	0/0	0*	0*	0.92*
North-facing Spruce Clearing	NSC	No observations	2026	32/333	0*	0*	0.83*
North-facing Spruce Forest	NSF	Oct 07 – present	2024	31/331	~17	2.3	0.21
South-facing Spruce Clearing	SSC	No observations	2026	29/177	0*	0*	0.81*
South-facing Spruce Forest	SSF	Oct 07 – present	2021	28/174	~15	2.5	0.16

*in reference to the centre of the forest clearing.

2.3. Climate

The mean annual precipitation at the MCRB ranges from less than 600 mm at lower elevations to greater than 1100 mm at the higher reaches of the Twin Creek sub-basin, of which approximately 70 – 75 % is received as snowfall (Storr, 1967). However, no permanent snowpack or glaciers are present in the MCRB. Mean monthly air temperatures range from 14 ºC during the warmest month of July to -10 ºC during the coldest month of January (Figure 2.2), with differences in air temperature by elevation giving a mean environmental lapse rate of 0.58 ºC per 100 m. The mean monthly relative humidity typically ranges between 50 – 75 % for all elevations (Figure 2.3), with a pronounced drop in humidity during mid-summer periods. Mean monthly reference shortwave and longwave irradiances (i.e. irradiance to a level clearing site) are approximately 150 W m^{-2} and 268 W m^{-2}, respectively, with shortwave irradiance ranging from approximately 50 W m^{-2} during the winter to over 250 W m^{-2} during summer periods (Figure 2.4).

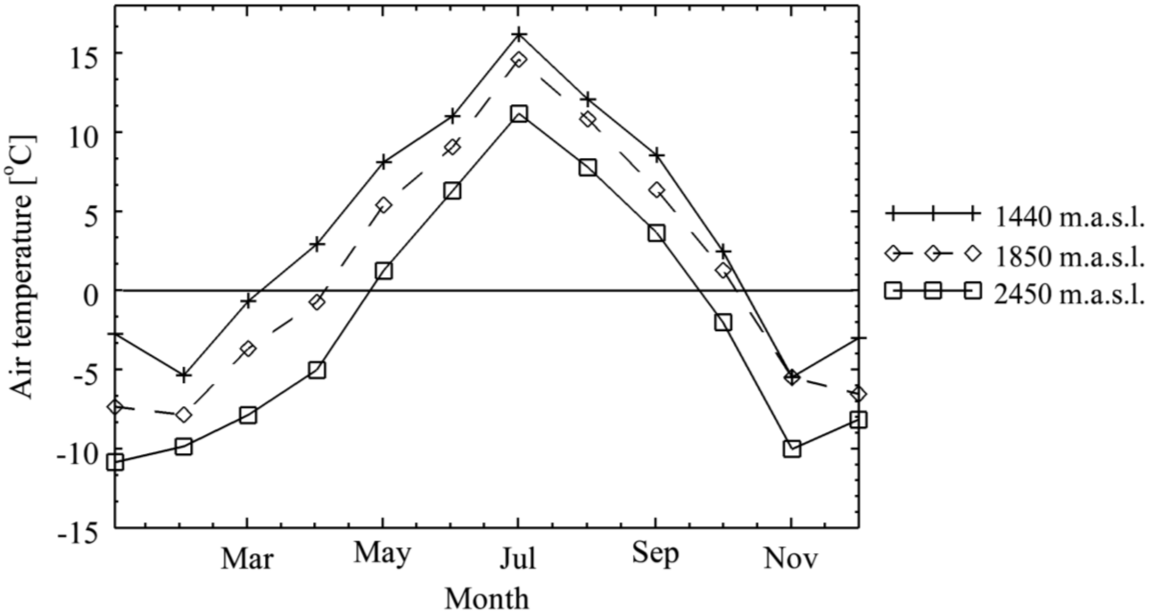

Figure 2. 2. Mean monthly air temperatures at elevations of 1440, 1850, and 2450 m.a.s.l. at the MCRB, 2005 – 2008.

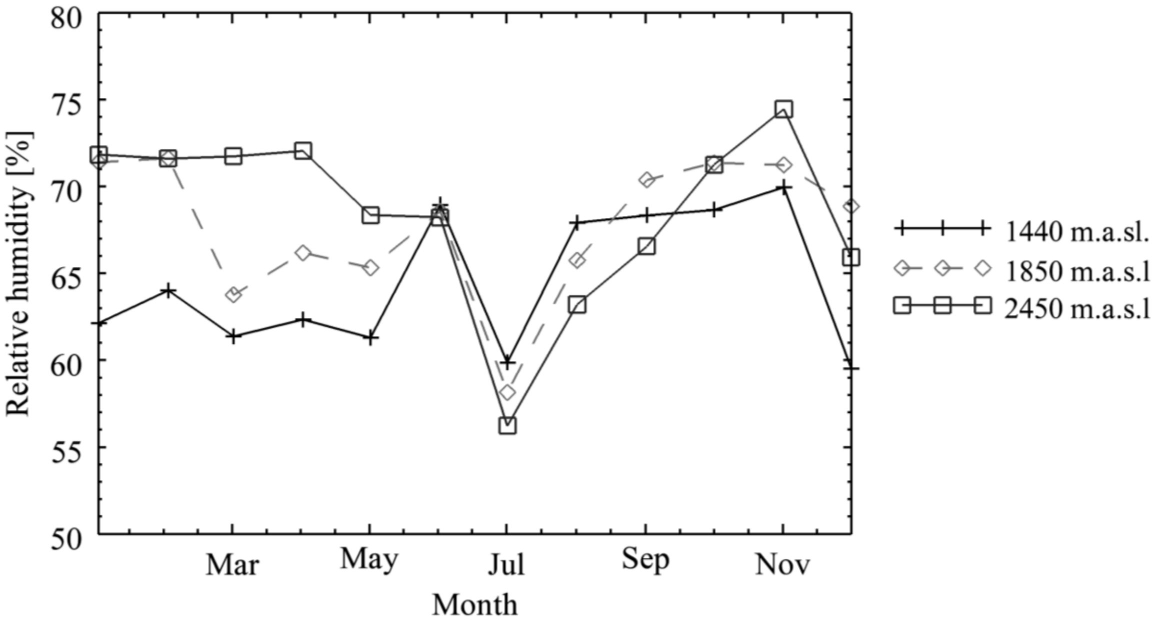

Figure 2. 3. Mean monthly relative humidity at elevations of 1440, 1850, and 2450 m.a.s.l. at the MCRB, 2005 – 2008.

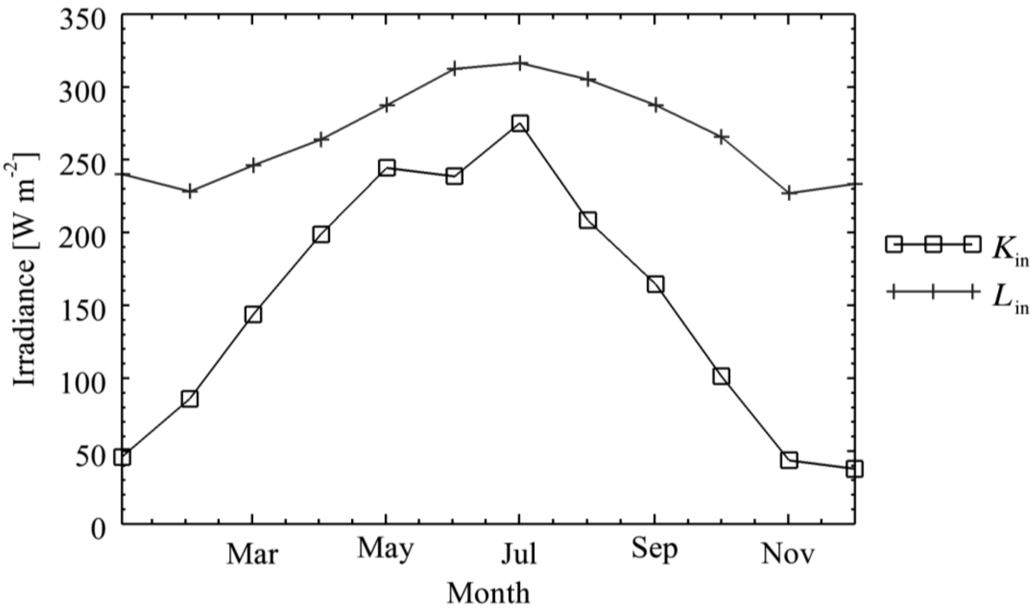

Figure 2. 4. Mean monthly shortwave irradiance (K_{in}) and longwave irradiance (L_{in}) observed at the MCRB, 2005 – 2008.

2.4. Instrumentation

At all meteorological observation sites, measurements of radiation, air temperature, relative humidity, wind speed, wind direction, snow depth, and snow surface temperature, as well as trunk and crown temperatures were made at instrumented tower installations partly dug into the ground and stabilised through guy wiring to ground anchors. Measurements of ground heat flux, ground temperature and moisture throughout the top 30 cm of the soil profile were made within soil pits located near each site tower. Meteorological observations were acquired at a 10 sec sampling frequency, with time-averaged values recorded at 15 min intervals for tower instrument observations, and 4 hr intervals for soil pit instrument observations. All instruments were controlled and measurements stored using Campbell scientific data loggers (models 10X and 23X). At the SPF site, an AM 16/32 relay multiplexer was installed to facilitate the operation of the large amount of instrumentation at the site by a single data logger. The sections below give a brief description of the meteorological instrumentation and their installation at the MCRB observation sites, with technical specifications for radiometers given in Table 2.2, and specifications for other meteorological instrumentation in Table 2.3.

2.4.1. Radiation observations

At all forest and clearing sites, separate measurements of incoming and outgoing fluxes of shortwave radiation (K_{in}, K_{out}) and longwave radiation (L_{in}, L_{out}) were made using recently calibrated pyranometers and pyrgeometers. Radiometers at all observation sites were positioned inclined parallel to their respective ground surfaces; thus radiation fluxes are always expressed in terms of the direction normal to the ground surface. Incoming and outgoing shortwave and longwave fluxes were measured separately over snow at each site by single Kipp and Zonen radiometers, with the exception of the SPF site where two additional upward-facing shortwave and longwave sensors were installed to better characterise the heterogeneous forest-cover. All radiometers were positioned at locations in each site representative of the surrounding forest-cover density based on analysis of hemispherical photographs.

Table 2. 2. Technical specifications of radiometers deployed at the meteorological observation sites (expected instrument accuracies are stated as according to manufacturer specifications).

Radiation Flux	***Sensor model***	***Employed at site***	***No. sensors/site***	***Sensor class****	***Spectral range***	***Expected accuracy (for daily totals)***
K_{in}/K_{out}	Kipp & Zonen CM-3 pyranometer	LPC, LPF, NPF, SPF, NSF, SSF	2	2	305 – 2800 nm	± 10 %
L_{in}/L_{out}	Kipp & Zonen CG-3 pyrgeometer	LPC, LPF, NPF, SPF, NSF, SSF	2	2	5 – 50 μm	± 10 %
K_{in}	Kipp & Zonen CM-5 pyranometer	SPF	2	2	300 – 2800 nm	± 10 %
L_{in}	Kipp & Zonen CG-1 pyrgeometer	SPF, LSC	2	2	5 – 42 μm	± 10 %
L_{in}	Kipp & Zonen CM-21 pyranometer	SPC, LSC	1	1	305 – 2800 nm	± 2 %

*according to World Meteorological Organization (WMO) standard.

At the LPF and SPF sites, additional measurements of K_{in} and L_{in} were made by a 10-pyranometer and a 12-pyrgeometer array to provide a better representation of the spatial variation in sub-canopy fluxes at these sites (Figure 2.5). At both sites, paired pyranometers and pyrgeometers of the array were positioned randomly under forest-cover upon the snow surface, and were controlled by a portable data logger unit (Figure 2.6). Observations of radiation were averaged and stored at 5 min intervals for the period of DOY 67 – 74 at the SPF and DOY 74 – 78 at the LPF. To account for slope effects at the SPF site, array radiometers were inclined normal to the force of gravity from DOY 67 – 71, and inclined parallel to the slope from DOY 71 – 74. During both the LPF and SPF array observation periods, K_{in} and L_{in} reference observations were also made in a nearby level clearing by a single pyranometer-pyrgeometer pair (Figure 2.7).

Figure 2. 5. Paired pyranometer and pyrgeometer radiometers shown inclined with the ground slope at the Southeast-facing Pine Forest site (SPF) (left), and at the Level Pine Forest site (LPF) (right).

Figure 2. 6. Portable data logger system used in the control of array radiometer sensors and data recording.

Figure 2. 7. Paired pyranometer-pyrgeometer sensors at nearby clearing for observations of reference shortwave and longwave irradiance.

In forest environments, the determination of net shortwave radiation to snow from pyranometer observations is made difficult by the presence of exposed vegetation and leaf litter within the view of the downward facing sensor. To minimize these errors, periodic snow reflectance measurements were obtained at the forest sites using an *ASD FieldSpect Pro* portable spectroradiometer (Figure 2.8). This device provides light reflectance measurements by a 512-channel silicon photodiode array at a spectral resolution of approximately 1.4 nm across a visible/near-infrared band of 350 – 1050 nm. Spectroradiometer measurements were collected via a fibre-optic lead housed within a fore-optic device (shown held in Figure 2.8) having a field of view of 8°, from which reflectance of snow was determined relative to that of measurements over a white reference surface.

Figure 2. 8. Picture of portable spectroradiometer (model *ASD FieldSpect Pro*) showing the main spectroradiometer unit, fore-optic lead device, and laptop used in device operation.

2.4.2. Air temperature and humidity

Observations of within-canopy air temperature and humidity were made using Vaisala HMP35C and HMP45C hygrothermometers, having an expected temperature error of ±0.2 °C at 20 °C (Vaisala (Campbell Scientific) technical manual, 2008). Sensors were installed at approximately 2 m height from the ground surface at each site and housed within white gill shields to minimise measurement errors from shortwave heating. This is with the exception of the LPF, NPF, and SPF sites during the winter of 2005-06, when hygrothermometer probes were instead housed within fan-ventilated enclosures to reduce shortwave heating.

2.4.3. Snow and forest surface temperature

Measurements of snow surface, forest crown, and trunk surface temperatures were made using Exergen IRt/c.5-K-50F/10C (capacitor removed) infrared thermocouples (IRt/c), having a field of view of 5:1 and an expected sensor error of less than ±0.5 °C of true temperature (Omega IRt/c operator’s manual, 1994). To reduce measurement errors from shortwave heating, thermocouples were housed within enclosures covered by reflective taping (Figure 2.9). Trunk surface temperature measurements were also made of south-exposed trunk surfaces at the forest sites, and the north-exposed trunk surface at the SPF site.

Figure 2. 9. Installations of infrared thermocouples measuring trunk surface temperature (left) and crown foliage temperatures (right).

2.4.4. Wind speed and direction

At the LPC, observations of open site wind speed and direction were made by a RM Young propeller wind-vane anemometer with a specified starting threshold of 1 m s^{-1}. (RM Young (Campbell Scientific) operation manual, 2009). In contrast, the relatively low wind speeds at the forest sites were measured using sonic-based anemometers of a reduced starting threshold of 0.1 m s^{-1} (Met One 50.5 (Campbell Scientific) instrumentation manual, 2001). However, intermittent failure of the sonic anemometers required the temporary installation of met one 3-cup anemometers at the LPF, NPF and SPF over the 2006-07 season, of starting thresholds equal to 0.45 m s^{-1}. Anemometers at all sites were installed at the same height as the hygrothermometers for the purpose of calculating sensible and latent heat fluxes.

2.4.5. Soil heat flux, soil temperature and soil moisture

At each observation site, measurements of soil heat flux, temperature, and moisture content were made by instrumentation installed within dug and backfilled soil pits. Soil heat flux measurements were made using a HFT-3 heat flux plate positioned at depth corresponding to the mineral soil-organic soil interface (which ranged from approximately 3 – 7 cm depth among sites), and orientated parallel to the ground surface. Soil temperature and moisture were measured respectively along the soil profile depth using Fenwal thermister and CS616 reflectometer probes positioned 5, 15 and 30 cm below the ground surface.

2.4.6. Precipitation

Within the MCRB, precipitation was measured using Geonor T-200 all-weather precipitation gauges at the LPC and LSC sites housed within Alter shields to reduce potential measurement errors resulting from wind-under catch. Such all-weather gauges provide measurement of both rainfall and snowfall through the collection and retention of precipitation within an enclosed drum, from which a precipitation depth is determined as function of the change in drum weight measured by an internal vibrating wire load sensor (Geonor technical manual, 2009). Tipping bucket gauges were also installed at these sites to permit the differentiation between rain and snow phases of precipitation.

Table 2. 3. Technical specifications of instrumentation (excluding radiometers) deployed at meteorological observation sites. Expected instrument accuracies are stated as according to manufacturer specifications.

Variable	***Sensor model***	***Deployed at sites:***	***No. sensors/ site***	***Measurement Range***	***Expected accuracy (for daily values)***
Air temperature/ humidity	Vaisala HMP45C212 & HMP35C	All	1	temperature: -50 – 50 ºC humidity: 0 – 10 %	temperature: ± 0.1 ºC humidity: ± 2 – 3 %
Precipitation	Geonor T-200	LPC, LSC	1	1000 – 1500 mm capacity	0.05 – 0.1 mm
Precipitation	TR-525i Tipping Bucket Rain Gauge,	LPC, LSC	1	1 pulse/0.25 mm	1 % – 50 mm hr^{-1}
Wind speed/direction	Metone 50.5 2-D sonic anemometer	LPF, SPF, NPF, NSF, SSF	1	0 – 50 m s^{-1} (stall speed: 0.1 m s^{-1})	speed: ± 0.5 m s^{-1} (≤ 5 m s^{-1}) direction: ± 3º
Wind speed/direction	Met One 014A 3-cup anemometer	SPF, LSC	1	0 – 45 m s^{-1} (stall speed: 0.45 m s^{-1}	0.11 m s^{-1}
Wind speed/direction	RM Young 05103 Propeller anemometer	LPC	1	0 – 100 ms^{-1} (stall speed: 1.0 m s^{-1})	0.3 m s^{-1}
Crown/trunk/snow surface temperature	Exergen IRt/c.5-K-50F/10C (capacitor removed)	All	1	-45 – 650 ºC	0.01 ºC (at 0 ºC); 2 ºC (at 24 ºC)
Snow depth	SR50	All	1	0.5 – 10 m	± 1 cm (or 0.4 % of reading)
Soil heat flux	HFT-3	All	1	± 100 W m^{-2}	greater than 5 % of reading
CS616	Water content reflectometer CS616	All	3	0 – 50 % vwc	± 2.5 % vwc
Soil temperature	Thermistor Fenwal 107B	All	3	-35 – 50 ºC	± 0.2 ºC

2.4.7. Snow depth and density

At all observation sites, snow depth was determined via both time-continuous point measurements from a SR50 sonic depth gauge and manual snow surveys along established transects at a sampling spacing of approximately 2 m at clearing sites, and 1 m at forest sites. Through the establishment of regression relationships between sonic gauge and snow survey depths, a dataset of time-continuous and spatially representative snow depths for each site was constructed. Measurements of snow density were derived from snow mass samples taken approximately every fifth snow survey depth using an ESC-30 snow tube and calibrated weight scale, or alternatively, using a Perla-type 'RIP' volumetric snow cutter from which samples were taken along a snow pit profile and weighed in the field using an electronic balance (Figure 2.10). Comparison of snow tube density measurements to those obtained by a volumetric snow cutter indicate a good agreement between the two sampling methods (Figure 2.11), having an average absolute difference of 11.8 kg m^{-3}, with densities from the calibrated snow tube scale giving a systematic 4 % under-prediction of snow cutter density values. From point measurements of snow depth and density, determination of the spatially-representative snow water equivalent ($\overline{\mathrm{SWE}}$) [kg m^{-2}] at each site was made using the following adaptation of Pomeroy and Gray's (1995) expression:

$$\overline{\mathrm{SWE}} = \frac{\overline{\rho_\mathrm{s}}}{\rho_\mathrm{w}} \overline{h_\mathrm{s}} + \mathrm{cov}(\rho_\mathrm{s}, h_\mathrm{s}) \qquad \textbf{(2.1)}$$

where $\overline{\rho_\mathrm{s}}$ is the mean snow density [kg m^{-3}], ρ_w is the density of liquid water [kg m^{-3}], $\overline{h_\mathrm{s}}$ is the snow depth [m], and cov(ρ_s,h_s) denotes the covariance between ρ_s and h_s.

Figure 2. 10. Methods used for measuring snow density in the field: ESC-snow tube weighted by calibrated spring scale (left), and volumetric snow cutter from sample taken from dug snow pit weighted by electronic balance (right) (left photo courtesy of X. Fang).

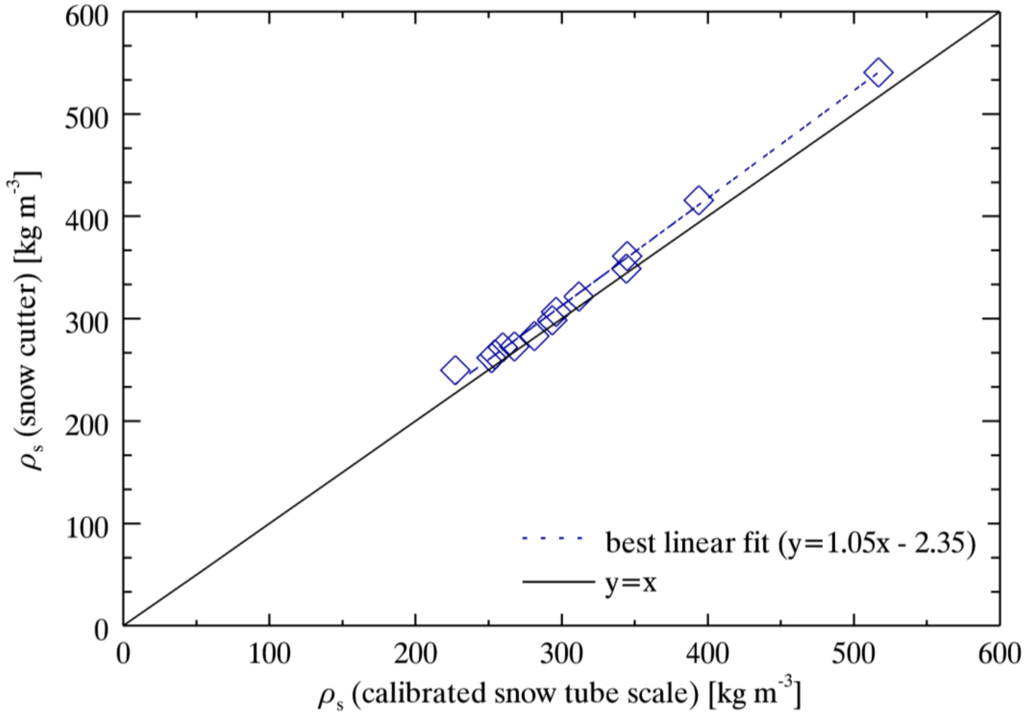

Figure 2. 11. Comparison between snow density (ρ_s) determinations from a calibrated ESC-30 snow tube and a volumetric snow cutter from samples obtained in forest and clearing sites.

2.4.8. Description of forest-cover

In order to quantify forest-cover density through non-destructive means, estimates were made from hemispheric photographs taken at each site using a Nikon Coolpix 5000 digital camera fitted with a 183° field of view fisheye converter lens. Forest-cover density was estimated through analysis of hemispherical photographs using GLA 2.0 software (Frazer et al., 2000), which computes the angular distribution of gap and non-gap fractions of a hemispherical forest scene by its division into 'sky' and 'non-sky' classes. Hemispherical photograph analysis was also performed using CANEYE software (Baret and Weisse, 2004) to provide additional information regarding the composition of the forest stand, including the relative amounts of green needleleaf and trunk foliage as determined via a colour-based classification scheme. Figure 2.12 shows a hemispherical photograph of the overlying forest scene at the LPF site and the corresponding post-processed image from CANEYE with colour classification of green crown foliage, trunk and branches, and open sky.

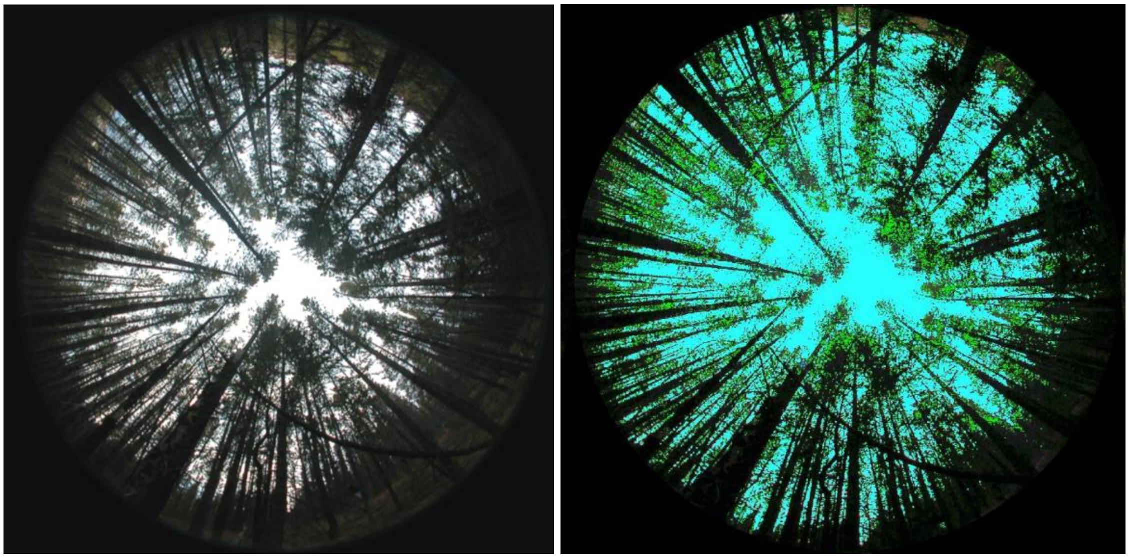

Figure 2. 12. Hemispherical photograph of overlying forest-cover at the Level Pine Forest site (LPF) (left) and corresponding post-processed image using CANEYE software showing colour classification of crown needleleaf foliage in green, trunks and branches in black, and sky in turquoise (right).

3. OBSERVATIONS OF FOREST-COVER EFFECTS ON RADIATION AND SNOWMELT

3.1. Chapter summary

Utilising extensive field observations, the effect of needleleaf forest-cover on radiation and snowmelt timing was quantified at pine and spruce forest sites and nearby clearings of varying slope and aspect in the MCRB. Compared to clearing sites, shortwave radiation was much reduced in forests, resulting in smaller differences in melt timing between opposing forest slopes relative to corresponding open slopes. In contrast, longwave radiation to snow was substantially enhanced under forest-cover, especially at the dense spruce forest sites where longwave radiation dominated total energy for snowmelt. At both pine and spruce locations, forest-cover substantially reduced total radiation to snow and delayed snowmelt on south-facing slopes, while increasing total radiation and advancing snowmelt on north-facing slopes. However, forest-cover effects were less pronounced on level terrain, where forest radiation and snowmelt rates were only slightly less than in the open. Forest-cover is also observed to greatly affect the magnitude of spring snowmelt by reducing forest snow accumulations through canopy sublimation losses, which decreased peak forest accumulations roughly half of those in open environments.

3.2. Chapter introduction: radiation to forest snowcover

Snowmelt is one of the most important hydrological events in mountain regions, responsible for soil moisture recharge (e.g. Grant et al., 2004), vegetation growth (e.g. Cooper et al., 2006) and ecosystem productivity (e.g. Arp et al., 2006). Mountain snowmelt is the source of the majority of river flows in western North America (Marks and Winstral, 2001) and are hence of great importance to downstream water users. As much of North American mountain terrain is covered by evergreen needleleaf forest, turbulent energy exchanges to sub-canopy snowcovers are suppressed (Harding and Pomeroy, 1996) and snowmelt is driven primarily by radiation (United States Army Corps of Engineers, 1956). This is with exception of more coastal mountain environments where large amounts of snowmelt energy may be delivered through rainfall, having the potential to cause rapid melt and flooding (Beaudry and Golding, 1983; Marks et al., 1998; Mazurkiewicz et al., 2008). However, for interior mountain ranges, effective prediction of the timing and magnitude of snowmelt runoff is expected to require an understanding of how needleleaf forest-cover influences radiation for snowmelt across complex terrain. Extensive field studies by Golding and Swanson (1978) and Troendle and Leaf (1981) have shown the timing and rate of snowmelt to differ substantially between level forests and clearings. Yet, comparatively less has been reported regarding the combined effects of forest-cover with slope and aspect on mountain snowmelt. Such information is expected to be important in anticipating how the changes in forest-cover (e.g. clear cutting, fire, disease) may impact the timing of snowmelt in mountain regions (Gary, 1980).

Quantification of net all-wave radiation to snow (R^*) is made by the sum of net shortwave (K^*) and net longwave (L^*) balances, each composed of incoming and outgoing fluxes, i.e.

$$R^* = K^* + L^* = K_{\mathrm{in}} - K_{\mathrm{out}} + L_{\mathrm{in}} - L_{\mathrm{out}} \tag{3.1}$$

Here, K^* is related to K_{in} by the snow albedo (α_{s}) through

$$K^* = K_{\mathrm{in}} - K_{\mathrm{out}} = K_{\mathrm{in}}(1 - \alpha_{\mathrm{s}}) \tag{3.2}$$

Forest-cover has been observed to have a countering effect on radiation to snow by reducing shortwave irradiance via canopy extinction (i.e. reflection and absorption) (Link and Marks, 1999) while increasing longwave irradiance from foliage thermal emissions (Black et al., 1991; Reifsnyder and Lull, 1965). Here, the reduction of shortwave irradiance in forests is commonly expressed in terms of the forest shortwave transmittance (τ)

$$\tau = \frac{K_{\mathrm{in}}}{K_{\mathrm{o}}} \tag{3.3}$$

where K_{in} and K_{o} denote the sub-canopy and above-canopy shortwave irradiance fluxes, respectively. The offsetting of shortwave reductions in forests by canopy longwave emissions is promoted particularly during conditions of high snow albedo (Jeffrey, 1970) and in high latitudes or altitude environments where atmospheric longwave emissions are relatively low (Sicart et al., 2004).

Although much focus has been placed on quantifying radiation for snowmelt in level needleleaf forests (e.g. Gryning and Batchvarova 2001; Metcalfe and Buttle, 1995), how variations in topography (i.e. slope and aspect) and forest-cover control radiation to snow in mountain systems is comparatively lacking in the literature. Such information would improve the understanding of how radiation to snow varies across complex terrain and help identify needs for future developments of spatially distributed snowmelt models (e.g. Marks et al., 1999; Stork et al., 1998).

The primary objective of this chapter is to quantify the effects of both forest-cover and topography on radiation to snow and the timing of snowmelt in mountain environments. Particular focus will be placed on examining how topography and forest-cover determine the relative amounts of shortwave and longwave radiation to snow, as well as their contributions to snowmelt energy in low-elevation pine stands and high-elevation spruce stands. This will be accomplished through analysis of radiation and other field meteorological observations, as well as snow survey data collected at paired forest-clearing sites of varying elevation and slope orientation in the MCRB. Although analysis relies primarily upon field observations, appropriate corrections and estimations of radiation fluxes and meteorological variables are made where necessary.

3.3. Observations of radiation, snow accumulation and melt

Within this chapter, analysis focuses primarily upon near-surface meteorological observations and corresponding snow measurements collected over the spring of 2005 at pine forest and clearing sites, and the spring of 2008 at the spruce forest and clearing sites. To allow a comparison of radiation and snowmelt between a greater number of paired sloped forest-clearing sites, simulations of shortwave irradiance were made to a hypothetical North-facing Pine Clearing (NPC), assigned the same slope gradient and aspect as the NPF. Similar simulations were also made to the non-instrumented NSC and SSC clearing sites based on the calculation procedure outlined in Appendix A. Analysis of the 2005 pine and 2008 spruce meteorological and snow survey datasets focuses on two primary observation periods: (i) the *spring* observation period spanning from February 15 – May 15 at both pine and spruce sites, allowing a comparison of meteorological conditions over the same seasonal period, and (ii) the period of *snowpack warming and melt*, extending from March 13 – April 4, 2005 (DOY 72 – 95) at the pine sites, and from March 30 – May 29, 2008 (DOY 90 – 150) at the spruce sites. Reference meteorological conditions observed at the LPC and LSC sites during the respective February – May *spring* observation periods as well as *snowpack warming and melt* periods are given in Table 3.1.

As described in Section 2.4.7, measurements of snow water equivalent (SWE) at each site were obtained from surveys of snow depth and density repeated approximately every 2 – 3 weeks prior to snowmelt and every 2 – 3 days during snowmelt. Snow depth measurement were made along established transects at a sampling spacing of approximately 2 m at the clearing sites, and a spacing of about 1 m at the forest sites to account for the greater spatial variation of forest snow depth.

Representation of site irradiance by observations from fixed-position radiometers

Instructive assessment of forest-cover effects on irradiance and snowmelt processes through analysis of field data requires that these observations provide a suitable representation of the site from which they are collected. Acquisition of site-representative observations of K_{in} or L_{in} under forest-cover is made difficult not only from instrument errors, but also sampling errors caused by the large spatial variation in sub-canopy irradiance typical of many forest stands (Link et al. 2004; Essery et al., 2007; Pomeroy et al., 2008). Such instrument and sampling errors may be either random or systematic in nature (Moore and Rowland, 1990); however, for this study, due to the use of recently calibrated radiometers at all sites, systematic instrument errors were considered minimal, leaving random instrument errors which are specified according to the manufacturer in Table 2.2. Alternatively, to assess the degree of potential instrument sampling bias, K_{in} and L_{in} observations from the permanent, fixed-position *site* radiometers were compared to observations collected by a 10-pyranometer, 12-pyranometer *array* at the LPF and SPF sites, which were made at these sites due to their heterogeneous canopy-coverage.

At both the LPF and SPF, *array* radiometers were positioned randomly around the fixed-position *site* radiometers, and located at varying proximity to forest trunks. Quantification of the differences between *site* and *array* sub-canopy irradiance observations is made by the mean bias (MB) coefficient between the irradiance values, as determined by:

$$\mathrm{MB} = \frac{\sum_{t=0}^{t=n} I_{\mathrm{in}}\ (array)}{\sum_{t=0}^{t=n} I_{\mathrm{in}}\ (site)} \qquad \textbf{(3.4)}$$

where I_{in} denotes either K_{in} or L_{in}, and $t = 0$ to $t = n$ correspond to the first and last data values over the period of *array* observations. In general, determined MB values for K_{in} and L_{in} over daily time scales and the entire period indicate a near stable bias between *site* and *array* observations at both the LPF and SPF sites (Table 3.2). Accordingly, at each site, K_{in} and L_{in} observations over the *spring* and *snowpack warming and melt* periods are corrected by the overall MB in Table 3.2 by

$$\text{corrected } I_{\mathrm{in}} = \text{observed } site\ I_{\mathrm{in}} \times \mathrm{MB} \qquad \textbf{(3.5)}$$

Although uncertainty exists to the degree to which the determined MB values represent *site-array* differences over seasonal time scales, these shifts may be limited considering the stability of sub-canopy irradiance patterns observed over extended time periods (Pomeroy et al., 2008; Essery et al., 2008).

3.3.1. Radiation observations

Shortwave irradiance (K_{in})

Over the February – May *spring* period at both the pine and spruce forest locations, mean daily shortwave irradiance (K_{in}) between sites varied substantially, ranging from approximately 1.5 MJ m^{-2} at the north-facing NPF and NSF forests, to greater than 15 MJ m^{-2} at the south-facing SPC and SSC clearings; which are equal to corresponding ratios of 0.1 and 1.2 that observed at their respective level clearings (LPC and LSC sites) (Table 3.3). In general, forest-cover greatly reduced the absolute differences in K_{in} produced by slope orientation effects, especially between the spruce forest sites where the low forest shortwave transmittances (τ) of 0.12 at the NSF and 0.11 at the SSF gave corresponding low daily K_{in} daily values of 1.5 and 1.7 MJ m^{-2}. By comparison, shortwave transmittances exhibited much greater variation among the pine forest sites, with mean τ values ranging from 0.34 at the SPF to 0.13 at the NPF, and corresponding daily K_{in} magnitudes of 5.4 and 1.4 MJ m^{-2} (Table 3.3).

Table 3. 1. Summary of mean daily meteorological conditions observed at the Level Pine Clearing (LPC) and Level Spruce Clearing (LSC) reference sites over the respective 2005 pine and 2008 spruce *spring* observation periods and periods of *snowpack warming and melt*.

Site	*Period*	*Shortwave irradiance* (K_{in})	*Longwave irradiance* (L_{in})	*Relative humidity*	*Air temperature* (T_a)
		[MJ m^{-2}]	[MJ m^{-2}]	[%]	[°C]
Level Pine Clearing (LPC)	*spring* (2005, DOY 46 – 135)	13.2	23.4	62	2.4
Level Pine Clearing (LPC)	*snowpack warming and melt* (2005, DOY 74 – 95)	12.1	23.0	60	0.9
Level Spruce Clearing (LSC)	*spring* (2008, DOY 46 – 136)	14.5	21.5	66.2	-1.3
Level Spruce Clearing (LSC)	*snowpack warming and melt* (2008, DOY 90 – 150)	15.1	22.5	63.4	-3.4

Table 3. 2. Mean bias (MB) of daily shortwave irradiance (K_{in}) and longwave irradiance (L_{in}) from *site* radiometers observations at the Level Pine Forest site (LPF) and the Southeast-facing Pine Forest site (SPF) as determined by comparison to irradiance observed by a multi-sensor radiometer *array*. Also stated are the mean K_{in} and L_{in} over the period, and the mean difference in K_{in} and L_{in} between *site* and *array* radiometers.

DOY:	*67*	*68*	*69*	*70*	*71*	*72*	*73*	*74*	*75*	*76*	***Overall Mean Bias Index (MB)***	*Mean daily irradiance (array)* [MJ m^{-2}]	*Mean daily irradiance (site)* [MJ m^{-2}]	*array-site irradiance* [MJ m^{-2}]
K_{in} MB (SPF)	0.99	0.98	0.98	0.96	0.95	0.98	0.97	–	–	–	**0.98**	4.56	4.70	0.14
L_{in} MB (SPF)	1.03	1.03	1.06	1.07	1.06	1.03	1.03	–	–	–	**1.04**	25.2	24.2	1.00
K_{in} MB (LPF)	–	–	–	–	–	–	–	0.99	0.99	0.99	**0.99**	2.50	2.47	0.03
L_{in} MB (LPF)	–	–	–	–	–	–	–	1.00	1.02	1.00	**1.01**	24.9	24.7	0.20

Table 3. 3. Mean daily shortwave irradiance (K_{in}) at each observation site for February 15 – May 15 *spring* period and the ratio of irradiance at the corresponding level reference site (*). Also stated for the forest sites is the forest shortwave transmittance (τ) for the period.

Site	Mean daily K_{in} [MJ m^{-2}]	Ratio to level reference site []	Forest shortwave transmittance (τ) []
*LPC	13.2	1	–
LPF	2.9	0.22	0.22
NPC	10.5	0.80	–
NPF	1.4	0.11	0.13
SPC	15.8	1.20	–
SPF	5.4	0.41	0.34
*LSC	14.5	1	–
NSC	11.8	0.81	–
NSF	1.5	0.10	0.12
SSC	16.4	1.13	–
SSF	1.7	0.12	0.11

Among the pine forest sites, the high shortwave transmittance (τ) at the SPF resulted a notable increase in daily sub-canopy K_{in} with above-canopy K_o (i.e. K_{in} at the LPC reference site), but little to no such relation at the lower transmitting LPF and NPF sites. Consequently, differences in daily sub-canopy K_{in} between the pine forest sites progressively increase with above-canopy K_o, as seen in the observations over a 4-week, April period in Figure 3.1. By comparison, the low τ of spruce forest-cover results in little response in sub-canopy K_{in} at either the north-facing NSF or south-facing SSF site to changes in above-canopy K_o (i.e. K_{in} at the LSC reference site) (Figure 3.2). Consequently, similarly low magnitudes of sub-canopy K_{in} are maintained at both the NSF and SSF sites regardless of fluctuations in above-canopy K_o.

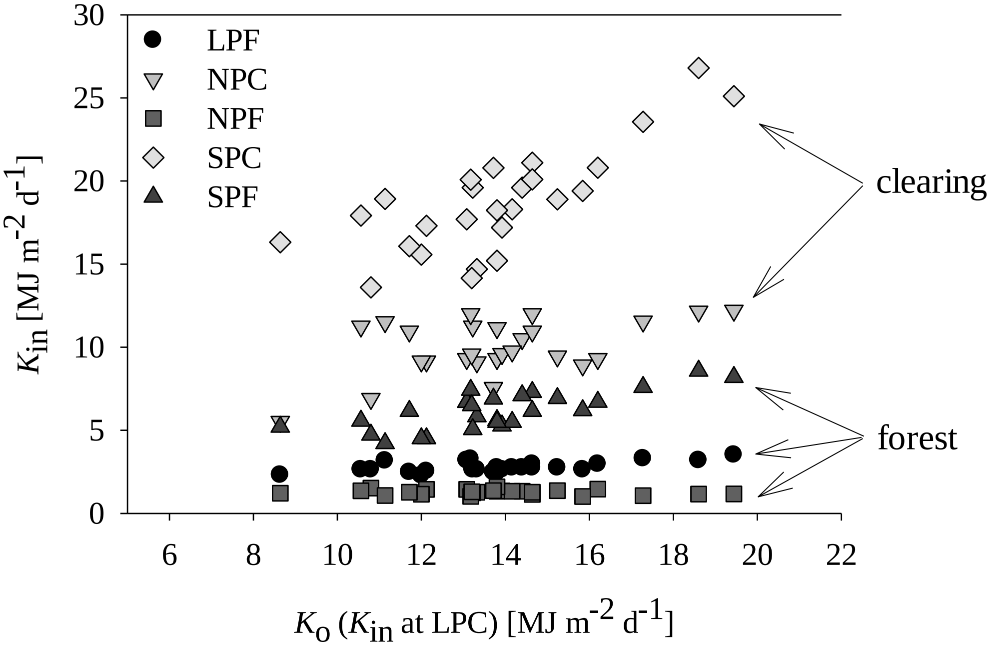

Figure 3. 1. Relation between the daily above-canopy shortwave irradiance (K_o) as observed at the Level Pine Clearing (LPC) compared to sub-canopy irradiance (K_{in}) observed at the Level Pine Forest (LPF), the Southeast-facing Pine Clearing (SPC), the Southeast-facing Pine Forest (SPF), the North-facing Pine Forest (NPF), and simulated at the North-facing Pine Clearing (NPC) for the period of April 3 – April 29, 2005.

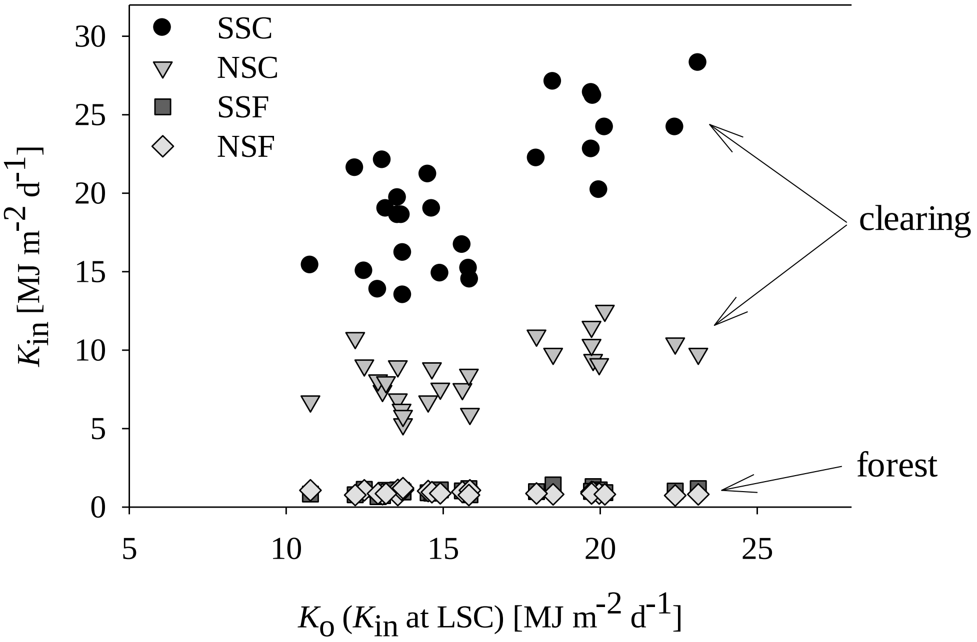

Figure 3. 2. Relation between the daily above-canopy shortwave irradiance (K_o) observed at the Level Spruce Clearing (LSC) site compared to sub-canopy irradiance (K_{in}) observed at the North-facing Spruce Forest (NSF) and South-facing Spruce Forest (SSF) sites, and simulated K_{in} at the North-facing Spruce Clearing (NSC) and South-facing Spruce Clearing (SSC) sites for the period of April 3 – April 29, 2008.

Longwave irradiance (L_{in})

As a result of canopy longwave radiation emissions, longwave irradiance (L_{in}) to snow at the forest sites was much greater than at the clearing sites over the February – May *spring* period (Table 3.4). Note here that as no L_{in} observations were made at the sloped clearing sites, magnitudes at these sites were considered equal to that of their respective level clearing sites (i.e. LPC, LSC), as substantial differences of L_{in} in the open are expected only from variations in longwave emissions from surrounding terrain during clear sky conditions (Sicart et al., 2004). As shown in Table 3.4, despite a lower overall L_{in} at the spruce forest sites relative to the pine forests, the amount of sub-canopy longwave enhancement relative to that above-canopy was similar among all pine and spruce forest sites. Enhancements in sub-canopy longwave are attributed primarily to increased thermal emissions from canopy foliage, which are further increased at the LPF and SPF due to the substantial heating of the canopy above air temperatures. Canopy heating is most pronounced at the SPF, where the sparse canopy combined with the south-facing orientation of the sites allows for increased penetration of shortwave irradiance to the lower trunk layer. As a result, heating of the SPF trunks is greatest during midday periods of high shortwave irradiance, when south-exposed trunks reach temperatures > 20 ˚C warmer than surrounding air temperatures. Similar canopy heating effects and resulting enhancements in sub-canopy longwave have been described and quantified by Pomeroy et al. (2009) in various needleleaf forest stands. However, no noticeable canopy shortwave heating was observed in the spruce forest stands, which is attributed to the extinction of shortwave irradiance higher within the denser canopies prohibiting irradiance and heating of the lower canopy layers.

Net shortwave radiation (K^*)

For sites at which both incoming and outgoing shortwave fluxes were observed, net shortwave radiation (K^*) to snow was determined via Eq. 3.2. However, in forest environments, acccurate determinations of K^* to snow using K_{out} observations are subject to error due to the exposure of dark understory vegetation as snowcover ablates. To minimise such errors, K_{out} observations were used for determining K^* only during times of complete snowcover within the field-of-view of the downward-facing radiometer, as determined from daily field notes and photographs of snowcover at each site during melt. For periods of partial snowcover, K^* was instead estimated through a linear extrapolation of the daily albedo decay rates determined over continous snowcover. Although this method is unlikely to provide an exact representation of the many factors governing snow albedo or the rate of albedo decay over time among sites, it does allow for a general approximation of K^* for the purpose of further analysis.

Table 3. 4. Mean longwave irradiance (L_{in}) at each site for the February 15 – May 15 *spring* period stated in terms of mean irradiance and the ratio of irradiance at the respective level reference site* (note that with the exception of the SPC site, sloped clearing sites are assigned the same L_{in} as their respective level clearing site).

	Longwave irradiance (L_{in})		
Site	Mean [MJ m^{-2} d^{-1}]	Ratio of level reference site []	Difference to level reference site [MJ m^{-2} d^{-1}]
*LPC	22.0	1.0	0.0
LPF	25.9	1.17	3.9
NPC	22.0	1.0	0.0
NPF	26.1	1.18	4.1
SPC	22.2	1.01	0.2
SPF	26.6	1.21	4.5
*LSC	19.8	1.0	0.0
NSC	19.8	1.0	0.0
NSF	24.2	1.22	4.4
SSC	19.8	1.0	0.0
SSF	24.4	1.22	4.4

At the NPC site, α_s was approximated by values observed at the LPC. However, at the NSC and SSC sites, where α_s observations from a nearby clearing were not available, daily α_s was alternatively estimated by regression relations developed between daily forest α_s values from radiometer measurements and α_s at the corresponding clearing site from reflectance measurements obtained using a portable spectroradiometer (Analytical Spectral Devices FieldSpec-FR). Spectroradiometer reflectance measurements were made at the NSC and SSC approximately every 48 hours for a period of 10 days prior to, and following the start of snowmelt (i.e. DOY 130) following the procedure outlined by Melloh et al. (2001) in which 50 spectroradiometer measurements were obtained at each site to reduce random sampling errors and minimise the ratio of noise-to-signal returns. To account for the effects of differential angular reflectance from snow, measurements were obtained over varying orientations to the snow surface. Best approximation of clearing α_s from forest α_s values were made via separate linear regression relations for periods before and after the start of melt (i.e. melt occurring at one or both sites), with strongest relations between paired forest-clearing sites obtained for the pre-melt period (i.e. $R^2 = 0.90$ (NSC-NSF); $R^2 = 0.97$ (SSC-SSF)). By comparison, weaker relations during the melt period ($R^2 = 0.72$ (NSC-NSF); $R^2 = 0.73$ (SSC-SSF)) resulted from the divergence in albedo decay rates for melting and non-melting snow between paired clearing-forest sites. To maintain a realistic representation of snow albedo, estimated α_s values were constrained to a minimum of 0.6, which closely corresponds to the lower limit of values obtained from spectroradiometer measurements over unlittered snow. Also, upon the complete disappearance of snowcover, α_s was set to 0.2 to approximate bare ground albedo.

Net longwave radiation (L*)

Similar to that of reflected shortwave irradiance, no direct observations of longwave exitance from snow (L_{out}) were obtained at the NPC, NSC, and SSC sites. Instead, L_{out} was estimated from snow surface temperatures (T_s) at these sites using the following the longwave-psychrometric formulation by Pomeroy and Essery (2010)

$$T_s = T_a + \frac{\varepsilon_s (L_{in} - \sigma T_a^4) + \lambda_s (\omega_a - \omega_s) \rho_a / r_a}{4 \varepsilon_s \sigma T_a^3 + (c_p + \lambda_s \Delta) \rho_a / r_a} \tag{3.6}$$

where ε_s is the thermal emissivity of snow [0.98] (Oke, 1987), σ is the Stephan-Boltzmann constant [5.67×10^{-8} W m^{-2} K^{-4}], ω_a and ω_s are the respective specific and saturation mixing ratios [], c_p is the specific heat capacity of air [MJ kg^{-1} K^{-1}], ρ_a is the density of air [kg m^{-3}], λ_s is the latent heat of sublimation for ice [MJ kg^{-1}], r_a is the aerodynamic resistance [s m^{-1}], and Δ is the slope of the saturation vapour pressure curve [kPa K^{-1}]. In Eq. 3.6, T_a was approximated from observations at the corresponding forest sites, as well were wind speeds upon account for forest wind sheltering effects. Comparison of simulated T_s to observations at the LPC over a two-week period indicated good estimation by the approach, with mean simulated and observed T_s of -12.5 °C and -13.7 °C, respectively; both substantially colder than the mean air temperature of -8.1 °C over the period.

With estimation of T_s, the net longwave radiation (L*) at each site was resolved as the balance of incoming longwave irradiance to snow and longwave exitance from snow by

$$L^* = \varepsilon_s (L_{in} - \sigma T_s^{\ 4}) \qquad \textbf{(3.7)}$$

Net radiation and ablation rates during periods of snowpack warming and melt

Time series data of snow water equivalent (SWE) and corresponding magnitudes of daily net shortwave (K^*) and daily net longwave radiation (L^*) are shown over the respective periods of *snowpack warming and melt* for the pine sites (2005) in Figure 3.3, and for the spruce sites (2008) in Figure 3.4. Here, comparison between pine and spruce sites reveals a marked difference in snow accumulations, with those at the higher elevation spruce location approaching five-fold the accumulations at the lower elevation pine sites. Although it must be noted that this comparison is made between observations from different winter seasons, snow survey data from other winters indicate that these amounts largely typify snow accumulations at these locations, both in absolute terms and in the relative amounts between sites. Large differences in snow accumulations are also seen between forest and clearing sites, with canopy interception losses ranging from about 40 – 60 % in both pine and spruce forests.

In general, forest-cover influences on snowmelt timing differed substantially with respect to the slope orienation (i.e. aspect) of the site. On south-facing aspects, the start of snowmelt was delayed under forest-cover to that in the open by approximately 8 days at the pine sites (Figure 3.3a) and 15 days at the spruce sites (Figure 3.4a). On level topography, snowmelt at both the pine LPC and LPF sites began on DOY 85, with only slightly faster melt in the pine clearing. Observations at the north-facing spruce sites show snowmelt starting at both the NSC clearing and NSF forest sites on DOY 130, but after which much slower melt occured in the clearing site where a substantial snowpack remained at the end of the observation period.

In addition to snowmelt rate differences between paired forest and clearing sites, overall snowmelt at the pine sites was notably slower compared to the spruce sites. Here, mean melt rates ranged from 4.6 – 1.6 mm SWE d^{-1} at the pine SPC and NPF sites, respectively, compared to the much faster rates of 12.9 – 5.4 mm SWE d^{-1} at the spruce SSC and NSC sites (note that no snowmelt observations were made at the hypothetical NPC site for comparison). Among the pine forest sites alone, considerable differences in melt rates were also observed, equal to 3.7, 2.8 and 1.6 mm SWE d^{-1} at the SPF, LPF, NPF, respectively. In comparison, much faster melt occurred under spruce forest-cover, but exhibited little difference between the north-facing NSF and south-facing SSF sites, having corresponding melt rates equal to 11.3 and 11.1 mm SWE d^{-1}.

Over the *snowpack warming and melt* period (Figures 3.3 and 3.4), radiation at all pine and spruce clearing sites was dominated by net shortwave gains, as net longwave (L^*) was strongly negative. Longwave losses were especially pronounced at the pine clearing sites, where mean L^* losses exceeded 3 MJ m^{-2} d^{-1} compared to the more modest longwave losses of roughly 2 MJ m^{-2} d^{-1} at spruce clearing sites. Alternatively, much smaller K^* and L^* magnitudes were realised at all forest sites, with slightly negative and positive L^* balances among the pine forest sites; but a sizeable positive L^* balance at the spruce forest sites that dominated total radiation to snow (R^*). Longwave gains to spruce forest snow were most pronounced during periods of active snowmelt (i.e. periods starting DOY 104, 118, and 130) when air and canopy temperatures warmed above-freezing, and snow longwave exitance (L_{out}) was limited by a maximum snow surface temperature (T_{s}) of 0 °C.

A summary of the net radiation balances during snowmelt at the pine sites (starting DOY 84) and at the spruce sites (staring DOY 130) is provided in Figure 3.5. At each site, mean daily radiation balances are shown compared to the energy consumed by snowmelt (Q_{M}) [MJ m^{-2} d^{-1}], as determined from the mean snowmelt rate (M) [kg m^{-2} d^{-1}] by:

$$Q_{\mathrm{M}} = \beta \, \lambda_f \, M \qquad \textbf{(3.8)}$$

where β is the fraction of ice in wet snow, which was specified in Eq. 3.8 equal to 0.96, and λ_f is the latent heat of fusion for ice [MJ kg^{-1}]. Overall, Figure 3.5 shows a general correspondence in R^* and Q_{M} among sites, with $R^* < Q_{\mathrm{M}}$ at the clearing sites a possible consequence of additional energy from increased turbulent fluxes to snow (Link and Marks, 1999). At all sites, R^* is positive during melt except at the hypothetical NPC site where longwave losses exceeded shortwave gains, resulting in a slightly negative radiation balance over the period. Also evident in Figure 3.5 is the dissimilarity in radiation balances between forest and clearing sites, with relatively large shortwave gains and longwave losses at the clearing sites compared to the small radiation balances at the forest sites. Marked differences also occur in terms of shortwave and longwave contributions to R^* under pine and spruce forest-cover, seen in the largely shortwave-dominated radiation balances at the pine forest sites and longwave-dominated radiation balances at the spruce forest sites.

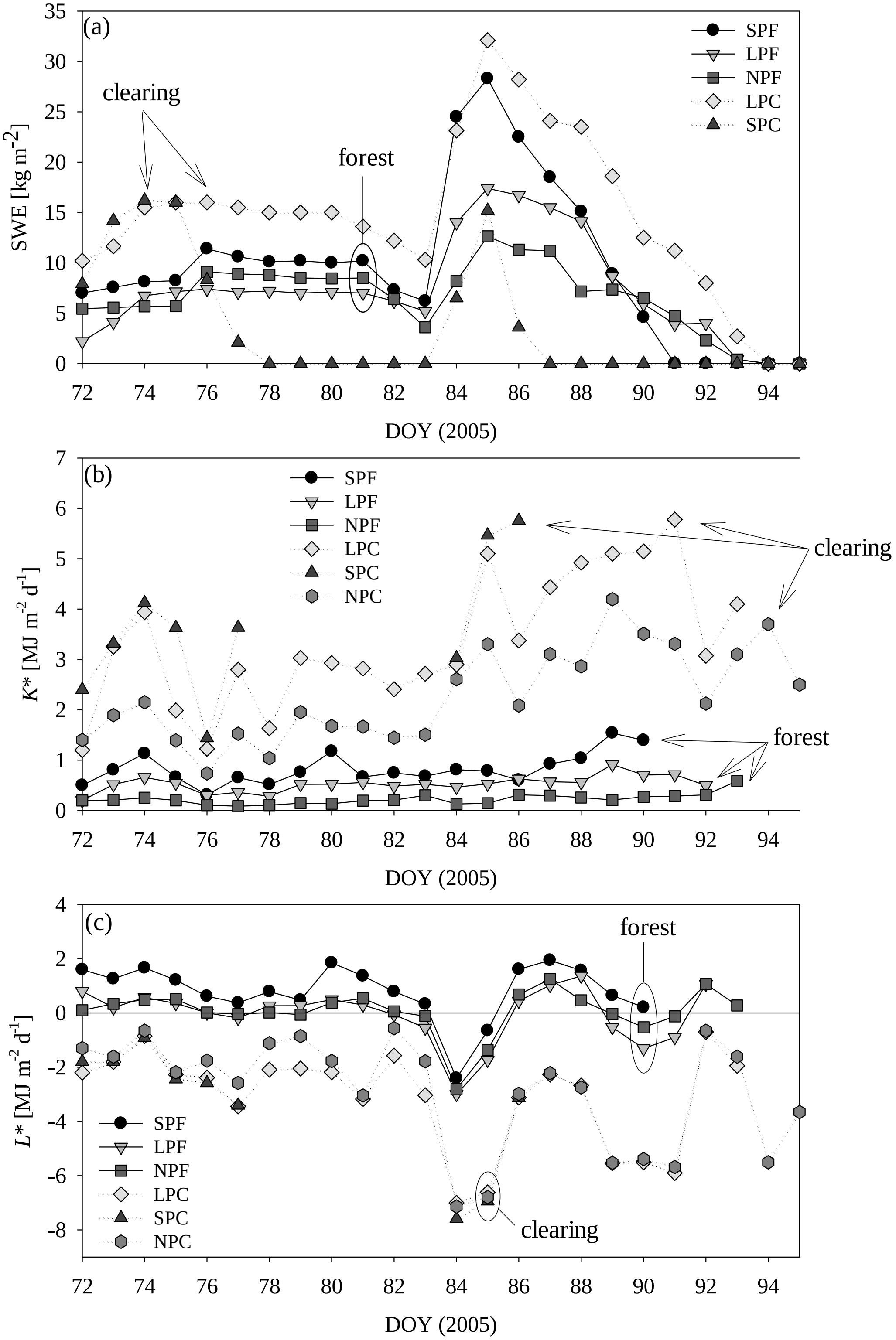

Figure 3. 3. Time series plots at the pine forest sites over the 2005 *snowpack warming and melt* period of: (a) snow water equivalent (SWE), (b) daily net shortwave radiation to snow (K*), and (c) daily net longwave radiation to snow (L*).

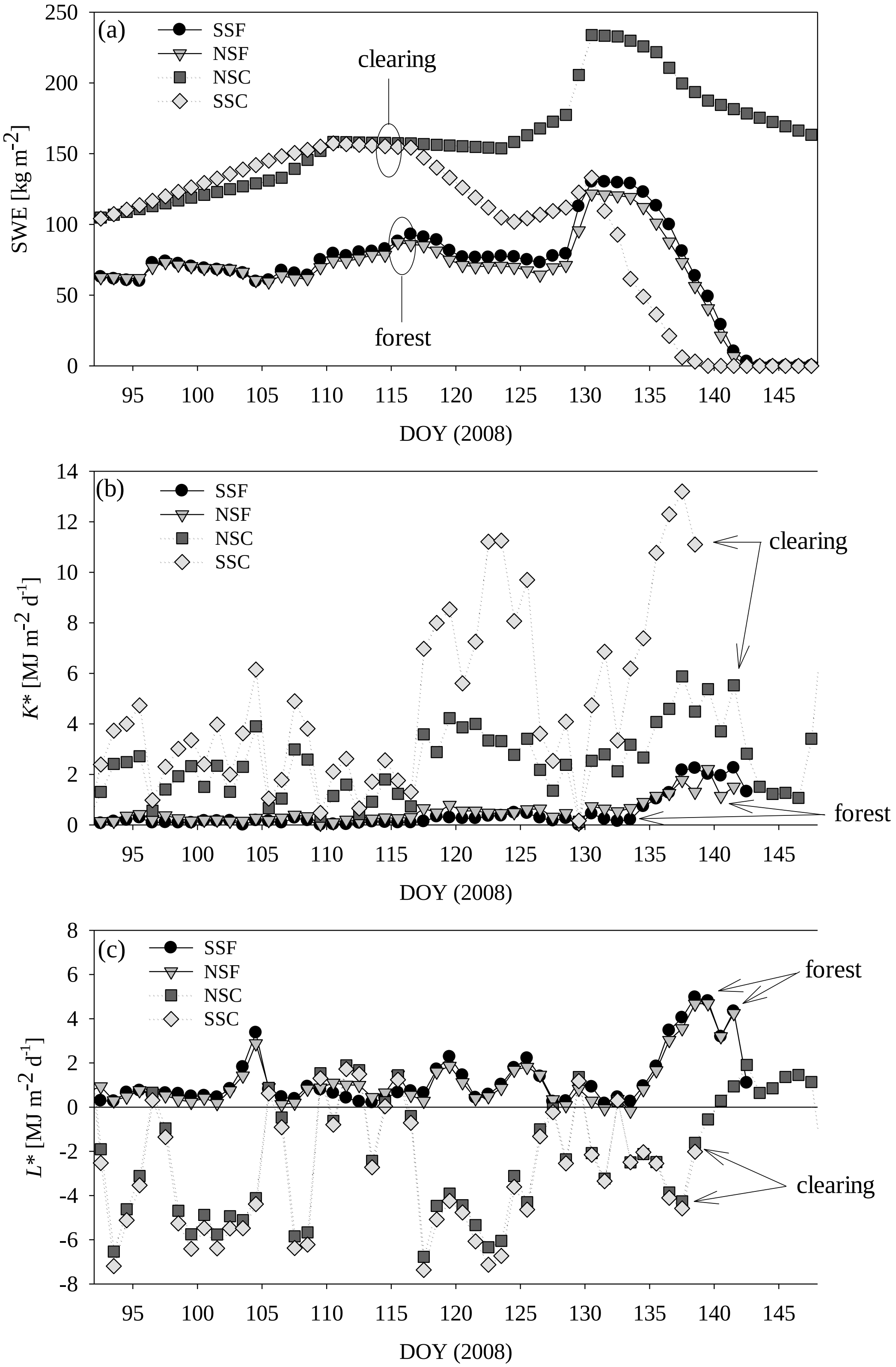

Figure 3. 4. Time series plots at the spruce forest sites over the 2008 *snowpack warming and melt* period of: (a) snow water equivalent (SWE), (b) daily net shortwave radiation to snow (K^*), and (c) daily net longwave radiation to snow (L^*).

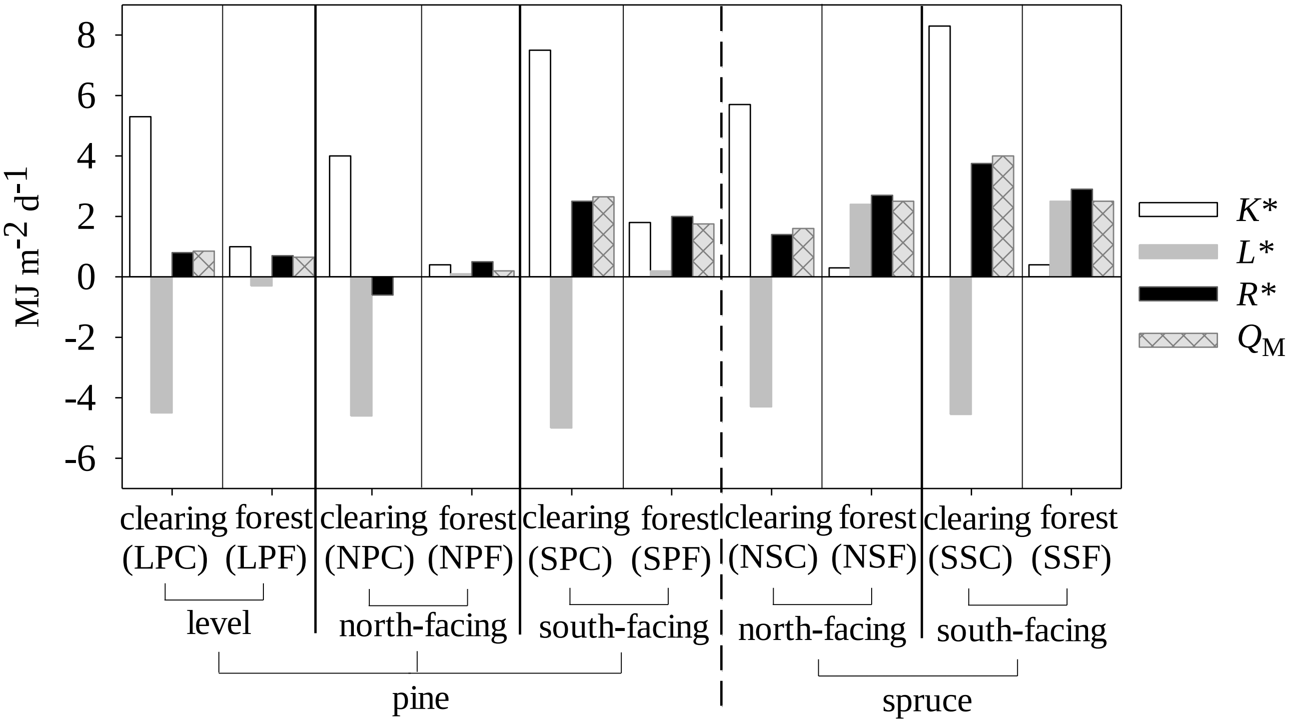

Figure 3.5. Mean daily net shortwave radiation to snow (K^*), net longwave radiation to snow (L^*), net all-wave radiation to snow (R^*), and snowmelt energy (Q_M) during snowmelt at the pine forest sites (starting DOY 84) and the spruce forest sites (starting DOY 130).

3.4. Chapter discussion

The above results illustrate the strong control of both slope orientation and forest-cover on radiation and snowmelt in mountain environments. At these latitudes during the springtime, topographical self-shading of north-facing slopes contributes in producing substantial differences in shortwave irradiance between opposing open south-facing and north-facing landscapes. By contrast, shortwave differences from slope/aspect effects are much reduced under forest-cover, especially in the spruce forests where the high shortwave extinction by the dense canopy-cover resulted in only small shortwave contributions to net snow radiation and melt energy. As a result, longwave fluxes dominated radiation to snow under spruce cover, and represented the main energy source for snowpack warming and melt. Longwave gains to spruce snowcovers were particularly pronounced during periods of above-freezing air and canopy temperatures, being of sufficient magnitude to facilitate rapid snowmelt. In contrast, shortwave fluxes dominated radiation to snow in pine forests during snowpack warming and melt, as the sparser canopy allowed for greater shortwave transmittance while simultaneously reducing canopy longwave emissions relative to denser spruce canopies. Higher shortwave transmittance through the pine cover also produced a sizeable variation in shortwave radiation to pine forest snowcovers with respect to slope orientation. Although variations in pine forest shortwave may be partly attributed to the small differences in canopy-cover density between the pine sites, they also result by the control of slope orientation on above-canopy irradiance and the extinction pathlength through sloping canopies. Alternatively, such topographic controls on shortwave irradiance were not observed across spruce-covered landscapes as they were effectively masked by the dense spruce canopy.

In general, snowmelt proceeded much faster at the spruce forest and clearings sites to that at the pine sites, which is ascribed to the elevation differences between the lower pine and higher spruce site locations. At the higher-elevation spruce sites, the increased snowfall and cooler temperatures result in deep cold snowpacks of high thermal deficits. Consequently, melt of these high-elevation snowpacks is delayed until the late spring, when shortwave irradiance is greater due to higher solar angles and longer days, and forest longwave emissions are increased by warmer canopy temperatures. As a result, shortwave and longwave gains to snow would be expected to be substantially higher during these later spring melt periods, being capable of producing faster melt compared to the earlier melt at the lower-elevation pine sites when potential shortwave and longwave gains to snow are less.

Observations at both pine and spruce locations show that slope orientation may strongly influence forest-cover effects on radiation to snow and snowmelt timing. On north-facing landscapes, shortwave reductions from forest shading are offset or slightly exceeded by longwave enhancements from canopy emissions, resulting in similar or greater amounts of total radiation to forest snow. At the spruce sites, increased radiation to snow at the north-facing spruce forest corresponded with a sizeable advancement in snowmelt timing relative to that in the nearby north-facing clearing where low shortwave gains and high longwave losses resulted in a substantial delay in melt of the deep snowpack. By contrast, radiation to snow was less under pine and spruce forest-cover on south-facing slopes to that in the open, as shortwave reductions from the canopy exceeded longwave enhancements from added canopy emissions. As a result, forest-cover on south-facing slopes substantially delayed the start of snowmelt, and slowed snowmelt at both the pine and spruce locations. Such results suggest that snowmelt timing in similar mountain basins may be most sensitive to forest-cover changes on south-facing landscapes.

Compared to the south-facing and north-facing sites, the effects of forest-cover on radiation to snow and snowmelt timing were less pronounced on level topography. At the level pine sites, shortwave reductions under the forest-cover were largely counterbalanced by longwave emissions from the canopy, resulting in only slightly decreased radiation and snowmelt rates in the forest. Thus, unlike the marked effects of forest-cover on radiation and snowmelt timing at the sloped sites, impacts are less clear on level topography as the small decrease in radiation observed under pine forest-cover would be eliminated or reversed by only slight increases in either snow albedo or canopy temperature over the winter. Yet, this result is instructive as it demonstrates how responses in snowmelt timing to forest-cover changes at level sites may provide a poor proxy of anticipated effects on sloped topography. Instead, observations illustrate the large range in snow radiation and snowmelt timing that may occur at sites of differing forest-cover and topography, and the strong influence on these effects from changing meteorological conditions.

4. SIMULATION OF SHORTWAVE IRRADIANCE TO SNOW IN MOUNTAIN NEEDLELEAF FORESTS

4.1. Chapter summary

This chapter outlines the theoretical development and evaluation of a model designed to estimate shortwave irradiance to snow in mountain needleleaf forests. The model is intended particularly for conifer forest stands that exhibit a high degree of forest structuring within crowns and trunks that allows for substantial transmittance of shortwave irradiance through canopy gaps. Estimation of canopy shortwave transmittance is made by resolving the fractions of sub-canopy snowcover shadowed by non-transmitting trunks and partially-transmitting crowns with respect to varying slope orientation of the site. Model evaluation is accomplished by comparing model simulations to observations of sub-canopy shortwave irradiance and forest shortwave transmittance at pine forests of level topography (i.e. LPF site), north-facing topography (i.e. NPF site), and southeast-facing topography (i.e. SPF site) during the spring of 2005 at the MCRB. The model was parameterised using detailed forest mensuration data of tree density, tree height, crown height and width, and trunk height and width collected at each site, as well as information from hemispherical photograph analysis. Overall, results show the model able to characterise the substantial differences shortwave transmittance and shortwave irradiance to snow between sites, which were strongly controlled by both forest-cover density and site topography. The model was subsequently used to assess the effects of forest-cover on irradiance to snow at sites of varying slope orientation, which indicated forest-cover changes are expected to produce the largest response in shortwave radiation to snow at south-facing sites, with comparatively little response at north-facing sites. The good performance of the model provides encouragement towards its use in examining forest shortwave radiation dynamics with respect to changing forest-cover density and stand structure.

4.2. Chapter introduction: estimation of sub-canopy shortwave irradiance

Compared to open environments, shortwave irradiance (K_{in}) to snow in forests is reduced by reflection and absorption from the canopy. Disregarding shortwave radiation enhancements to snow by multiple reflections between snow and forest layers, K_{in} to snow may be related to the above-canopy shortwave irradiance (K_o) by

$$K_{\mathrm{in}} = K_{\mathrm{o}}(1 - R - \kappa) = K_{\mathrm{o}}\tau \qquad \mathbf{(4.1)}$$

where R, κ and τ are the relative fractions of shortwave irradiance reflected, absorbed, and transmitted by the forest stand, respectively. Here, forest K_{in} is most commonly related to K_{o} by the forest shortwave transmittance (τ) through differential analysis of probability statistics (e.g. Nilson, 1971; Myneni and Asrar, 1993) in which the forest stand is abstracted as a homogenous medium composed of sufficiently small extinction particles of isotropic spatial distribution and random orientation. Following this approach, each infinitesimally small canopy layer (X) consists of a non-transmitting (x), and transmitting ($1–x$) component, giving a probability (p) for transmission through the layer of $1–x/X$. With substitution of k for x/X, the probability of irradiance transmission through n canopy layers is given by

$$p = (1 - k)^n \qquad \mathbf{(4.2)}$$

Extending Eq. 4.2 across a forest pathlength (l) [m] composed of an infinite number of canopy layers, τ is evaluated by the limit of Eq. 4.2 for $n \rightarrow \infty$, giving the basic form of the Beer-Bourger Law, i.e.

$$\tau = \exp(-kl) \qquad \mathbf{(4.3)}$$

In this context, k is termed the extinction coefficient, which for plant canopies is commonly related to the forest leaf area density (L_{d}) [$\mathrm{m}^2\ \mathrm{m}^{-3}$] or leaf area index ($LAI$) [$\mathrm{m}^2\ \mathrm{m}^{-2}$]. However, as this approach presumes a homogenous shortwave extinction medium, its direct application in mountain needleleaf forests is uncertain considering the pronounced structuring of forest material and considerable irradiance transfer through canopy gaps (Melloh et al., 2003). This effect is illustrated in Figure 4.1 by the distinct patterns of irradiance and shadow across snowcover at the LPF site. Consequently, effective employment of Beer-Bourger type approaches in highly structured conifer forest stands is limited by the uncertainty in specifying k without calibration.

Figure 4. 1. Scene beneath a mature lodgepole pine forest stand (LPF site) showing the distinct spatial patterns of shortwave irradiance and shadows produced by forest trunks, crowns and canopy gaps on the sub-canopy surface.

Alternatively, more sophisticated methods estimating sub-canopy shortwave irradiance may provide for more realistic representation of shortwave dynamics in forests through explicit account for extinction by trunks and crowns, and transmission through forest gaps. Here, individual trunk and crowns are often abstracted using simple geometric shapes (Federer, 1971; Satterlund, 1983; Rowland and Moore, 1992; Stadt and Lieffers, 2000; Corbaud et al., 2003), allowing their application to sloped surfaces. However, many such models typically require extensive calibration, which may not be possible in mountain environments due to the (i) vast combinations of site topography and forest-cover density and (ii) the lack of sub-canopy irradiance measurements across mountain landscapes (Wang et al., 2006). As a result, few shortwave transmittance models have been evaluated in needleleaf forests with substantial variations in slope orientation (i.e. aspect).

4.3. Chapter objectives

There are three major objectives of this chapter. The first is to outline the theoretical development of a shortwave transmittance model for application in mountain needleleaf forests.

The second is an evaluation of the model, completed by comparing simulations of τ and K_{in} to observations collected at forests of varying cover densities and topography. Lastly, the model is applied to investigate the effects of changing forest-cover density on K_{in} to snowcover for sites of varying slope orientation.

4.4. Model outline: estimation of forest shortwave transmittance

In the model, above-canopy shortwave irradiance (K_{o}) consists of two components: (i) non-directional diffuse irradiance (K_{d}), which is received in equal amounts by the ground surface from the overlying sky hemisphere, and (ii) directional direct-beam irradiance (K_{b}), which is received directly from the position of the sun. Accordingly, forest K_{in} is determined as the sum of K_{b} and K_{d}, weighted by their respective shortwave transmittances, i.e.

$$K_{\mathrm{in}} = K_{\mathrm{o}}\,\tau = K_{\mathrm{b}}\,\tau_{\mathrm{b}} + K_{\mathrm{d}}\,\tau_{\mathrm{d}} \tag{4.4}$$

where τ_{b} and τ_{d} are the corresponding forest transmittances of direct-beam and diffuse shortwave irradiance [] (K_{b} and K_{d} are estimated by the atmospheric transmittance index (k_{t}) as outlined in Appendix A). To resolve τ_{b} and τ_{d}, the fractions of snowcover shadowed by (i) non-transmitting trunks (T_f) and (ii) partially-transmitting crowns (C_f) are determined, from which the remainder of forest snowcover is considered occupied by the (iii) fully-transmitting gap fraction (G_f). These forest-fractional areas are determined in order of least to greatest transmittance, such that the areas occupied by formerly resolved fractions are unavailable to the next:

$$T_f = 0 \rightarrow 1 \tag{4.5}$$

$$C_f = C_{f(\mathrm{o})}\,(1 - T_f) \tag{4.6}$$

$$G_f = (1 - C_f + T_f) \tag{4.7}$$

where $C_{f(\mathrm{o})}$ denotes the calculated crown fractional area prior to adjustment by $(1 - T_f)$. Shadows projected from trunk and crown shapes across snowcover (x is used here to denote either trunk and crown geometric shapes) include a component that may overlap with other projected shadows (x_{o}), and a non-overlapping shadow component (x_{no}) (Figure 4.2).

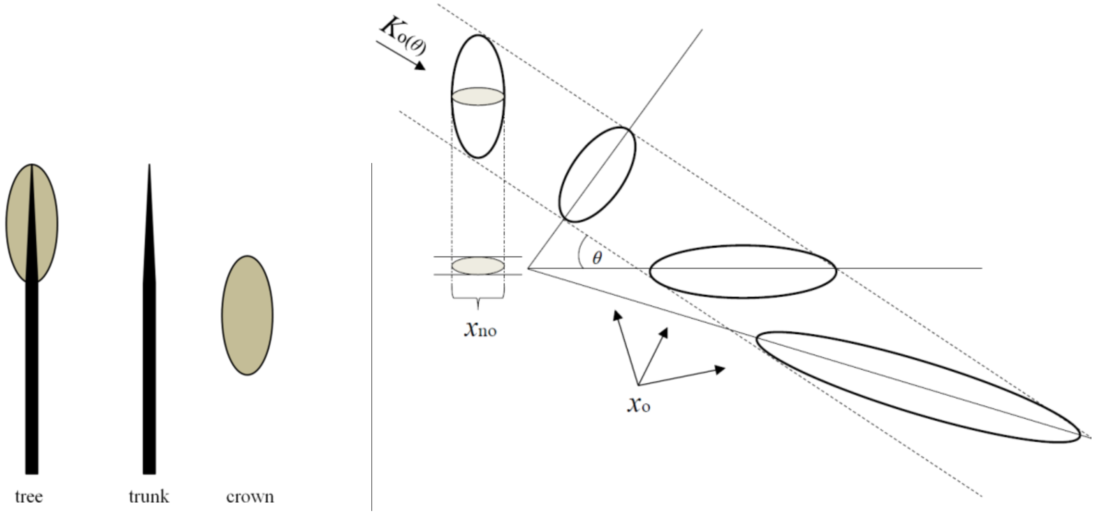

Figure 4. 2. Left: schematic representation of the basic trunk and crown geometric shapes; right: illustration of the non-overlapping shadow component (x_{no}) (shown in grey) and overlapping (x_o) (shown in white) shadow component of a crown prolate spheroid from irradiance (K_{in}) received from elevation angle θ projected upon varying slope incriminations.

From this, determination of the total fraction of area H shadowed by non-overlapping shadows (X_{no}) cast from a ray received from elevation θ is made by the summation of n number of x_{no}, shadows, i.e.

$$X_{no}(\theta) = \sum_{i=1}^{n} \frac{x_{no}(\theta)}{H} \tag{4.8}$$

However, due to shadow overlap, the total trunk/crown fraction areas (X_f) (here X_f denotes T_f or C_f) is less than $n \cdot x_o$. To account for shadow overlap, Federer (1971) related the additional fraction area shadowed (i.e. X_f) by the addition of a single overlapping trunk/crown shadow (i.e. $\frac{x_o}{H}$) to the antecedent fraction of the area not in shadow (i.e. $1–X_f$) by

$$\frac{dX_f}{d\frac{x_o}{H}} = 1 - X_f \tag{4.9}$$

which may be rearranged to

$$d\frac{x_o}{H} = \frac{dX_f}{1 - X_f} \tag{4.10}$$

Integration of $\frac{x_o}{H}$ from 0 → n gives

$$\frac{x_o\, n}{H} = -ln(1 - X_f) \tag{4.11}$$

which may be rearranged to

$$X_f = 1 - exp(-\frac{x_o\, n}{H}) \tag{4.12}$$

As X_f in Eq. 4.12 refers to only the total overlapping shadow component (X_o) (i.e. $X_o = X_f$), total X_f with respect to θ is given by the sum of the overlapping and non-overlapping shadow components, i.e.

$$X_f(\theta) = X_{no}(\theta) + X_o(\theta) \tag{4.13}$$

$$= \frac{x_{no}(\theta)n}{H\omega} + 1 - exp(-\frac{x_o(\theta)\, n}{H\omega}) \tag{4.14}$$

Here, account for effect of slope orientation on $X_f(\theta)$ is made by adjusting H in Eq. 4.14 by the slope correction factor ω [] (calculation of ω provided in Appendix A). Considering that there is no shortwave transmittance through the forest trunk fraction (i.e. $\tau(T_f) = 0$), the determination of τ is simplified to:

$$\tau = C_f\, \tau(C_f) + G_f \tag{4.15}$$

Estimation of direct-beam transmittance (τ_b) through the C_f for irradiance received from a solar elevation of θ_s is made by the following expression which assumes a spherical vertical foliage orientation (i.e. 0.5) (Barclay, 2001):

$$\tau_{\mathrm{b}}(C_f(\theta_{\mathrm{s}})) = exp[-0.5L`l(C_f(\theta_{\mathrm{s}}))] \quad \textbf{(4.16)}$$

where L_{d} is the total crown leaf area density [$\mathrm{m}^2\ \mathrm{m}^{-3}$], and l_{c} is the mean extinction pathlength through C_f for irradiance received from θ_{s} [m] which is determined as the product of the pathlength through a single representative crown ($l_{\mathrm{c}(i)}$) [m] and the crown overlap factor (c_{o}) [] for irradiance received from θ_{s}, i.e.

$$l_{\mathrm{c}}(\theta_{\mathrm{s}}) = l_{\mathrm{c}(i)}(\theta_{\mathrm{s}})\ c_o(\theta_{\mathrm{s}}) \quad \textbf{(4.17)}$$

Here, c_{o} for n number of crown areas apparent from θ_{s} ($c_{\mathrm{area}}(\theta_{\mathrm{s}})$) [$\mathrm{m}^2$] is given by an expression similar in form to Eq. 4.12:

$$c_{\mathrm{o}}(\theta_{\mathrm{s}}) = 1 - exp\mathbf{(}-\frac{c_{\mathrm{area}}(\theta_{\mathrm{s}})\ n}{H\omega}\mathbf{)} \quad \textbf{(4.18)}$$

Alternatively, l_{c} is determined by the crown volume-to-area ratio (i.e. $C_{\mathrm{volm}}/C_{\mathrm{area}}$), which is calculated for the case of a prolate spheroid by:

$$l_{\mathrm{c}}(\theta) = \frac{C_{\mathrm{volm}}}{C_{\mathrm{area}}(\theta)} = \frac{2\pi a^2 b}{3\,C_{\mathrm{area}}(\theta)} \quad \textbf{(4.19)}$$

where a and b are the respective minor (horizontal) and (major vertical) axes of the prolate spheroid (Figure 4.3) and $C_{\mathrm{area}}(\theta)$ is given by:

$$C_{\mathrm{area}}(\theta) = \{a \sin(\theta) + [a^2 \sin2(\theta) + b^2 \cos^2(\theta)]^{1/2}\}\ \pi\ a/2 \quad \textbf{(4.20)}$$

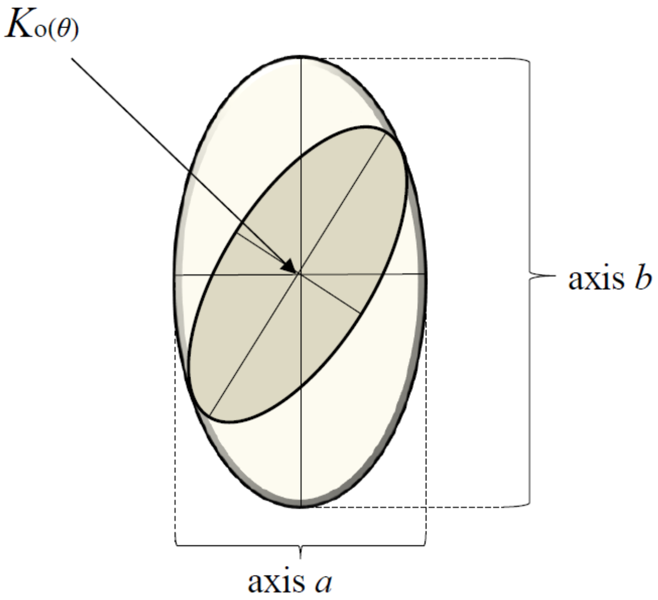

Figure 4. 3. Illustration of the apparent crown area (C_{area}) (dark grey) within a prolate spheroid volume (C_{volm}) shown for irradiance received from θ.

Assuming no azimuthal preference in diffuse irradiance, determination of diffuse irradiance transmittance (τ_{d}) is made via integration of Eq. 4.16 throughout the sky hemisphere, which, without similar azimuthal preference in foliage distribution is evaluated by

$$\tau_{\mathrm{d}} = \int_{0}^{\pi/2} exp[-0.5L`l_{\mathrm{c}}(C_f(\theta))]\cos\theta \sin\theta\, \delta\theta \tag{4.21}$$

Enhancement of shortwave irradiance from snow-forest reflections

Upon transmission through forest-cover, multiple reflections of irradiance between snow and forest layers result in a K_{in} enhancement to snow. In the model, the amount of reflection from the forest layer is related to the forest albedo (α_f) and the fraction of the overlying forest sky view (v) occupied by canopy (i.e. $1-v$) using an expression of similar form to that of Nijssen and Lettenmaier (1999) and Bewley et al. (2007):

$$K_{\mathrm{in}} = \frac{K_{\mathrm{o}}\tau}{1-\alpha_{\mathrm{s}}\alpha_f(1-v)} \tag{4.22}$$

where α_s is the snow surface albedo which may be set by *in situ* measurements or estimated (e.g. Hardy et al., 1998; Melloh et al., 2002). In Eq. 4.22, it is assumed that $v \approx \tau_d$, with α_f specified equal to 0.15 according to albedo observations in a jack pine forest by Pomeroy and Dion (1996). For summary, the main computations involved in estimating K_{in} to snow in the model are shown in Figure 4.4.

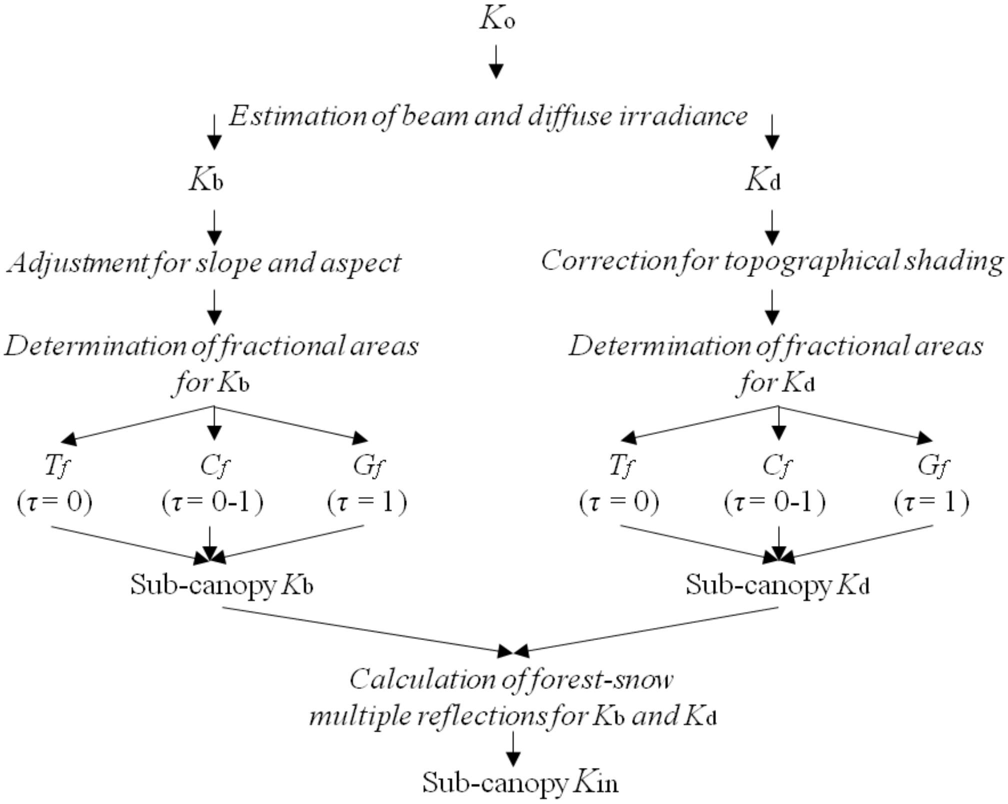

Figure 4. 4. Flow diagram depicting the main procedures and simulations products in model determination of sub-canopy shortwave irradiance.

4.5. Model evaluation

Simulations of τ and K_{in} to forest snow were made at the Level Pine Forest (LPF), North-facing Pine Forest (NPF) and Southeast-facing Pine Forest (SPF) sites at the MCRB for the period of March 15 – April 15, 2005. This period was selected as it extends from the start of radiation observations at all sites and includes the time of spring snowmelt. This time also coincides with the collection of sub-canopy shortwave irradiance observations at the LPF and SPF by a 10-pyranometer array, providing a much greater spatial representation of sub-canopy

K_{in} at these sites. Above-canopy shortwave irradiance (K_{o}) to the NPF and SPF was estimated through adjustment of observations at the Level Pine Clearing (LPC) reference site following the procedure outlined in Appendix A.

4.5.1. Model Parameterisation

Model parameterisation of tree density and the dimensions of trunk and crown geometric shapes were made from detailed forest surveys performed at the LPF, NPF, and SPF sites. Survey data was collected within 5 m × 5 m grids surrounding the radiometer at each site, giving a total surveyed area of approximately 100 m^2 at the LPF and NPF, and 50 m^2 at the smaller SPF site. Within each grid, the number of trees taller than 1 m was tallied, for each the diameter of breast height (dbh) of each trunk was measured. In addition, measurements of tree height, as well as crown height and width were obtained using a handheld laser distance finder. A summary of the forest mensuration data obtained at all sites is provided in Table 4.1. For each site, estimates of crown leaf area density (L_{d}) were provided from hemispherical photograph analysis using CANEYE software (Baret and Weiss, 2004; Weiss et al., 2004; Jonckheere et al., 2004). This particular software was used for its ability to discriminate between trunk and crown foliage material, allowing for separate quantification of trunk and crown foliage. CANEYE also permitted the simultaneous analysis of multiple hemispherical photographs, thus providing an assessment of each forest stand as a whole.

Table 4. 1. Summary of forest mensuration data collected at the LPF, NPF, and SPF sites. Data of tree dimensions are expressed both as the mean and standard deviation (sd) of single tree measures at the site (*estimated from hemispherical image analysis using CANEYE software).

	LPF	NPF	SPF
Total area surveyed [m^2]	625	625	225
Total no. of trees []	316	385	86
Mean tree density [m^{-2}]	0.51	0.62	0.38
Mean tree spacing [m]	1.98	1.62	2.62
Tree height (mean) [m]	12.2	13.8	11.4
Tree height (sd) [m]	1.4	1.2	2.3
Crown height (mean) [m]	2.5	3.8	4.2
Crown height (sd) [m]	0.8	1.3	1.8
Crown width (mean) [m]	0.6	0.45	0.57
Crown width (sd) [m]	0.26	0.31	0.43
dbh (mean) [m]	0.12	0.12	0.14
dbh (sd) [m]	0.04	0.05	0.06
Crown foliage density* [m^{-2} m^{-3}]	1.34	1.43	1.44

From the forest mensuration datasets obtained by field surveys, the representative dimensions (R_d) of the geometric crown and trunk shapes for each site was specified both in terms of the:

(i) the arithmetic mean of all mensuration data values ($d_v(i)$), i.e.

$$R_d = \frac{1}{n}\sum_{i=1}^{n} d_v(i) \tag{4.23}$$

where *n* is the number of mensuration datum values within each dataset, and

(ii) the mean of all datum points weighted by the relative size rank (*R*) of the mensuration value, i.e.

$$R_d = \sum_{i=1}^{n} \frac{1}{R(i)} R(i)\, d_v(i) \tag{4.24}$$

where $R(i)$ is the rank of mensuration value i, which for the smallest datum value $R(i) = 1$, and the largest datum value $R(i) = n$. Simulations of daily τ and K_{in} were made at all forest sites using the trunk and crown geometric shape dimensions determined via (*i*) and (*ii*) above at 5° azimuth and zenith band resolutions about the sky hemisphere. Model performance for (*i*) and (*ii*) was assessed by the following measures: the model bias (MB) index, the model efficiency (ME) index, and the root mean square difference (RMSE). These indexes were used as they provide a rather complementary evaluation of model performance, with the MB comparing the total simulated output to the total of observations; the ME an indication of model performance compared to the mean of the observations; and the RMSE a quantification of the absolute amount of unit error between simulations and observations. Here, the MB is calculated as

$$\mathrm{MB} = \frac{\sum_{i=1}^{n} x_{sim}}{\sum_{i=1}^{n} x_{obs}} \qquad \textbf{(4.25)}$$

where x_{sim} and x_{obs} are the simulated and observed values at a given timestep, and n is the total number of paired simulated and observed values. Accordingly, MB < 1 signifies an overall under-prediction by the model and MB > 1 an overall over-prediction by the model. The model efficiency (ME) index is given by

$$\mathrm{ME} = 1 - \left[\frac{\sum_{i=1}^{n} (x_{sim} - x_{obs})^2}{\sum_{i=1}^{n} (x_{obs} - x_{avg})^2} \right] \qquad \textbf{(4.26)}$$

where x_{avg} is the mean value of n number of observations. Accordingly, model efficiency increases as the ME index approaches 1, which represents a perfect match between simulations and observations; 0 indicates an equal efficiency between simulations and the x_{avg}, with increasingly negative values signifying a progressively superior estimation by the x_{avg}. Finally, the root mean square error (RMSE) is determined by

$$\mathrm{RMSE} = \sqrt{\frac{1}{n}\sum_{i=1}^{n}(x_{sim} - x_{obs})^2} \qquad \textbf{(4.27)}$$

where x_{sim} and x_{obs} are the respective simulated and observed values for n number of paired values.

4.6. Model evaluation: comparison to sub-canopy shortwave irradiance

Using the above measures, a comparison of simulation and observed daily τ and K_{in} at all sites is shown in Table 4.2 for crown and trunk dimensions parameterisation using both the (*i*) arithmetic mean and (*ii*) the weighted mean of forest mensuration data. Overall, both the arithmetic and weighted forest dataset means gave model outputs that well characterised the large variation in both τ and K_{in} between forest sites, which ranged from a mean daily $\tau = 0.36$ ($K_{\mathrm{in}} = 58.8$ W m^{-2}) at the SPF, to a $\tau = 0.13$ ($K_{\mathrm{in}} = 10.9$ W m^{-2}) at the NPF. However, best simulation results were clearly provided using the weighted mean to parameterise crown and trunk dimensions, by evidence of the smaller RMSE, the higher ME, and MB values closer to 1 at all sites (Table 4.2).

In terms of simulation performance at individual sites, greatest absolute errors in τ (and K_{in}) were realised at the SPF, having a RMSE for $\tau = 0.06$ (6 W m^{-2} for K_{in}), compared to a RMSE for $\tau = 0.03$ (2.6 W m^{-2} for K_{in}) at the NPF. However, these differences are largely attributed to the respective large and small τ (and K_{in}) values the SPF and NPF. Alternatively, in terms of the MB and ME indexes, best simulations of both τ and K_{in} were obtained at the SPF, with poorest simulations at the NPF.

Table 4. 2. Comparative statistics between observed daily K_{in} and τ at the LPF, NPF, and SPF sites and simulations made for crown and trunk dimensions parameterised by the (*i*) arithmetic mean and (*ii*) weighted mean of forest mensuration datasets at each site.

	Daily K_{in}				*Daily τ*			
	Mean [W m^{-2}]	MB []	RMSE [W m^{-2}]	ME []	Mean []	MB []	RMSE []	ME []
observed LPF	**36.6**	–	–	–	**0.25**	–	–	–
simulated LPF (arithmetic mean)	42.6	1.17	4.54	0.76	0.27	1.09	0.04	0.35
simulated LPF (weighted mean)	35.2	0.97	3.61	0.82	0.24	0.95	0.03	0.43
observed NPF	**10.9**	–	–	–	**0.13**	–	–	–
simulated NPF (arithmetic mean)	16.8	1.54	3.42	0.25	0.18	1.46	0.03	0.07
simulated NPF (weighted mean)	12.3	1.13	2.66	0.31	0.14	1.07	0.03	0.14
observed SPF	**58.6**	–	–	–	**0.36**	–	–	–
simulated SPF (arithmetic mean)	66.9	1.14	8.69	0.84	0.42	1.15	0.08	0.48
simulated SPF (weighted mean)	57.5	0.98	6.12	0.87	0.35	0.99	0.06	0.56

Using the superior weighted mean parameterisation of trunk and crown shapes, simulations of daily τ at all forest sites are shown compared those observed in Figure 4.5. Overall, τ simulations are able to represent the substantial variations in transmittance between sites, from which good approximation of daily K_{in} at each site is also made (Figure 4.6). Encouraging K_{in} determinations by the model are also evident in the close correspondence of cumulative values throughout the period, due partly to the offsetting of underestimates and overestimates of daily values (Figure 4.7).

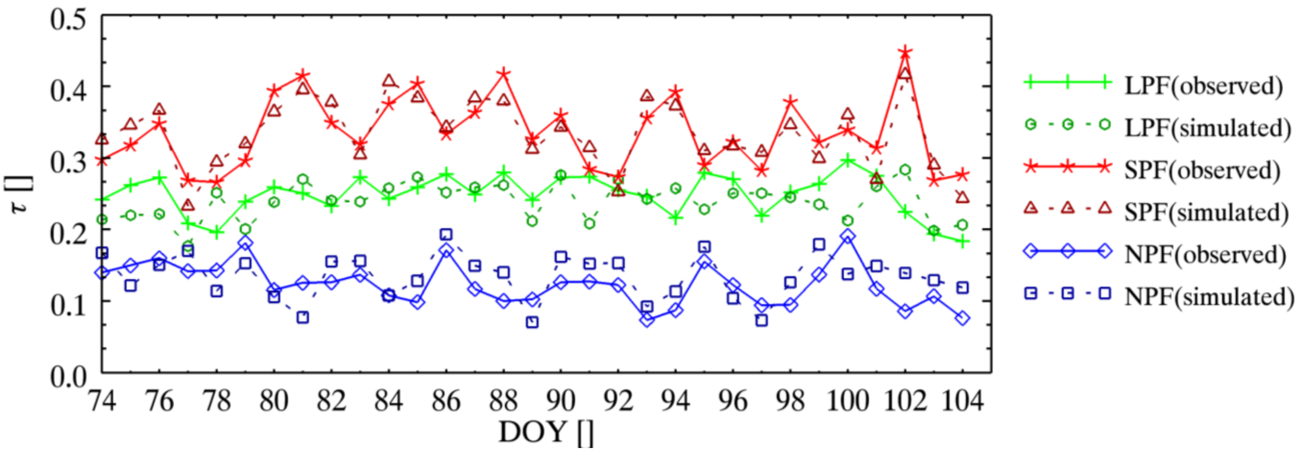

Figure 4. 5. Time series of observed and simulated daily forest shortwave transmittance (τ) at the LPF, NPF, and SPF sites.

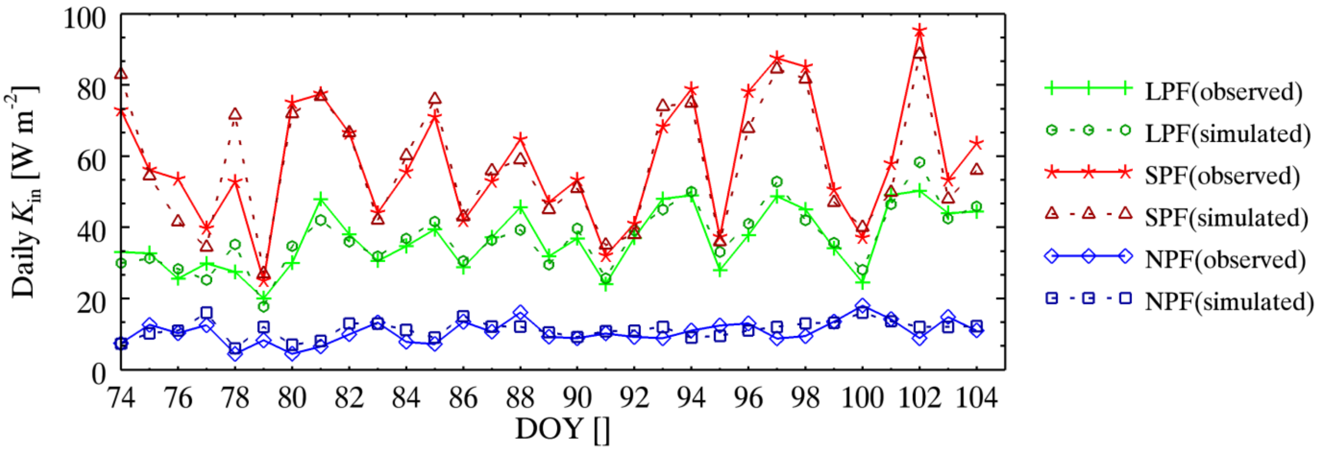

Figure 4. 6. Time series of observed and simulated daily shortwave irradiance (K_{in}) at the LPF, NPF, and SPF sites.

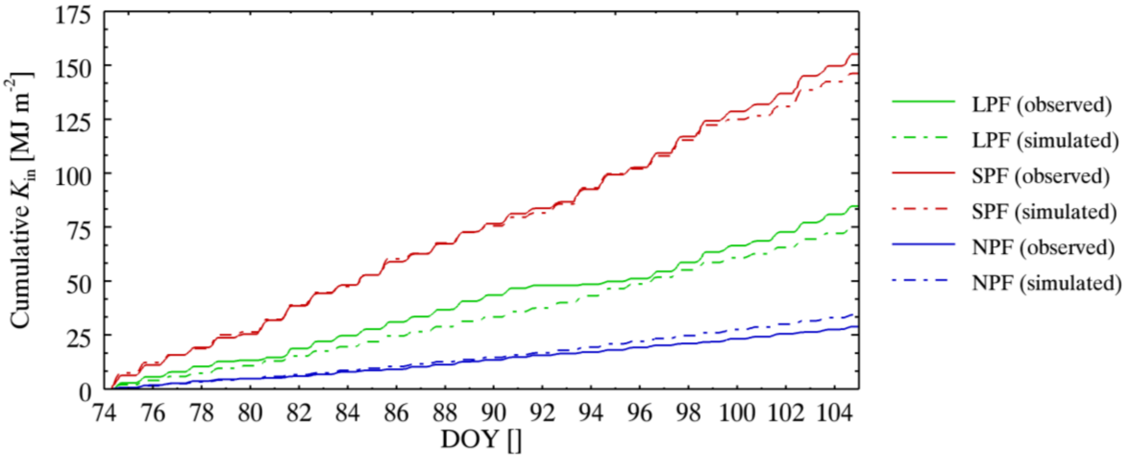

Figure 4. 7. Time series of cumulative observed and simulated daily shortwave irradiance (K_{in}) at the LPF, NPF, and SPF sites.

To demonstrate the manner in which τ and K_{in} are estimated by the model, time series determinations of the crown fractional area (C_f), trunk fractional area (T_f), and gap fractional area (G_f) are shown for all sites over the period of DOY 75 – 80 in Figure 4.8. Here, a marked difference in G_f is evident among sites, not only in terms of overall values but also the temporal pattern of values throughout the day. At the SPF for example, the relatively large G_f values early in the day corresponds to when the forest extinction pathlength is shortest due to the sun position closely facing the slope orientation of the site. Conversely, a sharp drop in G_f values occurs at this site in the afternoon when the more oblique solar angles produce longer extinction pathlengths. At the LPF and NPF by comparison, the orientations of these sites more away from the sun produce much smaller G_f values, of which are influenced more by the changing fractions of direct-beam (k_b) and diffuse (k_d) irradiance (i.e. sky condition). The effect of sky condition on the fractional areas at the LPF and NPF is exemplified in the pronounced differences in G_f values on DOY 75 and 79, which correspond to days of relatively high and low direct-beam irradiance (k_b). On DOY 75, relatively low G_f values are determined at the LPF and NPF as the increased direct-beam irradiance results in higher extinction along the extended, oblique extinction pathlength through the forest stand. By contrast, the shorter pathlength travelled by diffuse irradiance passing vertically through the forest stand on DOY 79 gives for comparatively greater G_f values at both sites.

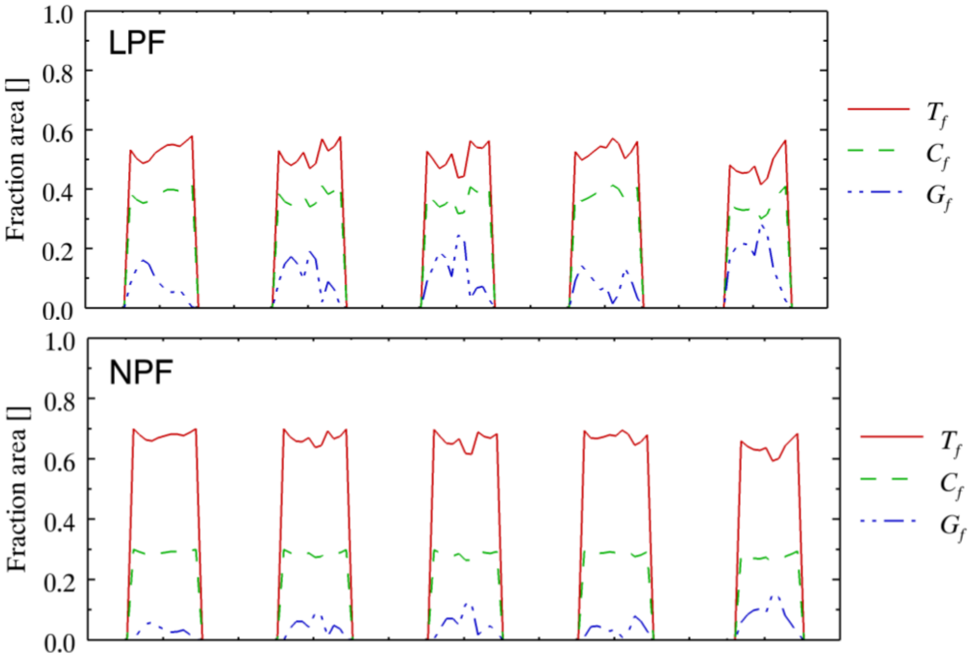

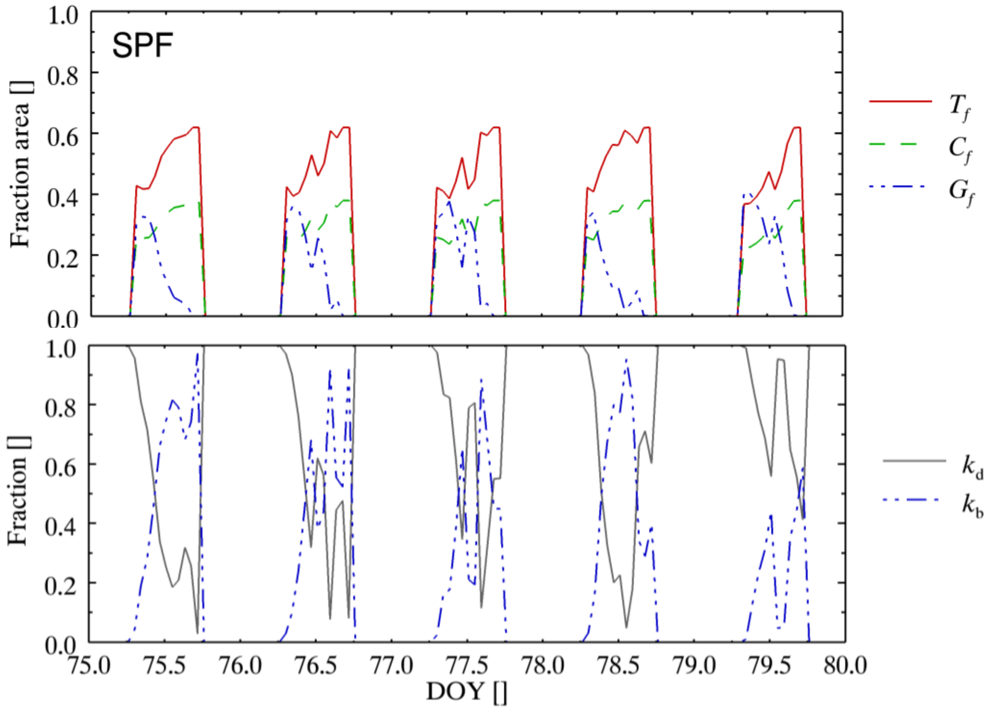

Figure 4. 8. Top (previous page): time series of the simulated trunk fractional area (T_f), crown fractional area (C_f), and gap fractional area (G_f) at the LPF, NPF, and SPF sites. Bottom: corresponding time series of the (estimated) direct-beam fraction (k_b) and diffuse fraction (k_d) of shortwave irradiance.

Further evaluation of the model's accounting for slope orientation effects upon forest shortwave transmittance is provided by comparing simulated and observed τ with respect to elevation and azimuth through the forest stand. Figure 4.9 shows the simulated τ throughout the sky hemisphere at all forest sites compared to values provided by CANEYE hemispherical photograph analysis. For all sites, simulated τ with respect to the sky hemisphere position is shown to roughly correspond to the outputs from photograph analysis, which at the LPF exhibit little preference with azimuth but a progressively increase with sky elevation angle. By contrast, at the sloped sites, simulated and photograph outputs show increased τ values at sky azimuths generally corresponding to the slope (azimuth) orientation of the site. Figure 4.9 also shows the range of the daily sun track over the 2005 March – April period to provide an indication of direct-beam transmittance through each site's canopy. Here, greatest potential for direct-beam transmittance is shown for the SPF, as the position of the sun largely overlaps with the regions of high τ values within the sky hemisphere. Alternatively, lower transmittance of direct-beam irradiance is determined at the LPF and NPF sites, as the sun position tracks along the lower τ regions of the sky hemisphere due to the longer extinction pathlengths travelled through these canopies.

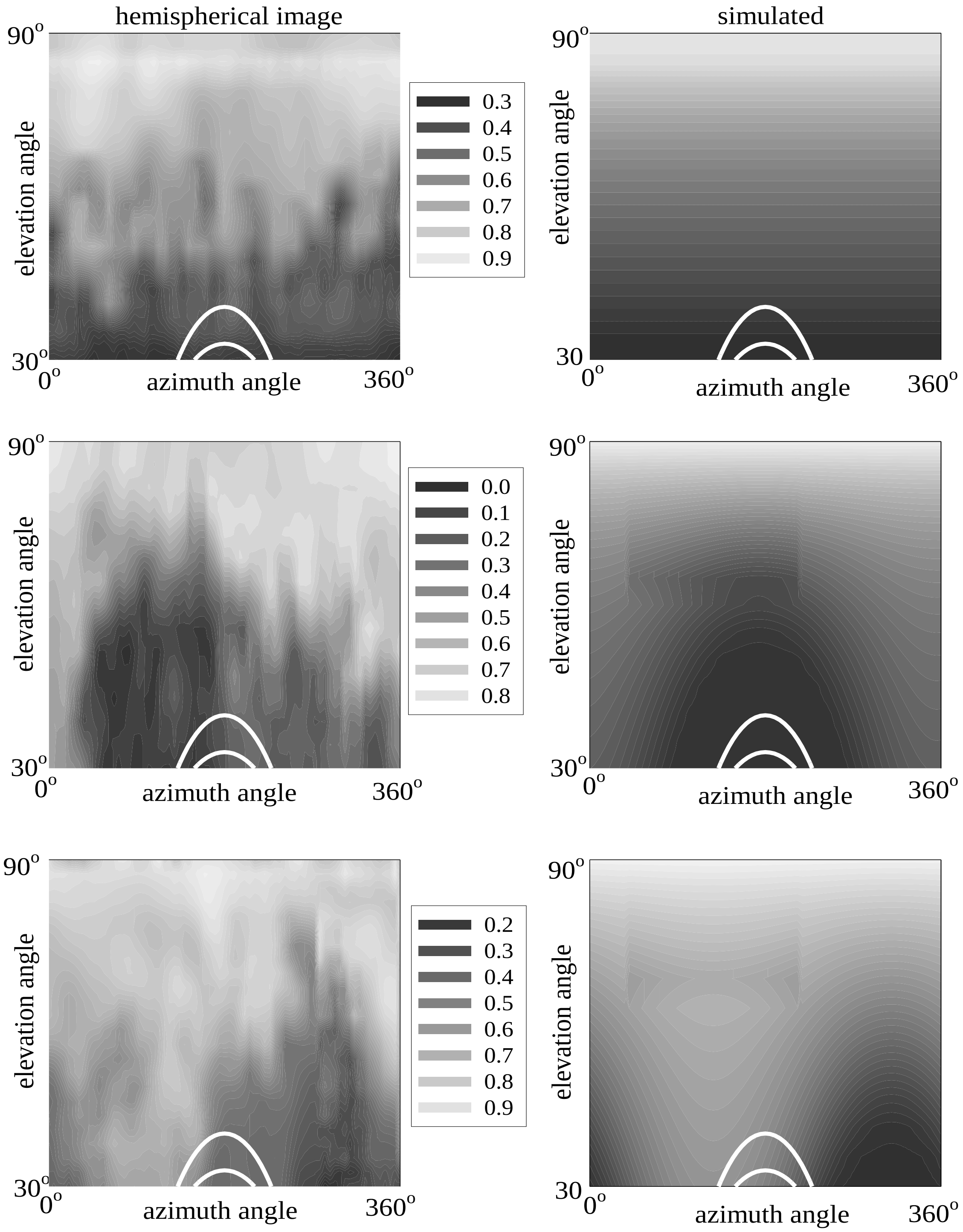

Figure 4. 9. Forest shortwave irradiance transmittance (τ) with respect to elevation and azimuth of the sky hemisphere as determined from hemispherical photograph analysis using CANEYE software (left) and model simulations (right) for the LPF site (top), the NPF site (middle) and the SPF site (bottom). The range of daily sun track over the observation period is delineated by the solid white line.

4.7. Sensitivity analysis

To investigate the potential effects on shortwave irradiance to snow brought about by changes in forest-cover density across varying topography, simulations of K_{in} were performed over a range of cover densities on a (i) site of level topography, (ii) a site on a 30° slope site of north-facing aspect, and (ii) a site on a 30° slope site of south-facing aspect over the 2005 March 15 – April 15 period. Here, forest-cover density is expressed in relation to the number of trees of representative trunk and crown dimensions at the LPF site (e.g. a forest-cover density of 0.5 is equivalent to a stand containing half the number of trees of representative dimensions at the LPF).

As expected, determinations of K_{in} to each site provided greatest irradiance to the south-facing site and least irradiance to the north-facing sites, with differences in magnitude between sites diminishing with denser forest-cover (Figure 4.10). At all sites, K_{in} responses to incremental changes in cover-density (i.e. changes equal to 0.5 of the representative LPF forest stand) are most pronounced at lower cover-densities, with only small responses observed with changes at higher cover-densities (Figure 4.11).

In general, the influence of slope orientation on K_{in} is seen in the differing sensitivity of irradiance to incremental changes in forest cover-density among the sites. As shown in Figure 4.11, increased above-canopy shortwave irradiance combined with the higher transmittance produced by the topographical orientation of the south-facing site gives for a considerable response in K_{in} to incremental changes across all cover-densities. By contrast, the longer shortwave extinction pathlength through forest-cover at the north-facing site produces little sensitivity in K_{in} to incremental cover-density changes, with greatest responses at this site occurring only at changes across very low cover-densities.

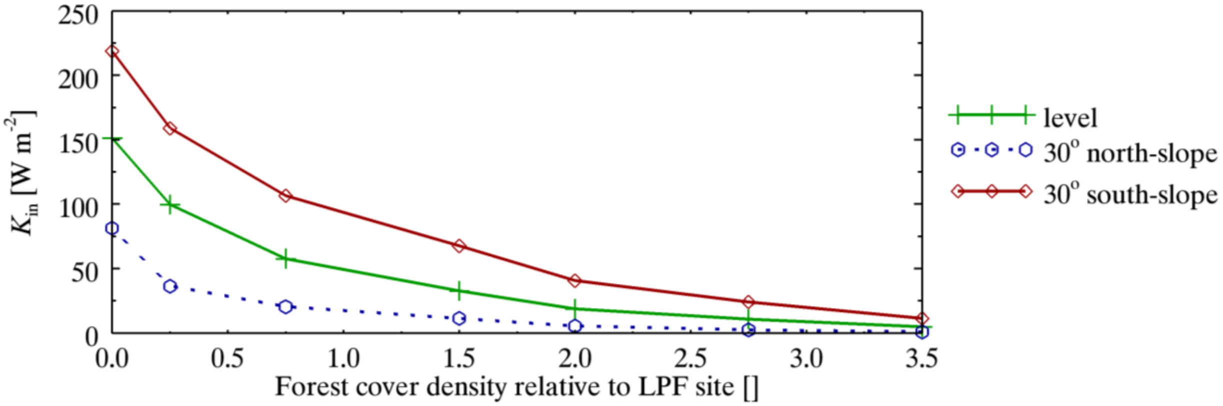

Figure 4. 10. Simulated K_{in} with respect to forest-cover density (ratio of measured LPF cover density) at a (i) level site, (ii) a site of 30° north-facing slope, and (ii) a site of 30° south-facing slope for the period extending March 15 – April 15, 2005.

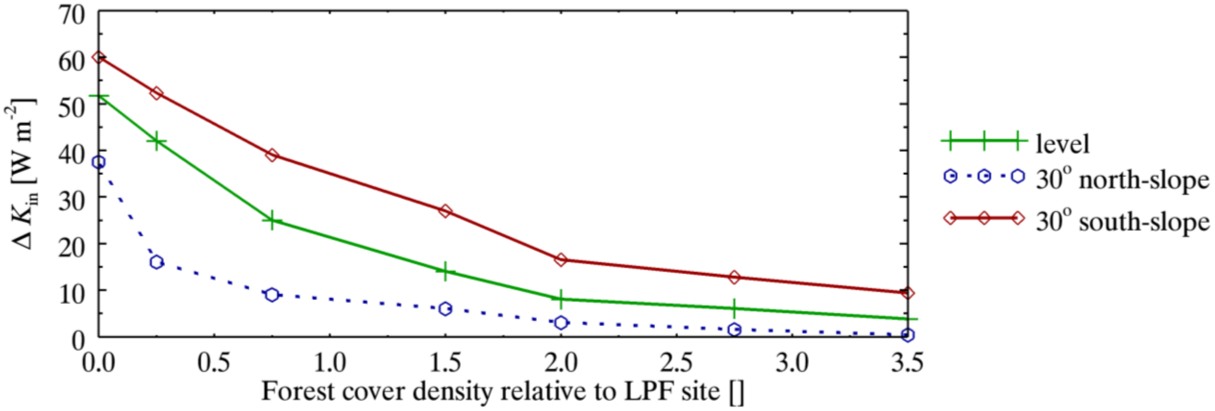

Figure 4. 11. Change (Δ) in simulated K_{in} with change in forest-cover density (ratio of measured LPF cover density) at a (i) level site, (ii) a site of 30° north-facing slope, and (ii) a site of 30° south-facing slope for the period extending March 15 – April 15, 2005.

4.8. Chapter discussion

Overall, results from the model evaluation presented in this chapter show it is capable of characterising the considerable differences in shortwave irradiance to snowcover in mountain needleleaf forests brought about by varying combinations of forest-cover density, slope orientation, and meteorological conditions. Despite some disagreement between simulated and observed K_{in} among sites, a generally good approximation of K_{in} was provided by the model, as seen in the representation of the substantial variations in forest shortwave transmittance (τ) created by the differences in forest-cover density and topography of the observation sites. At the SPF, the higher τ resulting from the shorter extinction pathlength and the sparser stand resulted in greater K_{in} to snowcover, both with respect to overall magnitude and the degree of variation in daily values throughout the period. Consequently, simulations errors were greatest at this site in terms of absolute magnitudes of K_{in}, but were lowest in terms of model efficiency as simulations were much better in representing the large variation in daily K_{in} at the SPF. By contrast, the relatively dense stand and longer extinction pathlength of the NPF resulted in substantially less K_{in} to snowcover, acting to reduce the amount of absolute error by the model, but degraded model performance in terms of the model efficiency index. In general, the accuracy of model determinations of K_{in} at each site reflected the accuracy of corresponding τ determinations; of which the best results for both were gained at the SPF, and least favourable results at the NPF. The relatively poor model performance at the NPF is partly attributed to the oblique orientation of the north-facing canopy to the sun, producing increased extinction of irradiance in the upper canopy from where the representative characteristics of the crown layer (i.e. crown dimensions) are more difficult to properly measure through ground-based surveying.

Application of the model in determining K_{in} to mountain snowcover further demonstrates the influence of site topography (i.e. slope orientation) on forest shortwave radiation transfers. In general, topography-controlled differences in shortwave irradiance diminish rapidly with increasing forest-cover density. Changes in forest density have the greatest impact on K_{in} in terms of absolute magnitude at the south-facing site, with comparatively little response in K_{in} with changes at the north-facing site. This difference is partly attributed to the shorter extinction pathlength irradiance travels through south-facing canopies compared to those of level or north-facing canopies. Consequently, substantial shifts in K_{in} with forest-cover changes at sites of more north-facing topography are expected to occur at only very low cover densities.

The good results provided by the model for sites of varying combinations of forest-cover density and topography are encouraging towards the estimation of shortwave radiation to mountain snowcover with decreased reliance on calibration, which is critical for application in remote regions where meteorological observations are sparse or absent. Although proper application of the model requires detailed forest stand information typically not included in most standard forest inventories, developing remote sensing technologies such as LiDAR show promise in providing sufficiently accurate, high-resolution spatial data of forest stand characteristics over extensive areas (e.g. Lefsky et al., 1999; Essery et al., 2007).

A distinct advantage to the model includes its explicit representation of irradiance transmission through crown, trunk, and gap components of the canopy. As such, it demonstrates potential for use in assessing how changes in forest-cover density, and particularly, changes in forest stand structure influence shortwave radiation dynamics in conifer stands. Such approaches, when used in combination with appropriate hydrological simulation models, may provide a useful tool toward investigating the hydrological impacts from forest changes in mountain environments.

Parts of this chapter have been published in:

Ellis, C. R., and J. W. Pomeroy. 2007. Estimating shortwave irradiance through needleleaf forests on complex terrain. *Hydrol. Process*. 21: 2581-2593, doi: 10.1002/hyp.6794.

5. SENSITIVITY OF RADIATION TO MOUNTAIN SNOWCOVER WITH VARYING FOREST-COVER AND METEOROLOGY

5.1. Chapter summary

This chapter investigates the influence of needleleaf forest-cover on radiation to snow in Canadian Rocky Mountain environments using a simple physically-based modelling approach which is evaluated against sub-canopy radiation observations in mountain forests of varying slope orientation and canopy density. Simulations are used to examine how shortwave and longwave radiation fluxes to snow respond to varying canopy openness, slope orientation, and snow albedo under both theoretical and observed meteorological conditions throughout the winter-spring period. The model is extended to provide a better representation of longwave exchanges between canopy and snow layers produced by shortwave heating of the canopy and snow surface cooling from sublimation losses. Results show that during the early winter, increased radiation to snow is realised under closed forest canopies regardless of slope orientation, as forest-cover acts to minimise longwave losses. However, with increasing shortwave irradiance into the spring, this balance is reversed at sites of south-facing and level topography where increased radiation to snow occurs under more open canopy-covers, especially for conditions of low snow albedo. By contrast, greater radiation to north-facing snowcovers and snowcovers of higher snow albedo is maintained under more closed-canopies late into the spring. These results illustrate the disparate effects forest-cover has upon radiation for spring snowmelt across complex mountain terrain, and the considerable influence of meteorological conditions on how forest-cover impacts snow radiation.

5.2. Chapter introduction: the forest radiation paradox

Needleleaf forest-cover strongly influences radiation to snow by its extinction of shortwave radiation and emission of longwave radiation. From a hydrological perspective, radiation to snow is of significance as it is the primary energy source for snowpack warming and melt in many environments. From a theoretical standpoint, forest-cover impacts on radiation to snow may be viewed in terms of the balance between opposing shortwave reductions and longwave enhancements by the canopy. Although increased canopy-closures have generally been observed to decrease total radiation to snow and slow melt rates (Link and Marks, 1999), longwave gains under forest-cover may more than compensate for shortwave losses, particularly for conditions of low atmospheric shortwave and longwave irradiance, high snow albedo, and warmer canopy temperatures (Sicart et al., 2004). This counterbalancing of shortwave reductions against longwave gains under forest canopies may be viewed as a special case of Ambach's (1974) 'radiation paradox', which describes the effects of atmospheric conditions upon radiation to snow in open environments. Similarly, investigations by Bohren and Thorud (1973) and Sicart et al., (2004) have illustrated the substantial influence meteorological conditions have in determining forest-cover impacts on snow radiation balances; yet these investigations have been largely confined to select meteorological conditions and level terrain. Considering the large variation in shortwave irradiance across mountain landscapes combined with changing meteorological conditions throughout the winter-spring period, such focused investigations are unlikely to adequately represent the range of forest-cover impacts on radiation to mountain snow.

Due to the lack of detailed radiation measurements for the varying combinations of canopy openness, slope orientation, and meteorological conditions typical of mountain environments, insight into forest-cover influences upon radiation to snow and snowmelt often appeal to information provided via physically-based determinations. Challenges exist however in establishing a modelling approach that maintains a physical representation of forest radiation and snowmelt dynamics using a simple and instructive index to describe forest-cover density. Although many simulation exercises (e.g. Bohren and Thorud, 1973; Yamazaki and Kondo 1992; Davis et al. 1997; Sicart et al., 2004) have provided valuable insight of the theoretical considerations of forest-radiation dynamics in snow-covered environments, such approaches are often limited in representing longwave exchanges between the forest and snow layers as influenced by canopy heating from shortwave absorption and snow surface temperature depressions via sublimation losses. As such, this chapter outlines the development of a modelling approach designed to represent the effects of varying needleleaf forest-cover density, topography, and meteorology on shortwave and longwave radiation fluxes to mountain snowcovers using a simple index describing forest-cover density. A facility particular to this model lies in its determination of longwave radiation to forest snowcovers with explicit account for (i) shortwave heating of the canopy and (ii) sublimative cooling of the snow surface. Evaluation of the model is provided through a comparison between simulated and observed fluxes of shortwave and longwave radiation to snow in mountain needleleaf forests of varying canopy-openness (i.e. forest-cover density) and slope orientation (i.e. slope and aspect). The model is subsequently applied to examine how needleleaf forest-cover and meteorological conditions influences radiation to mountain snowcovers in the MCRB.

5.3. Simulation of sub-canopy shortwave and longwave irradiance

5.3.1. Description of forest-cover density

In the model, forest-cover density is quantified by the following two interrelated terms: the optical depth of the forest ($L`$) and the forest sky view factor ($v$). Formally defined, $L`$ is given as the negative logarithm of vertical radiation transmittance (τ_f) through the forest layer, i.e.

$$\tau_f = e^{-L`} \tag{5.1}$$

Here, $L`$ may otherwise be referred to as the radiation extinction coefficient of the forest layer [$m^{-1}$]. Accordingly, $L`$ pertains only to the canopy foliage affecting radiation transfer through the forest layer, and discounts additional canopy foliage material that is self-shaded from either structuring or orientation effects (Chen and Black, 1992). Assuming $L`$ and τ_f are invariant with azimuth and elevation angles throughout the overlying sky hemisphere, the forest sky view factor (v) may be evaluated by the following integration of Eq. 5.1

$$v = 2\int_0^{\pi/2} e^{-\frac{L`}{\sin\theta}} \cos\theta \sin\theta \cdot \delta\theta = 2\int_0^{\pi/2} \tau_f(\theta) \cos\theta \sin\theta \cdot \delta\theta \tag{5.2}$$

where θ is the solar elevation angle above the horizon [radians]. Under this framework, the compliment of the overlying hemisphere not occupied by v is occupied by forest-cover, termed here the ‘canopy-closure’ (i.e. $1-v$), which is completely non-transmitting to irradiance. Consequently, this gives an overlying hemisphere comprised of a fully-transmitting radiation compliment and a non-transmitting compliment, in proportions weighted respectively by v and ($1-v$).

5.3.2. Determination of sub-canopy shortwave irradiance

Determination of shortwave irradiance to mountain forest snow is made through the separate determinations of: (i) above-canopy shortwave irradiance with respect to slope and aspect (K_o(S)), (ii) shortwave transmittance through forest-cover (τ) and (iii) shortwave enhancement to snow brought about by multiple reflections between snow and forest layers. Here, above-canopy shortwave irradiance to a sloped surface (K_o(L)) of aspect φ and slope gradient $\mathit{\Lambda}$ is determined by adjustment of level irradiance observations (K_o(L)) via separate corrections of direct-beam and diffuse components (e.g. Tian et al., 2004), i.e.

$$K_{\mathrm{o}}(\mathrm{S}) = (1 - k_{\mathrm{d}})\,K_{\mathrm{o}}(\mathrm{L})\ \omega(\mathit{\Lambda},\varphi) +\ k_{\mathrm{d}}K_{\mathrm{o}}(\mathrm{L})\,(1 - \mathit{\Lambda}/\pi) \qquad \textbf{(5.3)}$$

where $\omega(\mathit{\Lambda},\ \varphi)$ [] is the geometric correction factor for level direct-beam irradiance to a slope of gradient $\mathit{\Lambda}$ and aspect φ (calculation of $\omega(\mathit{\Lambda},\ \varphi)$ is provided in Appendix A), and k_d is the fraction of diffuse-to-total shortwave irradiance []. Determination of k_d is made through a semi-empirical relation to the atmosphere transmittance index (k_t) [] (Liu and Jordan, 1960; Iqbal, 1983) of the basic form:

$$k_{\mathrm{d}} = ak_{\mathrm{t}} + b \qquad \textbf{(5.4)}$$

where the a and b denote empirical coefficients for varying locations and climates (determination of k_t is provided in Appendix A). As diffuse irradiance is considered to be received equally throughout the sky hemisphere, the forest shortwave transmittance (τ) for completely diffuse conditions equals v. However, such sky conditions are seldom encountered as irradiance is often received disproportionately from the sun as direct-beam irradiance. Thus, the forest transmittance of direct-beam shortwave irradiance (τ_b) with geometric pathlength adjustment of L` for solar elevation angle θ, slope gradient $\mathit{\Lambda}$, and aspect (e.g. Duursma et al., 2003) is made by ξ in the following modification of Eq. 5.1

$$\tau_{\mathrm{b}}(\theta,\mathit{\Lambda},\varphi) = e^{-L`\xi(\theta,\mathit{\Lambda},\varphi)} = e^{-\frac{L`}{\omega(\mathit{\Lambda},\varphi)\sin(\theta)}} \qquad \textbf{(5.5)}$$

Thus, assuming the forest transmittance of diffuse irradiance (τ_d) equals the forest sky view factor (i.e. $\tau_d = v$), and combining Eq. 5.3 and Eq. 5.5, the effective forest shortwave transmittance (τ) is resolved by

$$\tau = v\,k_d + (1 - k_d)\,\tau_b \tag{5.6}$$

Note here that unlike τ_f in Eq. 5.1, τ in Eq. 5.6 represents the forest transmittance of non-vertical shortwave irradiance. Upon transmittance through the forest layer, shortwave irradiance to snow (K_{in}) with account for enhancements by multiple reflections between the snow and forest layers is given by the following expression similar form to Eq. 4.21 (Chapter 4)

$$K_{in} = \frac{K_{o,s}\tau_f(1 - \alpha_s)}{1 - \alpha_s\alpha_f(1 - v)} \tag{5.7}$$

where α_s and α_f are the respective snow and forest albedo values [].

5.3.3. Determination of sub-canopy longwave irradiance

Determination of sub-canopy longwave irradiance (L_{in}) is made by the sum of above-canopy longwave irradiance (L_o) and estimated canopy longwave emissions, weighed respectively by the forest sky view factor (v) and the canopy closure ($1–v$) as

$$L_{in} = vL_o + (1 - v)\,\varepsilon_f\,\sigma T_{eff}^{\,4} \tag{5.8}$$

where ε_f is the thermal emissivity of the forest layer [], σ is the Stephan-Boltzmann constant [W m^{-2} K^{-4}], and T_{eff} is effective temperature of the forest layer [K]. Although T_{eff} is routinely approximated by air temperature (T_a), this approach has been shown to substantially underestimate forest longwave emissions by expressions similar to Eq. 5.8 due to canopy heating above T_a from absorption of shortwave irradiance (Pomeroy et al., 2009). A further assessment of the errors associated with T_a approximations for determining sub-canopy longwave radiation in mountain forests is provided in Section 5.7.1, which also outlines a procedure accounting for canopy shortwave heating in the specification of T_{eff}.

5.4. Evaluation of model sub-canopy irradiance determinations

To evaluate the model's ability in representing sub-canopy K_{in} and L_{in}, simulated radiation fluxes were compared to those observed in five needleleaf forests of varying canopy density and topographical orientation in the MCRB. Sub-canopy K_{in} and L_{in} were observed at the Level Pine Forest site (LPF), North-facing Pine Forest (NPF), and the Southeast-facing Pine Forest (SPF) for the period extending from January 1 – June 1, 2006, and at the higher elevation North-facing Spruce Forest (NSF) and South-facing Spruce Forest (SSF) over January 1 – June 1, 2008. Simulations at each site were performed by approximating above-canopy shortwave irradiance (K_{o}) and longwave irradiance (L_{o}) from radiation observations collected at the nearby Level Pine Clearing (LPC) and Level Spruce Clearing (LSC) reference sites. Topographic and forest-cover descriptions of the forest and clearing sites as well as the mean observed K_{in} and L_{in} at each site over the observation periods are given in Table 5.1. For model evaluation, simulations of K_{in} and L_{in} at each forest site were made on an hourly timestep over the respective pine and spruce observation periods for forest sky view factors (v) ranging along a continuum of 0 – 1. The mean daily observed K_{in} and L_{in} are compared to that simulated for 0 – 1 v values at each site using the following two measures: (i) the mean bias index (MB) (Eq. 4.23) to compare the total simulated and observed irradiance over the period, and (ii) the model efficiency index (ME) (Eq. 4.24) to quantify the model's ability in representing the observed variability among daily irradiance values.

Figure 5.1 shows the MB and ME values determined for simulations of daily K_{in} and L_{in} at each forest site. Here, mean daily values are compared to reduce the spatial variation in sub-canopy shortwave irradiance typical over sub-daily time scales (Essery et al., 2007). Although simulations were made for v values of 0 – 1 at each site, ME and MB indexes are shown over the narrower range of 0 – 0.5 to provide a clearer illustration of results. For both K_{in} and L_{in} simulations, a pronounced convergence in MB and ME values toward unity (i.e. the optimal simulation result) occurs about a single v value at each site, which is shown to generally correspond to the v values determined via hemispherical photograph analysis (Table 5.1). Although some noticeable separation in optimal index values is noticeable for the respective K_{in} and L_{in} simulations at each site, their general convergence about a single v value indicates the model is capable of providing good approximation of both K_{in} and L_{in} through a single parameterisation of forest-cover density by v. Particularly encouraging from the evaluation is the good representation by the model of the substantial differences in K_{in} produced by the varying combinations of forest-cover density and slope orientation of the forest sites.

5.5. Determination of net radiation to snow

From the estimation of K_{in} with account for multiple reflection between snow and forest layers by Eq. 5.7, the net shortwave radiation flux to snow (K^*) is given by

$$K^* = K_{\mathrm{in}}(1 - \alpha_{\mathrm{s}}) \qquad \textbf{(5.9)}$$

Alternatively, the balance of L_{in} and longwave exitance from snow (L_{out}) yields the net longwave radiation flux to snow (L^*) through

$$L^* = \varepsilon_{\mathrm{s}}(L_{\mathrm{in}} - \sigma T_{\mathrm{s}}^{\,4}) \qquad \textbf{(5.10)}$$

where ε_{s} is the thermal emissivity of snow [], and T_{s} is snow surface temperature [K].

Table 5. 1. Topographic and forest-cover descriptions of the five forest and clearing meteorological observation sites used in model evaluation. Forest-cover descriptions are provided by hemispherical photograph analysis using CANEYE software (Baret and Weisse, 2004), with the exception of the forest optical depth, $L`$ parameter, which was determined from the forest sky view factor (v) through rearrangement of Eq. 5.2. Also stated are the mean shortwave irradiance (K_{in}) and longwave irradiance (L_{in}) at each site during the respective observation periods.

Site:	*Observation period*	*Elevation* [m.a.s.l.]	*Slope* (Λ)/ *aspect* (φ) [°]	*Forest sky view factor* (v) []	*Forest optical depth* ($L`$)* []	*Green foliage fraction* (g_f) []	*Crown foliage fraction* (f_C) []	*Mean* K_{in} [W m^{-2}]	*Mean* L_{in} [W m^{-2}]
Level Pine Forest (LPF)	Jan 20 – Jun 1, 2006	1492	0/0	0.22	0.96	0.32	0.41	32.7	287.9
North-facing Pine Forest (NPF)	Jan 1 – Jun 1, 2006	1480	29/351	0.19	1.05	0.38	0.55	17.9	285.5
Southeast-facing Pine Forest (SPF)	Jan 1 – Jun 1, 2006	1523	26/125	0.34	0.69	0.42	0.47	64.1	292.8
Level Pine Clearing (LPC)	Jan 1 – Jun 1, 2006	1457	0/0	0.98	–	–	–	149.4	244.2
North-facing Spruce Forest (NSF)	Jan 7 – Jun 1, 2008	2037	28/348	0.16	1.16	0.48	0.62	17.9	288.1
South-facing Spruce Forest (SSF)	Jan 7 – Jun 1, 2008	2008	28/176	0.09	1.53	0.52	0.68	18.5	287.5
Level Spruce Clearing (LSC)	Jan 7 – Jun 1, 2008	1848	0/0	0.96	–	–	–	138.4	239.5

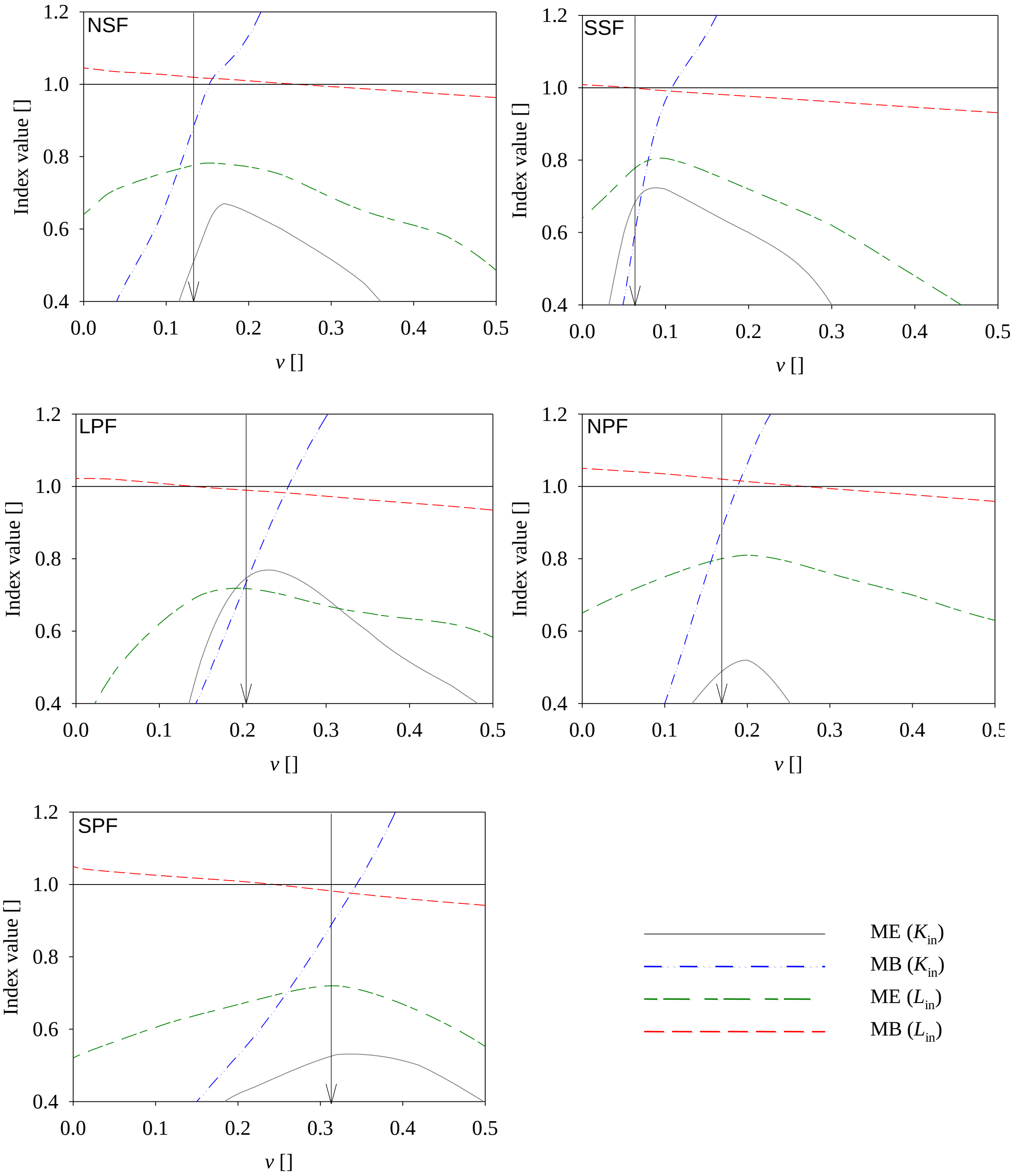

Figure 5. 1. Determined model efficiency (ME) and model bias (MB) indexes of simulations of daily sub-canopy shortwave irradiance (K_{in}) and sub-canopy longwave irradiance (L_{in}) for forest sky view factors (*v*) ranging from 0 – 0.5 at the LPF, NPF, SPF, NSF, SSF sites over the respective pine and spruce January 1 – June 1 observation periods. The *v* for each forest site as estimated from hemispherical photograph analysis (Table 5.1) is indicated by the vertical arrow.

5.6. *Model Application 1*: Forest-cover effects on radiation to mountain snowcover for theoretical meteorological conditions

In order to assess the impacts of forest-cover on radiation fluxes to snow, the influence of changing atmospheric conditions such as from cloud-cover fluctuations must be examined. In general, cloud-cover has a countering effect on sky radiation by its extinction of shortwave irradiance and enhancement of longwave irradiance through increased atmosphere thermal emissivity (Ambach, 1974; Plüss and Ohmura, 1997). This effect is illustrated in Figure 5.2, which shows a generally negative relation in atmospheric shortwave transmittance (i.e. k_t) to the effective atmospheric emissivity (ε_{atm}) which is calculated from observations at the LSC site by

$$\varepsilon_{atm} = \frac{L_o}{\sigma T_a} \quad \textbf{(5.11)}$$

where L_o and T_a are the respective observed longwave irradiance and near-surface air temperatures. Although near-surface temperatures are not expected to provide an exact proxy of atmospheric temperatures in Eq. 5.11, resultant errors are expected to be small considering that most sky longwave radiation is emitted from lower atmospheric layers (Brustaert, 1982). From Figure 5.2, the best linear relation between k_t and ε_{atm} is given by

$$\varepsilon_{atm} = -0.5k_t + 0.99 \quad \textbf{(5.12)}$$

which has a correlation coefficient (R^2) of 0.76, and a standard error for the estimation of ε_{atm} equal to 0.056.

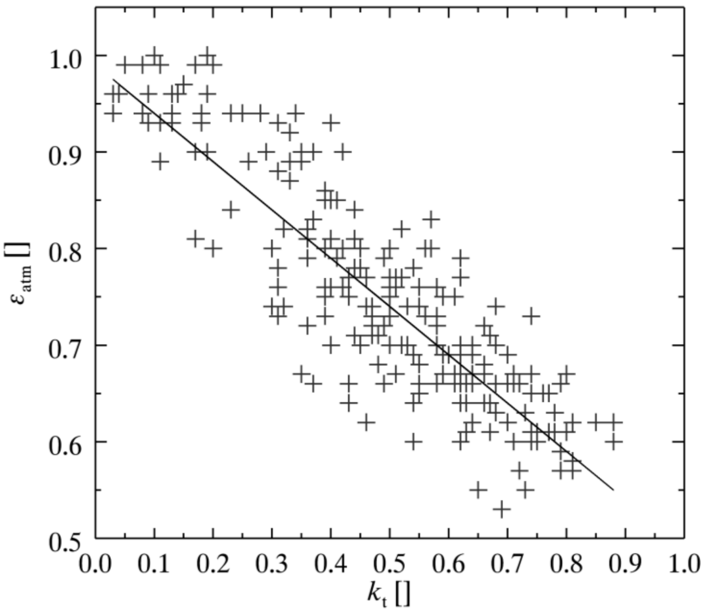

Figure 5. 2. Relationship between daily atmospheric shortwave transmittance (k_t) and effective atmospheric emissivity (ε_{atm}) calculated from data collected at the LSC reference site over January 1 – June 1, 2008.

Despite the considerable degree of scatter in the k_t - ε_{atm} relationship shown in Figure 5.2, the derived relation of Eq. 5.12 is useful as it allows the theoretical approximation of the following sky radiation conditions by a single value of k_t:

(i) K_o (via rearrangement of Eq. 3.3 (Chapter 3));
(ii) direct-beam and diffuse shortwave irradiance (via rearrangement of Eq. 5.4) and;
(iii) L_o (via rearrangement of Eq. 5.11).

Thus, using k_t to index the above sky radiation conditions, the effect of forest-cover on net radiation to mountain snowcover (R^*) was investigated through the simulation of K^* and L^* for v values ranging from 0 – 1 over the period of January 1 – June 1. To assess the influence of topography on R^*, simulations were made to the following hypothetical sites in the MCRB: a level slope site (LS), a 30° sloped site of north-facing aspect (NS), and a 30° sloped site of south-facing aspect (SS). To illustrate the effects of varying sky conditions representative of those at the MCRB, simulations were made for a k_t = 0.3 and 0.7, which closely correspond to a single standard deviation less than and greater than the mean k_t for the distribution of values in

Figure 5.2. As no appreciable shifts in the distribution of k_t values were observed over the January – June period, the k_t values of 0.3 and 0.7 were held constant for simulations. Finally, to approximate a representative T_a throughout the period, the mean daily T_a was specified by the following the relationship constructed from a 68-year dataset of monthly T_a observations collected at a meteorological station located 13 km northeast of the MCRB:

$$T_a\,(\mathrm{DOY}) = 0.13\mathrm{DOY} - 14.06 \qquad (\mathrm{R}^2 = 0.97) \tag{5.13}$$

where DOY denotes the day of the calendar year. It is noted here that for these simulations, estimation of forest and snow longwave emissions were made with T_{eff} in Eq. 5.8 and T_s in Eq. 5.10 equal to T_a; the errors from which are assessed in Section 5.7. Determination of K^* to snow was made for snow albedo values (α_s) of 0.8 and 0.7, intended to represent relatively high and low seasonal snow albedo conditions, respectively, based upon reflectance measurements over fresh and old snowcovers obtained using a portable spectroradiometer (Chapter 3).

Under these theoretical meteorological and snow conditions, the effects of forest-cover and topography on R^* are illustrated in Figure 5.3 in terms of the forest sky view factor (v) at which maximum R^* ($v(R^*_{max})$) occurs and the corresponding R^*_{max} for simulations to the LS, NS, and SS sloped sites. Here, $v < v(R^*_{max})$ indicates a decrease in radiation from R^*_{max} by way of shortwave reductions to snow, while, $v > v(R^*_{max})$ indicates a decrease in radiation from R^*_{max} via longwave losses to snow. Overall, simulation results in Figure 5.3 show a general increase in $v(R^*_{max})$ at all sites over the winter-spring period. During the early winter, R^*_{max} is obtained under very low v (i.e. low canopy openness) at all sites regardless of sky k_t or snow albedo (α_s), as longwave enhancements under forest-cover more than compensate for the small shortwave reductions from canopy extinction. Consequently, $R^*_{max} = 0$ during this time, due to a complete counterbalancing between forest and snow longwave emissions. However, moving into spring, the increasing K_o with higher solar elevations give R^*_{max} at progressively higher v values (i.e. more open canopies), starting first at the south-facing SS site followed by the level LS site. By contrast, R^*_{max} at the north-facing NS is maintained under very low v until mid-April, when the site ceases to be topographically self-shaded from shortwave irradiance, resulting in a rapid rise in $v(R^*_{max})$ under high k_t and low α_s conditions. Yet, for a higher α_s of 0.8 at the NS, R^*_{max}

remains at very low *v* values through the spring. This sizeable shift in $R^*_{\max}$ with snow albedo at the NS reveals the close balance between shortwave and longwave exchanges with changing canopy openness at this site.

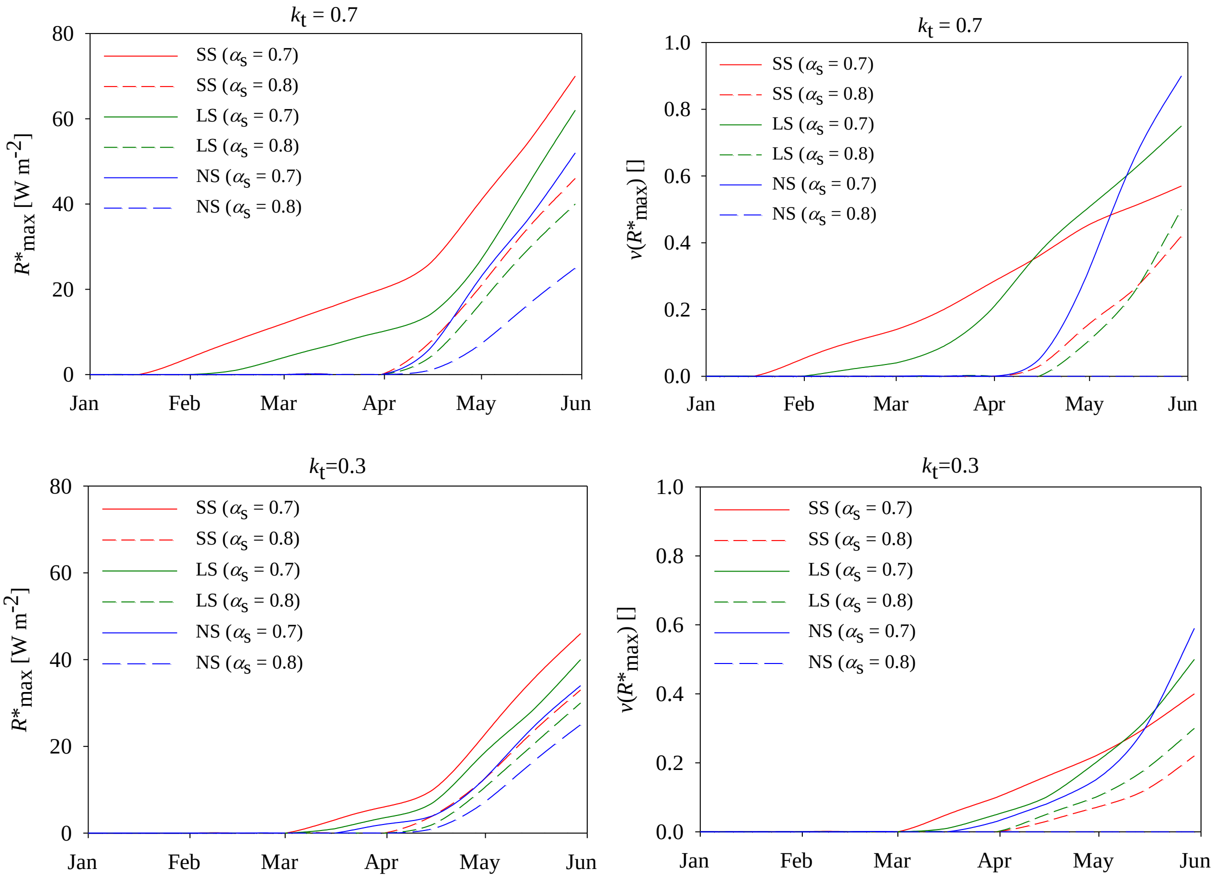

Figure 5. 3. Maximum daily net radiation to snowcover ($R^*_{\max}$) and the corresponding forest sky view factor ($v(R^*_{\max})$) simulated to a level slope site (LS), a 30° sloped site of north-facing aspect (NS), and a 30° sloped site of south-facing aspect (SS) for theoretical atmospheric transmittances (k_t) of 0.3 and 0.7 and snow albedo (α_s) of 0.7 and 0.8.

As expected, topographic differences in radiation are intensified with higher k_t and lower α_s as these conditions maximise the topography-controlled shortwave variations between slopes. Similarly, the influence of α_s upon radiation to snow is greatest for conditions of relatively clear skies (i.e. k_t = 0.7), with much reduced responses under high cloud-cover. Due to higher shortwave irradiance to the south-facing SS, R^* is most sensitive to changes in k_t and α_s at this site, and conversely least responsive at the north-facing NS where radiation is dominated more by longwave fluxes. However, regardless of meteorological and snow albedo conditions, a progressive increase in R^*_{max} is observed on all slopes throughout the January – June period, punctuated by a pronounced R^*_{max} increase in early April when longwave losses from the warming snowpack become constrained by a maximum T_{s} of 0 °C in Eq. 5.10.

5.7. Improved representation of longwave emissions from forest-cover and snow for observed meteorological conditions

As forest and snow surface temperatures are rarely observed directly, estimation of forest and snow longwave emissions by expressions such as Eq. 5.8 and Eq. 5.10 often approximate the effective canopy temperature (T_{eff}) and snow surface temperature (T_{s}) using air temperature (T_{a}) observations. However, substantial errors in forest and snow longwave estimates may result from this approximation due to canopy heating above T_{a} from shortwave irradiance absorption, and by snow surface cooling below T_{a} via sublimation energy losses. Although differences in T_{eff} and T_{s} relative to T_{a} are typically small, resultant errors in approximating longwave exchanges between forest and snow layers may be considerable, especially when viewed over extended timescales. However, due to the numerous meteorological factors governing forest shortwave heating and snow surface cooling, proper representation of each requires appeal to physically-based determinations. Accordingly, the following sections outline: (i) the development and evaluation of a modelling procedure to account for sub-canopy longwave enhancements resulting from shortwave heating of the canopy, and (ii) an evaluation of the snow surface temperature modelling procedure developed by Pomeroy and Essery (2010) for application to mountain forest snowcovers.

5.7.1. Impact of canopy shortwave heating on sub-canopy longwave irradiance

5.7.1.1. Observations in mountain forests

As shown by extensive field measurements by Pomeroy et al. (2009), the absorption of shortwave irradiance by forest foliage may result in substantial canopy heating and elevated longwave irradiance to the sub-canopy. Using meteorological observations collected at the five forest sites in the MCRB, sub-canopy longwave enhancements from forest shortwave heating are assessed by the effective radiating temperature of the forest (T_{eff}) [°C], which may be evaluated through the following rearrangement of Eq. 5.8:

$$T_{eff} = \sqrt[4]{\frac{(L_{\mathrm{in}} - vL_{\mathrm{o}})/\varepsilon_f \sigma}{(1-v)}} - 273.15 \tag{5.14}$$

Figure 5.4 shows time series data of T_{eff}, T_{a}, as well as the forest crown surface temperatures (T_{crown}) and trunk surface temperatures (T_{trunk}) at the pine and spruce forest study sites. Also shown for each time series is the above-canopy shortwave irradiance (K_{o}) observed at the corresponding LPC and LSC meteorological reference sites. At all forest sites, T_{eff} was determined via Eq. 5.14 from L_{in} observations collected by single pyranometers, with the exception of the LPF and SPF where L_{in} was taken as the mean of observations obtained by a 12-pyrgeometer array. Overall, Figure 5.4 shows that at the sparse SPF site, substantial elevations in T_{eff} over T_{a} occur, which are most pronounced during periods of increased K_{o} when T_{eff} reach temperatures 3 – 6 °C warmer than T_{a} and T_{crown}. This warmer T_{eff} is attributed largely to added longwave emissions from heated trunks, as T_{trunk} typically exceeds both T_{a} and T_{crown} by more than 20 °C during periods of high K_{o} (Figure 5.4: middle, bottom).

Substantial elevations in T_{eff} over T_{a} are also observed at the LPF site (Figure 5.5), which unlike at the SPF, occur more through heating of the crown layer by evidence of the substantial T_{crown} elevations during high K_{o}. Considering the similar K_{o} to the SPF and LPF sites, the warmer LPF crown temperatures are ascribed to sparser green foliage in the crown, which permits greater heating of crown branches by exposure to shortwave irradiance. Alternatively, at the NPF site, despite the similar sparse green foliage and K_{o} conditions to the LPF, little shortwave heating of the forest occurs as observed in the similar T_{eff}, T_{crown}, T_{trunk}, and T_{a} (Figure 5.5) caused by the north-facing canopy preventing substantial shortwave penetration and heating of the lower forest layers. Similarly, negligible shortwave heating occurs at both the spruce NSF and SSF sites, where the dense canopy restricts shortwave penetration to lower foliage layers seen by the close tracking of T_{eff} and T_{crown} with T_{a} at both sites (Figure 5.6).

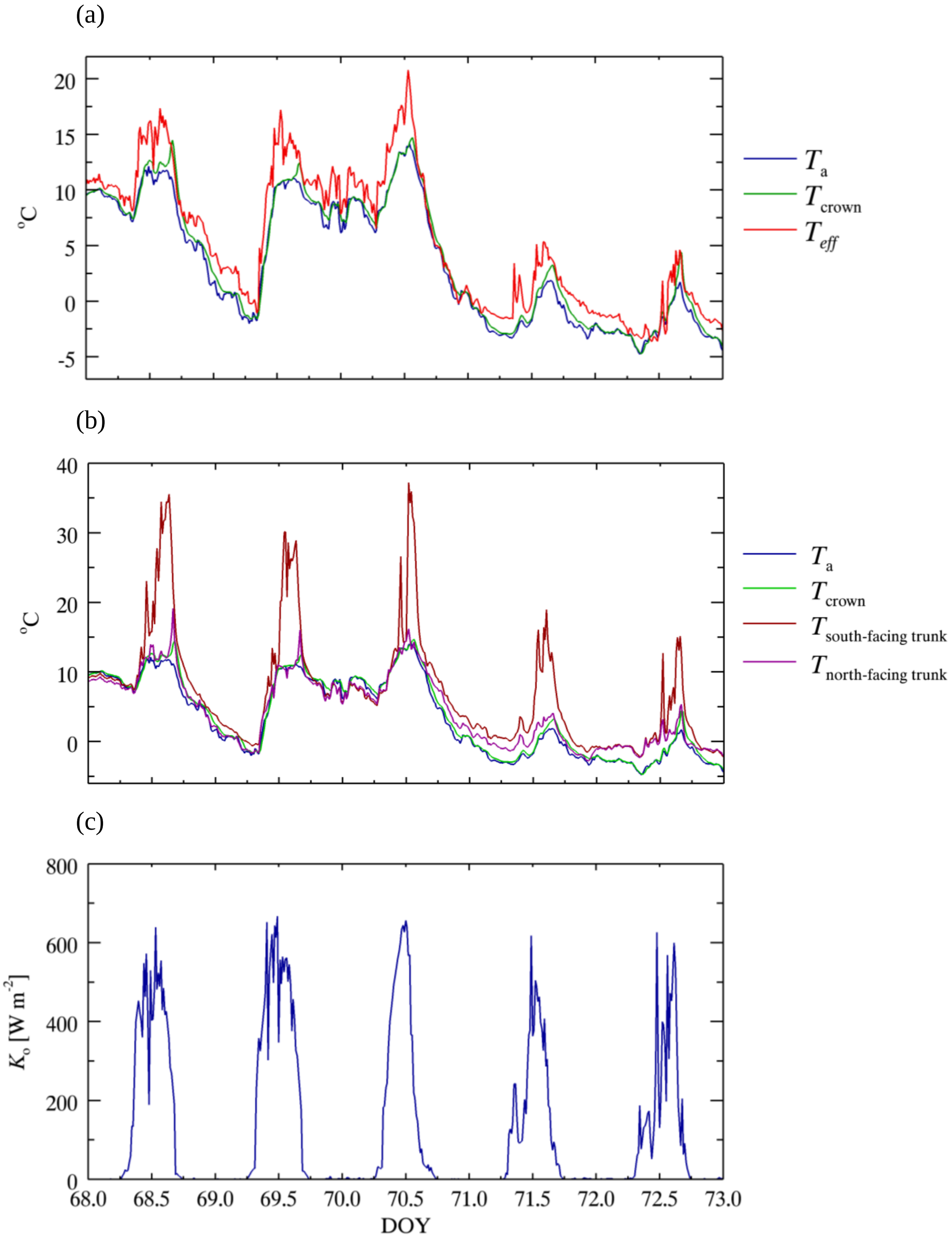

Figure 5. 4. (a): Time series of air temperature (T_a), forest crown surface temperature (T_{crown}), and the effective forest radiating temperature (T_{eff}) at the Southeast-facing Pine Forest site (SPF); (b): T_a and T_{crown} compared to the south-facing and north-facing trunk surface temperatures ($T_{north\text{-}facing\ trunk}$, $T_{south\text{-}facing\ trunk}$); (c): corresponding above-canopy shortwave irradiance (K_o) as observed at the LPC reference site.

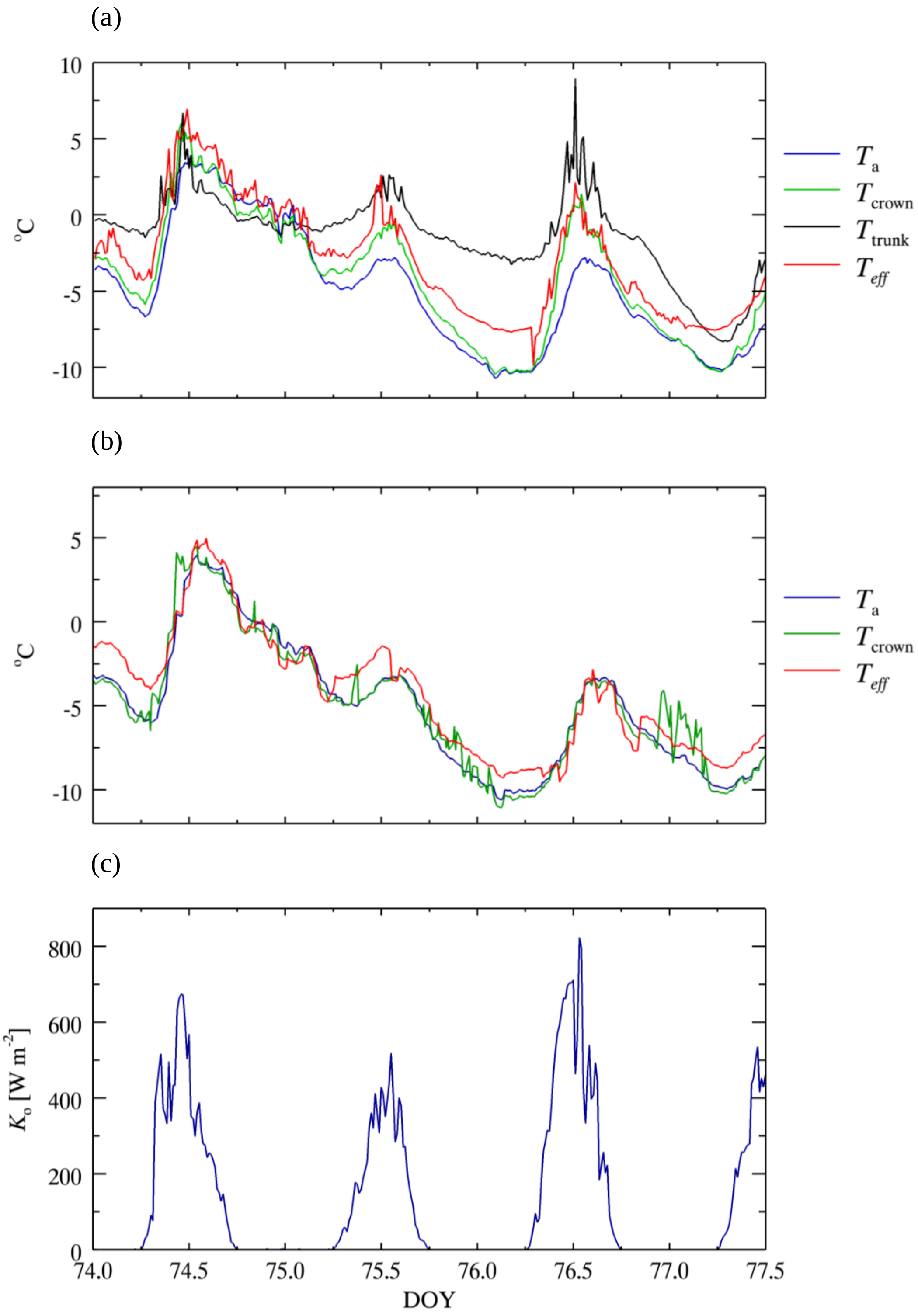

Figure 5. 5. (a): Time series of air temperature (T_a), forest crown surface temperature (T_{crown}), and effective forest radiating temperature (T_{eff}) at the Level Pine Forest (LPF) site (top) and (b): the North-facing Pine Forest (NPF) site; (c): time series data of above-canopy shortwave irradiance (K_o) as observed at the LPC reference site.

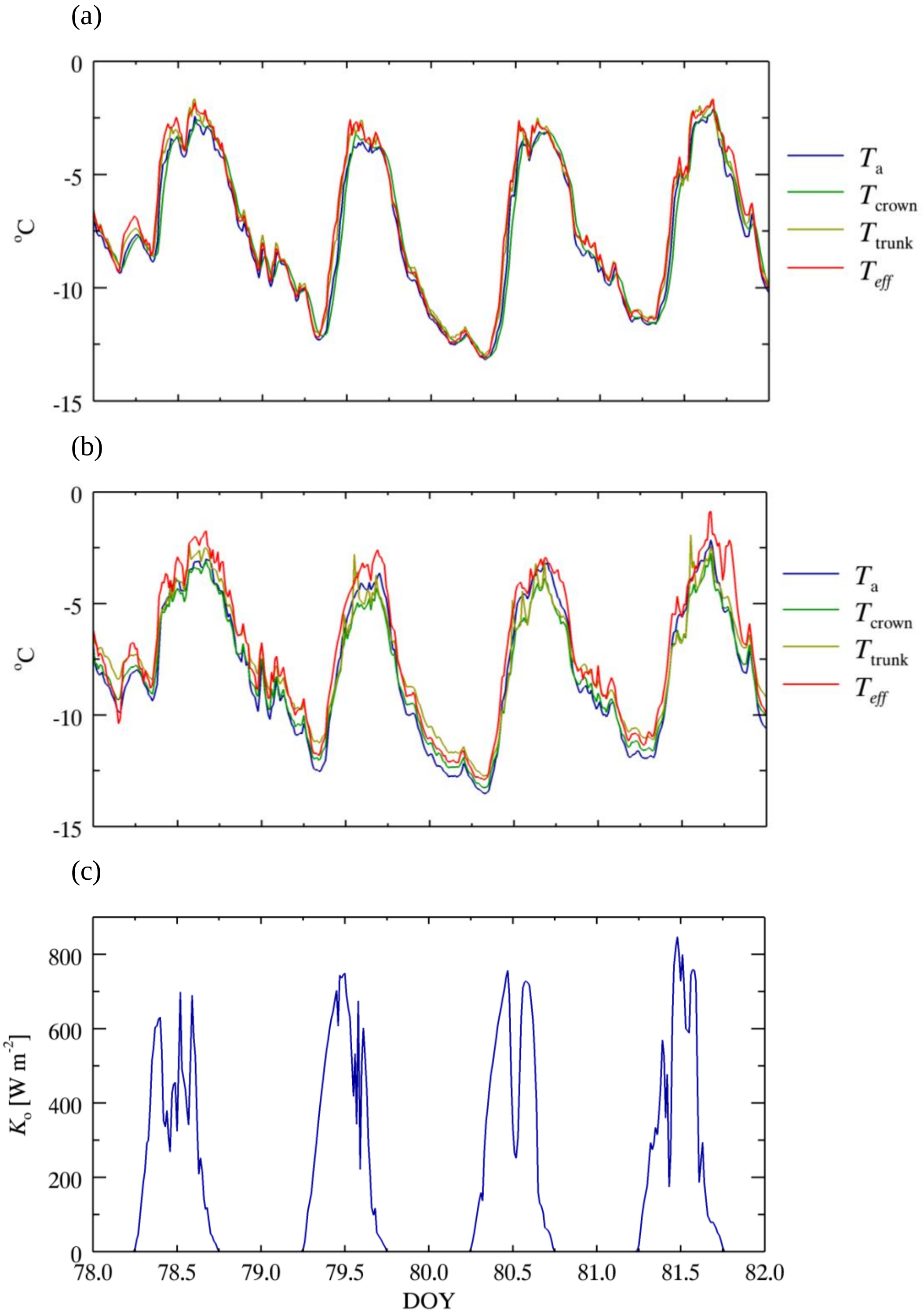

Figure 5. 6. (a): Time series of air temperature (T_a), forest crown surface temperature (T_{crown}) and effective forest radiating temperature (T_{eff}) at the North-facing Spruce Forest site (NSF) (top) and at (b): the South-facing Spruce Forest site (SSF); (c): corresponding above-canopy shortwave irradiance (K_o) as observed at the Level Spruce Clearing (LSC) reference site.

In addition to direct temperature measurements, the influence of forest shortwave heating upon sub-canopy longwave irradiance is further demonstrated through the combined use of thermal imaging and spatially-distributed radiation measurements. Thermal and visible images were taken of the north-edge and south-edge of a small forest clearing of approximate equal height and diameter located 15 km south of the MCRB throughout the day of March 16, 2006. In addition to thermal images, longwave irradiance (L_{in}) observations were made across the clearing by a 12-pyrgeometer array positioned along a north-south transect extending through the gap into the north-edge forest-cover.

As shown in Figure 5.7, corresponding thermal and visible images show little forest heating along the south forest-edge, but considerable heating along the north forest-edge. Heating of the north-forest edge is greatest during the early afternoon (i.e. 1330) when higher solar angles allow shortwave penetration through the clearing to the north forest-edge; evident by the largely sunlit forest scene in the 1330 visible image. However, as shown in the corresponding 1330 thermal image, foliage heating is confined mostly to trunks and branches, with comparatively little heating of green needleleaf foliage. Periods of trunk and branch heating correspond to increased longwave irradiance to snow about the north forest-edge as shown by radiometer array measurements in Figure 5.7 (bottom). With declining afternoon solar angles however, longwave elevations to snow from forest heating diminish, although noticeably higher L_{in} magnitudes are maintained at the north forest-edge relative to the south forest-edge.

South-edge of forest clearing (930):

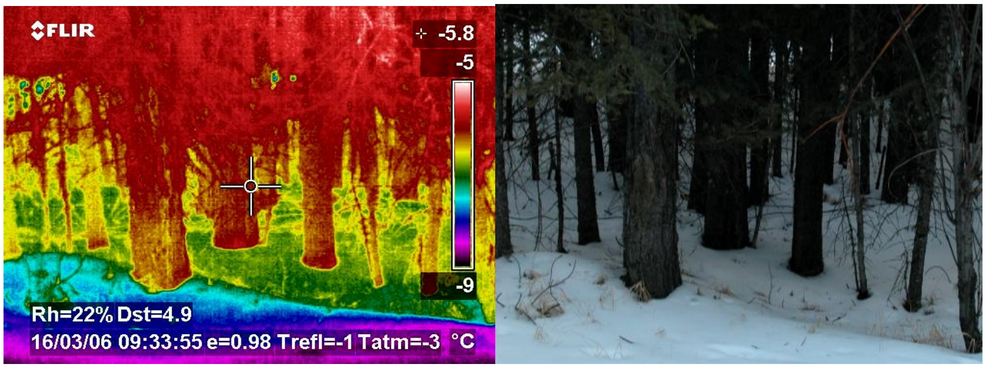

North-edge of forest clearing (930):

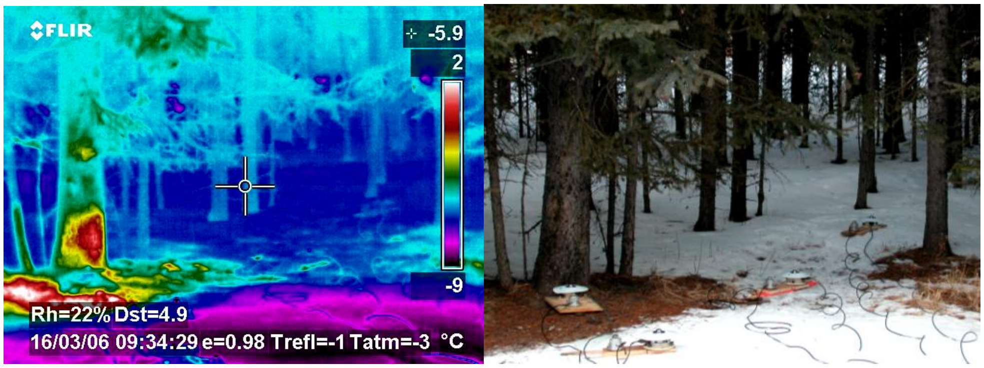

South-edge of forest clearing (1130):

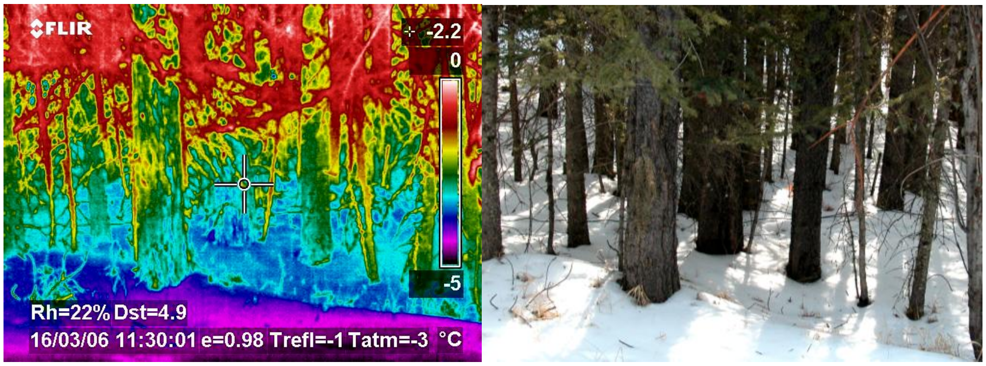

North-edge of forest clearing (1130):

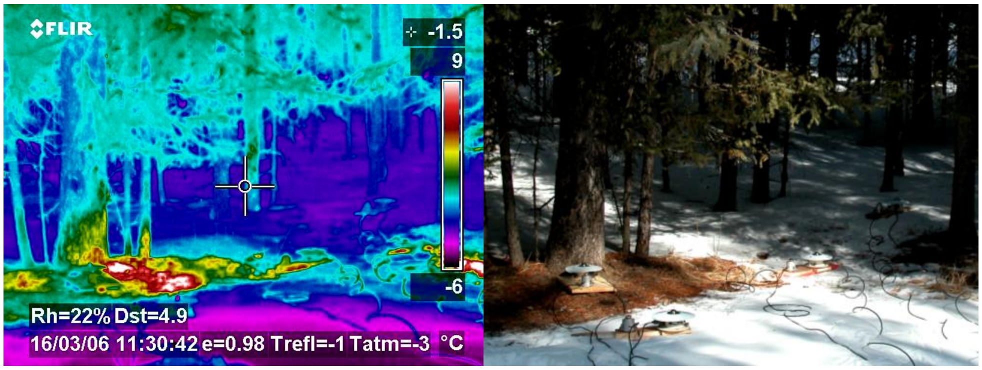

Figure 5.7: forest clearing thermal and visible images (see complete figure caption below).

South-edge of forest clearing (1330):

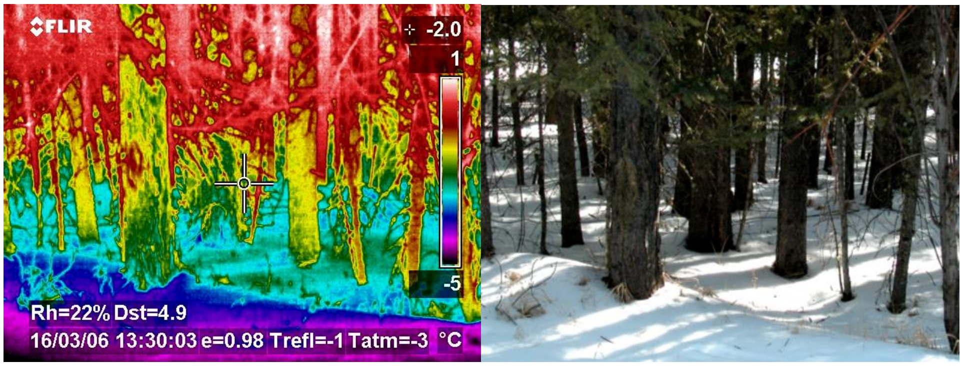

North-edge of forest clearing (1330):

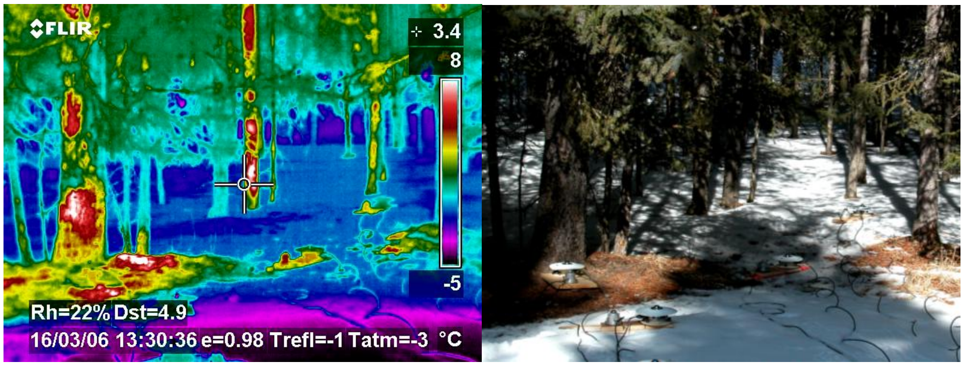

South-edge of forest clearing (1730):

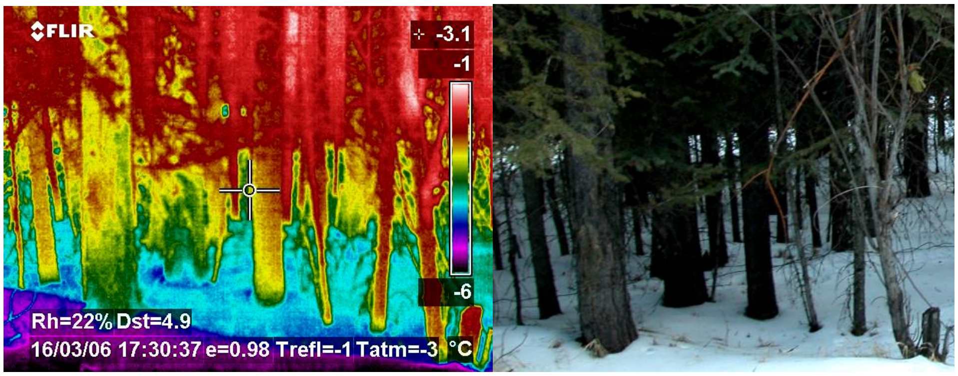

North-edge of forest clearing (1730):

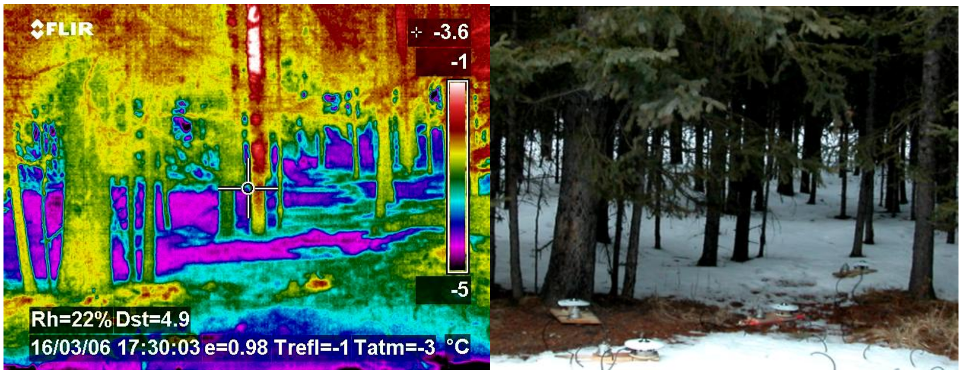

Figure 5.7: forest clearing thermal and visible images (see complete figure caption below).

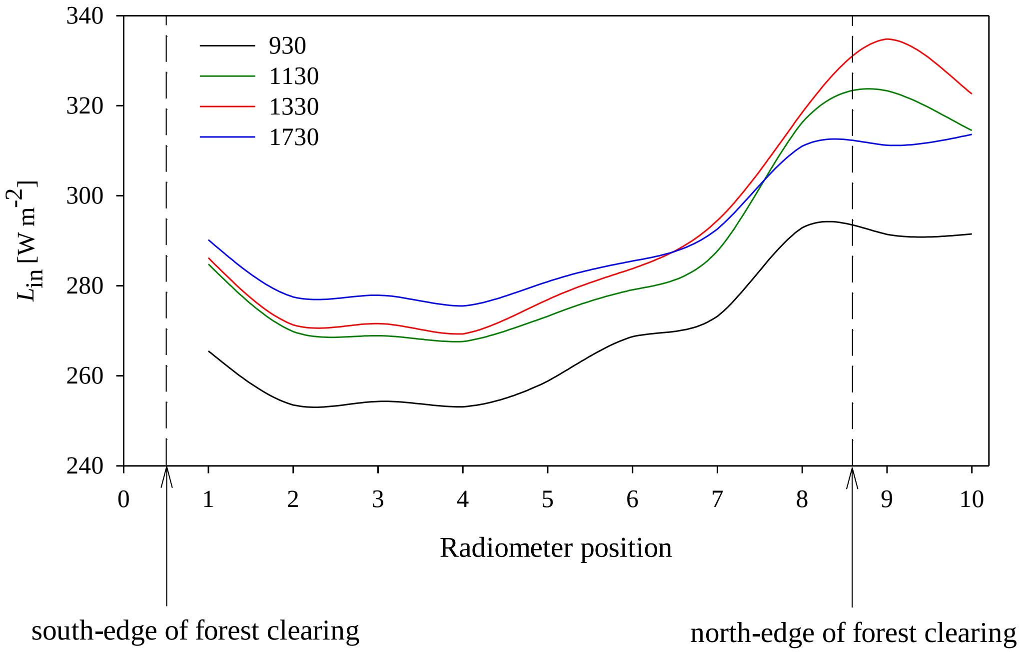

Figure 5. 7. Top (previous two pages): corresponding thermal and visible images of the south-edge and north-edge of a small forest clearing taken at 930, 1130, 1330 and 1730 throughout the day of March 16, 2006. Bottom: plot of longwave irradiance to snow (L_{in}) as observed by a 12-pyrgeometer array positioned along a south-north transect crossing the forest clearing at times corresponding to the thermal and visible images.

From the above observations, the following conclusions are made concerning the factors controlling sub-canopy longwave enhancements from canopy heating:

(i) In general, forest temperatures (T_{eff}, T_{crown}, T_{trunk}) do not fall below the surrounding canopy air temperature (T_a);

(ii) elevations in T_{eff} over T_a occur primarily from canopy heating by absorption of shortwave irradiance (K_o);

(iii) the degree to which $T_{eff} > T_a$ from shortwave heating varies with respect to both canopy density and topography (i.e. slope/aspect), which control the amount of shortwave penetration and heating in the lower canopy;

(iv) elevated canopy temperatures are largely the result of shortwave heating of branch and trunk material, and not of green needleleaf foliage which exhibits negligible heating.

Drawing upon these conclusions, the following section outlines the theoretical development of a physically-based model aimed to provide more realistic account of shortwave canopy heating on T_{eff} and sub-canopy longwave enhancements with respect to varying: (i) forest-cover density and canopy composition (i.e. relative amounts of green foliage, trunk and branch material), (ii) slope orientation and (iii) meteorological conditions (e.g. K_o and T_a). Evaluation of the model will be completed by the comparison of simulated T_{eff} to observations at the five forest sites over the winter-springtime period.

5.7.1.2. Calculation of longwave enhancements from canopy shortwave heating

Determination of forest canopy temperature (T_f)

Following the method to which forest-cover is described Section 5.3.1, the hemisphere overlying a fixed ground position is considered to be occupied by the forest sky view (v) and canopy-closure ($1–v$) compliments. Abstracting the canopy as a surface layer of a specified biomass depth (b_d) [m], changes in the forest canopy temperature (T_f) [K] may be related to changes in the net energy of the b_d layer ($Q*_f$) [MJ m^{-2}] by

$$\delta T_f = \frac{\delta Q*_f}{b_\mathrm{d}\rho_\mathrm{b}c_\mathrm{b}} \quad \textbf{(5.15)}$$

where ρ_b is the biomass density [kg m^{-3}] and c_b is the specific heat of biomass [MJ kg^{-1} K^{-1}] of the b_d. Optimisation of the thermal capacitance of the b_d for approximating surface heating of forest material was determined via an empirically-based approach using observations at a single tree at the SPF site (Appendix B). In Eq. 5.15, $Q*_f$ is determined by the following energy-balance of the b_d layer:

$$Q*_f = K*_f + L*_f + H*_f + E*_f \quad \textbf{(5.16)}$$

where $K*_f$ is the net shortwave radiation, $L*_f$ is the net longwave radiation, $H*_f$ is the net sensible heat transfer, and $E*_f$ is the net latent heat transfer [units of all terms in MJ m^{-2}]. In Eq. 5.16, positive values denote energy gains and negative values energy losses to the b_d layer. The calculation of the individual energy terms in Eq. 5.16 are outlined in Appendix C.

Determination of the effective forest radiating temperature (T_{eff})

As demonstrated by the forest temperature and radiation observations shown above, elevations in sub-canopy L_{in} brought about by shortwave heating of the canopy vary substantially with respect to forest-cover density, foliage composition of the stand, and the slope orientation of the site. In general, not all longwave emissions from heated canopy foliage are received at the sub-canopy due to the extinction of heated emissions by lower foliage layers, resulting in an effective canopy temperature to the sub-canopy (i.e. T_{eff}) less than the temperature of the shortwave heated canopy (i.e. T_f). Observations also reveal the negligible shortwave heating of green needleleaf foliage in forest crowns, which may be quantified by the green foliage fraction of forest-cover (g_f) as determined from hemispherical photograph analysis and stated for each site in Table 5.1. Based on these observations, T_{eff} is related to elevations in heated canopy temperatures above air temperature (i.e. $T_f - T_{\mathrm{a}}$) by the following expression

$$T_{eff} = (1 - g_f)\, p_f\, (T_f - T_{\mathrm{a}}) + T_{\mathrm{a}} \qquad \textbf{(5.17)}$$

where p_f is the transfer probability of heated longwave emissions from the canopy to the sub-canopy surface []. As elevations in T_f above T_{a} are considered to occur primarily through shortwave heating of the canopy, determination of p_f in Eq. 5.17 first accounts for the distribution of shortwave absorption along the vertical forest profile by

$$p_1\left(\frac{z_{\mathrm{d}}}{h}\right) = e^{-L^{\backprime}\xi_{\mathrm{s}}\frac{z_{\mathrm{d}}}{h}} \qquad \textbf{(5.18)}$$

where z_{d}/h is the fraction of the vertical depth from the forest top relative to total forest height (h). The probability distribution in Eq. 5.18 is used as it follows that of Beer-Bourger Law type expressions describing radiation distribution though an idealised forest medium. In Eq. 5.18, ξ_{s} represents the correction factor of $L^{\backprime}$ for oblique shortwave transmission pathways through the forest layer, which may be determined for total shortwave irradiance by the following rearrangement of Eq. 5.5 and Eq. 5.6:

$$\xi_{\mathrm{S}} = \frac{-\ln(v)k_{\mathrm{d}} + (1-k_{\mathrm{d}})(-\ln(\tau_{\mathrm{b}}))}{L`} \qquad \textbf{(5.19)}$$

With the vertical distribution of shortwave heating in the canopy described by p_1 in Eq. 5.18, the probability of longwave emissions from shortwave heating at z_{d}/h being transferred to the sub-canopy is described by the p_2 probability, given by

$$p_2(\frac{z_{\mathrm{d}}}{h}) = e^{-L`(1-\frac{z_{\mathrm{d}}}{h})} \qquad \textbf{(5.20)}$$

Thus, the overall probability of heated foliage longwave emissions at z_{d}/h being transferred to the sub-canopy ($p_f(z_{\mathrm{d}}/h)$) is given by the joint p_1 and p_2 probabilities, i.e.

$$\begin{aligned} p_f(\frac{z_{\mathrm{d}}}{h}) &= p_1(\frac{z_{\mathrm{d}}}{h}) \cdot p_2(\frac{z_{\mathrm{d}}}{h}) \qquad \textbf{(5.21)} \\ &= e^{-L`\xi_{\mathrm{s}}\frac{z_{\mathrm{d}}}{h}} \cdot e^{-L`(1-\frac{z_{\mathrm{d}}}{h})} \\ &= e^{-L`[\xi_{\mathrm{s}}\frac{z_{\mathrm{d}}}{h}+(1-\frac{z_{\mathrm{d}}}{h})]} \end{aligned}$$

which may be calculated as a single function of z_{d}/h via

$$p_f(\frac{z_{\mathrm{d}}}{h}) = e^{-\left[L`+(L`\xi_{\mathrm{s}}-L`)\frac{z_{\mathrm{d}}}{h}\right]} \qquad \textbf{(5.22)}$$

and integrated over the entire forest height (h) by

$$p_f = \frac{e^{-L`}(1-e^{-(L`\xi_{\mathrm{s}}-L`)})}{L`\xi_{\mathrm{s}}-L`} \qquad \textbf{(5.23)}$$

A demonstration of the how the canopy longwave transfer functions described by Eq. 5.18, Eq. 5.20, and Eq. 5.21 vary with canopy depth (i.e. z_{d}/h) is provided schematically in

Figure 5.8, which shows the determined p_1, p_2, and p_f probability distributions along the vertical profile of two hypothetical forest stands of equal canopy density (i.e. $L`$) but differing shortwave transmission pathlengths (i.e. ξ_s). Behaviour of the p_f function is also shown by the determined daily p_f values at the MCRB pine and spruce forest sites over their respective 2006 and 2008 January – June observation periods (Figure 5.9). Of note in Figure 5.9 is the substantial range in p_f among the sites, with the greatest transfer probabilities for the sparse south-sloping canopy at the SPF, and lowest probabilities for the north-sloping NPF and NSF canopies and the dense SSF canopy.

To evaluate the approximation of T_{eff} in mountain needleleaf forests by the approach, simulations were performed at the MCRB pine and spruce sites during their respective 2006 and 2008 January – June periods with forest-cover parameters specified as stated in Table 5.1. Throughout the simulation period, calculation of Q^*_f was made on an hourly timestep; alternatively, p_f was calculated on a daily timestep due to the uncertainty in the determination of p_f during periods prior to and after sunset when no shortwave heating occurs. Evaluation of the model's ability to estimate total sub-canopy longwave enhancements from canopy heating (i.e. $T_{eff} - T_a$) at each site is made by comparing the mean observed and simulated $T_{eff} - T_a$ over the January – June period in Figure 5.10. Here, a general correspondence in the simulated and observed T_{eff} elevations is seen among the forest sites, with greatest canopy heating at the SPF and LPF sites, and only modest heating and the NPF and both spruce forest sites. Encouraging results are also seen in the much improved ME of daily T_{eff} provided by simulations at the SPF and LPF compared to approximations by T_a (Table 5.2). Alternatively, as expected with the low amount of shortwave heating at the NPF and spruce forest sites, only marginal improvements in T_{eff} determinations were given by the model relative to that by T_a.

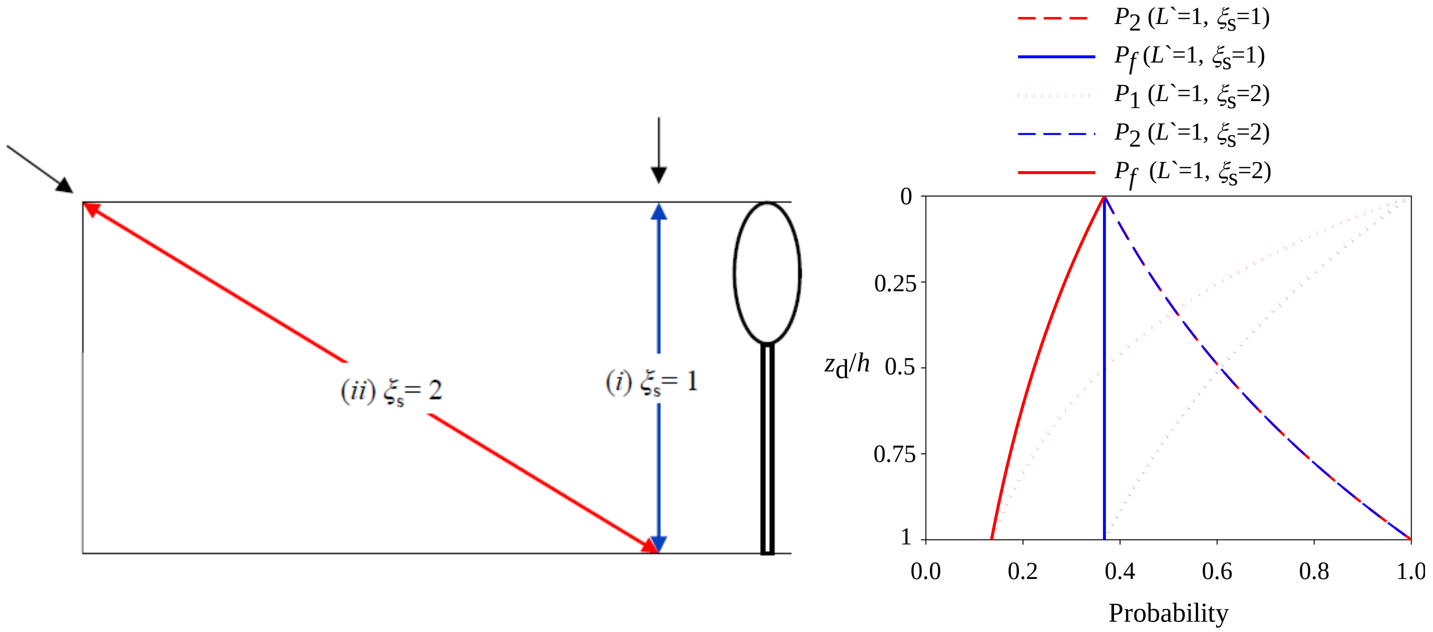

Figure 5. 8. Schematic illustrating the p_1, p_2 and p_f probabilities calculated by Eq. 5.18, Eq. 5.20, and Eq. 5.21 with respect to penetration depth into the forest layer (z_d/h) for a hypothetical forest-cover density of L` = 1 and shortwave transmission pathlengths equal to (*i*) a single forest height (i.e. $\xi_s = 1$) and (*ii*) that twice the forest height (i.e. $\xi_s = 2$).

A demonstration of the energy-balance approach of the model in determining canopy heating and resulting sub-canopy longwave enhancements is provided in Figure 5.11, which shows time series data of the calculated canopy energy balance (Q^*_f), individual energy terms, and the simulated and observed T_{eff} at the SPF for the same 5-day period as in Section 5.7.1. Overall, a general correspondence is observed in T_{eff} and Q^*_f fluctuations throughout the day, with positive Q^*_f magnitudes from shortwave gains (K^*_f) heating the canopy well above air temperatures during the midday, followed by decreased Q^*_f and canopy cooling toward T_a with declining shortwave gains into the evening. During daytime periods of shortwave heating, cooling of the canopy is brought about largely through longwave (L^*_f) and sensible heat (H^*_f) losses. However, due to the thermal capacitance of the model's b_d biomass layer, canopy temperature cooling lags to that of the surrounding air temperature, which acts to provide a crude representation of canopy heat storage effects. Despite this simplistic representation of forest biomass heat transfers, this energy-balance approach is seen to provide a much improved approximation of T_{eff} in forests of varying cover-density and slope orientation compared to conventional approximations by T_a (Table 5.2).

Table 5. 2. Determined model efficiency index (ME) of daily observed effective canopy temperature (T_{eff}) provided from model simulations and approximation by air temperature (T_a).

Site:	Observation period	ME simulated T_{eff} []	ME observed T_a []
Level Pine Forest (LPF)	Jan 20 – Jun 1, 2006	0.89	0.77
North-facing Pine Forest (NPF)	Jan 1 – Jun 1, 2006	0.92	0.89
Southeast-facing Pine Forest (SPF)	Jan 1 – Jun 1, 2006	0.93	0.72
North-facing Spruce Forest (NSF)	Jan 7 – Jun 1, 2008	0.89	0.85
South-facing Spruce Forest (SSF)	Jan 7 – Jun 1, 2008	0.92	0.90

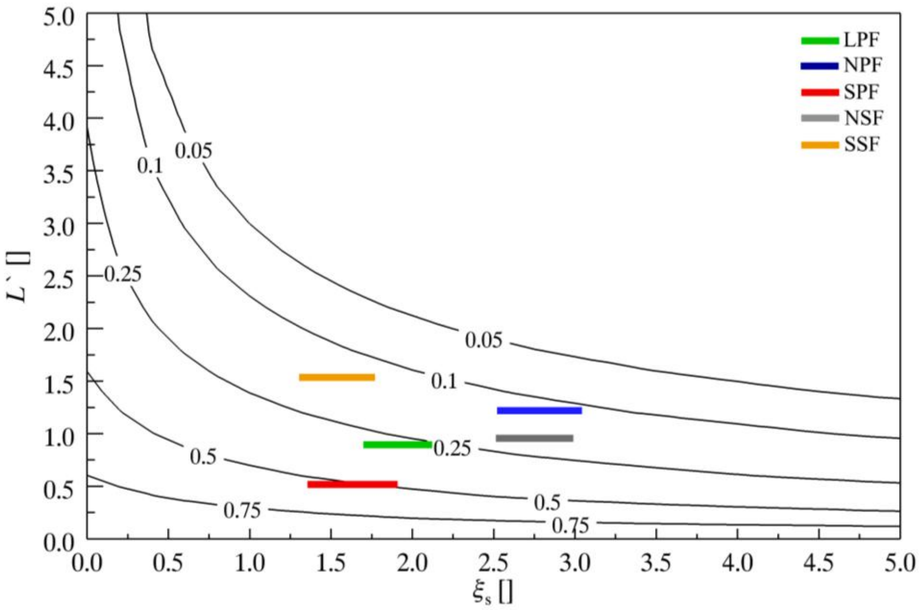

Figure 5. 9. Contour plot of the canopy longwave transfer function (p_f) described by Eq. 5.23 showing the range of the determined daily p_f values for the pine and spruce study sites during their respective January – June observation periods.

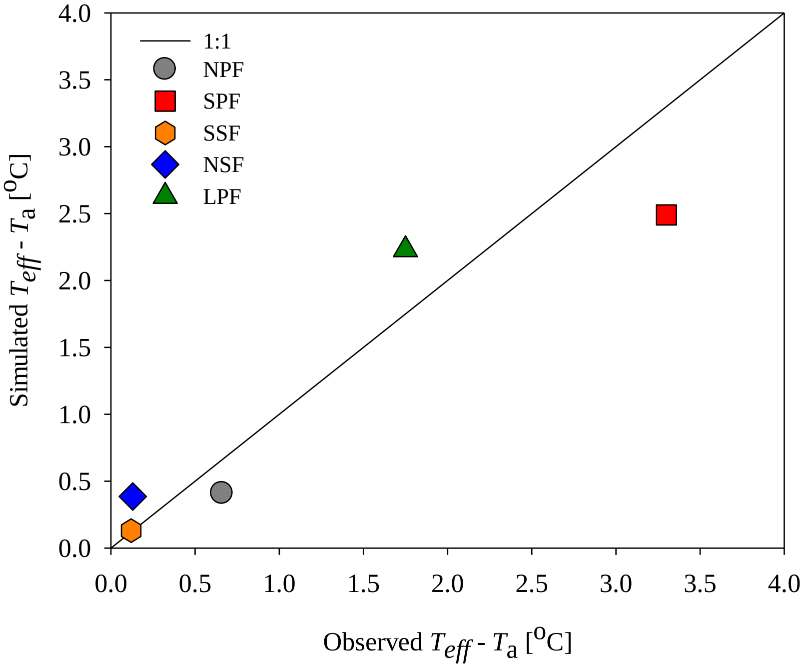

Figure 5. 10. Scatterplot between mean observed and simulated elevations in effective canopy radiating temperature over air temperature (T_{eff}–T_a) for the period of January – June, 2006 at the Level Pine Forest (LPF), North-facing Pine Forest (NPF), Southeast-facing Pine Forest (SPF), as well as for the period of January – June, 2008 at the North-facing Spruce Forest (NSF) and South-facing Spruce Forest (SSF) sites.

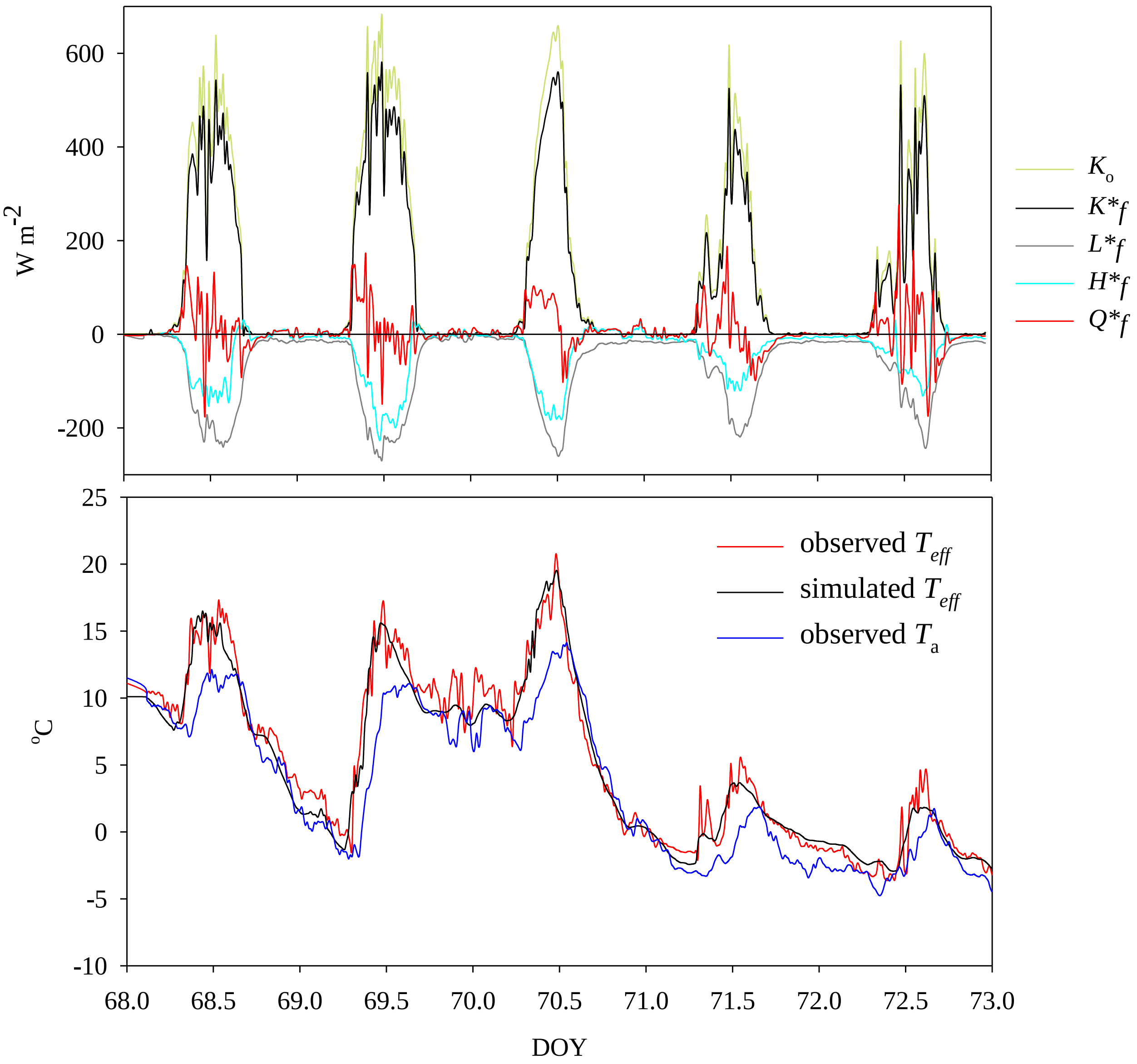

Figure 5. 11. Southeast-facing Pine Forest site (SPF): time series of the determined canopy net energy balance (Q^*_f) showing the individual energy balance terms in Eq. 5.16 (top), and the corresponding simulated T_{eff} compared to observed T_{eff} and T_a (bottom) for the period of DOY 68 – 73, 2005.

5.7.2. Simulation of sub-canopy snow surface temperatures

Similar to that of forest canopy temperatures, air temperature (T_a) observations may also provide a good general approximation of snow surface temperatures (T_s). However, substantial deviations between T_s and T_a may result through longwave cooling of the snow surface by sublimation energy losses. Account for T_s depressions below T_a from longwave and sublimative energy exchanges are made here using the longwave-psychrometric approach developed by Pomeroy and Essery (2010) (Eq. 3.6, Chapter 3).

Although good estimations of T_s by this approach have been obtained over open snowcovers, its effectiveness in forest environments has not as yet been evaluated. To provide such an evaluation, simulations of T_s using the longwave-psychrometric approach at all forest study sites were compared to T_s observations provided from infrared thermometer measurements for periods of complete snow cover. All terms in Eq. 3.6 were approximated or calculated using meteorological observations collected at each of the forest study sites. Comparison of T_s observations to simulations from Eq. 3.6 and T_a approximations at all forest sites is made in Table 5.3 in terms of: (i) the mean difference in temperatures over entire observation period and (ii) the ME index for estimates of daily values.

Overall, simulations are seen to provide a substantial improvement over approximates by T_a at all sites, especially at the SPF site where the T_s was observed to be on average 4.4 ˚C cooler than T_a over the period, which is attributed to the increased wind ventilation through the sparser canopy of the site. The important control of near-surface metrological conditions on T_s cooling is illustrated by time series data in Figure 5.12 of observed and simulated T_s, T_a, as well as the corresponding longwave irradiance (L_{in}), relative humidity (rh), and forest wind speed (u) over a two-week period at the South-facing Spruce Forest (SSF) site. Despite the generally low u from wind-sheltering at the densely-covered site, substantial cooling of the snow surface below T_a is observed during periods of higher u is and lower rh (e.g. February 26th and 28th). Alternatively, snow surface cooling is minimal during higher rh and lower u, as evident by the similar T_s and T_a during the early periods of February 24th and 27th. The close tracking of observed and simulated T_s during both these periods demonstrates the approaches' effective representation of the varying meteorological factors affecting snow surface cooling.

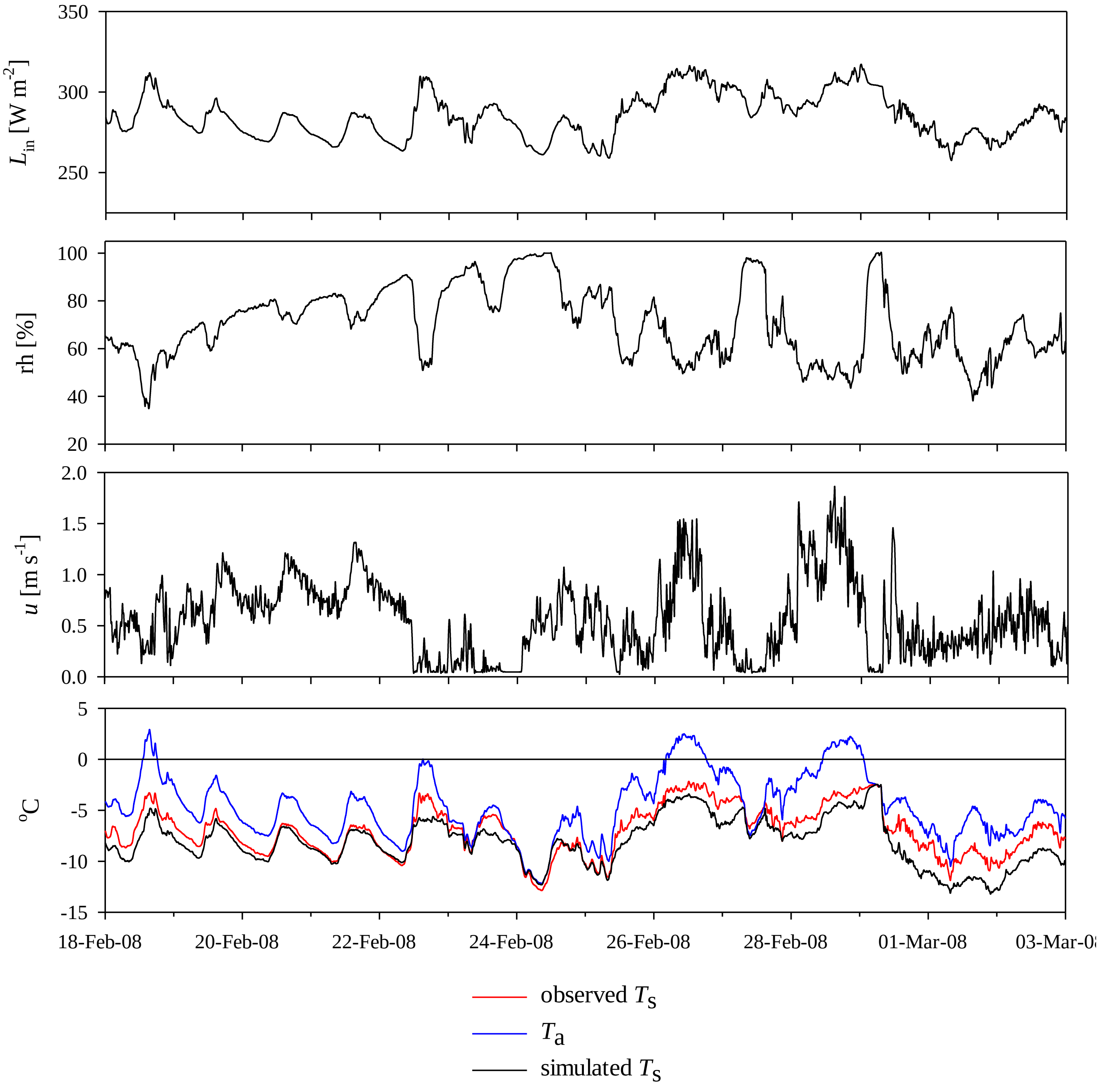

Figure 5. 12. Time series of sub-canopy longwave irradiance (L_{in}), relative humidity (*rh*), wind speed (*u*), air temperature (T_a), as well as observed and simulated snow surface temperatures (T_s) at the South-facing Spruce Forest (SSF) site over the period of February 18th – March 3rd, 2008.

Table 5. 3. Determined mean difference (i.e. mean temperature difference over the period) of snow surface temperatures (T_s) simulated by the Pomeroy and Essery (2010) longwave-psychrometric approach (Eq. 3.5, Chapter 3) and approximated by observed near-surface air temperature (T_a), including the determined model efficiency index (ME) values for approximation of daily T_s values throughout the respective observation periods.

Site:	Observation period	Mean difference (sim. T_s – obs. T_s) [°]	Mean difference (obs. T_a – obs. T_s) [°]	ME (sim. T_s) []	ME (obs. T_a) []
Level Pine Forest (LPF)	Jan 20 – Mar 1, 2006	-0.62	3.5	0.89	0.81
North–facing Pine Forest (NPF)	Jan 1 – Mar 1, 2006	0.84	2.9	0.87	0.82
Southeast-facing Pine Forest (SPF)	Jan 1 – Mar 1, 2006	0.76	4.4	0.86	0.76
North-facing Spruce Forest (NSF)	Jan 7 – May 1, 2008	-0.63	3.8	0.88	0.80
South-facing Spruce Forest (SSF)	Jan 7 – May 1, 2008	-0.56	3.7	0.89	0.79

5.8. *Model Application 2*: Forest-cover effects on radiation to mountain snowcover under observed meteorological conditions

Utilising the improved representation of longwave fluxes between forest and snowcover demonstrated by the estimation procedures outlined above, the effect of forest-cover on radiation to mountain snowcover (R^*) is further investigated here through simulations under observed seasonal meteorological conditions. This simulation exercise follows the basic procedure of *Model Application 1* (Section 5.6), but for meteorological conditions observed over the period of January – June, 2008 at the LSC. As with *Model Application 1*, the influence topography on forest-cover effects are assessed through separate simulations to a hypothetical site of level topography (LS), a 30˚ sloped site of north-facing aspect (NS), and a 30˚ sloped site of south-facing aspect (SS). At the Level Spruce Clearing (LSC) reference site, the following meteorological data were collected over the January – June period of 2008 for model forcing: above-canopy shortwave irradiance (K_o), above-canopy longwave irradiance (L_o), and air temperature T_a (Figure 5.13 (top)). Alternatively, forest wind speeds were estimated through a simple correction of LSC wind speeds for canopy sheltering effects by the following adaptation of Hellström's (2000) expression:

$$u_{\text{forest}} = u_{\text{open}}(0.2 + 0.8v) \tag{5.24}$$

where u_{open} and u_{forest} denote the observed open wind speeds and estimated forest wind speeds.

Also similar to that for simulations performed in *Model Application 1*, forest-cover effects on radiation to snow (R^*) at each of the hypothetical sloped sites are illustrated in terms of the forest sky view factor at which maximum R^* occurs (i.e. $v(R^*_{\text{max}})$) and the corresponding R^*_{max} for mean season snow albedo (α_s) values of 0.7 and 0.8 (Figure 5.13: middle, bottom). Here, results show that unlike under the theoretical meteorological conditions of *Model Application 1*, the more varied observed meteorological conditions result in greater fluctuations in $v(R^*_{\text{max}})$ and R^*_{max} values over the winter-spring period. However, similar trends in $v(R^*_{\text{max}})$ and R^*_{max} are observed between theoretical and observed meteorological conditions, with R^*_{max} generally occurring under high canopy-closures (i.e. low v) during the early winter, and under progressively more open canopies (i.e. high v) into the spring. Also similar are the earlier increases in $v(R^*_{\text{max}})$ and R^*_{max} at the south-facing SS site relative to that at the level LS and north-facing NS for both high and low snow albedo (α_s) conditions. At the NS, $v(R^*_{max})$ and R^*_{max} again remain low until early April when the site is no longer self-shaded from shortwave irradiance, resulting in a sudden elevation in $v(R^*_{max})$ and R^*_{max} values for low α_s conditions. During this time, large fluctuations in $v(R^*_{max})$ occur at the NS with varying meteorological conditions due to the close balance between shortwave and longwave exchanges with changing v. Again, this close balance between shortwave and longwave exchanges at the NS is demonstrated by the sharp sensitivity of $v(R^*_{max})$ to snow albedo; seen in the large divergence in springtime $v(R^*_{max})$ values between high and low α_s conditions.

During the later spring, meteorological influences upon $v(R^*_{max})$ and R^*_{max} become increasingly evident at all sites. Meteorological effects are particularly marked at the NS where the close balance between shortwave and longwave exchanges produces large fluctuations in $v(R^*_{max})$ with varying K_{in} and T_a. However, these shifts in $v(R^*_{max})$ translate into little change in R^*_{max} at the NS, which is attributed to the low shortwave irradiance to the north-facing slope. Alternatively, the higher shortwave irradiance to the LS and SS give for a much larger response in R^*_{max} to changes in $v(R^*_{max})$, especially under low α_s conditions when shortwave influences are greatest.

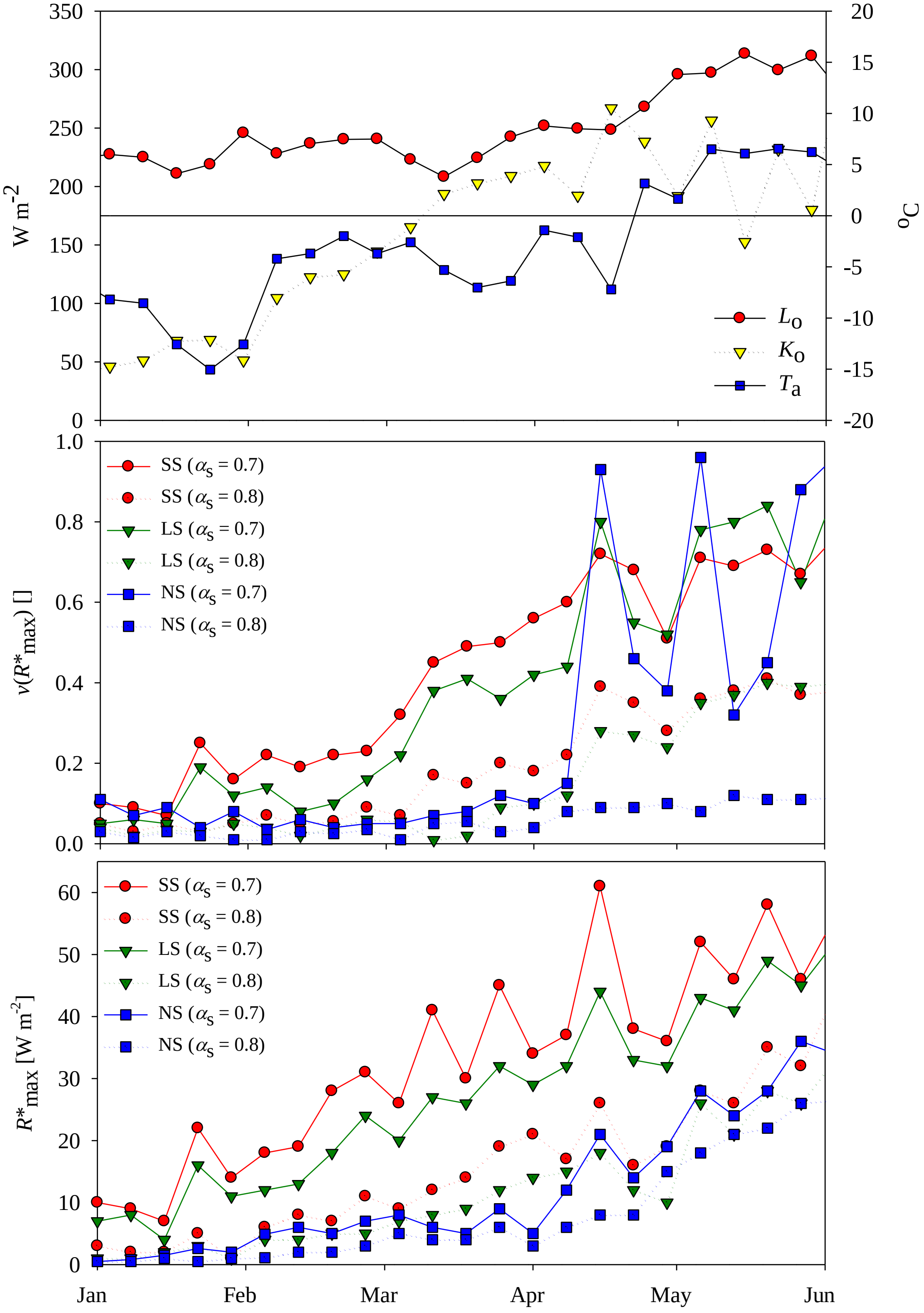

Figure 5. 13. *Model Application 2*: mean weekly above-canopy shortwave (K_o) and longwave (L_o) irradiance for the period of January – June, 2008 (top) showing the simulated forest sky view factor of maximum R^* ($v(R^*_{max})$) (middle) and corresponding maximum net radiation to snowcover (R^*_{max}) (bottom) at a hypothetical level site (LS), a 30° sloped site of north-facing aspect (NS), and a 30° sloped site of south-facing aspect (SS) for snow albedo (α_s) conditions of 0.7 and 0.8.

5.9. Chapter discussion

As demonstrated through model simulation exercises, the influence of needleleaf forest-cover on radiation to mountain snowcover is highly variable with respect to differing combinations of slope orientation, meteorology, and snowcover conditions. With increasing forest-cover, shortwave reductions to snow are compensated by additional longwave emissions from the canopy. Such longwave enhancements under forest-cover may overwhelm shortwave reductions during winter periods of low solar elevations and shortwave irradiance, particularly at north-facing sites where low potential shortwave gains are maintained into the spring. Alternatively, for sites of south-facing topography at these latitudes, rapid gains in shortwave irradiance with rising solar elevations result in greater radiation to snow under progressively more open canopies into the spring. Yet, the effects of topography and forest-cover on radiation to snow are strongly varied by meteorological conditions, especially that of cloud-cover and air temperature due to their respective controls on shortwave and longwave fluxes to forest snow.

Despite the simplistic approach of the model outlined by this chapter in describing forest radiation dynamics, its effective representation of shortwave and longwave radiation in forests of varying canopy-density, slope orientation, and meteorological conditions indicates it capable of characterising the essential processes controlling forest-snow radiation exchanges in mountain environments. The primary advantage of the model lies in its description of forest-cover density using a single index: the forest sky view factor (v), which provides a simple and intuitive metric of forest-cover density for model simulations. Although this approach neglects the considerable spatial variation in forest-cover caused by the structuring of canopy foliage in trunks and crowns, as well as complex physical processes such as shortwave scattering within the canopy, evaluation results provide encouragement toward its use in assessing how forest-cover changes may influence radiation to mountain snowcovers.

According to detailed field observations, air temperature provides a useful approximation of canopy and snow surface radiating temperatures, but substantial errors may result from this approximation by canopy shortwave heating or snow surface cooling through sublimation energy losses. Observations of longwave irradiance and canopy temperatures in mountain forests reveal the considerable enhancements in sub-canopy longwave radiation possible through shortwave heating of the canopy. However, the degree to which canopy shortwave heating translates into sub-canopy longwave enhancements varies widely across mountain forests with canopy-cover density, foliage composition, and slope orientation. Among the forest study sites, longwave enhancements from canopy heating were greatest at the south-facing SPF site, where the increased exposure to the sun and sparser canopy allowed for greater shortwave penetration and heating of the lower trunk layer from where longwave emissions were directly transferred to the sub-canopy. By contrast, the extinction of shortwave irradiance and heating higher within dense and/or north-sloping canopies gave for only small sub-canopy longwave enhancements, as emissions from higher in the canopy were masked by lower foliage layers. An additional factor observed in limiting longwave enhancements to the sub-canopy is that of amount of green foliage contained in the crown, which exhibits negligible heating due to its close coupling with canopy air temperatures.

Field observations were instructive for extending the original model to account for shortwave heating effects on sub-canopy longwave irradiance through determination of the canopy energy-balance and the probability of heated foliage emissions being transferred to the sub-canopy. Despite its simple approach, the method well approximated the varying amounts of longwave enhancement from canopy heating with differing topographic exposure, forest-cover density, foliage composition, and meteorological conditions. However, the approach is expected to be most limited by its crude representation of heat storage effects within forest biomass, which is made by the specification of a single active biomass layer to which all thermal exchanges occur. Accordingly, improvements to the model would be expected by a more explicit representation of the thermal transfers within forest biomass, such as those describing radial heat diffusion within trunks (e.g. Meesters and Vugts, 1996; Haverd et al., 2007) or the application of force-restore type approaches (e.g. Silberstein et al., 2003). Notwithstanding these limitations, evaluation of the approach demonstrates its promise in assessing how changes in forest-cover density and composition may impact longwave transfers to sub-canopy snow at sites of varying topography and meteorological conditions.

Further improvement in describing longwave radiation to forest snowcover was provided through the more accurate determination of snow surface temperatures using the physically-based psychrometric approach developed by Pomeroy and Essery (2010). The need for such provision is demonstrated in the sizeable snow surface temperatures depressions below near-surface air temperature observed at all forest sites. Even with the high degree of wind-sheltering in dense spruce forest stands, the low sub-canopy wind speeds at these sites were sufficient to facilitate considerable sublimation cooling of the snow surface evident in the pronounced snow temperature depressions during periods of increased snow ventilation by dry air. Both model simulations and observations illustrate the large sensitivity of snow surface temperature to changing near-surface meteorological conditions, suggesting that the effective employment of the model over larger spatial scales will be limited by the detail of available near-surface metrological forcing data.

The improved estimation of longwave emissions from forest-cover and snow through more accurate determinations of their emitting temperatures illustrates the potentially large estimation errors that may result by air temperature approximations. In general, air temperatures underestimate canopy temperatures and overestimate snow surface temperatures, the errors of which may combine in providing a substantial underestimation of total longwave radiation to forest snow. Although such errors may be of small magnitude over short time periods, their accumulation over the winter-spring season is likely to result in a substantial underestimation of radiation for snowpack warming and melt.

Considering that radiation often dominates energy fluxes to forest snow, chapter results also pose potentially important hydrological implications regarding the timing of snowmelt in mountain forests. Results suggest that changes in mountain forest-cover at these latitudes will have markedly different effects on radiation for snowmelt on landscapes of varying slope orientation, especially during the later spring when topography-controlled shortwave variations intensify. Notwithstanding the confounding effects produced by varying meteorological and snow albedo conditions, model determinations clearly indicate forest-cover removal on south-facing aspects to result in greater radiation to snow through increased shortwave irradiance, but less radiation on north-facing aspects due to reduced canopy longwave emissions. Such disparate results illustrate the complex interaction of forest-cover, slope orientation, meteorological and snow conditions in determining radiation to snow over complex topography, and demonstrate the considerable range of effects that forest-cover changes may have on radiation to mountain snowcovers.

6. SIMULATION OF SNOW ACCUMULATION AND MELT IN NEEDLELEAF FOREST ENVIRONMENTS

6.1. Chapter summary

Drawing upon numerous field studies and modelling exercises investigating snow processes, the Cold Regions Hydrological Model (CRHM) was developed to simulate the four season hydrological cycle in cold regions. This chapter outlines the development and evaluation of a module incorporated into the CRHM platform representing forest-snow processes. CRHM includes modules describing radiative, turbulent and conductive energy exchanges to snow in open and forest environments, and provides account for canopy snow sublimation and rain evaporation losses. Due to the physical-basis and rigorous testing of module algorithms, minimal need exists for model calibration in CRHM. To evaluate CRHM, simulations of snow accumulation and melt were compared to observations collected at paired forest and clearing sites of varying latitude, elevation, forest-cover density, and climate. Overall, results show that CRHM is capable of characterising the variation in snow accumulation between forest and clearing sites, achieving a model efficiency of 0.51 for simulations at individual sites. Simulations of canopy sublimation losses slightly overestimated observed losses from a weighed cut tree, having a model efficiency of 0.41 for daily losses. Good model performance was demonstrated in simulating energy fluxes to snow in the clearings, but results were degraded under forest-cover due to errors in simulating sub-canopy net longwave radiation. However, expressed as cumulative energy to snow over the winter, simulated values were 96 and 98 % of that observed at the forest and clearing sites, respectively. The generally good representation of the substantial variations in mass and energy between forest and clearing sites suggests that CRHM may be useful for investigating snow processes in cold region forests environments.

6.2. Chapter introduction: simulation of forest snow processes

Needleleaf forests dominate much of the mountain and boreal regions of the northern hemisphere where snowmelt is the most important hydrological event of the year (Gray and Male, 1981). The retention of foliage by evergreen needleleaf tree species over the winter acts to decrease snow accumulation via canopy interception losses (Schmidt, 1991; Lundberg and Halldin, 1994; Pomeroy et al., 1998a) and greatly modify energy exchanges to snow (Link and

Marks, 1999; Gryning and Batchvarova, 2001). However, forest-cover is often discontinuous, containing clearings of varying dimensions which may differ considerably in snow accumulation (McNay, 1988) and melt characteristics (Metcalfe and Buttle, 1995). As such, management of water derived from forest snowmelt is expected to benefit from the effective prediction of snow accumulation and melt in both forest and clearing environments.

Forest-cover effects on snow accumulation may exhibit considerable variation among sites of differing physical characteristics and climate. Although numerous mechanisms have been proposed to explain decreased snow accumulations in forests, sublimation of canopy snow has been shown to be the primary factor controlling forest snow losses (Troendle and King, 1985; Schmidt et al., 1988; Pomeroy and Schmidt, 1993; Lundberg and Halldin, 1994; Parviainen and Pomeroy, 2000). Investigations by Pomeroy and Gray (1995) and Pomeroy et al. (1998a) found that 30 - 45 % of annual snowfall in western Canada may be lost by canopy sublimation due to the increased exposure of intercepted snow to the above atmosphere. As such, estimation of canopy sublimation losses have often made appeal to physically-based 'ice-sphere' models (e.g. Schmidt, 1991) that adjust sublimation losses from a single, small ice-sphere to account for the decreased exposure of canopy snow to the atmosphere. Such approaches have been shown to well approximate canopy sublimation losses over multiple snowfall events through the coupling of the multi-scale sublimation model to a needleleaf forest interception model (Pomeroy et al., 1998a).

Alongside interception effects, needleleaf forest-cover also influences energy exchanges to snow. The forest layer acts to effectively decouple the above-canopy and sub-canopy atmospheres, resulting in a large suppression of turbulent energy fluxes (Harding and Pomeroy, 1996; Link and Marks, 1999). Consequently, energy to sub-canopy snow is dominated by radiation; itself modified by the canopy through the shading of shortwave irradiance while increasing longwave irradiance through canopy emissions (Link et al., 2004; Sicart et al., 2004; Pomeroy et al., 2009). Forest-cover may also affect sub-canopy shortwave radiation by altering snow surface albedo through deposition of forest litter on snow (Hardy et al., 2000; Melloh et al., 2002). As such, simulations of forest effects on energy to snow have largely focused on the adjustment of shortwave and longwave fluxes (Hardy et al., 2004; Essery et al., 2008; Pomeroy et al., 2009), although methods estimating turbulent energy transfer in forests have also been described (Hellström, 2000; Gelfan et al., 2004).

Since the first successful demonstration of snowmelt simulation using an energy-balance approach by Anderson (1976), numerous such snowmelt models have developed (e.g. EBSM, Gray and Landine, 1988; SNTHERM, Jordan, 1991; SHAW, Flerchinger and Saxton, 1989; Snobal, Marks et al., 1999; Andreadis et al., 2009). Due to the differing objective specific to each model, there is considerable variation in the detail to which snow energetics are described, as well as forcing data and parameterisation requirements. In general, more sophisticated snowmelt models possess information requirements that may prohibit their successful employment in more remote environments, where forcing data and parameter information is typically lacking or poorly approximated. Instead, more basic models that maintain a physically-based representation of forest-snow processes in cold regions are expected to be better suited for such environments.

Although much focus has been placed on simulating forest snow accumulation and melt processes separately, fewer simulations over the entire snow accumulation and melt period have been demonstrated. To this end, this chapter outlines and evaluates the simulation of snow accumulation and melt in paired forest and clearing sites of varying forest-cover density and climate using the Cold Regions Hydrological Model (CRHM). CRHM is a deterministic model of the hydrological cycle containing process algorithms (modules) developed from field investigations in cold region environments, with modest data and parameter requirements. This chapter assesses the potential for CRHM to be used to analyse and predict how changes in climate and forest-cover may affect snow processes in cold region forests.

6.3. Description of the Cold Regions Hydrological Model (CRHM)

Described in detail by Pomeroy et al. (2007), CRHM operates through interaction of its four main components: (1) observations, (2) parameters, (3) modules, and (4) variables and states. The description of each component below focuses on the requirements of CRHM in forest environments:

1. Observations: CRHM requires the following meteorological forcing data for each simulation timestep, t (units in []):
    a. air temperature , T_a [°C];
    b. humidity, either as vapour pressure, e_a [kPa] or relative humidity, rh [%];

c. precipitation, P [kg m^{-2}];

d. wind speed, observed either above, or within the canopy, u [m s^{-1}];

e. shortwave irradiance, K_{in} [W m^{-2}];

f. longwave irradiance, L_{in} [W m^{-2}] (in the absence of observations, L_{in} may be estimated from T_{a} and e_{a}).

2. Parameters: provides a physical description of the site, including latitude, slope and aspect, forest-cover density, height, species, and soil properties. In CRHM, forest-cover need only be quantified by an effective leaf area index (LAI`) and forest height ($h$); the forest sky view factor ($v$) may be specified explicitly or estimated from $LAI$`. The heights at which meteorological forcing data observations are collected are also specified here.
3. Modules: algorithms implementing the particular hydrological processes are selected here by the user.
4. Initial states and variables: specified within the appropriate module.

6.3.1. Modules

The following provides a general outline of the main modules and associated algorithms involved in the development of the forest module within CRHM. Note that during the initial incorporation of forest routines within CRHM, separate handling of mass and energy determinations were made by the *needleleaf* and *trees* modules, respectively. However, as of spring of 2010, both forest mass and energy routines are contained within the single module *canopy*, the programming source code (C++ language) of which is provided in Appendix E.

6.3.1.1. Observation module

To allow for the distribution of meteorological observations away from the point of collection, appropriate corrections are applied in the *observation* module. These include the correction of air temperature, humidity, and the amount and phase of precipitation for elevation, as well as correction of shortwave and longwave irradiance for topography.

6.3.1.2. Snow mass-balance module

In CRHM, snow is conserved within a single defined spatial unit, with changes in mass occurring only through a divergence of incoming and outgoing fluxes. In clearing environments, snow water equivalent (SWE) [kg m^{-2}] at the ground may be expressed by the following mass-balance of vertical and horizontal snow gains and losses

$$\mathrm{SWE} = \mathrm{SWE}_o + (P_s + P_r + H_{in} - H_{out} - S - M)t \qquad \textbf{(6.1)}$$

where t is the model calculation timestep, SWEo is the antecedent SWE [kg m^{-2}], P_s and P_r are the respective snowfall and rainfall rates, H_{in} is the incoming horizontal snow transport rate, H_{out} is the outgoing horizontal snow transport rate, S is the sublimation loss rate, and M is the melt loss rate [all units kg m^{-2} t^{-1}]. In forest environments Eq. 6.1 is modified to

$$\mathrm{SWE} = \mathrm{SWE}_o + (P_s - (I_s - U_l) + P_r - (I_r - R_d) - M)t \qquad \textbf{(6.2)}$$

in which I_s is canopy snowfall interception rate, U_l is the rate of canopy snow unloading, I_r is the canopy rainfall interception rate, and R_d is the rate of canopy rain drip [all units kg m^{-2} t^{-1}].

The amount of snowfall intercepted by the canopy depends on various physical factors, including tree species, canopy density of the forest, and the antecedent intercepted snowload ($I_{s,o}$) [kg m^{-2}]. In CRHM, a dynamic canopy snow-balance is calculated, in which the amount of snow interception (I_s) is determined by

$$I_s = (I^*_s - I_{s,o})(1 - e^{-C_l P_s t / I^*_s}) \qquad \textbf{(6.3)}$$

where C_l is the 'canopy-leaf contact area' per unit ground area [], and I^*_s is the species-specific maximum intercepted snowload [kg m^{-2}], which is determined as a function of the mean maximum snowload per unit area of branch, $\bar{S}$ [kg m^{-2}], the density of falling snow, ρ_s [kg m^{-3}], and $LAI`$ by

$$I^*_s = \bar{S}\left(0.27 + \frac{46}{\rho_s}\right) LAI` \qquad \textbf{(6.4)}$$

Sublimation of intercepted snow is estimated following Pomeroy et al.'s (1998) multi-scale model, in which the sublimation rate coefficient for intercepted snow, V_i [s^{-1}], is multiplied by the intercepted snowload to give the canopy sublimation flux, q_e [kg m^{-2} s^{-1}], i.e.

$$q_{\mathrm{e}} = V_{\mathrm{i}}\, I_{\mathrm{s}} \tag{6.5}$$

Here, V_{i} is determined by adjusting the sublimation flux for a 500 μm radius ice-sphere, V_{s} [s^{-1}], by the intercepted snow exposure coefficient, C_{e} [], i.e.

$$V_{\mathrm{i}} = V_{\mathrm{s}}\, C_{\mathrm{e}} \tag{6.6}$$

in which C_{e} was defined by Pomeroy and Schmidt (1993) as

$$C_{\mathrm{e}} = k \left(\frac{I_{\mathrm{s}}}{I^*_{\mathrm{s}}} \right)^{-F} \tag{6.7}$$

where k is a dimensionless coefficient indexing the shape of intercepted snow (i.e. age and structure) and F is an exponent value of approximately 0.4. The ventilation wind speed of intercepted snow may be set in CRHM as an observed within-canopy wind speed, or approximated from above-canopy wind speed by

$$u_{\xi} = u_{\mathrm{h}}\, e^{-\psi\xi} \tag{6.8}$$

where u_{ξ} [m s^{-1}] is the estimated within-canopy wind speed at a fraction ξ of the entire forest depth [], u_{h} is the observed wind speed above the canopy [m s^{-1}], and ψ is the canopy wind speed extinction coefficient [], which is determined as a linear function of LAI` for various needleleaf species (Eagleson, 2002). An evaluation of Eq. 6.8 in approximating canopy wind speeds is provided in Appendix F. Unloading of intercepted snow to the sub-canopy is calculated as an exponential function of time following Hedstrom and Pomeroy (1998). Additional unloading resulting from melting intercepted snow is estimated by specifying a threshold ice-bulb temperature (T_{b}) in which all intercepted snow is unloaded when exceeded for three hours.

6.3.1.3. Rainfall interception and evaporation module

Although the overall focus of this chapter is that of snow forest interactions, winter rainfall may represent substantial water and energy inputs to snow. The fraction of rainfall to sub-canopy snow received as direct throughfall is assumed to be inversely proportional to the fractional horizontal canopy coverage (C_c) []. All other rainfall is intercepted by the canopy, which may be lost via evaporation (E) [kg m^{-2} t^{-1}] or dripped to the sub-canopy if the canopy rain storage (C_R) [mm] exceeds the maximum canopy storage (S_{max}) [mm]. All direct throughfall and drip to the sub-canopy are added to the water equivalent of the snowpack. The intercepted rainload ($I_{r,o}$) [kg m^{-2}] in CRHM is estimated using a simplified Rutter model approach (Rutter, 1971) in which a single storage is determined and scaled for sparse canopies by C_c (e.g. Valente et al., 1997). Evaporation from a fully-wetted canopy (E_p) [kg m^{-2} t^{-1}] is calculated using the Penman-Monteith combination equation (Monteith, 1965) for the case of no stomatal resistance, i.e.

$$E = C_c E_p \qquad \text{for } C_R = S_{max} \tag{6.9}$$

For partially-wetted canopies E is reduced in proportion to the degree of canopy saturation, i.e.

$$E = C_c E_p C_R / S_{max} \qquad \text{for } C_R < S_{max} \tag{6.10}$$

6.3.1.4. Snow energy-balance module

Energy to snow (Q^*) is resolved in CRHM as the sum of radiative, turbulent, advective and conductive energy fluxes to snow, i.e.

$$K^* + L^* + Q_H + Q_E + Q_G + Q_P = \frac{dU}{dt} + Q_M = Q^* \tag{6.11}$$

where Q_M is the energy for snowmelt, dU/dt is the change in internal (stored) energy of snow, K^* and L^* are net shortwave and longwave radiations, respectively, Q_H and Q_E are the net sensible and latent heat turbulent fluxes, respectively, Q_G is the net ground heat flux, and Q_P is the energy from rainfall advection [all units MJ m^{-2} t^{-1}]. In Eq. 6.11, positive magnitudes represent energy gains to snow and negative magnitudes are energy losses. The amount of melt (M) is calculated from Q_{M} by

$$M = \frac{Q_{\mathrm{M}}}{\rho_{\mathrm{w}}\, B\, \lambda_f} \qquad \textbf{(6.12)}$$

where ρ_{w} is the density of water [kg m^{-3}], B is the fraction of ice in wet snow [~ 0.95 – 0.97], and λ_f is the latent heat of fusion for ice [MJ kg^{-1}].

6.3.2. Adjustment of energy fluxes to snow for needleleaf forest-cover

For the purpose of brevity, the following section outlines the algorithms in CRHM estimating energy fluxes in forest environments only. For an overview of energy flux estimations by CRHM in open environments, refer to Pomeroy et al. (2007).

Shortwave radiation to forest snow

In CRHM, net shortwave radiation to forest snow (K*) is equal to the above-canopy irradiance (K_{o}) transmitted through the canopy less the amount reflected from snow, expressed here as

$$K^{*} = K_{\mathrm{o}}\, \tau(1-\alpha_{\mathrm{s}}) \qquad \textbf{(6.13)}$$

in which α_{s} is the snow surface albedo [], the decay of which is approximated as a function of time subsequent to a snowfall event, and τ is the forest shortwave transmittance [], which is estimated by the following variation of Pomeroy and Dion’s (1996) formulation (Pomeroy et al., 2009)

$$\tau = e^{-\frac{1.081\theta \cos(\theta) LAI^{`}}{\sin(\theta)}} \qquad \textbf{(6.14)}$$

where θ is the solar angle above the horizon [radians].

Longwave radiation to forest snow

As stated previously, longwave irradiance to forest snow (L_{in}) may be enhanced relative to that longwave irradiance in the open (L_{o}) as the result of thermal emissions from the canopy. Simulation of forest L_{in} is made as the sum of sky and forest longwave emissions weighted by the forest sky view factor (v), i.e.

$$L_{\mathrm{in}} = vL_{\mathrm{o}} + (1-v)\varepsilon_f \sigma T_f^{\,4} \tag{6.15}$$

Here, ε_f is the forest thermal emissivity [], σ is the Stefan-Boltzmann constant [W m^{-2} K^{-4}], and T_f is the forest temperature [K]. Longwave exitance from snow (L_{out}) is determined by

$$L_{\mathrm{out}} = \varepsilon_{\mathrm{s}} \sigma T_{\mathrm{s}}^4 \tag{6.16}$$

where ε_{s} is the thermal emissivity of snow [], and T_{s} is the snow surface temperature [K] which is resolved using the longwave-psychrometric formulation by Pomeroy and Essery (2010) (Eq. 3.6, Chapter 3).

Sensible (Q_{H}) *and latent* (Q_{E}) *heat fluxes*

Determination of Q_{H} and Q_{E} [MJ m^{-2} t^{-1}] in forest and clearing sites are made using the following semi-empirical formulations developed by Gray and Landine (1988):

$$Q_{\mathrm{H}} = -0.92 + 0.076u_{\mathrm{mean}} + 0.19T_{\mathrm{max}} \tag{6.17}$$

$$Q_{\mathrm{E}} = 0.08(0.18 + 0.098u_{\mathrm{mean}})\,(6.11 - 10ea_{\mathrm{mean}}) \tag{6.18}$$

where u_{mean} is the mean daily wind speed [m s^{-1}], T_{max} is the maximum daily air temperature [°C], and ea_{mean} is the mean daily vapour pressure [kPa]. For the case of rainfall to melting snow (i.e. $T_{\mathrm{s}} = 0$ °C), the energy delivered to the snowpack via rainfall advection (Q_{P}) [MJ m^{-2} t^{-1}] is given by

$$Q_{\mathrm{P}} = 4.2 \times 10^{-3}(P_{\mathrm{r}} - I_{\mathrm{r}})T_{\mathrm{r}} \tag{6.19}$$

where T_r is the rainfall temperature [°C], which is approximated by T_a. Due to the typically small contributions of ground heat fluxes to total snowmelt energy (Pomeroy and Granger, 1997), Q_G is approximated in CRHM simply as a fraction of the determined net radiation to snow (R^*). The primary mass and energy balance calculation routines for both forest and clearing environments within CRHM are summarised in Figure 6.1.

6.4. Model application

Simulations of snow accumulation and melt using the forest module incorporated within CRHM were performed at five paired forest and clearing sites of varying location, climate, forest species, and forest-cover density (Table 6.1). With the exception of the Marmot Creek sites, all simulations were performed as part of the second snow model inter-comparison project (SnoMIP2) (Rutter et al., 2009; Essery et al., 2009). This initiative involved the off-line simulation of snow accumulation and melt in paired forest-clearing sites located in Canada, Switzerland, Finland, and the United States. Hourly standard meteorological forcing data, site descriptions, and initial states were provided to each participant by the SnoMIP2 facilitators. All simulations in SnoMIP2 were executed ‘blindly’ with the exception of the Switzerland location for the 2002-03 season where SWE field data were provided to allow for the option of model calibration. Location, topography and forest-cover descriptions for all sites are given in Table 6.1, and site pictures in Figure 6.2. Simulations of snow accumulation and melt were performed for both forest and adjacent forest clearing sites at each location for the period extending from October 1 to approximately June 1. For each simulation timestep, appropriate energy, mass, and state variables were outputted by the model.

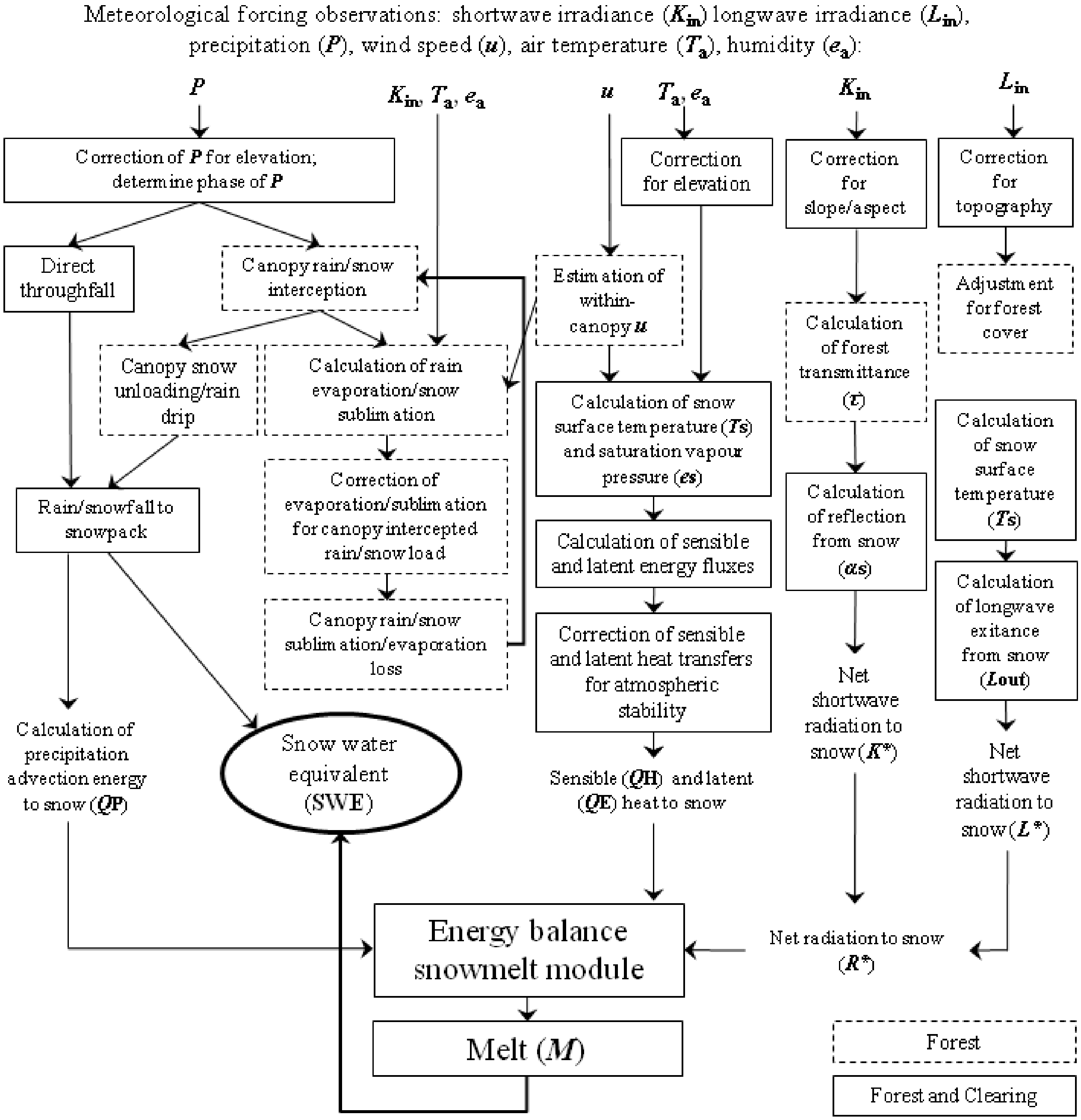

Figure 6. 1. Schematic outlining the primary mass and energy calculations involved in the forest component of the Cold Regions Hydrological Model (CRHM).

Table 6. 1. Location, topography, and forest-cover descriptions of paired clearing-forest sites used in simulations of snow accumulation and melt.

Site:	*Years*	*Latitude*	*Elevation*	*Slope, aspect*	*Height, species*	*LAI`*	*v*
Alptal, Switzerland (forest)	2002-04	47°3' N	1185 m	3°, west	25 m spruce and fir	2.5	0.04
Alptal, Switzerland (clearing)	2002-04	47°3' N	1220 m	11°, west	–	–	–
BERMS, Saskatchewan, Canada (forest)	2002-03	53°55' N	579 m	level	12–15 m jack pine	1.66	0.28
BERMS, Saskatchewan, Canada (clearing)	2002-03	53°57' N	579 m	level	–	–	–
Fraser, Colorado, USA (forest)	2003-05	39°53' N	2820 m	17°, 305°	~27 m pine, spruce/ fir	3	not given
Fraser, Colorado, USA (clearing)	2003-05	39°53' N	2820 m	17°, 305°	2–4 m sparse trees	0.4	not given
Marmot Creek, Alberta, Canada (pine forest)	2007-08	50°56' N	1500 m	level	~15 m lodgepole pine	1.5	0.20
Marmot Creek, Alberta, Canada (pine clearing)	2007-08	50°56' N	1430 m	level	–	–	–
Marmot Creek, Alberta, Canada (spruce forest)	2007-08	50°56' N	1850 m	level	17–20 m Engelmann spruce	2.0	0.15
Marmot Creek, Alberta, Canada (spruce clearing)	2007-08	50°56' N	1850 m	level	–	–	–

Alptal, Switzerland forest (left) and clearing (right) sites.

BERMS, Saskatchewan, Canada forest (left) and clearing (right) sites.

Fraser, Colorado, USA forest (left) and clearing (right) sites.

Marmot Creek, Alberta, Canada pine forest (left) and clearing (right) sites.

Marmot Creek, Alberta, Canada spruce forest showing suspended spruce tree (left), clearing (centre) and radiation reference (right) sites.

Figure 6. 2. (Includes previous page) Photographs of meteorological stations located at forest and clearing sites at Alptal, Switzerland; BERMS, Saskatchewan, Canada; Fraser, Colorado, USA; and pine and spruce sites at Marmot Creek, Alberta, Canada (with the exception of the Marmot Creek sites, site photographs were provided by the SnoMIP2 facilitators).

6.4.1. Simulation of snow accumulation and melt

Evaluation of model performance

Simulations of snow accumulation and melt by CRHM were evaluated in terms of the ability of representing:

i. the variation in mean and maximum seasonal SWE observed between all sites; and

ii. the timing and quantity of SWE accumulation and melt at individual sites.

For *i* and *ii* above, model performance was assessed by the model bias index (MB), the model efficiency index (ME), and the root mean square error (RMSE). These indexes were used as they provide a balanced evaluation of model performance, with the MB comparing the total simulation output to the total of observations, the ME an indication of model performance compared to the mean of the observations, and the RMSE a quantification of the absolute unit error between simulations and observations.

i. Simulation of mean and maximum winter SWE at all sites

Among all sites, considerable variation in mean and maximum seasonal SWE was observed, with mean SWE ranging from 20 – 160 kg m^{-2}, and maximum SWE ranging from 29 – 295 kg m^{-2}. Large variations in SWE were also observed between paired forest and clearings, with forest accumulations ranging from approximately 30 % of the clearing accumulation at the Alptal location (2003-04) to near even accumulations at the BERMS location.

Simulated and observed mean and maximum SWE at all sites are shown in Figure 6.3 and determined model performance index values given in Table 6.2. Here, simulations exhibit a small systematic under-prediction of mean SWE for all sites (MB = 0.97), with a slightly greater under-prediction for the forest sites. In comparison, a greater under-prediction of maximum SWE at all sites was realised (MB = 0.94). Yet, the high ME value indicates CRHM well represented the variability in mean and maximum SWE accumulations between sites. Similar to MB results, the ME shows superior prediction of mean SWE to that of maximum SWE, as well as better prediction for clearing accumulations relative to that in forests. However, due to less snow in the forest, the lower MB and ME indexes at the forest sites translate into similar magnitudes of absolute error to that in the clearings (i.e. RMSE $\approx$ 16 kg m^{-2}), and even lower absolute errors for the prediction of maximum forest SWE.

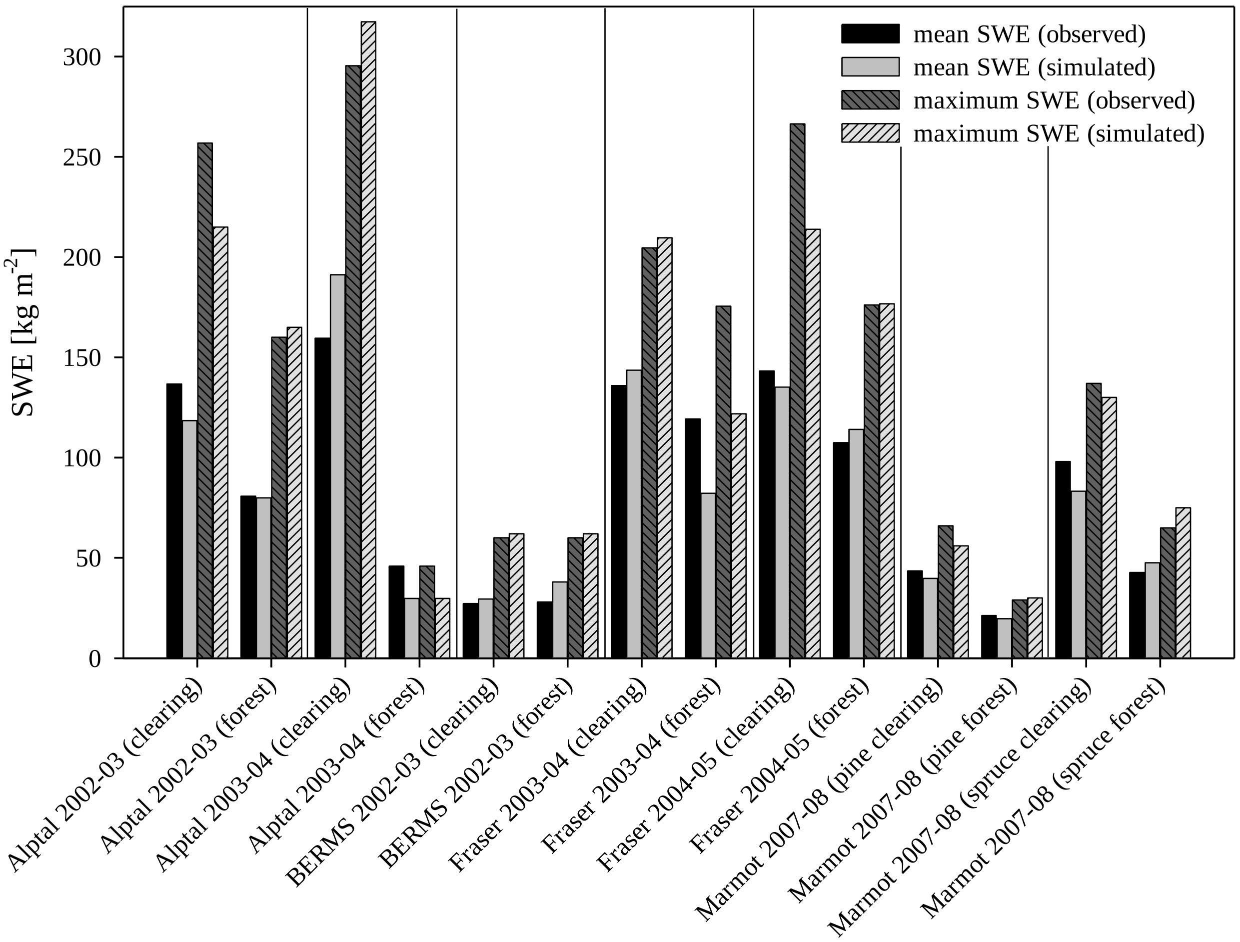

Figure 6. 3. Observed and simulated mean and maximum snow water equivalent (SWE) accumulations at forest and clearing sites.

Table 6. 2. Model bias index (MB), model efficiency index (ME), and root mean square error (RMSE) of simulated mean and maximum snow water equivalent (SWE) at clearing sites, forest sites, and all sites.

	Mean SWE			*Maximum SWE*		
	Clearing sites	Forest sites	All sites	Clearing sites	Forest sites	All sites
Model bias index (MB) []	0.99	0.94	0.97	0.94	0.94	0.94
Model efficiency index (ME) []	0.97	0.93	0.96	0.92	0.87	0.90
Root mean square error (RMSE) [kg m^{-2}]	16.0	16.1	16.0	27.0	21.6	24.4

ii. *Simulation of winter SWE accumulation and melt at individual sites*

Model simulations of snow accumulation and melt at individual sites exhibited considerable variation in the accuracy of estimating the quantity and timing of SWE. However, as seen by the time series plots in Figure 6.4, simulations are able to capture the general differences in the timing of accumulation and melt between paired forest and clearing sites. Model performance indexes for simulations at individual sites, as well as the mean index values for forest, clearing, and all sites are given in Table 6.3. Here, only small systematic underestimations of SWE are realised at both forest and clearing sites, having corresponding MB values of 0.94 and 0.99. In all, the mean ME for SWE simulations at individual sites was 0.51, with slightly lower efficiencies at the forest sites alone. Among simulations, the highest and lowest ME were both obtained at the Alptal forest site, with ME values of 0.93 and -0.03 for the 2002-03 and 2003-04 winters, respectively. Overall, the mean RMSE for all sites was 26.5 kg m^{-2}, with overall higher absolute errors for simulations at the clearing sites.

Due to the discontinuity of SWE observations over the winter at each site, exact determinations of the start, peak, and end of seasonal snow accumulation were not possible. Alternatively, an evaluation of the timing of snow accumulation was provided by the determination of the MB, ME, and RMSE of simulated SWE at the first, last, and maximum SWE observation at each site (Table 6.4). Here, results show for the first observation, SWE is slightly over-predicted at the clearing sites (MB = 1.07), with a large under-prediction of initial forest SWE (MB = 0.6). At maximum SWE, little systematic bias occurs for SWE simulations at all sites (MB = 0.99) due to the offsetting of the slight over-predictions and under-predictions of SWE at the clearing and forest sites, respectively. However, for the last observed SWE, the high MB values indicate a large over-estimation of SWE at the end of melt, suggesting a substantial lag in simulated snow depletion. Poor simulation of late-season SWE is also reflected in the low ME and high RMSE relative to that for the first and maximum SWE observations.

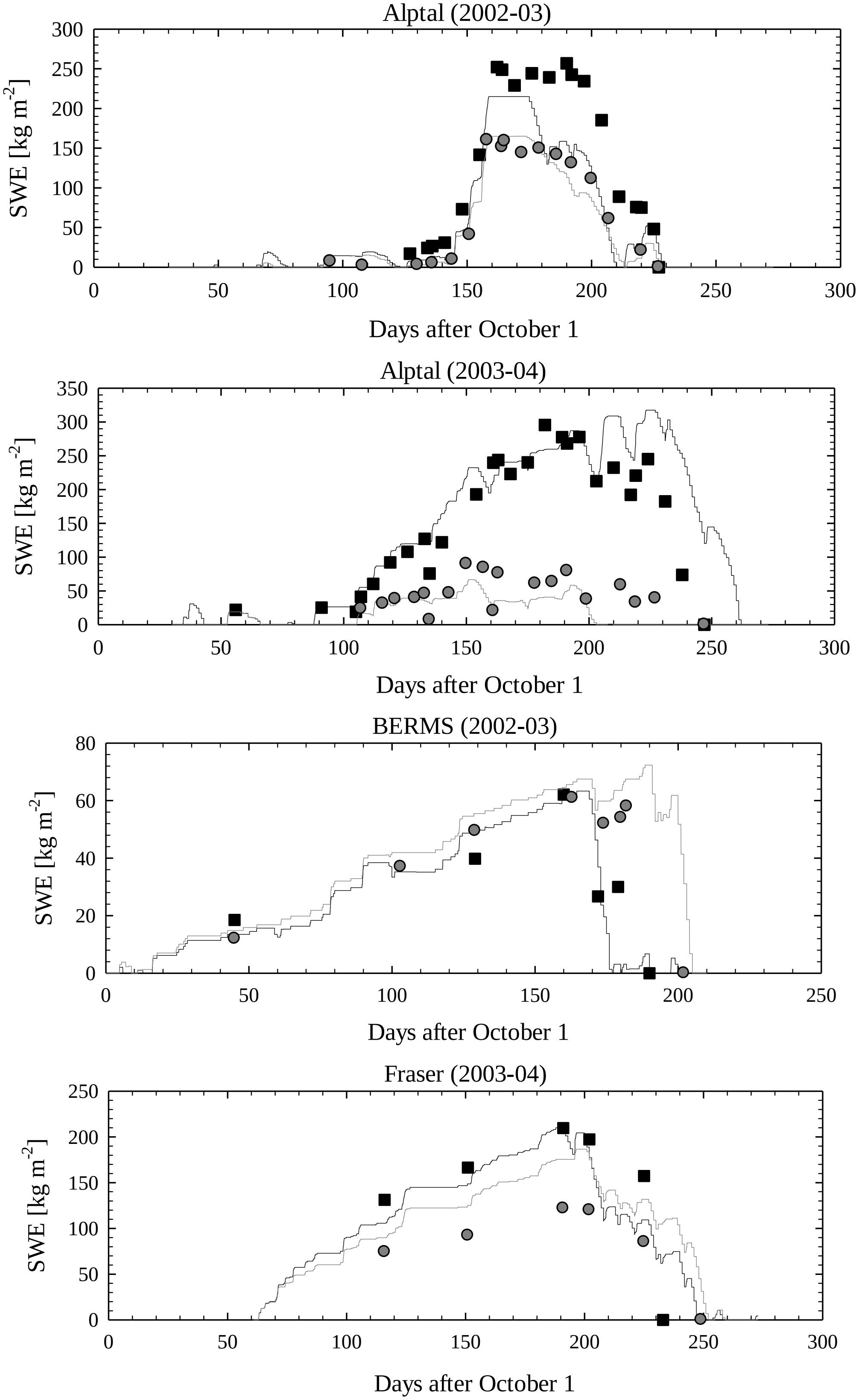

Figure 6.4. (top – see complete figure caption on following page).

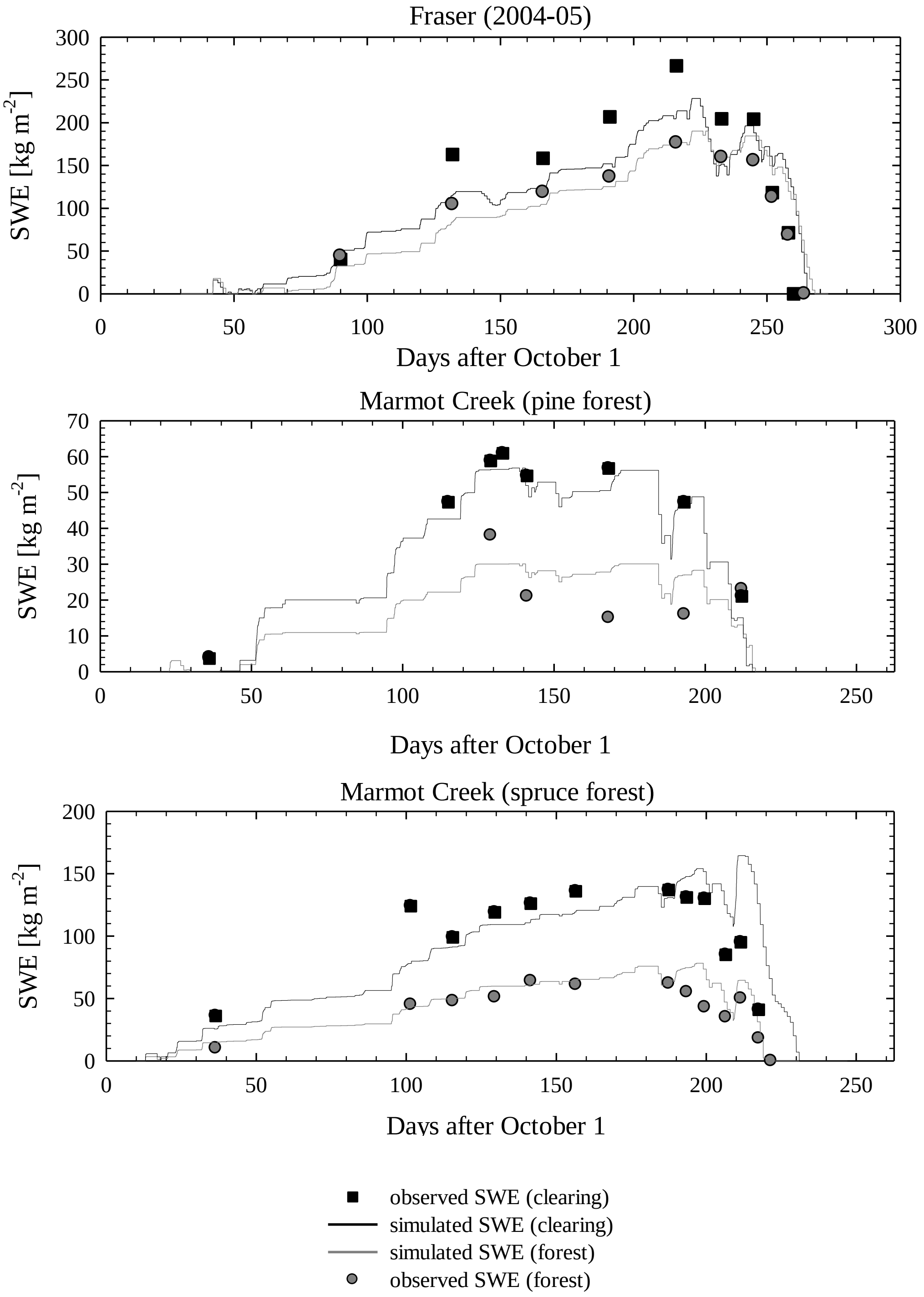

Figure 6. 4. (Includes previous page) Time series of observed and simulated SWE at paired forest and clearing sites.

Table 6. 3. Determined model bias index (MB), model efficiency index (ME), and root mean square error (RMSE) for simulations of snow water equivalent (SWE) at individual sites.

Site:	MB []	ME []	RMSE [kg SWE m^{-2}]
Alptal 2002-03 (clearing)	0.87	0.88	35.6
Alptal 2002-03 (forest)	0.99	0.93	17.6
Alptal 2003-04 (clearing)	1.20	0.64	51.1
Alptal 2003-04 (forest)	0.65	-0.03	25.9
BERMS 2002-03 (clearing)	1.14	0.70	12.6
BERMS 2002-03 (forest)	1.12	0.63	12.9
Fraser 2003-04 (clearing)	1.10	0.32	37.8
Fraser 2003-04 (forest)	0.70	0.46	40.2
Fraser 2004-05 (clearing)	0.95	0.33	37.9
Fraser 2004-05 (forest)	1.05	0.45	40.3
Marmot 2007-08 (pine clearing)	0.90	0.43	13.0
Marmot 2007-08 (pine forest)	0.95	0.13	9.50
Marmot 2007-08 (spruce clearing)	0.80	0.58	28.0
Marmot 2007-08 (spruce forest)	1.10	0.70	8.80
Clearing sites (mean)	0.99	0.55	30.8
Forest sites (mean)	0.94	0.47	22.2
All sites (mean)	0.97	0.51	26.5

Table 6. 4. Model bias index (MB), model efficiency index (ME) and root mean square error (RMSE) for simulations of SWE at the first SWE observation, maximum SWE observation, and last SWE observation at clearing sites, forest sites, and all sites.

	SWE at first observation			*At maximum observed SWE*			*SWE at last observation*		
	Clearing sites	Forest sites	All sites	Clearing sites	Forest sites	All sites	Clearing sites	Forest sites	All sites
MB []	1.07	0.60	0.89	1.08	0.95	0.99	3.85	3.59	3.64
ME []	0.96	0.91	0.93	0.87	0.89	0.88	-3.50	-5.97	-5.70
RMSE [kg SWE m^{-2}]	12.4	5.8	9.8	30.9	22.6	27.0	66.4	18.9	48.8

6.4.2. Simulation of canopy snow sublimation

The above results show CRHM is generally able to represent the observed differences in snow accumulation between paired forest and clearing sites. Considering that these differences are largely the result of canopy sublimation losses, model performance in estimating canopy sublimation is further investigated here. Evaluation of canopy sublimation was performed using canopy snowload measurements from a spruce tree cut and suspended from a load cell at the Marmot Creek (MCRB) spruce forest site (Figure 6.2). Changing tree weight was correlated to the intercepted snowload by the measured difference in snow accumulations between the forest and an adjacent clearing site (e.g. Hedstrom and Pomeroy, 1998). Decreases in tree tare from desiccation and needleleaf loss were accounted for, as was snow unloading from the canopy by measurements of snow collected in three lysimeters suspended under the canopy. Simulation of canopy sublimation was performed for the period of January 14 – March 3, 2008 using precipitation and incoming radiation data from the adjacent clearing with observations of within-canopy wind speed and humidity at the suspended tree.

Over the period, approximately one-half of snowfall was lost by canopy sublimation, with respective mean daily observed and simulated losses of 0.52 kg m^{-2} and 0.55 kg m^{-2}, giving a MB of 1.06 and a ME of 0.41. The time series of hourly canopy sublimation losses in Figure 6.5 (top) shows a general agreement between observed and simulated values, with higher rates corresponding to periods of higher wind speeds and lower relative humidity (Figure 6.5, bottom). Overall, the cumulative amounts of observed and simulated sublimation were similar, equal to approximately 24 and 26 kg m^{-2} for the period, respectively.

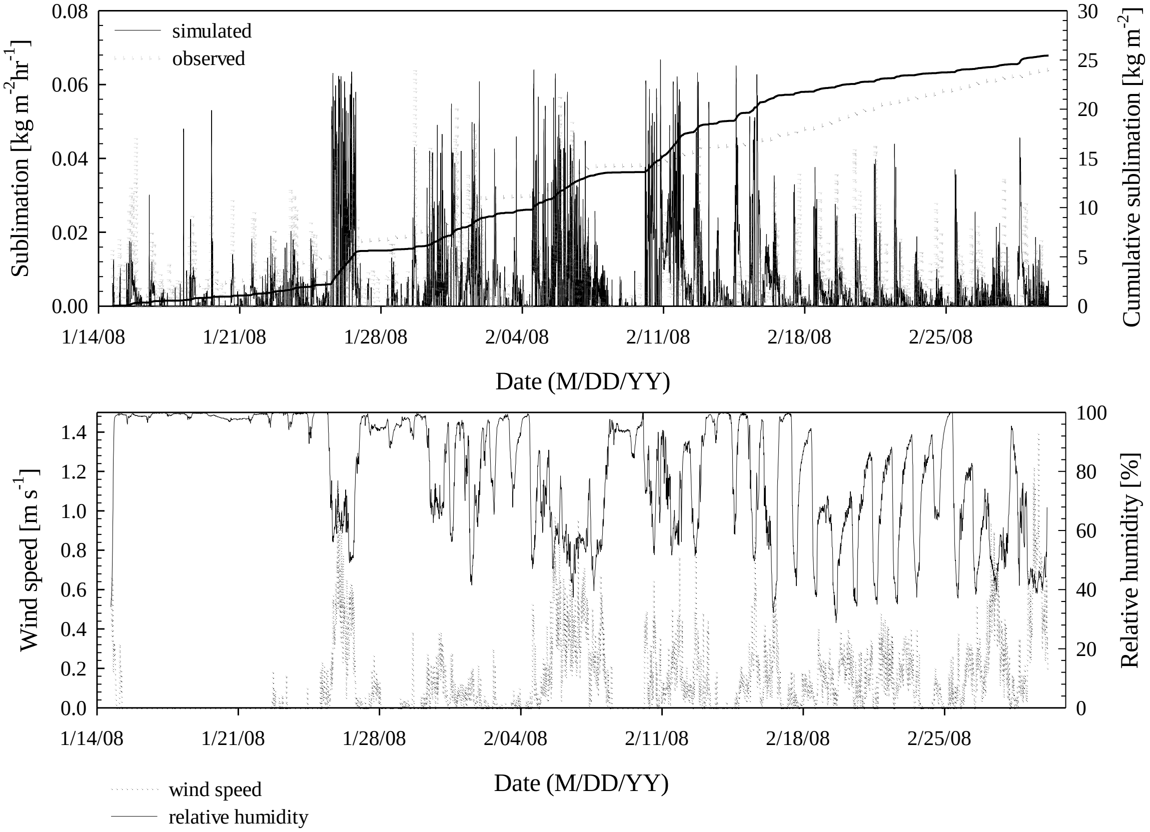

Figure 6. 5. Top: time series of observed and simulated hourly (and cumulative) canopy snow sublimation; bottom: corresponding observations of forest wind speed and relative humidity.

6.4.3. Simulation of energy fluxes to snow

To investigate CRHM's handling of energy fluxes, simulations of energy fluxes to snow were compared to measurements made at the Marmot Creek paired pine forest-clearing sites. Measurements from these sites include incoming and outgoing shortwave and longwave radiation, as well as ground heat fluxes. However, as no direct measures of sensible and latent heat were made, evaluation of the simulation of these fluxes was not possible.

Time series plots of observed and simulated energy terms to snowcover in Figure 6.6 and model indices in Table 6.5 show good agreement for all shortwave radiation terms at both the pine forest and clearing sites, as well as for prediction of net longwave radiation (L^*) at the clearing site. However, despite good prediction of the individual incoming and outgoing longwave fluxes (L_{in} and L_{out}) in the forest, model estimation of sub-canopy L^* was poor, which contributed to degrading estimates of total net radiation to forest snow (i.e. $R^*=K^*+L^*$). Despite the large errors in estimating the ground energy flux (Q_G) at the forest and clearing sites, little effect on overall model performance resulted due to the small contribution of Q_G to total snow energy (note that no energy to snow from rainfall, Q_P, was observed or simulated). In terms of systematic bias, the small negative and positive values of L^*, R^* and Q_G observed (and simulated) provided MB values that were often misleading and not instructive to model assessment. Alternatively, the systematic model bias of energy terms was evaluated simply as the difference between the mean of simulated and observed values. Here, the offsetting of small negative and positive biases of individual energy terms resulted in low bias errors of total energy to snow (Q^*) at the pine forest and clearing sites of -0.59 and -0.37 W m^{-2}, respectively. Moreover, the close comparison of total simulated and observed energy terms in Figure 6.7 demonstrate that CRHM was able to characterise the substantial difference in forest and clearing energy balances, and provide good estimation of total energy to snow. Also shown in Figure 6.7 are the simulated sensible and latent energy totals to snow, which were greater in absolute magnitude at the clearing relative to the forest, but provided approximately equal relative contributions to Q^* at both sites.

Table 6. 5. Model efficiency index (ME), root mean square error (RMSE), and the difference between mean simulated and observed values of: shortwave irradiance (K_{in}), reflected shortwave irradiance (K_{out}), net shortwave radiation (K^*), longwave irradiance (L_{in}), longwave exitance (L_{out}), net longwave radiation (L^*), total net radiation (R^*), net ground heat flux (Q_G), and total energy to snow (Q^*) (i.e. $Q^* = Q_M + dU/dt$) at the MCRB paired pine forest-clearing sites.

Site:	K_{in}	K_{out}	K^*	L_{in}	L_{out}	L^*	R^*	Q_G	$^{\dagger}Q^*$
ME (Clearing) []	–	0.94	0.94	–	0.82	0.67	0.80	-0.92	0.78
ME (Forest) []	0.87	0.82	0.83	0.90	0.79	0.08	0.27	-2.77	0.25
RMSE (Clearing) [W m^{-2}]	–	13.9	13.9	–	18.2	18.2	22.4	1.8	23.1
RMSE (Forest) [W m^{-2}]	6.1	5.3	2.7	9.24	13.1	8.56	9.08	2.2	9.64
Mean simulated – mean observed (Clearing) [W m^{-2}]	–	2.75	-2.75	–	-3.15	3.15	0.40	-0.03	-0.37
Mean simulated – mean observed (Forest) [W m^{-2}]	0.36	-0.02	0.38	-2.70	-1.70	-1.0	-0.60	0.02	-0.59

†excludes sensible and latent heat fluxes.

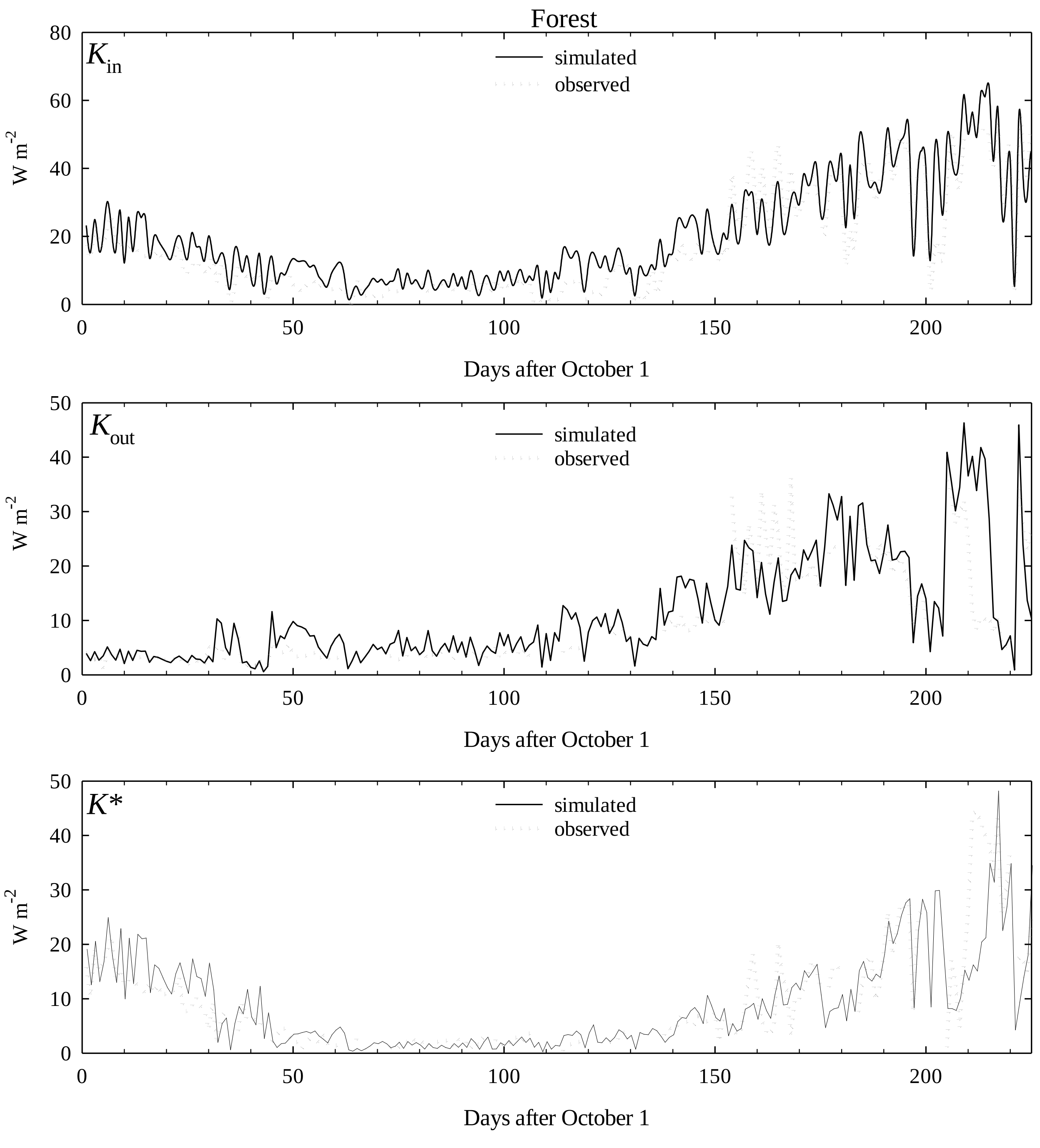

Figure 6.6 (see complete figure caption below). Observed and simulated shortwave fluxes at the MCRB Level Pine Forest (LPF) site.

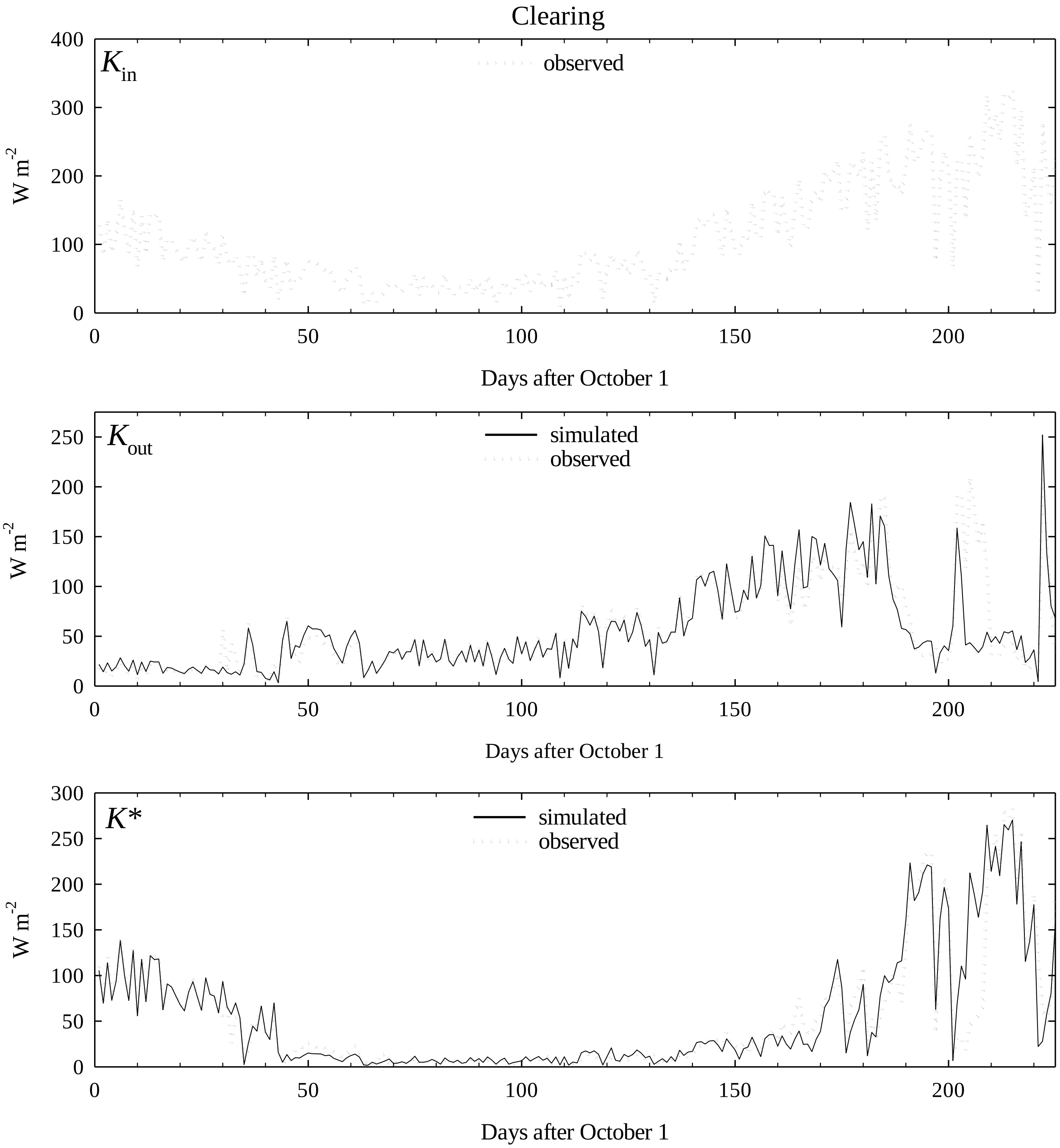

Figure 6.6. Observed and simulated shortwave fluxes at the MCRB Level Pine Clearing (LPC) site(see complete figure caption below).

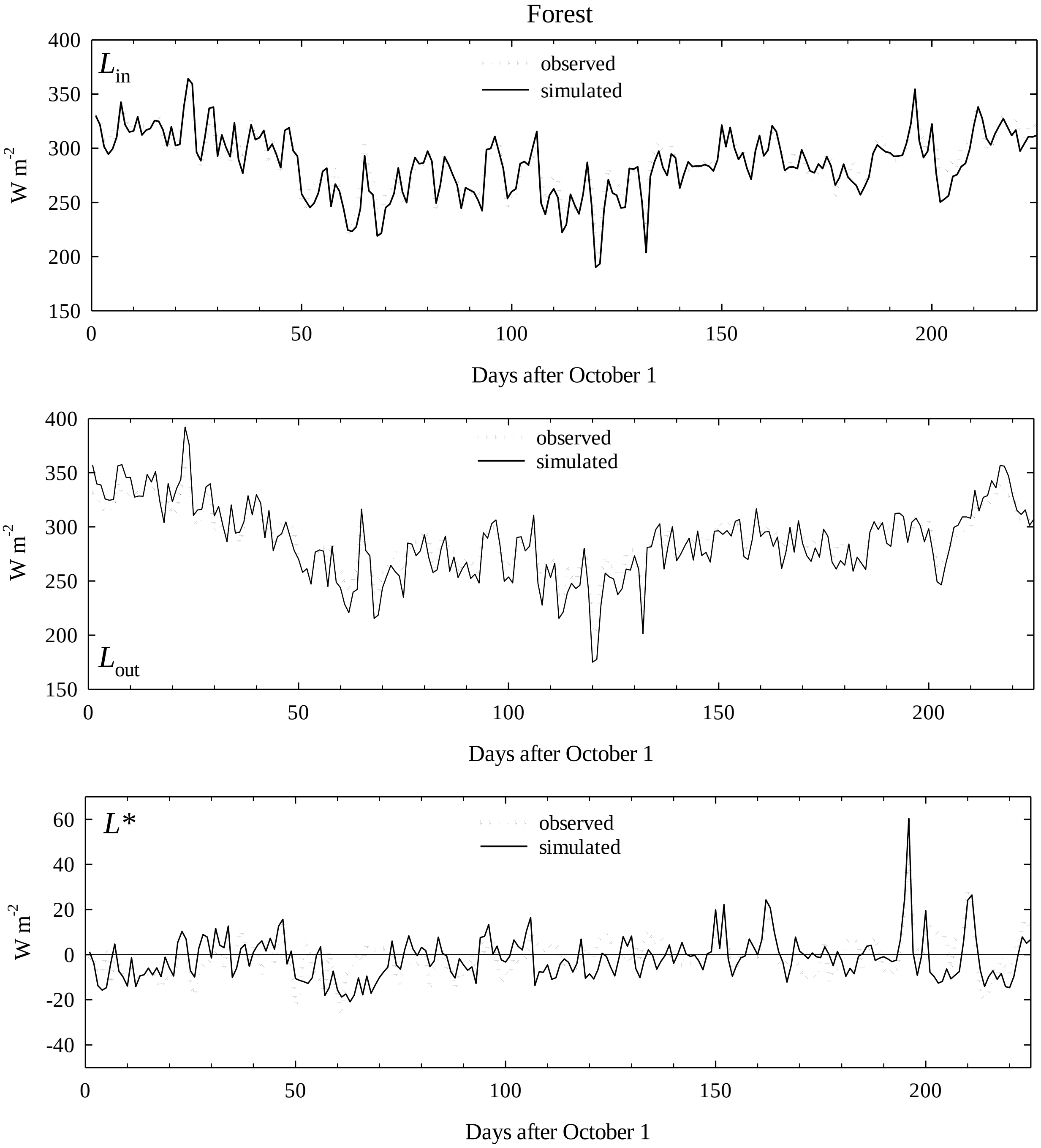

Figure 6.6. Observed and simulated longwave fluxes at the MCRB Level Pine Forest (LPF) site (see complete figure caption below).

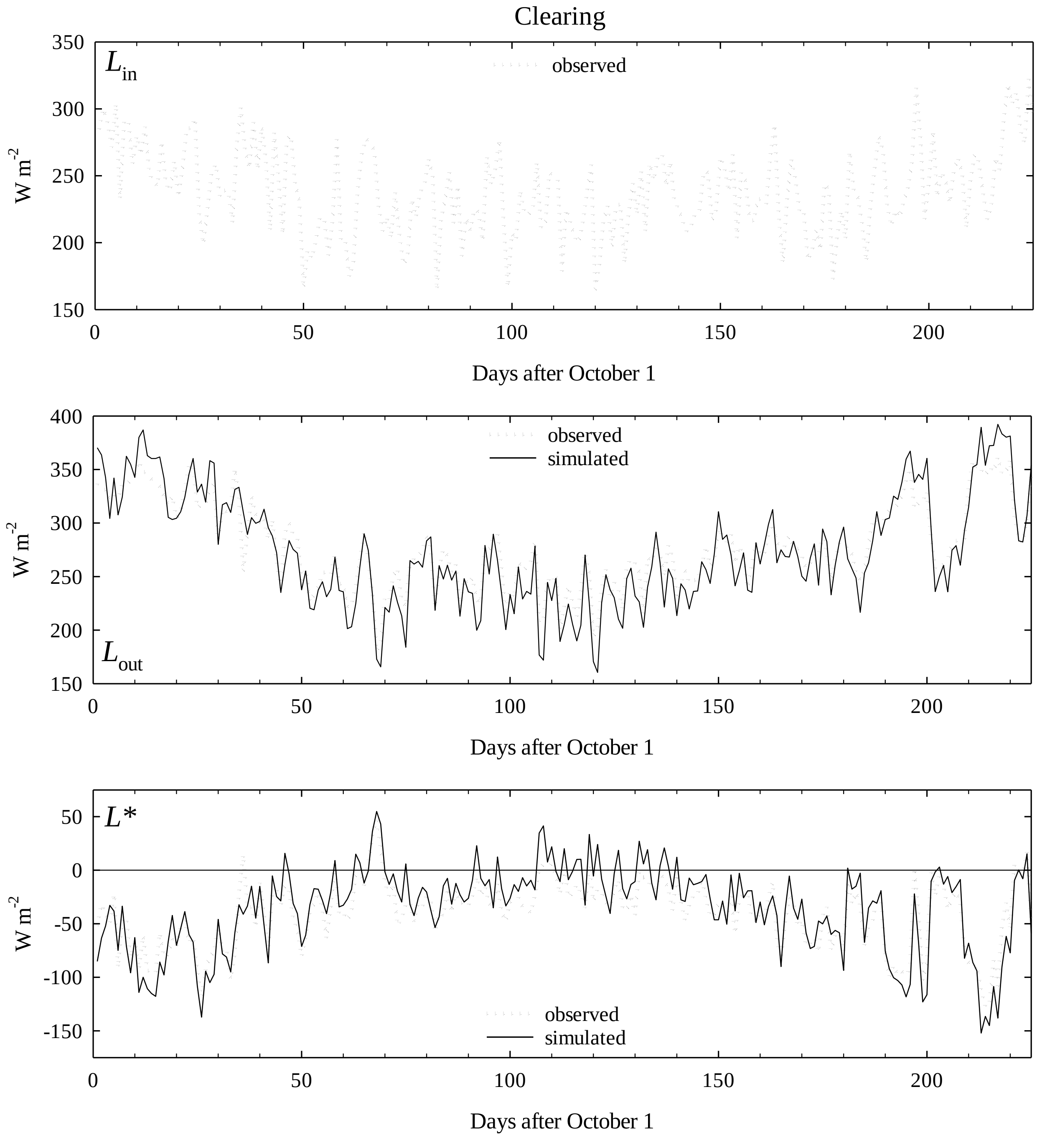

Figure 6.6. Observed and simulated longwave fluxes at the MCRB Level Pine Clearing (LPC) site (see complete figure caption below).

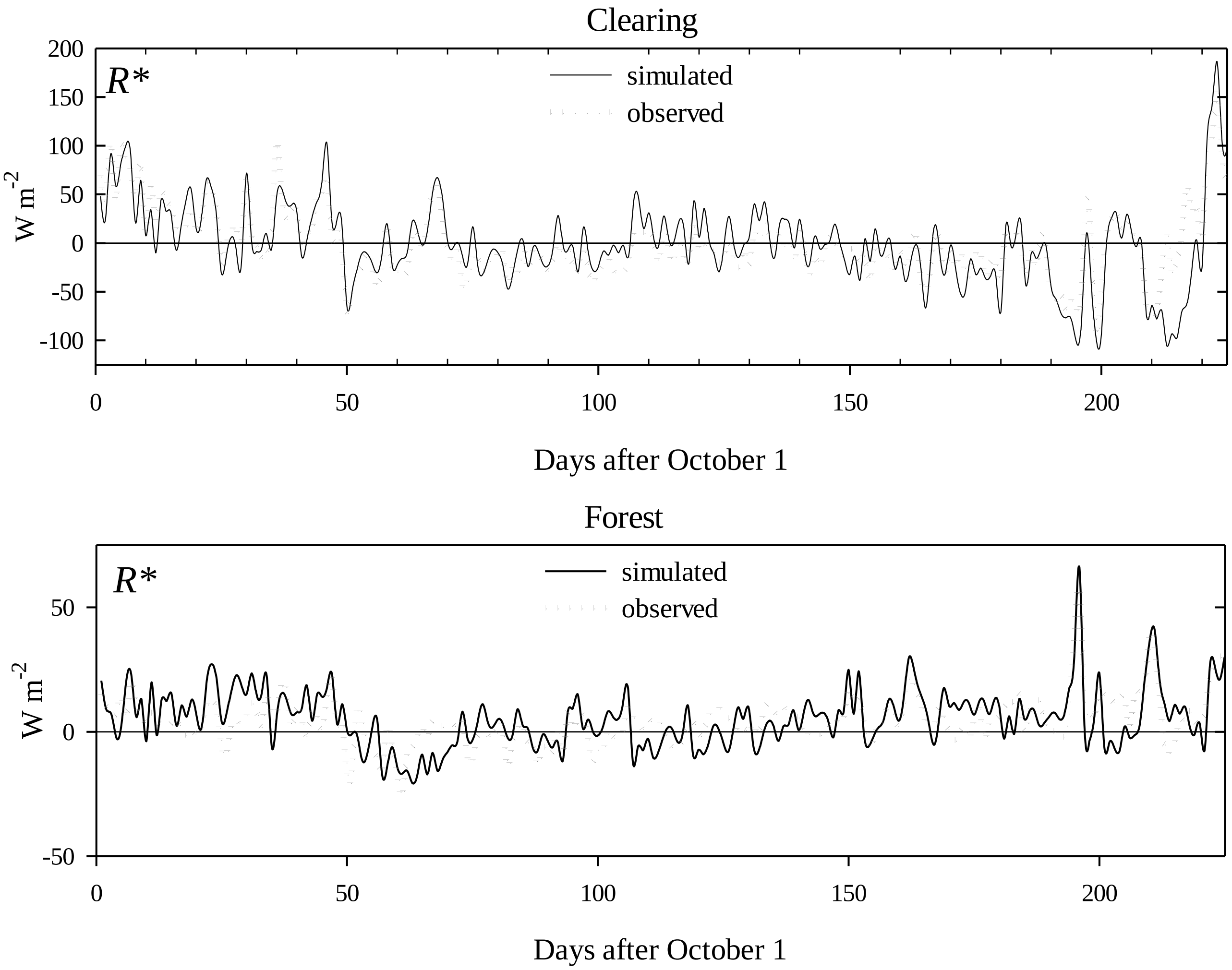

Figure 6.6 (cont.). Observed and simulated net shortwave radiation at the MCRB Level Pine Clearing site (LPC) and Level Pine Forest (LPF) site.

Figure 6. 6. (includes the previous four pages). Time series plots of mean daily simulated and observed shortwave (*K*) and longwave (*L*) radiation fluxes, as well as total net radiation to snow (*R**) at pine forest and clearing sites in the MCRB, Alberta, Canada (2007-08).

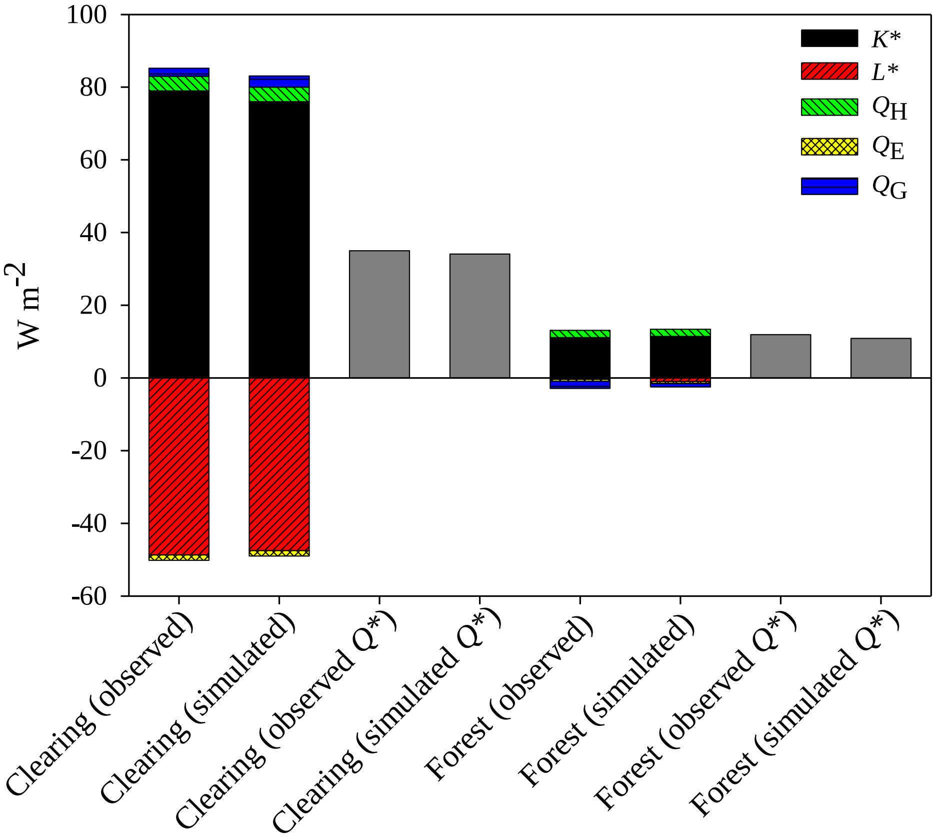

Figure 6. 7. Observed and simulated net energy terms and total energy to snow ($Q^* = dU/dt + Q_M$) at the MCRB pine forest and clearing sites (note that due to no observations of simulated sensible (Q_H) and latent (Q_E) heat fluxes, observations are assigned the same value as simulations).

6.5. Chapter discussion

Overall, results show that CRHM is able to well represent the quantity and timing of snow accumulation and melt under needleleaf forest-cover and in forest clearings. Good results were obtained in terms of characterising the substantial differences in snow accumulation and melt observed at forest and clearing sites of varying location and climate. The accurate approximation of the major energy balance terms at the MCRB pine forest and clearing sites suggests that despite modest data requirements, the physical-basis of the model is sufficient for representing forest-snow processes in environments of varying forest-cover and meteorology.

Simulations of mean and maximum seasonal SWE exhibited little systematic bias at forest sites, clearing sites, or all sites. This suggests that much of the errors incurred were random in nature, resulting either from errors in observations or model parameterisation. For simulations of SWE at individual sites, errors also appear to be random rather than systematic, considering that the best and worst model efficiencies were obtained for the same site over consecutive winters (i.e. Alptal forest). In all, the poorest model efficiencies of SWE determinations were realised at the 2003-04 Alptal forest and Marmot pine sites, which had substantially lower accumulations relative to most the other sites. Such results may be expected, as shallower snowpacks would be more sensitive to simulation errors of mass and energy, thus giving larger relative errors. Notwithstanding these limitations, encouraging simulation results were obtained in general, exemplified in the good representation of the extreme differences in forest and clearing snow accumulations over the two winters at the Alptal location.

Although good prediction of SWE was made for the start and peak of winter accumulations, poorer predictions were made at the end of accumulation, suggesting a lag in simulated melt rates. Particularly large lags in simulated snow depletion occurred at the Alptal (2003-04) clearing and Marmot spruce clearing sites, where the substantial late-season snowfall may have resulted in an overestimation of the additional energy deficit to the snowpack. This suggests that improvement in CRHM's representation of snowmelt timing and rate may require addressing the handling of internal snow energetics with large snowfalls.

Compared to observations of canopy snow load changes from a suspended tree, satisfactory model simulation of canopy sublimation was achieved both in terms of daily and cumulative losses. The correspondence of periods of high sublimation with higher wind speeds and lower relative humidity demonstrate the physically-based manner in which canopy sublimation is determined by CRHM, suggesting that such approaches are likely necessary to properly represent differences in forest and open site snow accumulation with variations in forest-cover density and climate. However, sensitivity analysis has shown sublimation estimates in CRHM to be very responsive to errors in the intercepted snowload, which may reflect its simplistic approach in the handling of canopy snow unloading. Consequently, increased confidence in the model's representation of canopy sublimation losses would be expected through a better understanding of the physical processes controlling canopy unloading of snow.

Although simulations of energy fluxes were evaluated against observations at only a single paired clearing-forest site, results show CRHM well represented the differences between open and sub-canopy energy balances. All errors in estimating shortwave and longwave radiation were small and below the measurement error of the radiometers used in their observation. However, the presence of forest-cover is seen to dramatically decrease the model's predictive capability for net radiation and total energy to snow, evident in the decreasing model efficiency (ME) with the increasing number of combined energy terms (Table 6.5). Cumulative errors in estimating total energy to snow were relatively modest, owing in part to the cancellation of errors from individual energy terms. Although no evaluation of sensible and latent energy terms was possible, simulated magnitudes were similar to those observed in cold-region needleleaf forest environments by Harding and Pomeroy (1996) and estimated by Pomeroy and Granger (1997).

Despite some uncertainly in model performance, results show CRHM is able to provide good characterisation of critical forest-snow processes in environments of highly variable forest-cover and climate, with only modest requirements for site information and meteorological forcing data. As simulations were performed without calibration to any objective function, there is increased confidence in CRHM's capability in representing effects on snow accumulation and melt brought about by changes in forest-cover or climate. Consequently, results from this model evaluation are encouraging for the use of CRHM as a diagnostic or predictive tool for investigating needleleaf forest-cover effects on snow processes in cold regions.

Parts of this chapter have been previously published in:

Ellis et al. 2010. Simulation of snow accumulation and melt in needleleaf forest environments. *Hydrol. Earth Syst. Sci*., 14, 925-940, doi:10.5194/hess-14-925-2010.

7. IMPACTS OF FOREST-COVER CHANGES ON RADIATION AND SNOWMELT IN THE EASTERN CANADIAN ROCKY MOUNTAINS

7.1. Chapter summary

Using a physically-based modelling approach built upon extensive field observations of radiation dynamics and snow processes in cold region forests, the impact of forest harvesting treatments on snow radiation and snowmelt was examined at the MCRB. Overall, results show irradiance to snow in forest clearings to vary markedly with seasonal meteorological conditions, clearing-size, and topography; with increased irradiance during the late winter – early spring promoted in larger clearings on south-facing slopes and smaller clearings on north-facing slopes. This situation however, reverses in the later spring as maximum radiation occurs in smaller forest clearings on south-facing slopes and larger clearings on north-facing slopes. Model simulations performed at open, forest-covered, and forest clearing ‘gap’ sites show snowmelt to be most delayed under forest-cover on south-facing slopes due to decreased sub-canopy radiation to snow. Conversely, on north-facing slopes, forest-cover removal delayed snowmelt by decreased melt energy from canopy longwave emissions. Consequently, forest-cover removal across the MCRB resulted in a pronounced de-synchronisation in melt timing between south-facing and north-facing landscapes, which substantially lengthened the spring melt period. Subsequent model application demonstrates the large shifts in snowmelt timing possible from topography-specific changes in forest-cover, and illustrates the potential impacts that prescribed forest harvesting practices may have on the magnitude and timing of mountain spring snowmelt runoff.

7.2. Chapter introduction: forest harvesting treatments at the MCRB

Located in the eastern slopes of the Canadian Rocky Mountains, the MCRB has been the site of numerous field research initiatives examining the effects of needleleaf forest-cover on snow accumulation and snowmelt processes. Initiated in the 1970s as part of the Eastern Slopes Alberta Watershed Research Program (Beckstead and Veldman, 1985), extensive prescribed forest clear-cutting treatments were completed within the MCRB to assess the potential impacts large-scale forest-cover changes may have upon the snow hydrology of a mountain headwater basin. At the MCRB, forest harvesting was carried out in two clear-cutting treatments: the first establishing 6 large forest clearings (3–13 ha) within the Cabin Creek sub-basin starting in 1974, followed by 2103 small forest-cover circular ‘gap’ clearings cut along the opposing banks of both Twin Creek tributaries through 1977 – 1979 (Figure 7.1). The small clear-cuts were spatially positioned to one another forming a honeycomb-like pattern within forest-cover, with individual clearing diameters ranging from ¾ – 1¼ to that of the surrounding forest height. In general, the intent of the large clear-cutting treatment was to evaluate the potential for increasing the basin’s snow accumulation and water yield by reduced canopy interception losses. Although water yield effects were also of interest with the Twin Creek forest treatment, of particular focus with the small clear-cuts was their prospect in promoting later-season streamflow through delayed snowmelt (Swanson and Golding, 1982).

The retarding of spring snowmelt in small honeycomb-patterned forest clearings follows Church’s (1912) assertion that this represented the ideal forest structure for snow conservation by promoting snow accumulation sheltered from radiation and turbulent energy exchanges. In terms of snow accumulation, this hypothesis has been largely supported by field observations, with substantially higher accumulations reported in forest clearings relative to under canopy cover by Golding and Swanson (1978), Gary (1980), and Troendle and Leaf (1981). However, conflicting results have been obtained regarding impacts on snowmelt timing, as snowmelt in forest clearings has been observed starting more than three weeks before forest snowmelt in Colorado (Gary and Troendle, 1982), while Golding and Swanson (1978) and Swanson and Golding (1982) reported substantial delays in clearing snowmelt to that in undisturbed Alberta forests. Although these opposing results were attributed to varying amounts of shortwave irradiance shading within the clearings produced by their differing opening size, topography, and latitude, these effects are unconfirmed due to a lack of direct meteorological observations. Yet, insight from direct measurements themselves are limited by the logistical challenges in obtaining sufficiently comprehensive datasets under the large range of possible combinations in forest clearing size, meteorology, and topography (Jost et al., 2007).

An alternative approach in using field observations to directly assess how forest-cover changes may impact snow processes is their employment in developing and evaluating physically-based simulation models. With rigorous, honest evaluation of algorithms describing hydro-meteorological processes, and meaningful physical site description through parameter specification, potential exists for employing physical models to assess the impacts of land-use changes (i.e. forest harvesting) on hydrological responses such as snowmelt. Such facility exists within the Cold Regions Hydrological Model (CRHM), which through various configurations of its process-based modules has been demonstrated to provide effective representation of snow processes in cold region needleleaf forest environments (Chapter 6). The deterministic nature of CRHM lends itself well toward identifying and understanding how physical changes forest-cover may impact snowmelt processes through the numerous mass and energy diagnostic variables that may be outputted to the user. Although CRHM is not explicitly a spatially-distributed hydrological model, the effect of varying physical site characteristics may be assessed effectively through appropriate parameter specification of separate hydrological response units (HRUs).

Using this modelling approach, this chapter examines how differing forest clear-cutting treatments impact radiation and the magnitude and timing of snowmelt over seasonal meteorological conditions observed at the MCRB. Estimation of irradiance to snow in sloped mountain forests is made following the procedures for adjusting shortwave and longwave radiation fluxes under canopy-cover outlined in Chapter 5. Alternatively, determination of irradiance to snowcover in forest clearings (i.e. circular clear-cuts) is made using a geometrically-based ‘forest gap radiation model’ developed by Link et al. (in preparation), which is adapted for sloped terrain as outlined in this chapter. Determinations of snowmelt in (i) open, (ii) forest-covered, and (iii) forest clearing (gap) environments are subsequently made through the coupling of corrected irradiance to the appropriate snow mass- and energy-balance routines in CRHM. With the necessary simplifying assumptions for model implementation at the MCRB detailed throughout the chapter, simulations are used to address the following:

1) How does the size (i.e. opening dimension) of forest (gap) clearings influence radiation to snow? How does this vary with topography (i.e. slope and aspect) and with seasonal meteorological conditions in an eastern Rocky Mountain basin?

2) How do snowmelt energetics differ in (i) open, (ii) forest-covered and (iii) forest clearing (gap) sites, and how are they influenced by topography? Are these differences reflected in the timing of snowmelt in these landcover environments?

3) What potential exists in altering the magnitude or timing of snowmelt in a headwater basin through prescribed forest-cover changes?

By addressing the above, information from model determinations will be used to offer insight and help explain effects on snowmelt attributed to the forest clear-cutting treatments at the MCRB. From this, results are intended to complement the valuable insight gained from earlier studies investigating the snowmelt impacts from the forest harvesting treatments at the MCRB, as well as that of previous modelling exercises assessing the hydrological responses caused by forest harvesting in other mountain basins (Stork et al., 1998; Moore and Scott, 2005).

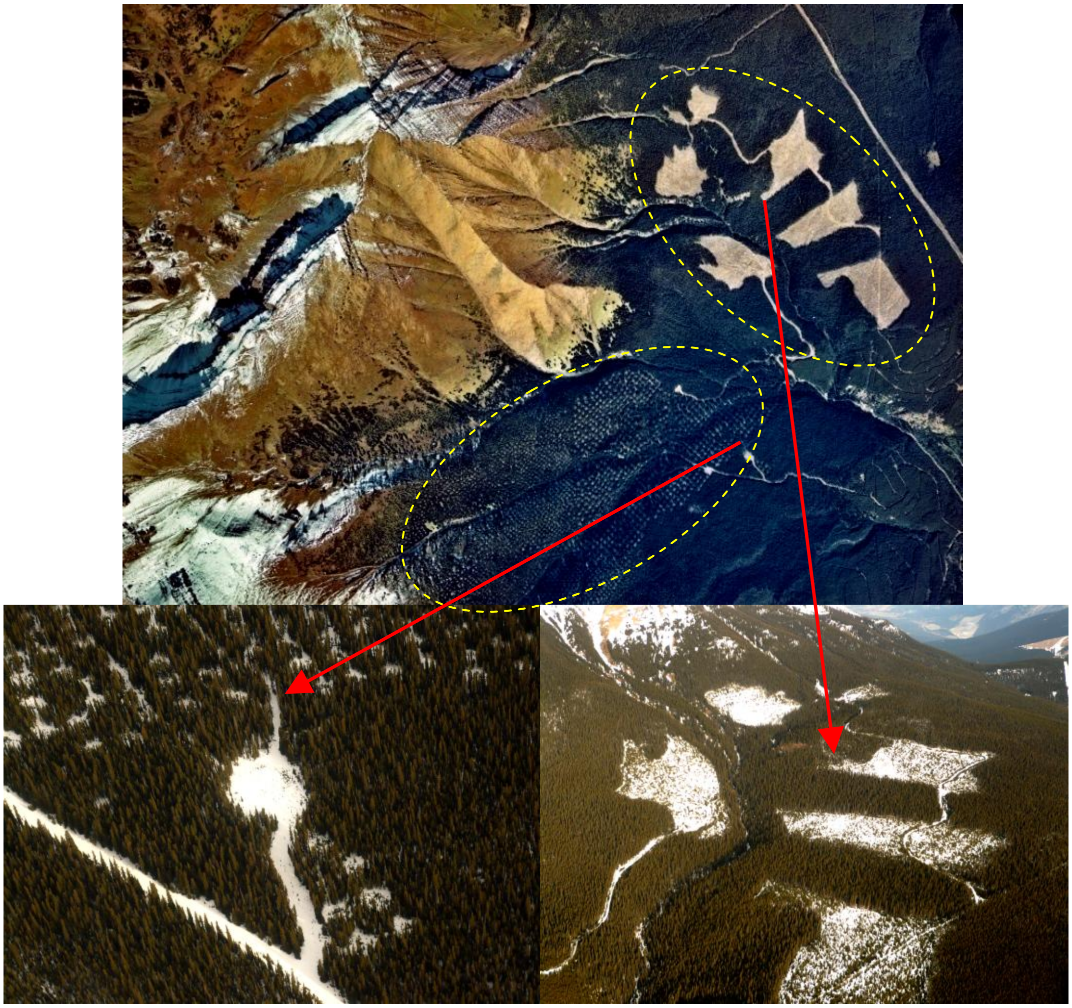

Figure 7. 1. Top: Aerial photograph of the MCRB showing the general locations of the large clear-cuts within the Cabin Creek sub-basin (bottom-right) and the 'honeycomb' pattern of small circular (gap) clear-cuts along the Twin Creek tributaries (bottom-left).

7.3. Determination of irradiance in *open*, *forest*, and *gap* sites

Within this chapter, three primary variations in forest landcover type are considered: (i) an *open* landcover type devoid of any canopy cover, (ii) a *forest* landcover type of continuous, relatively dense canopy-cover, and (iii) a forest *gap* landcover type in the form of circular clearings of varying opening dimension within forest-cover. The following outlines the calculation of irradiance within each of these landcover 'site' types:

7.3.1. *Open* site irradiance

Incoming all-wave irradiance to a level, open surface (R_{in}) is given by the sum of atmospheric shortwave irradiance (K_{in}) and longwave irradiance (L_{in}) fluxes:

$$R_{\mathrm{in}} = K_{\mathrm{in}} + L_{\mathrm{in}} \tag{7.1}$$

With no change in the overlying sky view obscured by surrounding topography, adjustment of level R_{in} for slope effects is made by the following correction of direct-beam shortwave irradiance (K_{b})

$$R_{\mathrm{in,s}} = \omega K_{\mathrm{b}} + K_{\mathrm{d}} + L_{\mathrm{in}} \tag{7.2}$$

where $R_{\mathrm{in,s}}$ is the all-wave irradiance to the slope, ω is the geometric correction factor of irradiance for slope (calculation in Appendix A), and K_{d} and L_{o} are the respective non-directional fluxes of diffuse shortwave and longwave irradiance.

7.3.2. *Forest* site irradiance

Under a forest canopy of assumed homogenous and isotropic spatial foliage distribution, radiation to the sub-canopy ($R_{\mathrm{in},f}$) is resolved by separate treatment of shortwave and longwave fluxes by

$$R_{\mathrm{in},f} = \omega K_{\mathrm{b}} \tau_{\mathrm{b}} + \tau_{\mathrm{d}}(K_{\mathrm{d}} + L_{\mathrm{in}}) + (1 - \tau_{\mathrm{d}}) \varepsilon_f \sigma T_f^{\,4} \tag{7.3}$$

where τ_{b} and τ_{d} are the respective forest transmittances of direct-beam and diffuse irradiance, and

ε_f and T_f are the respective thermal emissivity and temperature of the forest. In Eq. 7.3, τ_{b} may be approximated for sloped canopies by

$$\tau_{\mathrm{b}} = e^{-\frac{L`}{\omega \sin(\theta)}} \tag{7.4}$$

where $L`$ is the optical depth of the forest layer [] (see Section 5.3.1., Chapter 5), and θ is the solar elevation angle [radians].

7.3.3. *Gap* site irradiance

Using a similar convention to that for *open* and *forest* sites, irradiance within a forest *gap* site is determined using an adaptation of Link et al.'s (in preparation) forest gap radiation model. The model abstracts the *gap* as an upright circular opening within forest-cover of a diameter/height dimension defined by *d*/*h*, for which irradiance to the centre of the gap base is given by the following expansion of Eq. 7.3

$$R_{\mathrm{in,g}} = \omega K_{\mathrm{b}} \tau_{\mathrm{b,g}} + V_{\mathrm{gap}}(K_{\mathrm{d}} + L_{\mathrm{in}}) + (1 - V_{\mathrm{gap}})[\tau_{\mathrm{d}}(K_{\mathrm{d}} + L_{\mathrm{in}}) + (1 - \tau_{\mathrm{d}})\varepsilon_f \sigma T_f^{\,4}] \tag{7.5}$$

where $\tau_{\mathrm{b,g}}$ is the transmittance of direct-beam irradiance to the gap centre, and V_{gap} is the fraction of the overlying forest-cover opened by the gap, which is determined using Reifsnyder and Lull's (1965) expression:

$$V_{\mathrm{gap}} = \sin^2 \arctan\left(\frac{d}{2h}\right) \tag{7.6}$$

In Eq. 7.5, $\tau_{\mathrm{b,g}}$ is calculated with account for the reduced extinction pathlength from the gap by γ in the following modification of Eq. 7.4

$$\tau_{\mathrm{b,g}} = e^{-L`\gamma} \tag{7.7}$$

in which γ, with adjustment for slope effects by ω is given by the following adaptation of Link et al.'s (in preparation) formulation

$$\gamma = \frac{1}{\omega}\left(\sin^{-1}(\theta) - d/2h\cos^{-1}(\theta)\right) \qquad \textbf{(7.8)}$$

Figure 7.2 diagrams the various physical site components involved in determining *gap* site irradiance using the geometric forest gap model. Application of this model has provided satisfactory representation of irradiance in forest gaps of varying dimension, latitude and meteorology, as compared to shortwave and longwave irradiance observations collected using multi-sensor radiometer arrays (Link et al., in preparation).

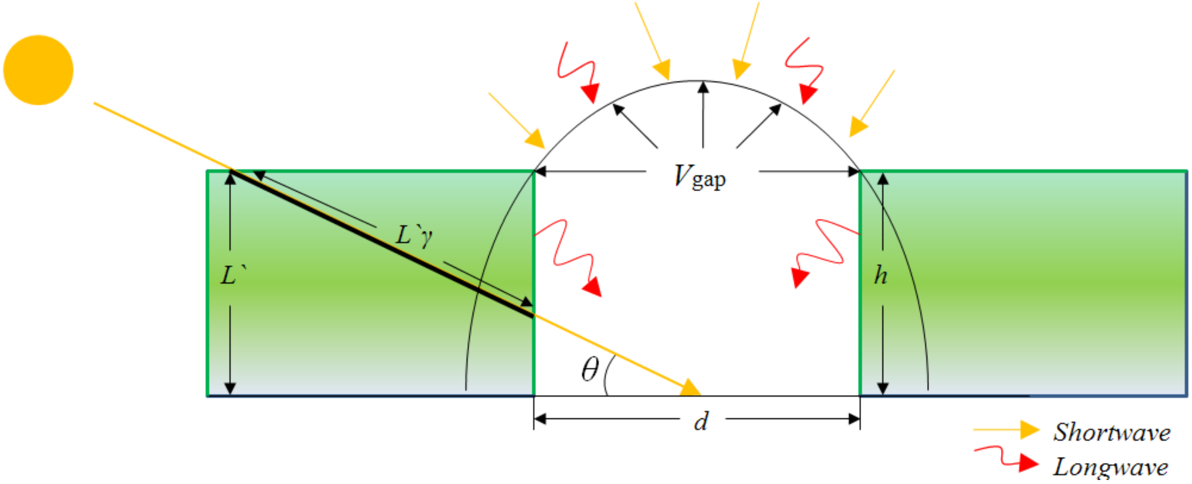

Figure 7. 2. Diagram depicting the main shortwave and longwave irradiance transfers and spatial site components involved for irradiance determinations within an idealised small, circular forest *gap* site.

7.4. Radiation to snow in mountain forest clearings

To illustrate the dynamic balance between shortwave and longwave radiation with respect to forest clearing (gap) size, simulations of daily net radiation to snow (R^*) were made to *gap* sites of varying d/h dimension under meteorological conditions observed at the MCRB for the period extending October 2007 – July 2008 (Figure 7.5). To assess the influence of topography and snow albedo (α_s) on R^* to the *gap* site, simulations were made to a hypothetical: level *gap* site (LG), a *gap* site on 30° slope of north-facing aspect (NG), and a *gap* site on a 30° slope of south-facing aspect (SG). For all *gap* sites, net shortwave radiation (K^*) and longwave radiation (L^*) were determined respectively by Eq. 5.9 and Eq. 5.10 (Chapter 5). Determinations of L^* were made by approximating snow surface temperatures by observed near-surface air temperatures for below-freezing conditions, and held at 0 ˚C for above-freezing air temperatures. For K^* determinations, the influence of varying snow albedo (α_s) upon R^* was evaluated through the specification of α_s values in Eq. 5.9 equal to 0.8 and 0.7, which are intended to represent conditions of relatively high and low seasonal snow albedo, respectively. Simulations are made in Eq. 7.5 with forest-cover surrounding the *gap* site having a diffuse irradiance transmittance (τ_d) equal to 0.2, specified as such to represent a dense spruce canopy (Link et al., 2004). Following a similar approach as Section 5.6 (Chapter 5), the effect of the gap opening-size on radiation to snow is assessed by the diameter-to-height ratio (d/h) providing maximum daily R^* at the *gap* site, which is denoted here by $d/h(R^*_{max})$. Accordingly, for gap openings of $d/h > d/h(R^*_{max})$, radiation is reduced from R^*_{max} through lost longwave emissions from forest-cover surrounding the *gap* site; conversely, dimensions of $d/h < d/h(R^*_{max})$ indicate decreased radiation by shortwave reductions from shading by the surrounding forest-cover.

As shown in Figure 7.3, R^*_{max} varies considerably throughout the October – June period, with pronounce differences evident with respect to site slope orientation. At the north-facing NG site, at which shortwave irradiance is least, R^*_{max} occurs in nearly completely closed gap openings (i.e. $d/h \rightarrow 0$), as longwave gains from surrounding canopy emissions exceed potential shortwave gains with larger gap openings. The small shortwave influence upon radiation at the NG is also evident by the insensitivity of $d/h(R^*_{max})$ and R^*_{max} at this site to changing snow albedo (α_s), especially during the mid-winter periods of low solar angles. By contrast, high shortwave irradiance to the south-facing SG site results in R^*_{max} for larger gap openings throughout the winter, punctuated by a pronounced increase in $d/h(R^*_{max})$ and R^*_{max} in late January when solar angles rise above the surrounding forest-cover allowing the penetration of direct-beam shortwave irradiance inside the gap. Similar, smaller increases in $d/h(R^*_{max})$ and R^*_{max} also occur at the NG and level LG sites, but are delayed until early spring as the orientation of these sites further away from the sun restricts earlier penetration of direct-beam irradiance.

During winter periods of low shortwave irradiance, increased R^* is generally promoted in smaller gap openings regardless of slope orientation as the surrounding forest-cover acts to minimise longwave losses to snow. However, as canopy-coverage is not complete by its partial transmittance of diffuse irradiance (i.e. τ_d), longwave losses from snow exceed longwave gains, resulting in a slightly negative R^* balance during this time. In the later spring, R^*_{max} is realised in smaller openings at the SG site relative to the other *gap* sites, as the direct penetration shortwave irradiance into the south-facing *gap* site permits a partial reduction in opening-size to increase longwave gains and maximise R^*. Alternatively, the sharp increase in $d/h(R^*_{max})$ at the NG site during the early spring results from the close balance between shortwave and longwave exchanges with changing gap opening-size on north-facing slopes. At the NG site, the long extinction pathlength through surrounding forest-cover created by the site's orientation away from the sun results in gap snow being largely shaded from shortwave irradiance during the early winter. However, upon solar elevations rising above the surrounding forest-cover in the spring, a sharp shift from longwave- to shortwave-dominated radiation occurs at the NG, but because of the north-facing slope of the site, requires a much greater opening-size than at the LG and SG to allow shortwave penetration inside the gap.

level *gap* site (LG):

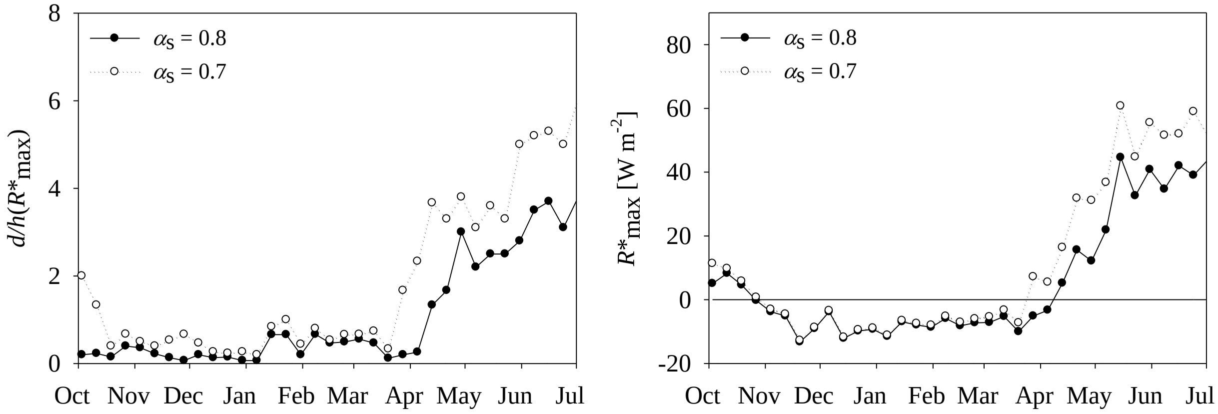

30˚ north-facing *gap* site (NG):

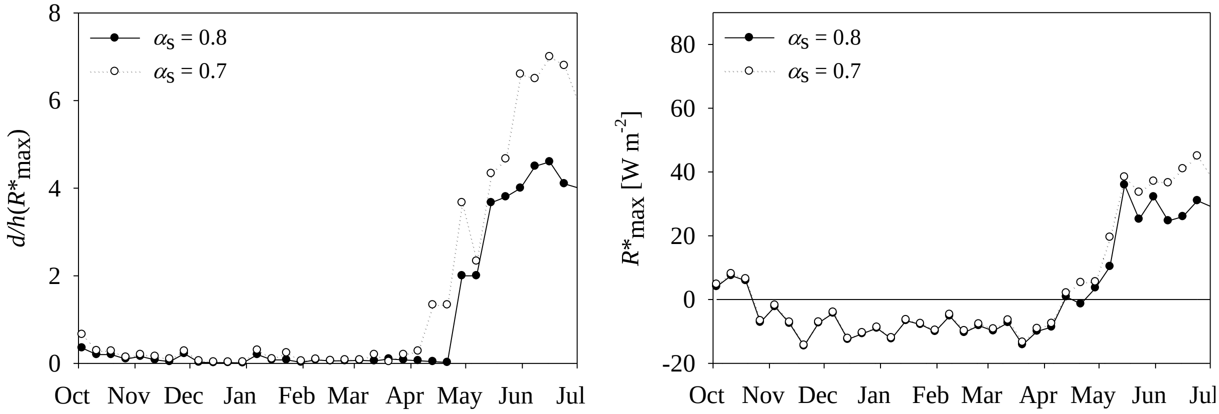

30˚ south-facing *gap* site (SG):

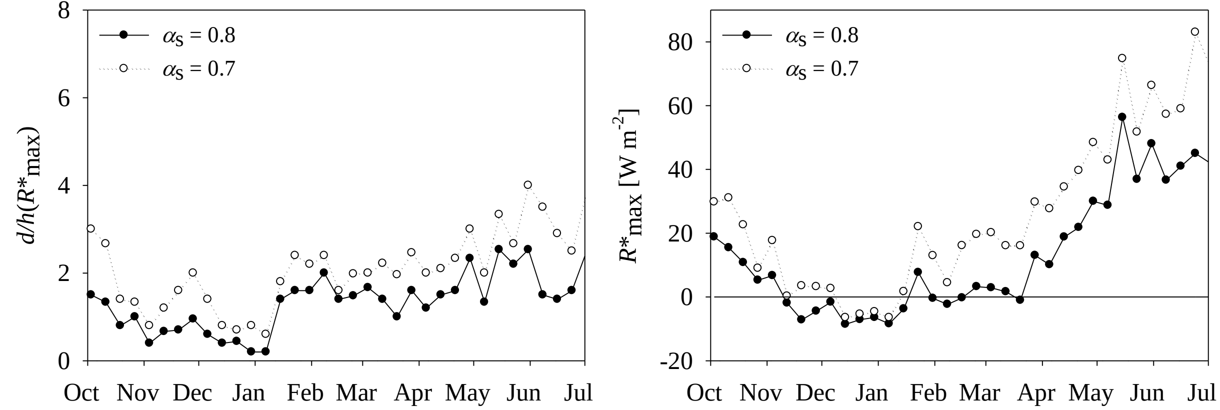

Figure 7. 3. Time series of the simulated maximum net radiation to snow (R^*_{max}) and the corresponding gap diameter/height dimension ($d/h(R^*_{max})$) for snow albedo (α_s) of 0.8 and 0.7 at a hypothetical level *gap* site (LG), a *gap* site on a 30˚ slope of north-facing aspect (NG), and a *gap* site on a 30˚ of south-facing aspect (SG) for the period of October 2007 – July 2008.

7.5. Simulation of snow accumulation and melt in *open*, *forest*, and *gap* sites

Through coupling of irradiance simulations in *open*, *forest*, and forest *gap* sites to the mass- and energy-balance routines within CRHM, this section examines forest-cover impacts on snow accumulation and melt through simulations at each site with the following added descriptions:

(i) *Open* sites: no canopy-cover; thus, no snow accumulation losses are incurred from canopy interception of snowfall or rainfall.

(ii) *Forest* sites: site under continuous canopy-cover of a diffuse transmittance (τ_d) equal to 0.2, intended to represent the dense canopy cover of high-elevation spruce stands. This τ_d value also closely approximates the mean forest sky view factor (v), as determined from analysis of hemispherical photographs acquired in various spruce stands in the MCRB. Thus, assuming $v \approx \tau_{d,}$ the parameterisation of the leaf area index effective for snow and rain interception ($LAI`$) is made by the following rearrangement of Pomeroy et al.'s (2002) relation:

$$LAI` = e^{-\frac{(v-0.45)}{0.29}} \quad \textbf{(7.9)}$$

(iii) *Gap* sites: composed of a circular forest clearing of equal diametre and height (i.e. $d/h = 1$). The *gap* site opening is considered to be sufficient width to allow for direct snowfall to the ground surface (i.e. no forest interception) while small enough to prevent substantial wind penetration to snow within the clearing. As such, precipitation inputs to *gap* sites are considered equal to that of *open* sites, and wind speeds equal to that in the *forest* sites.

The above *open*, *forest*, and *gap* sites are defined as such to generally represent the physical environment of: (i) the large Cabin Creek clear-cuts, (ii) undisturbed forest-cover, and (iii) the small forest clear-cuts along the Twin Creek tributaries within the MCRB. At each of the *open*, *forest*, and *gap* sites, the basic model configurations for the linking of irradiance determinations to the snow accumulation and melt modules in CRHM are shown in Figure 7.4.

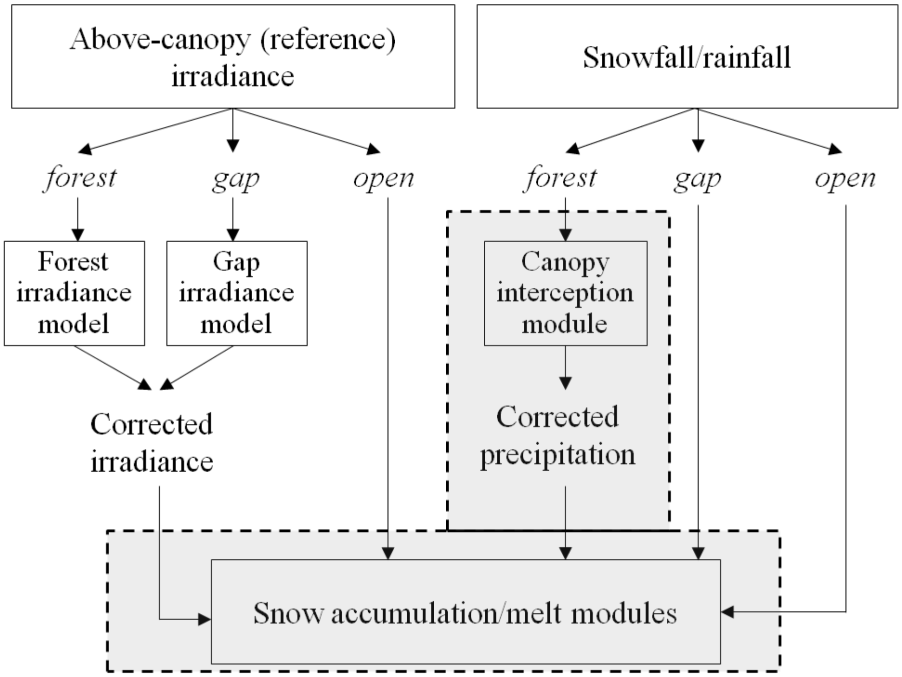

Figure 7. 4. Model configurations for determination of snow accumulation and melt at *open*, *forest*, and *gap* sites showing the linking of the irradiance simulations to the snow accumulation/melt modules in the Cold Regions Hydrological Model (CRHM). CRHM modules are shown in grey dashed outlines.

Similar to that for irradiance determinations in Section 7.3, the influence of slope orientation on snowmelt at *open*, *forest*, and *gap* sites are assessed through separate simulations to a level surface, a north-facing slope, and a south-facing slope. To examine forest-cover effects on snowmelt under realistic meteorological conditions, simulations are performed using hourly meteorological forcing data collected at the LSC reference sites over the period of October 2007 – July 2008 (Figure 7.5). Here, the correction of wind speed for forest sheltering effects is made through the rearrangement of Hellström's (2000) relation (Chapter 5, Eq. 5.24).

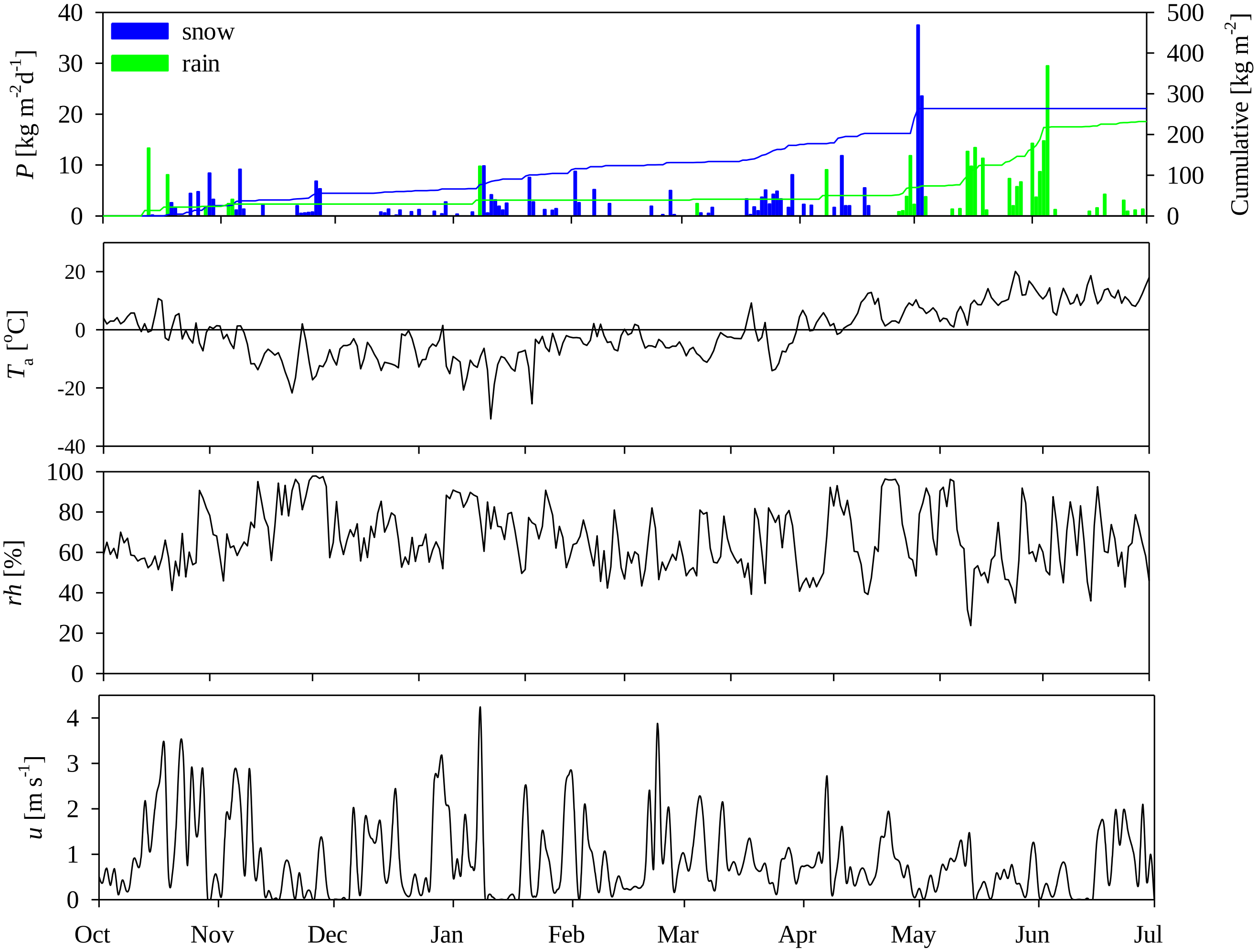

Figure 7. 5. Meteorological conditions for the simulation period of October 2007 – July 2008 showing daily snowfall and rainfall precipitation (P), air temperature (T_a), relative humidity (rh), and wind speed (u) as observed at the Level Spruce Clearing reference site (LSC). Note that snowfall and rainfall precipitation are divided by an air temperature threshold of 0 °C.

7.5.1. Comparison of irradiance between *open, forest,* and *gap* sites

Following the procedures outlined in Section 7.3, shortwave irradiance (K_{in}), longwave irradiance (L_{in}), and all-wave irradiance (R_{in}) were simulated to *open*, *forest*, and *gap* sites of the following slope orientations: (i) level topography, (ii) a 30˚ slope of north-facing aspect, and (iii) 30˚ slope of south-facing aspect. Simulated K_{in} and L_{in} for all site-topography combinations over the October – July period are shown in Figure 7.6, with irradiance totals over the period compared in Figure 7.7. Evident in both figures are the marked differences in K_{in} among the differing sites types and slope orientations, with greatest radiation at the south-facing *open* site, and least in the north-facing *forest* site. Compared to *open* and *gap* sites, large shortwave reductions occur under forest-cover irrespective of topography, giving only small differences in R_{in} among *forest* sites of opposing slope orientations, and resulting in R_{in} being dominated by longwave exchanges. By contrast, increased K_{in} produces a much greater topographical variation in R_{in} between the *open* sites, with even greater differences between opposing *gap* slopes due to the extremely low shortwave irradiance inside the north-facing *gap* site (Figure 7.6). Although shortwave reductions at the *forest* sites are partially offset by longwave gains from canopy emissions, total R_{in} over the winter-spring period remains considerably less under forest-cover than in the *open* and *gap* sites (Figure 7.7). Alternatively, the slight offsetting among shortwave and longwave totals between *open* and *gap* sites results in similar overall R_{in} magnitudes at these sites over the period.

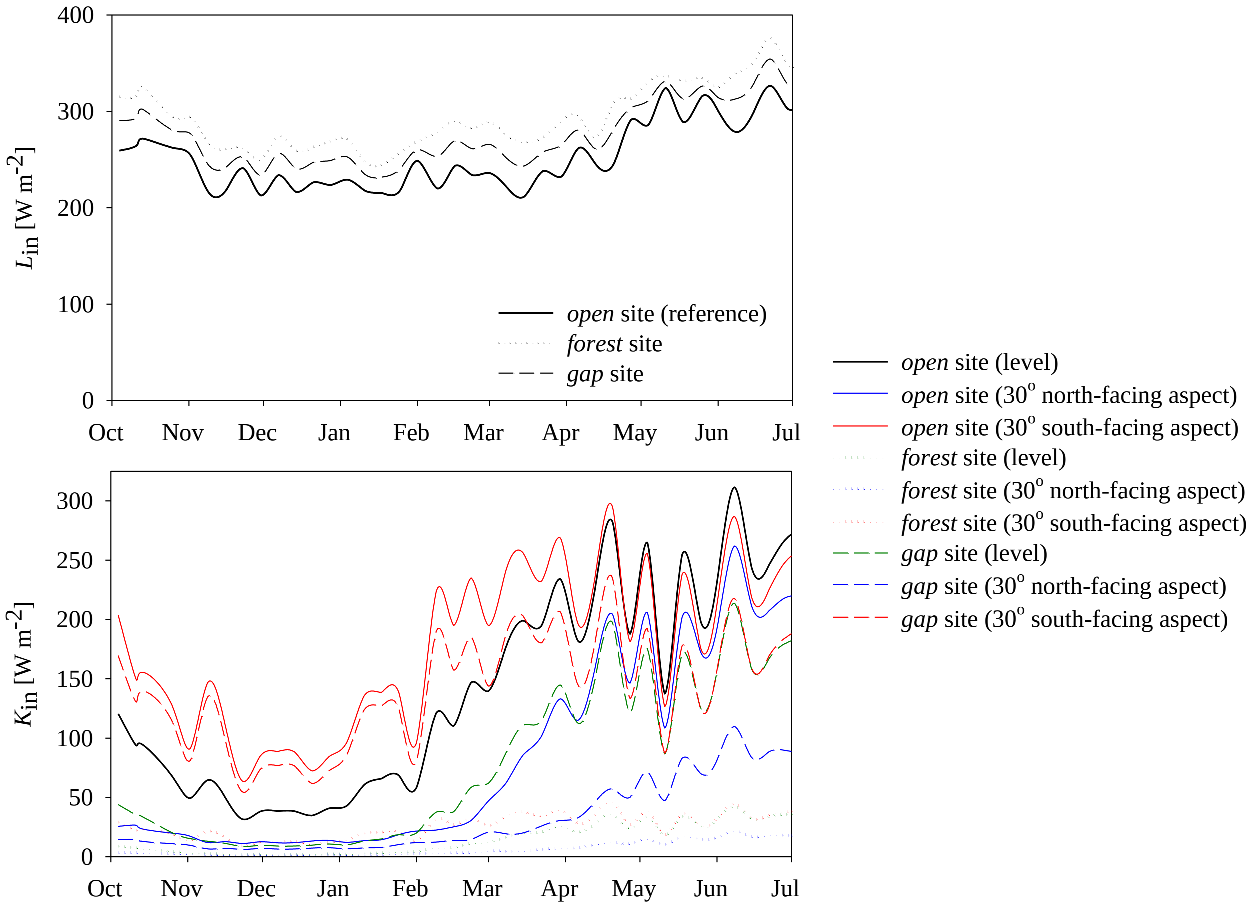

Figure 7. 6. Simulated weekly shortwave irradiance (K_{in}) and longwave irradiance (L_{in}) at *open*, *forest*, and *gap* sites of level topography, a 30˚ slope of north-facing aspect, and a 30˚ slope of south-facing aspect for the period of October 2007 – July 2008.

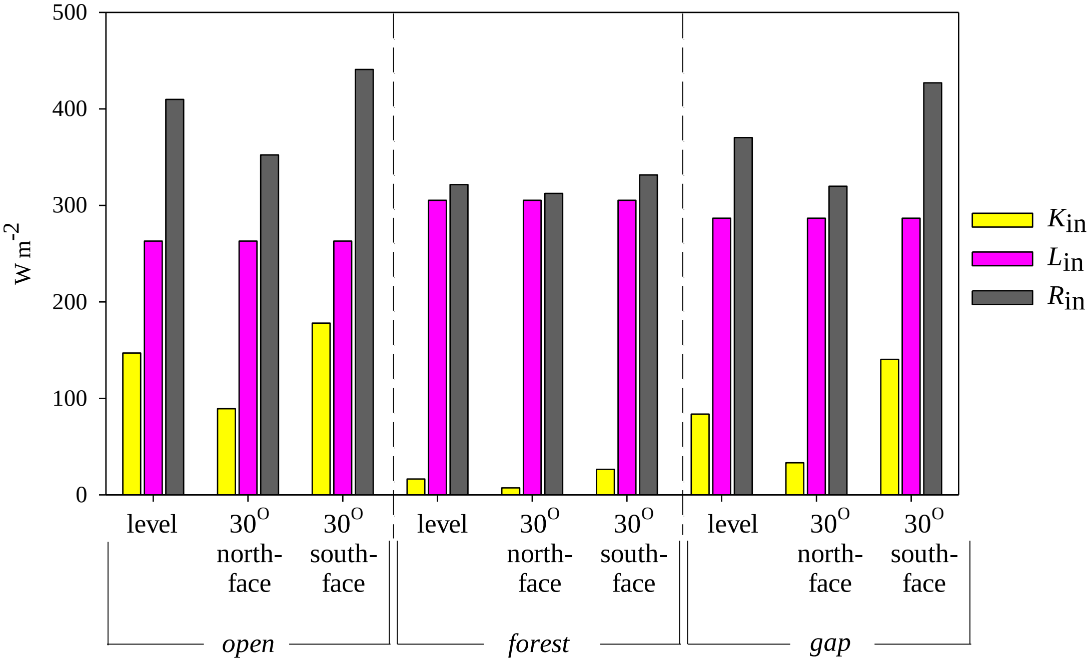

Figure 7. 7. Mean shortwave irradiance (K_{in}), longwave irradiance (L_{in}), and all-wave irradiance (R_{in}) simulated at *open*, *forest*, and *gap* sites of level topography, a 30˚ slope of north-facing aspect, and a 30˚ slope of south-facing aspect over the period of October 2007 – July 2008.

As seen by the time series meteorological observations of Figure 7.5, snowfall is generally evenly distributed throughout the winter and early-spring of 2007-08, followed by a large snowfall event in early May. This snowfall pattern is reflected in the simulated snow accumulation at all sites, with steadily rising winter accumulations punctuated by a marked increase corresponding to the May snowfall event (Figure 7.8). Evident however, are the marked reductions in snow accumulation determined at the *forest* sites, which from interception losses are nearly half those at the *open* and *gap* sites. Under forest-cover, the already small shortwave differences between opposing slopes is further reduced by shortwave reflection from snow, acting to elevate Q_L contributions to Q_M at all the *forest* sites. Consequently, the similar magnitudes of longwave-dominated Q_M under forest-cover produce a close synchronisation in snowmelt timing among the sloped *forest* sites. Here, rapid sub-canopy melt is facilitated by the large Q_L gains received when air (and canopy) temperatures warm above freezing, resulting in canopy longwave emissions exceeding snowcover longwave losses which are constrained by maximum radiating temperature of 0 ˚C.

In contrast to the *forest* sites, a pronounced de-synchronisation in snowmelt timing is observed between the opposing *open* and *gap* site slopes. This divergence reflects the large variation in the magnitude and composition of Q_M between the *open* and *gap* site slopes (Figure 7.8). Here, the high shortwave melt energy (Q_K) at the south-facing *open* and *gap* slopes are sufficient to facilitate substantial early snowmelt during the late-winter and early-spring periods. Alternatively, the low shortwave gains and decreased Q_M at the north-facing *open* and *gap* sites results in delayed melt relative to the north-facing *forest* site where increased sub-canopy Q_M is provided by canopy longwave emissions. Overall however, snowmelt is latest at the north-facing *gap* site where the small shortwave gains from surrounding forest-cover shading combined with longwave losses to the atmosphere result in a large negative snowpack energy balance. This energy deficit is sufficient to delay snowmelt in the north-facing *gap* site until late-spring, when it is finally overwhelmed by longwave gains from surrounding forest-cover emission with warming air and canopy temperatures.

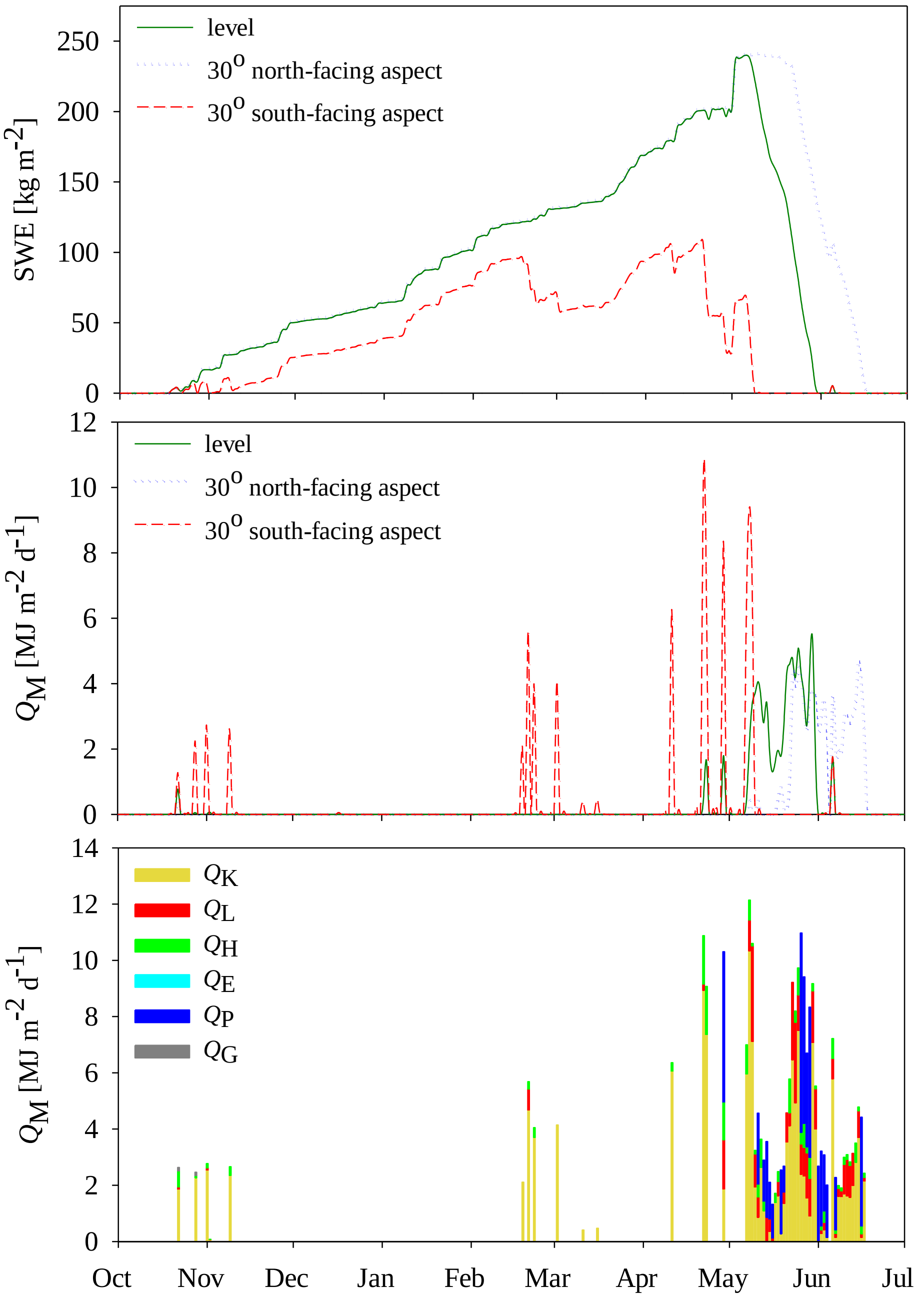

Figure 7.8. *open* sites (see complete figure caption below).

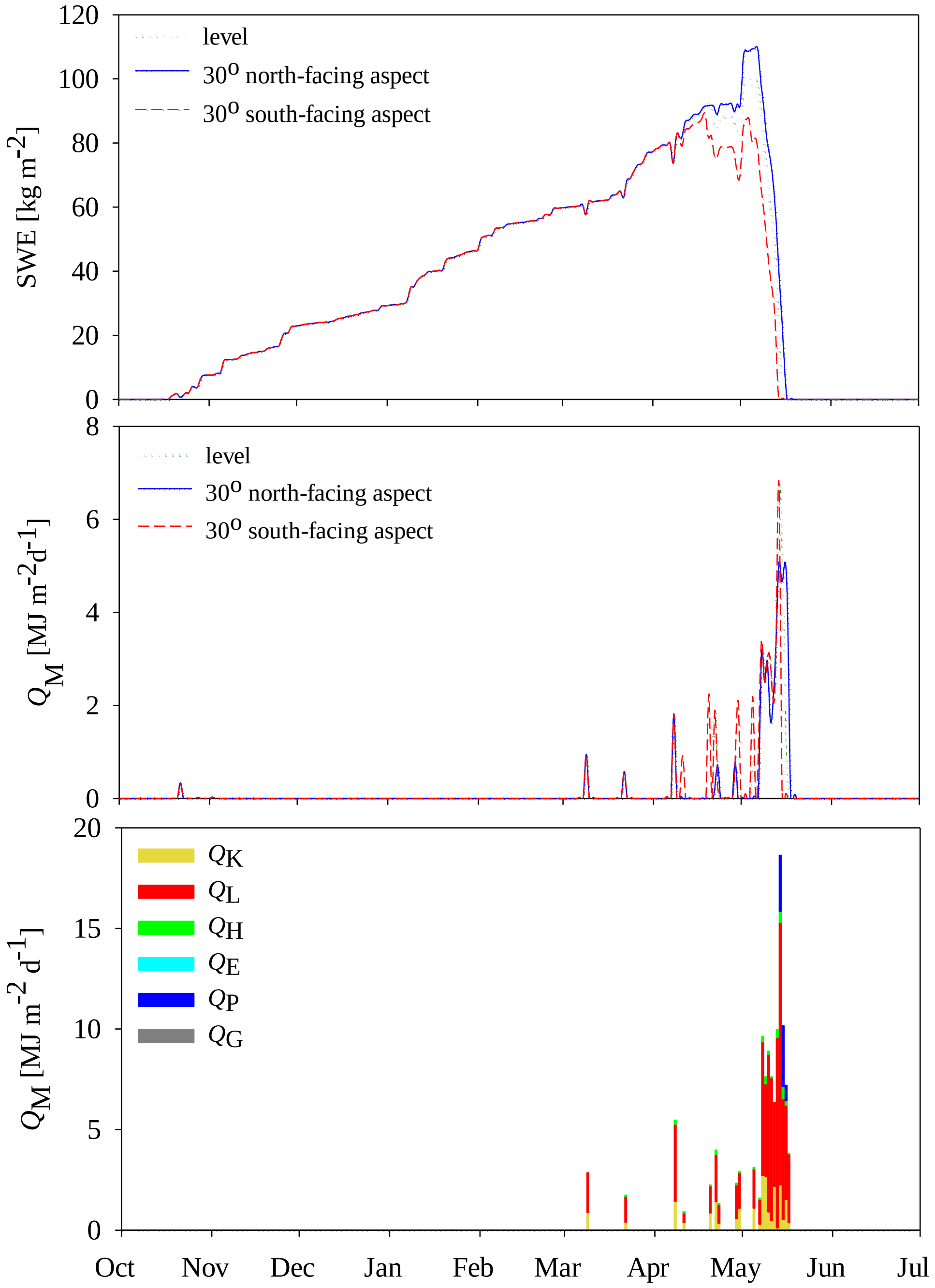

Figure 7.8. *forest* sites (see complete figure caption below).

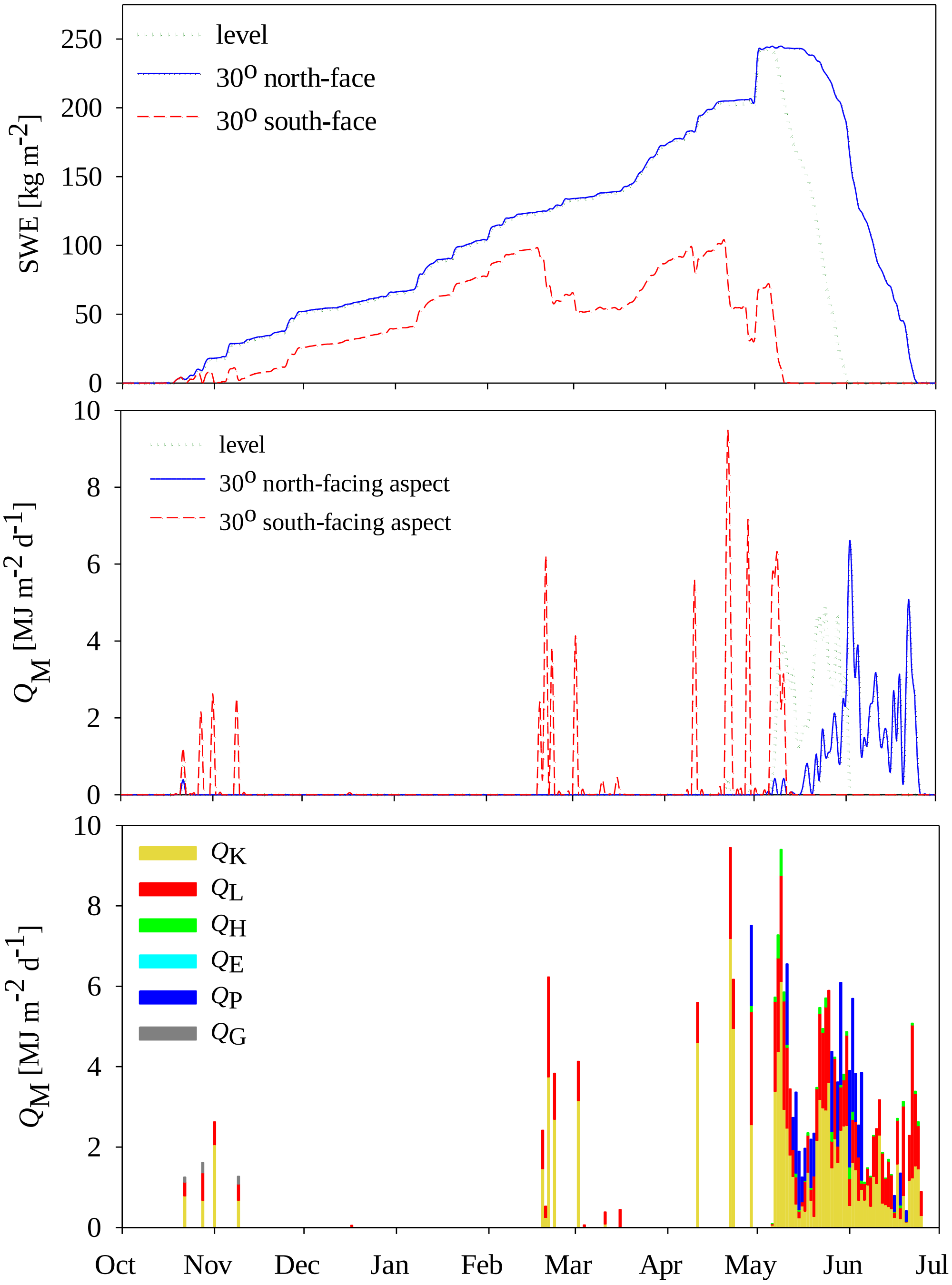

Figure 7.8. *gap* sites (see complete figure caption below).

Figure 7. 8. Simulated snow water equivalent (SWE) and snowmelt energy (Q_M), including contributions from shortwave radiation (Q_K), longwave radiation (Q_L), sensible heat (Q_H), latent heat (Q_E), advection from precipitation (Q_P), and ground heat (Q_G) at *open*, *forest*, and *gap* sites of: level topography, a 30° south-facing aspect, and a 30° north-facing aspect for the period of October 2007– July 2008.

7.5.2. Additional simulations: 2006-07 and 2008-09 winter seasons

To examine the influence of varying seasonal meteorological conditions on snowmelt at the *open*, *forest*, and *gap* sites, additional simulations were performed for the above site-topography combinations over the same seasonal period of 2006-07 and 2008-09, of which the meteorological conditions are shown in Figure 7.9. However, unlike that for the 2007-08 season, snowmelt at the *open*, *forest*, and *gap* sites of varying topography are shown in terms of the percentile of total snowmelt completed throughout the each season (Figures 7.10 and 7.11) and the corresponding snowmelt energy balances at each site.

In general, both the 2006-07 and 2008-09 simulations show similar snowmelt patterns at the respective *open*, *forest*, and *gap* sites to that for the 2007-08 season, with a substantial de-synchronisation of melt timing between the opposing *open* and *gap* site slopes. Among the *open* slopes, a gradient from high to low shortwave contributions toward snowmelt energy (i.e. Q_K) is evident moving from south-facing to north-facing slopes, which are countered by increasing contributions from longwave radiation (i.e. Q_L). This reversal among shortwave and longwave contributions crossing from south-facing to north-facing *open* slopes is even more pronounced between opposing *gap* slopes due to very low shortwave gains at the north-facing *gap* site where again, snowmelt is most delayed. Also similar to the 2007-08 season are the substantial reductions in forest snow accumulations over the 2006-07 and 2008-09 seasons incurred by canopy interception losses, with peak *forest* site accumulations approximately half that in the *open* and *gap* sites. Again, a marked synchronisation in snowmelt timing between the *forest* slopes occurs by consequence of the similar and large longwave contributions to Q_M at these sites, which upon air and canopy temperatures warming above freezing translate into rapid melt of the shallow forest snowpack.

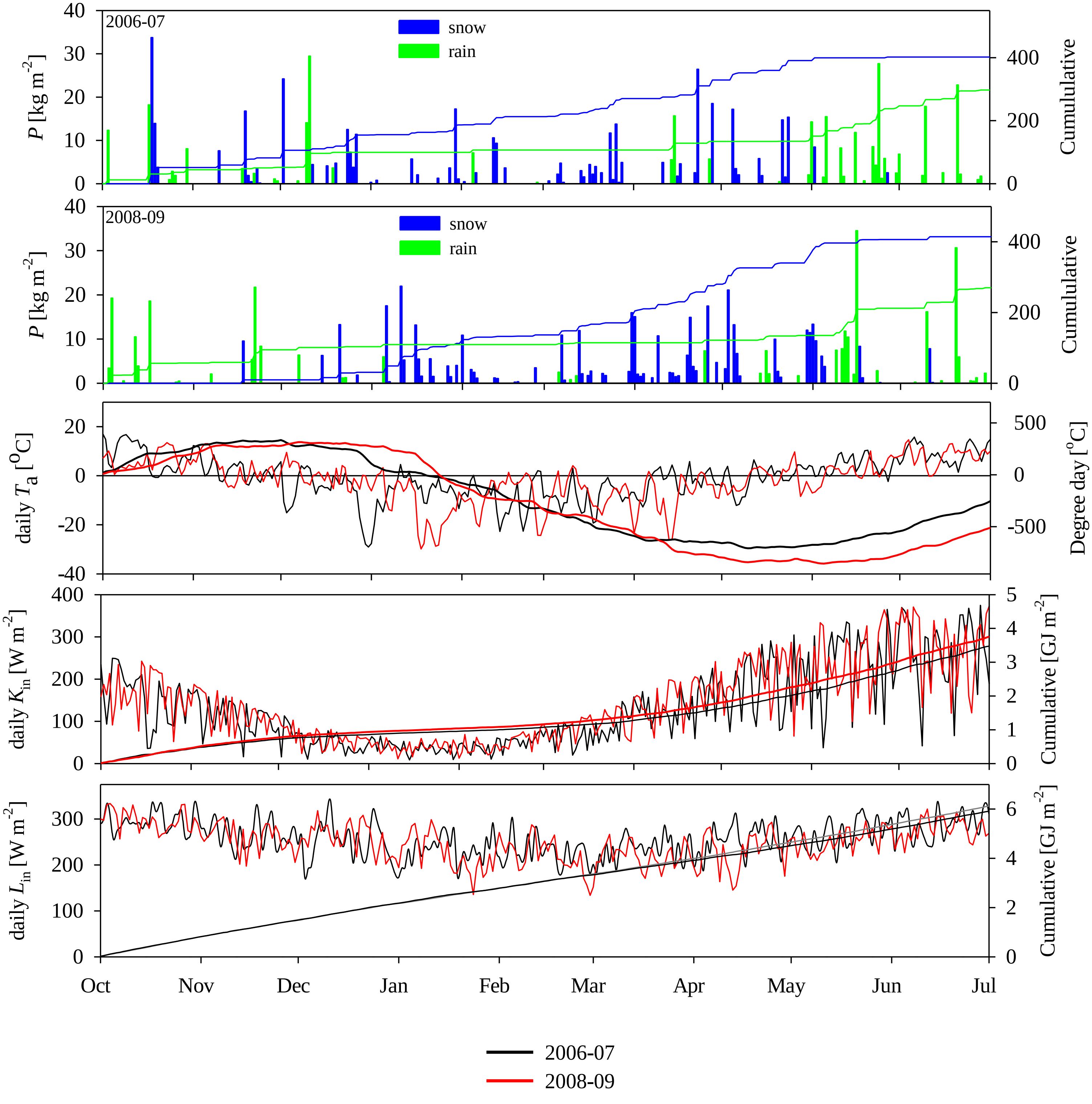

Figure 7. 9. Meteorological conditions over the 2006-07 and 2008-09 October–July periods observed at the Level Spruce Clearing (LSC) reference site. Cumulative amounts throughout each period are shown for comparison of seasonal totals.

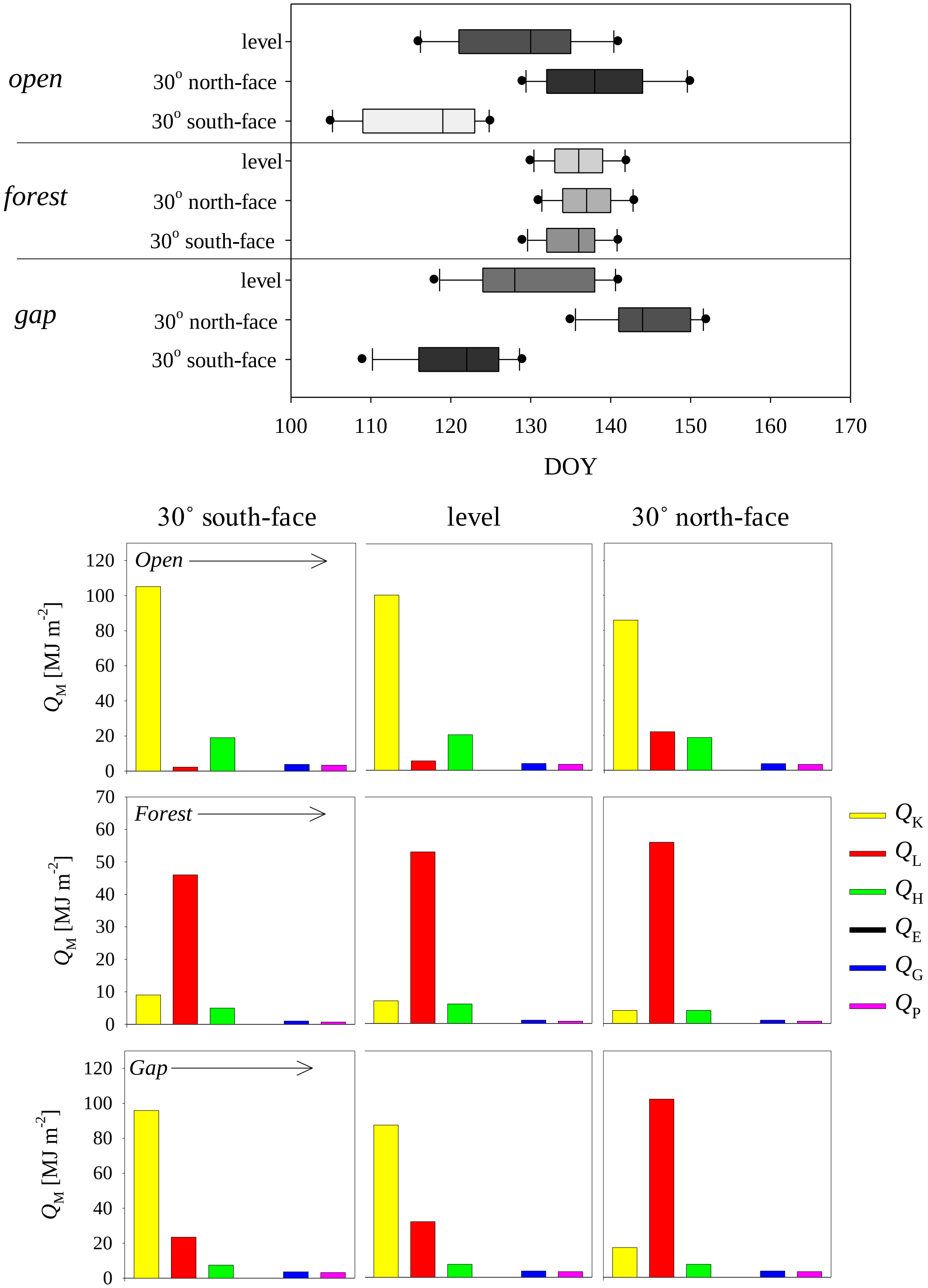

Figure 7. 10. Percentile of total snowmelt at *open*, *forest*, and *gap* sites of level, north-facing, and south-facing slope orientation over the 2006-07 season (top), and corresponding snowmelt energy balances for each site-topography combination (bottom). First dot, first whisker, left box edge, middle line, right box edge, last whisker, and last dot correspond to the 5th, 10th, 25th, median, 75th, 90th and 95th percentiles of total snowmelt.

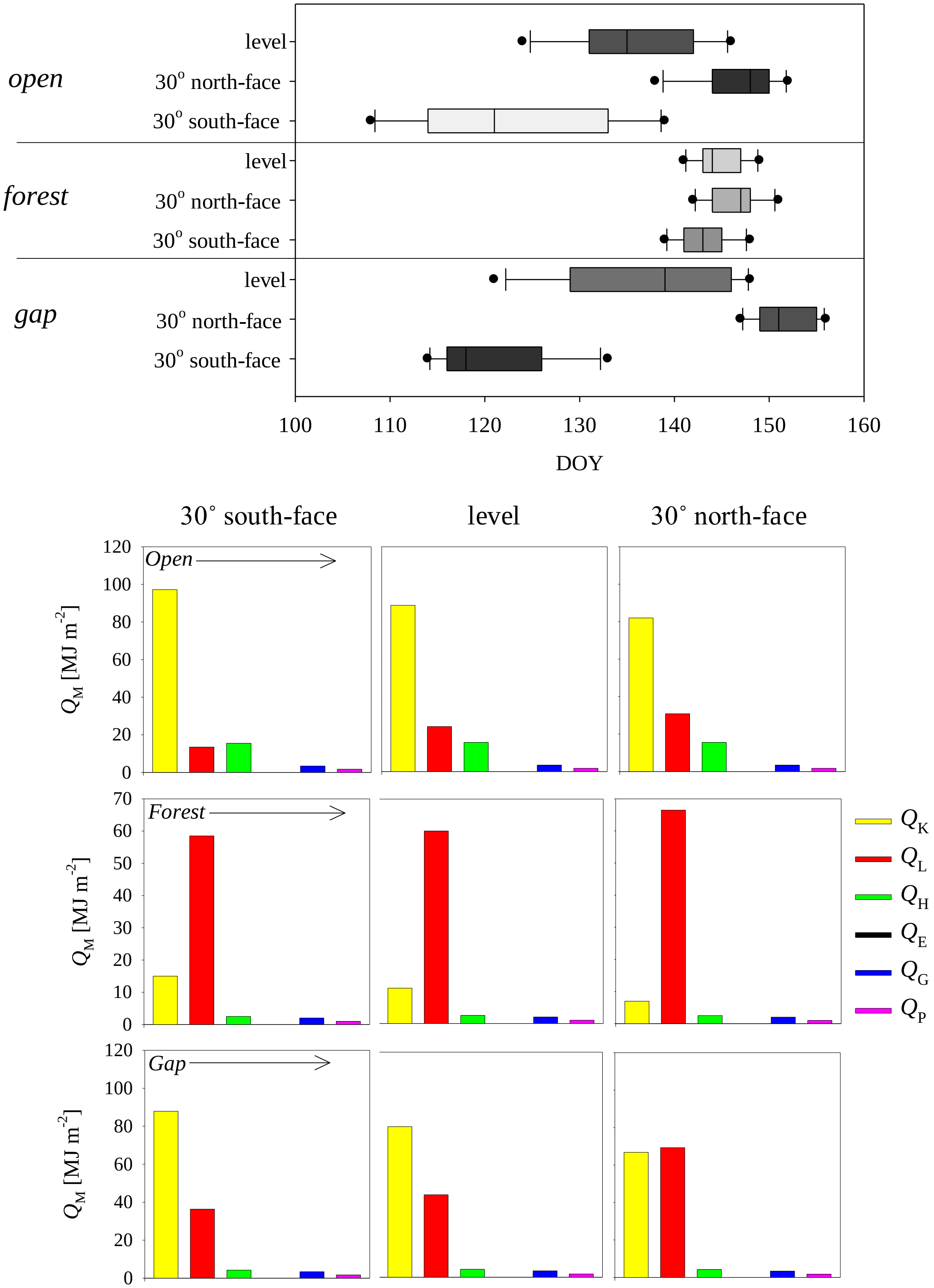

Figure 7. 11. Percentile of total snowmelt at *open*, *forest*, and *gap* sites of level, north-facing, and south-facing slope orientation over the 2008-09 season (top), and corresponding snowmelt energy balances for each site-topography combination (bottom). First dot, first whisker, left box edge, middle line, right box edge, last whisker, and last dot correspond to the 5th, 10th, 25th, median, 75th, 90th and 95th percentiles of total snowmelt.

7.6. Snowmelt sensitivity to meteorological conditions

One advantage particular to physically-based modelling approaches is the ability to examine how physical processes such as snowmelt respond to changes in meteorology or physical site characteristics. Here, a sensitivity analysis is conducted assessing the response of snowmelt timing and melt energetics to prescribed shifts in air temperature and snow albedo (α_s). Simulations are made for the same nine site-topography combinations described in previous sections of this chapter, under meteorological conditions observed over the 2006-07 and 2008-09 seasons with the following modifications:

(i) a systematic shift in air temperature of ±1 ˚C, ±2 ˚C, and ±3 ˚C relative to observed temperatures, and

(ii) an adjustment in snow albedo (α_s) of ±0.02, ±0.04, and ±0.06 relative to that simulated for unaltered (i.e. observed) meteorological conditions over the respective 2006-07 and 2008-09 seasons. As such, changes in α_s values are intended not only to represent explicit albedo effects on shortwave radiation to snow, but also varying shortwave irradiance (K_{in}) from cloud cover effects, etc.

For the above adjustments, resulting shifts in simulated snowmelt timing and corresponding melt energy contributions are shown in terms of the timing of the median snowmelt value throughout the 2006-07 season (Figure 7.12) and the 2008-09 season (Figure 7.13). As seen for both seasons, snowmelt timing is most sensitive to snow albedo (α_s) changes at the south-facing *open* and *gap* site slopes, with much smaller melt responses to α_s at the corresponding north-facing sites. As expected, this occurs as albedo adjustments affect Q_K gains to snow, resulting in higher topographical variation in snowmelt timing between opposing *open* and *gap* slopes with lower α_s.

Alternatively, adjustments in air temperature have the greatest impact on snowmelt at the *forest* sites, which is attributed changes in longwave emissions from the canopy, but also the shallower sub-canopy snowpack being more sensitive to energy changes compared to the deeper *open* and *gap* snowpacks. At the *open* and *gap* sites, only modest effects on snowmelt timing result from air temperature deviations; however, unlike that from snow albedo adjustments, changes occur through shifts of multiple snowmelt energy terms. Adjustments in air temperature also indirectly influence shortwave melt energy at all sites by modifying snow albedo through a change in the number and duration of snowmelt events throughout the season as defined by snow temperature. In the *open* sites where wind speeds are greatest, air temperature variations translate into moderate shifts in melt contributions from sensible heat exchange, with relatively small shifts at the wind-sheltered *forest* and *gap* sites. Changes in snowmelt energy from rainfall advection with warmer air temperatures are most marked at the *open* and *gap* sites where a greater amount of warmer rainfall fell directly to snow.

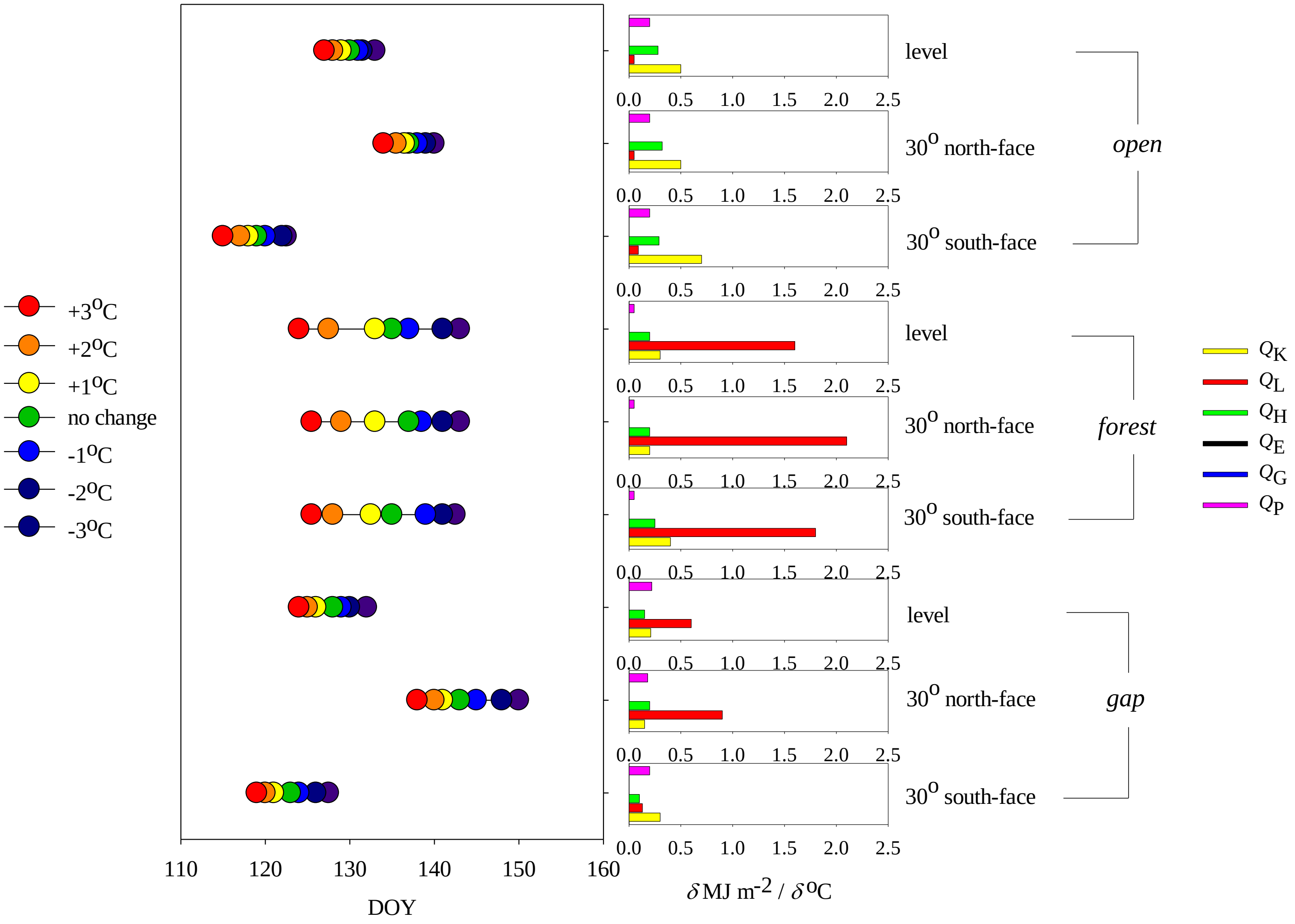

Figure 7.12. Response in snowmelt timing and energy to air temperature changes (2006-07) (see complete figure caption on next page).

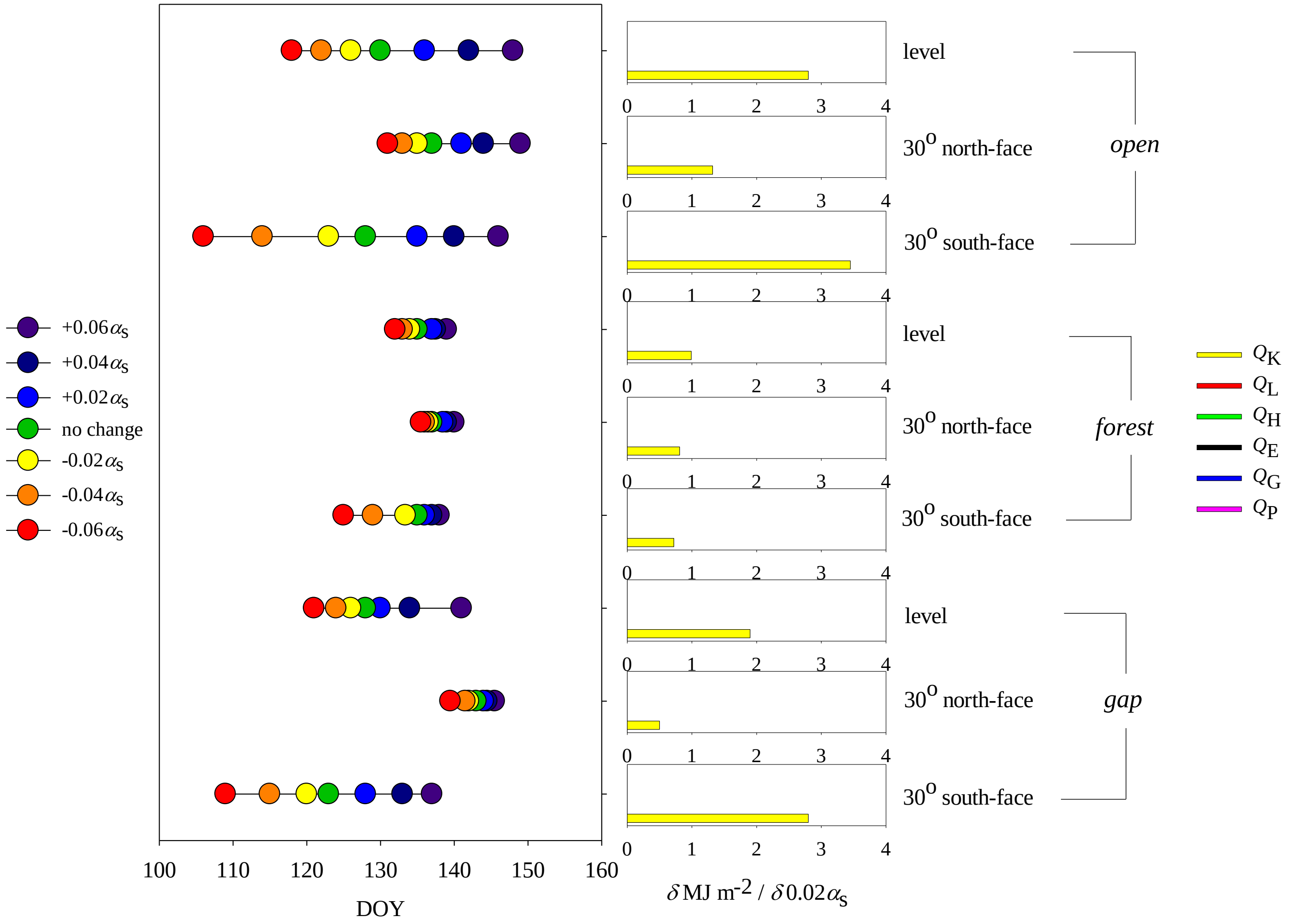

Figure 7. 12. Day of the median snowmelt value (left) and corresponding change in melt energy contributions (right) to adjustments in seasonal air temperature (previous page), and snow albedo (α_s) (this page) at *open*, *forest*, and *gap* sites of level, north-facing, and south-facing topography over the 2006-07 spring snowmelt period. Snowmelt timing at each site is expressed in terms of the day of year (DOY) corresponding to the median percentile of total snowmelt over the period.

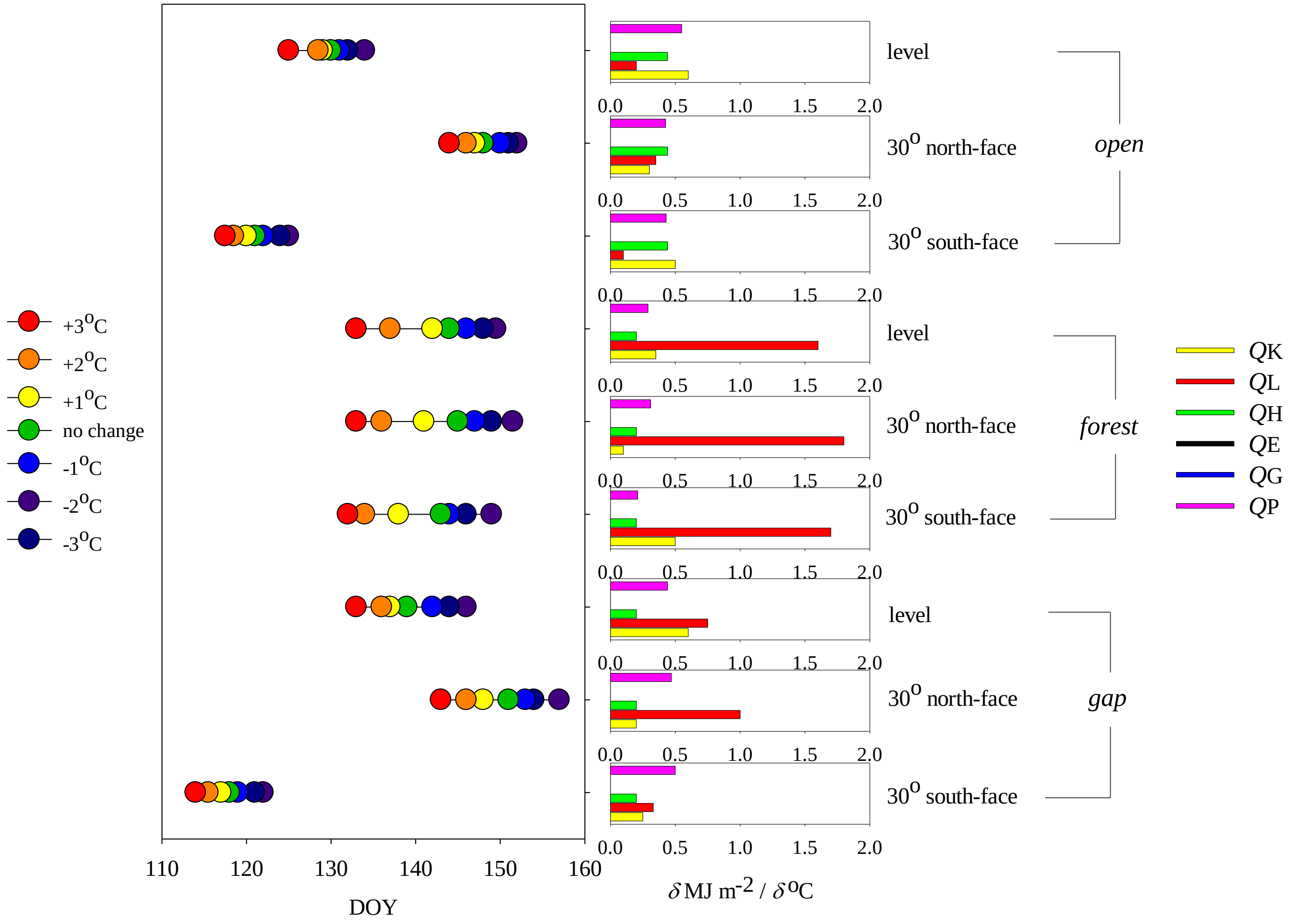

Figure 7.13. Response in snowmelt timing and energy to air temperature changes (2008-09) (see complete figure caption on next page).

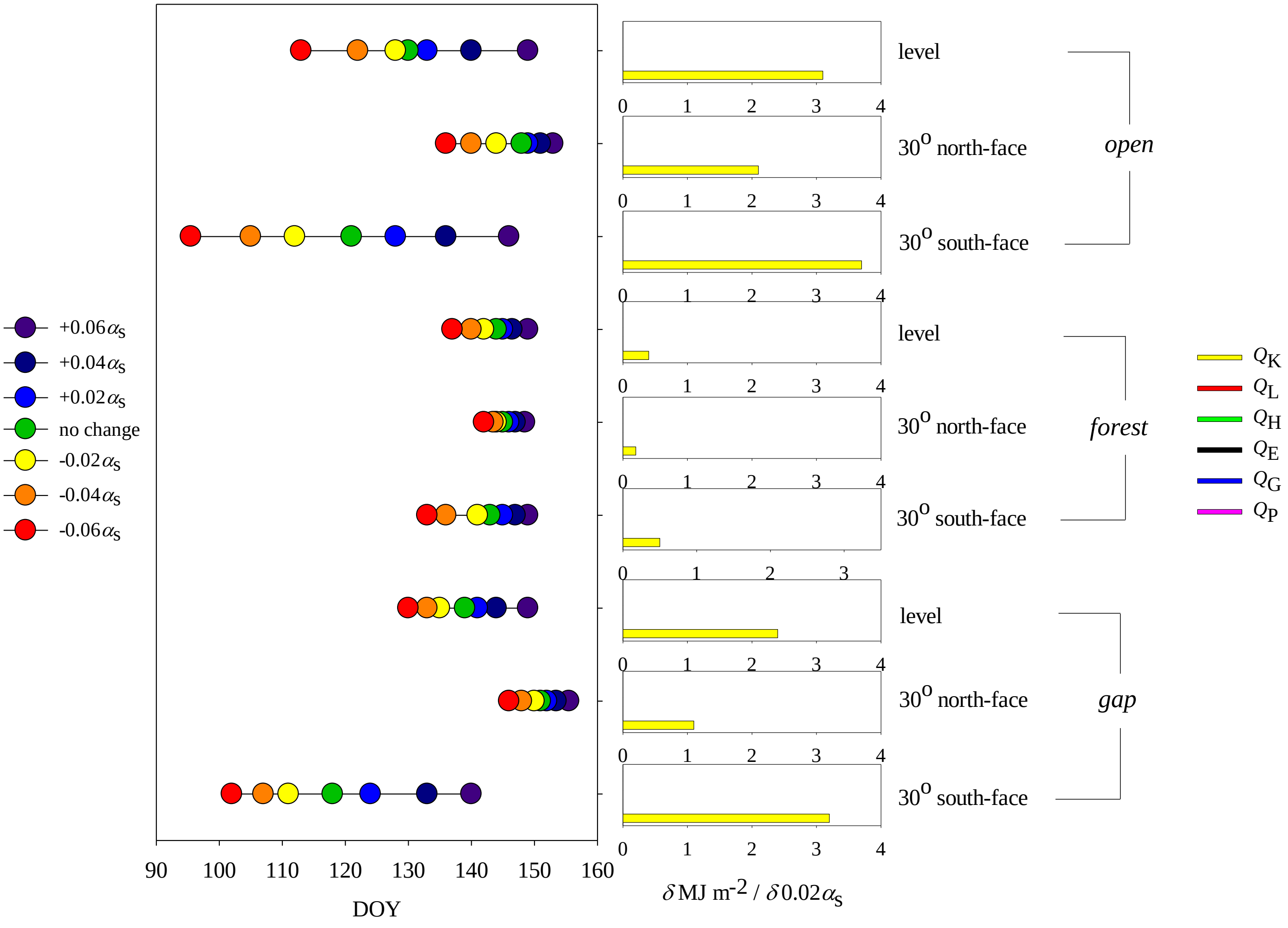

Figure 7. 13. Day of the median snowmelt value (left) and corresponding change in melt energy contributions (right) to adjustments in seasonal air temperature (previous page), and snow albedo (α_s) (this page) at *open*, *forest*, and *gap* sites of level, north-facing, and south-facing topography over the 2008-09 spring snowmelt period. Snowmelt timing at each site is expressed in terms of the day of year (DOY) corresponding to the median percentile of total snowmelt over the period.

7.7. Model application: determination of snowmelt across a mountain headwater basin

To provide a practical illustration of potential forest-cover effects on snowmelt across mountain terrain, simulations of snow accumulation and melt were made for varying configurations of landcovers composed of *open*, *forest*, and *gap* site types across the Twin Creek and Middle Creek sub-basins of the MCRB. This area was selected as it consists mostly of opposing north-facing and south-facing slopes, allowing an assessment of how differing combinations of forest-cover structure and topographic orientation impact the magnitude and timing of snowmelt. For this assessment, the sub-basin was divided into 6 separate topographically-based landscape units (LU), half of which are grouped as *north-facing LUs* (LUs 1, 3, 5) and the other half as *south-facing LUs* (LUs 2, 4, 6); all of which encompass the contiguous forest-cover of the Middle Creek and Twin Creek sub-basins. The classified LUs are shown within the MCRB in Figure 7.14, with basic descriptions of the area and topography of each given in Table 7.1. To simplify the modelling approach, a single slope and aspect value was assigned to each LU as defined by the mean value derived from a 1 m^2 resolution digital elevation model. Note that the degree of actual variation in slope and aspect within each LU is also quantified in Table 7.1 in terms of the standard deviation of all 1 m^2 grid cell values.

For the model application, one of the *open*, *forest*, or *gap* site landcovers was assigned to either the north-facing or south-facing LU groupings, giving a total of 9 possible landcover configurations over the sub-basin. Assigned landcover types are similar to those defined in the point-scale (i.e. ‘site’) simulations, comprised of the respective physical characteristics of the *open*, *forest*, and *gap* site types. However, in the aim of providing a more realistic representation of snow accumulation and melt at the landscape scale, site types for point-scale simulations are modified to give the following corresponding *landcover* types:

(i) *Open landcover*: potential snow accumulation losses may occur via sublimation losses from blowing snow, which are estimated by the blowing snow sublimation routines within CRHM developed by Pomeroy et al. (1993). Wind speeds within the *open* landcovers units (LUs) are approximated from observations collected at an open alpine location (Fisera Ridge) (indicated by star symbol in Figure 7.14). Although substantial wind redistribution of snow would be expected between adjacent *open* LUs, redistribution is restricted for simulations to examine landcover change impacts on snowmelt solely from snow accumulation and snowmelt energy effects.

(ii) *Forest landcover:* canopy-cover density in the *forest* LUs is specified the same as that for site point-scale simulations (Section 7.5.2), having a forest sky view factor (v) of 0.2 and corresponding effective leaf area index for snow interception (LAI`) of 2.1.

(iii) *Gap landcover*: to approximate the Twin Creek forest treatment, *gap* LUs are subdivided into *forest sites* and *gap* sites (*d/h* = 1) at a respective areal weighting of 60 % and 40 % (Beckstead. and Veldman, 1985). As such, snow accumulation and snowmelt within *gap* LUs are determined as the areal-weighted mean of *forest* and *gap* site snowmelt.

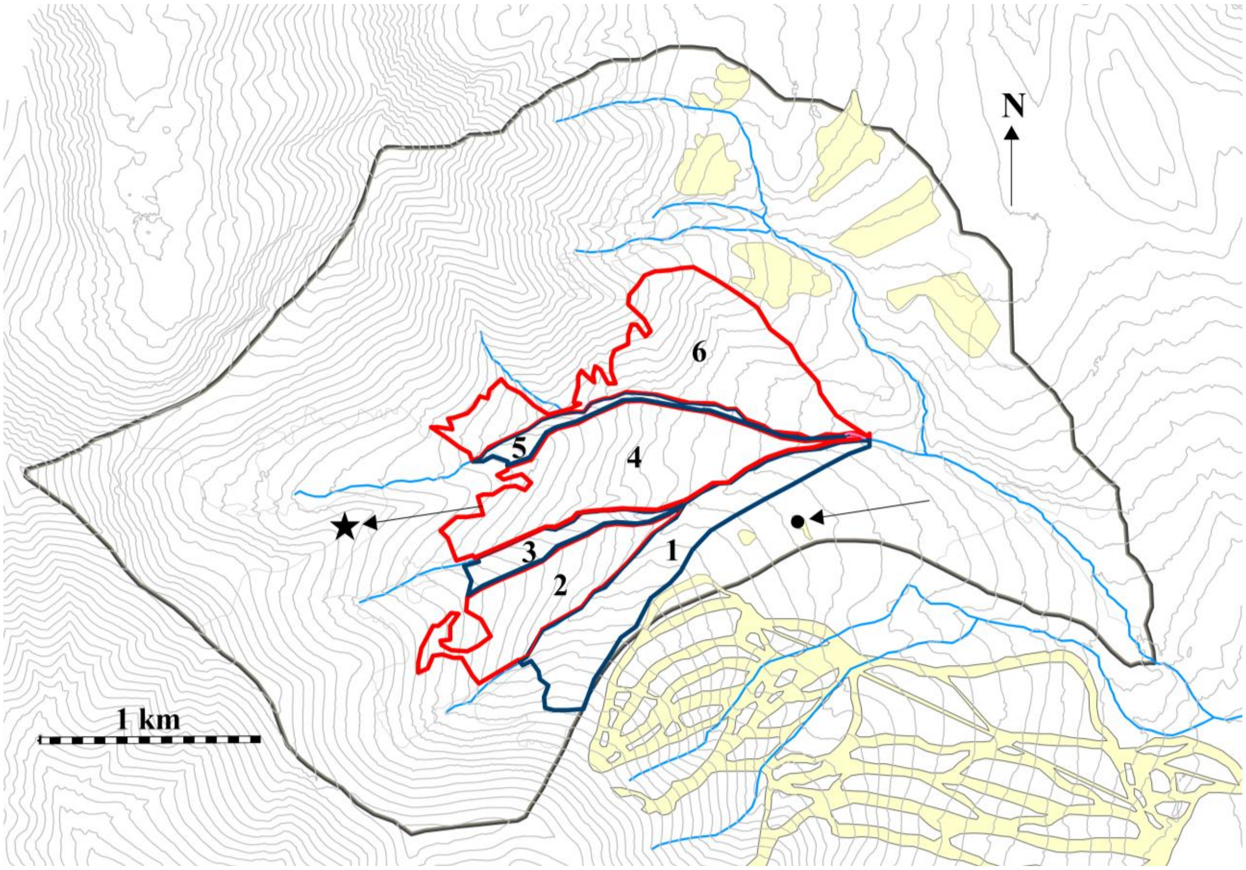

Figure 7. 14. Map showing the six landscape units (LU) as defined by forest-cover extend and topography along the Middle Creek tributary (LU 5 – 6) and the Twin Creek tributaries (LU 1 – 4) within the MCRB. Classified north-facing LUs are outlined in blue and south-facing LUs in red. The location of the Level Spruce Clearing (LSC) meteorological reference site is shown by the black dot, with the location of the open alpine wind speed observations (i.e. Fisera Ridge site) shown by the star symbol.

For each the *open*, *forest*, and *gap* landcover types assigned to the south-facing or north-facing LU groups, determinations of snow accumulation and melt were made using meteorological forcing data over the 2006-07 and 2008-09 seasons. Due to the higher elevation of all LUs relative to the LSC meteorological reference location, precipitation inputs to each LU were adjusted by a seasonally-averaged lapse rate of 0.063 mm km^{-1} established from precipitation observations within the MCRB. Determination of snowmelt across the entire sub-basin was made by the areal-weighted mean of snowmelt among all LUs, which are shown for each of the 9 landcover configurations in terms of cumulative snowmelt throughout the 2006-07 and 2008-09 spring melt seasons in Figure 7.15. Additional statistics describing snow accumulation and snowmelt for each landcover configuration over both seasons is given in Table 7.2.

Overall, a substantial variation in both the total amount and timing of snowmelt is evident for the differing landcover configurations, with greater total snowmelt obtained under progressively decreasing forest-cover (i.e. *forest→gap→open* landcovers) due to the greater winter snow accumulations in the more open landovers. However, differences in peak snow accumulations and total snowmelt between *open* and *forest* landcover types are reduced by sublimation losses in the *open* landcovers, equalling roughly 19 % and 22 % of total snow accumulation for the respective 2006-07 and 2008-09 winters.

Alongside differences in total snowmelt quantity, Figure 7.15 also illustrates the substantial variations in snowmelt timing provided by differing landcover configurations over the sub-basin. For both the 2006-07 and 2008-09 periods, early melt is influenced primarily by landcover changes on the south-facing LUs, with most advanced melt occurring in south-facing *gap* landcovers, closely followed by melt in *open* landcovers. By comparison, snowmelt is delayed on south-facing LUs of *forest* landcover by 15–20 days during both spring seasons. Over both snowmelt periods, landcover influences on snowmelt timing transfer from the south-facing LUs during early melt to north-facing LUs during later melt. Here, at the north-facing LUs, snowmelt begins earliest under forest-cover, followed by that in *open* landcovers, with most delayed melt occurring in the *gap* landcover type. Considering the relatively small contributing area of the north-facing LU grouping, these results demonstrate the strong retarding effect on snowmelt that may be produced through forest-cover removal on north-facing mountain landscapes, particularly with forest removal in the form of small clear-cuts.

Table 7. 1. General description of the area on topographical orientation of the 6 landscape units (LUs) defined within the Middle Creek and Twin Creek sub-basins in the MCRB (sd denotes standard deviation).

LU No.	*Sub-basin*	*Area* [km^2]	*General orientation*	*LU classification*	*LU area relative to smallest*	*Mean elevation (m.a.s.l.)*	*slope (mean)*	*slope (sd)*	*aspect (mean)*	*aspect (sd)*
1	Twin Creek	0.35	north	North-facing LU	4.41	1963.0	17.4	5.2	7.8	57.7
2	Twin Creek	0.27	southeast	South-facing LU	3.47	2077.0	20.9	4.7	102.1	13.6
3	Twin Creek	0.09	northeast	North-facing LU	1.20	2030.5	18.3	3.8	37.6	32.6
4	Twin Creek	0.53	southeast	South-facing LU	6.71	1973.5	18.5	6.2	104.1	16.4
5	Middle Creek	0.08	northeast	North-facing LU	1.00	1946.5	18.7	7.5	41.9	36.8
6	Middle Creek	0.56	southeast	South-facing LU	7.16	1986.5	20.5	7.9	126.8	41.4
LSC (reference)	n/a	n/a	n/a	n/a	n/a	1836	n/a	n/a	n/a	n/a

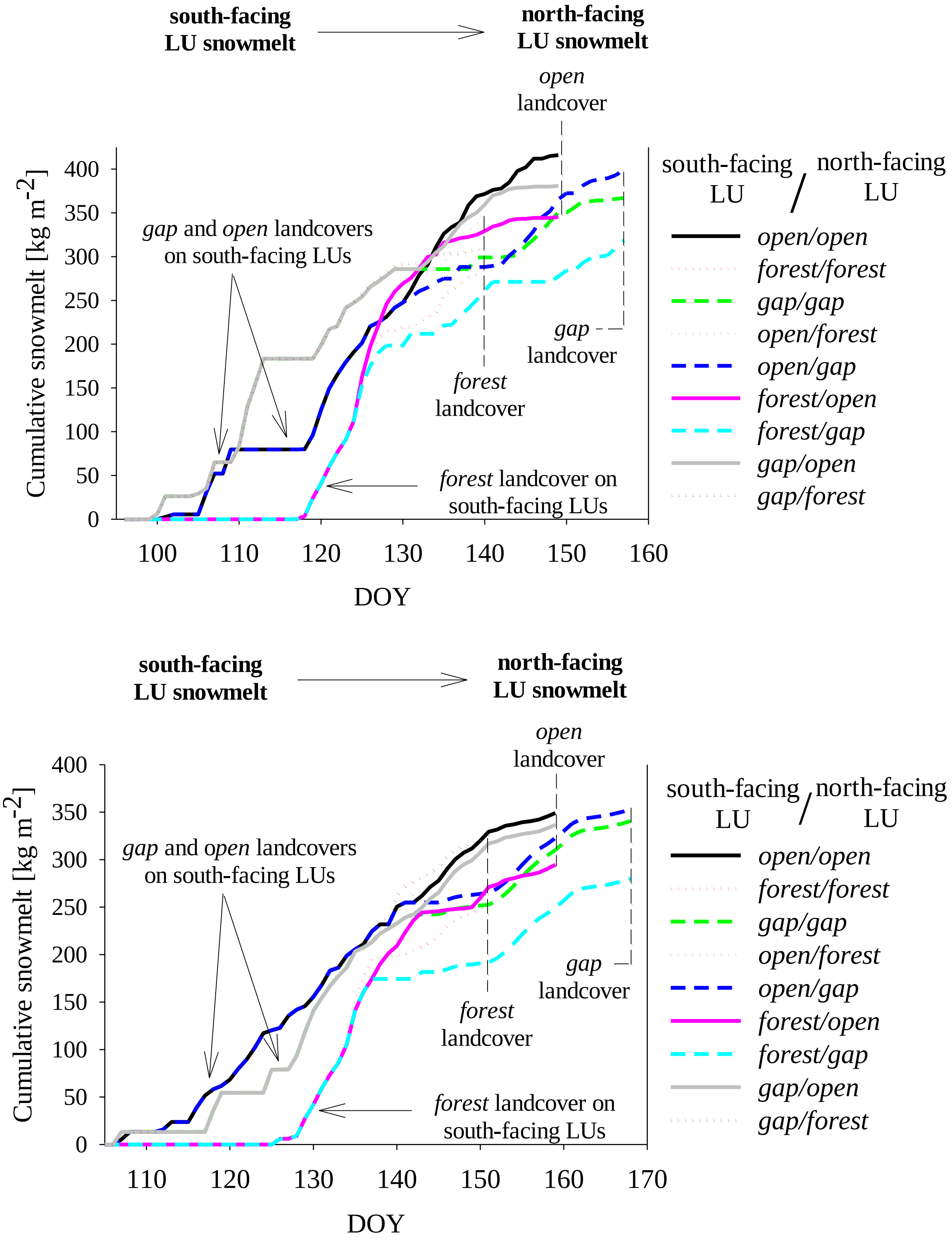

Figure 7. 15. Cumulative snowmelt over the Middle Creek and Twin Creek sub-basin for the spring of 2006-07 (top) and 2008-09 (bottom) simulated for specified configurations of *open*, *forest*, and *gap* landcovers on south-facing and north-facing landscape units (LU).

7.8. Chapter discussion

Building upon the extensive past field studies conducted at the MCRB investigating forest-cover impacts upon spring snowmelt, results presented here demonstrate the considerable potential for altering the magnitude and timing of mountain snowmelt through prescribed forest harvesting treatments. Although the findings here are premised primarily on model simulations, confidence in the results exists due to the rigorous physical-basis of the modelling approach and rigorous testing of the model algorithms. In addition to scenarios of undisturbed forest-cover and open environments, CRHM was also implemented to assess snowmelt dynamics in forest clearing (gap) environments through the coupling of a radiation model developed specifically for forest clearings to the appropriate snow accumulation and melt routines within CRHM. Good model agreement between simulations with snowmelt observations at sloped clearing sites in the MCRB demonstrates the robust flexibility of the modular CRHM framework by the linking of various physically-based simulation processes. Given the deterministic nature of the modelling approach, differences in simulation results with varying meteorology or forest-cover are not assessed in terms of formal tests for significance, but instead are intended to provide a physically-based representation of the expected responses in snowmelt processes.

At the MCRB, much of the initiative behind the forest harvesting treatments of the 1970s and 1980s involved assessing the potential for delaying streamflow through the introduction of small circular clear-cuts along the Twin Creek tributaries. This was premised largely upon observations of delayed snowmelt in small forest (gap) clear-cuts relative to that under forest-cover on level terrain (Troendle, 1983). However, as demonstrated by model simulations, differences in slope orientation heavily influence snowmelt timing in forest clear-cuts by varying the degree of shortwave penetration within the forest gap. As a result, the creation of small clear-cuts on south-facing slopes largely results in greater springtime radiation and earlier snowmelt relative to that under forest-cover, and decreased radiation and delayed snowmelt on north-facing slopes. Again, despite being based on simulations, these results are largely corroborated by the observations of radiation and snowmelt in forest and clear-cut sites across the southern Twin Creek tributary detailed in Chapter 3.

Although the impacts on snowmelt-generated snowmelt from the Twin Creek clear-cutting treatments are largely unknown or unreported, simulations suggest that the intended effect of delayed streamflow may have been substantially moderated due to the harvesting treatments being along both the north-facing and south-facing slopes of the tributary. Here, earlier snowmelt on the south-facing clear-cut slopes combined with delayed melt on the north-face would be expected to offset one another, acting to reduce changes in total streamflow from the sub-basin. Alternatively, a lengthening of the spring runoff period would result from the Twin Creek harvesting treatment by earlier snowmelt contributions from south-facing slopes and later snowmelt contributions from north-facing slopes. Based on this, the promotion of late-season flows from delayed snowmelt would be best delivered through the introduction of small forest clear-cuts on north-facing mountain landscapes alone, due to the low radiation gains and high snowpack energy deficits present in north-facing forest clearings.

Simulations of snow accumulation and melt at *open*, *forest*, and *gap* sites for meteorological conditions at the MCRB show forest-cover removal to generally advance snowmelt on south-facing slopes through increased shortwave melt energy, while delaying melt on north-facing slopes through losses in longwave melt energy. This generalisation however, is strongly contingent on springtime metrological conditions evident in the pronounced response of snowmelt timing to adjustments in air temperature and snow albedo. In *open* sites, the strong control of shortwave radiation on snowmelt energy is apparent in the large sensitivity of snowmelt timing to snow albedo. Consequently, snowmelt timing in *open* mountain landscapes would be expected to exhibit considerable inter-seasonal variation not only from differences in shortwave radiation caused by cloud-cover effects, but also the number of snowfall events that refresh snow albedo through the winter. In contrast, air temperatures strongly control the timing of forest snowmelt by affecting canopy longwave emissions, particularly in dense stands where topographic variations in shortwave irradiance are masked by canopy extinction, resulting in longwave-dominated snowmelt energy. From this, forest-cover is observed to exert an important hydrological control through the synchronisation of snowmelt across mountain landscapes.

Notwithstanding the varying effect of meteorological conditions on snowmelt energy, generally consistent patterns in snowmelt timing were found between opposing south-facing and north-facing slopes due to their disparate radiation and snowmelt energy balances. These differences gave for pronounced responses in melt timing across the Middle Creek and Twin Creek sub-basins under alternative *open*, *forest*, and *gap* landcover configurations. For seasons of differing snowfall amounts and meteorological conditions, similar shifts in the magnitude and timing of snowmelt occurred for the same landcover configurations on south-facing and north-facing landscapes. These results demonstrate the considerable potential in altering the timing of spring snowmelt through topography-specific forest-cover changes, and illustrate how forest changes across mountain landscapes may impact the magnitude and timing of spring snowmelt runoff.

8. CONCLUSIONS

Results presented in this dissertation illustrate the marked impacts that needleleaf forest-cover has on snow processes in mountain environments. Based on information from both field observations and modelling exercises contained within this work, the following conclusions are made regarding forest-cover effects on mountain snow accumulation and melt:

(i) The presence of needleleaf forest-cover has the potential to severely reduce mountain snow accumulations through interception losses from the canopy. Evidence from snow survey data, ‘hanging tree’ lysimeter measurements, and physically-based simulation exercises all indicate that canopy sublimation losses may reduce mountain winter snow accumulations by more than half compared to open environments. Such large snow losses result from the large interception potential of needleleaf canopies, which are able to support heavy snowloads over extended time periods. At the MCRB, high canopy sublimation losses are further promoted by the ventilation of intercepted snow by dry air masses, evident by the rapid sublimation observed during periods of concurrent high canopy wind speeds and low relative humidity.

(ii) Forest-cover strongly influences the timing and rate of mountain snowmelt by modifying energy exchanges to snow. Radiation for snowmelt is altered by the forest canopy through extinction of shortwave irradiance while enhancing longwave irradiance from canopy emissions, giving radiation balances of varying shortwave and longwave contributions. In mountain environments, canopy-cover exerts an important hydrological control by replacing variable, shortwave-controlled snowmelt across open landscapes with highly-synchronised, longwave-driven melt under forest-cover. Conversely, forest-cover removal results in a pronounced de-synchronization in snowmelt timing between mountain landscapes of differing slope orientations, for which forest removal across opposing north-facing and south-facing slopes results in a substantial lengthening the spring snowmelt period. This is premised based on insight provided by field observations and modelling exercises which show that changes in mountain forest-cover to have disparate effects on snowmelt timing between north-facing and south-facing slopes, with forest-cover removal on south-facing slopes advancing snowmelt through increased shortwave gains while delaying melt on north-facing slopes by decreased melt energy from canopy longwave emissions. Yet, forest-cover effects on radiation to mountain snow are strongly varied by seasonal meteorological conditions, resulting in canopy-cover generally increasing mid-winter radiation by limiting longwave losses from snow. However, with rising solar elevations in the spring, forest-cover acts more to decrease radiation to mountain snow through extinction of shortwave irradiance, particularly on south-facing slopes where potential shortwave gains are greatest. Alternatively, the low shortwave irradiance to north-facing sites throughout the spring results in greater radiation to snow maintained under forest-cover due to the enhancement in sub-canopy longwave radiation. These effects illustrate the dynamic balance between competing shortwave and longwave exchanges to snow with changing forest-cover, and the large modifying influence that slope orientation and meteorological conditions have in determining total radiation to mountain snowcovers.

(iii) The highly-variable shortwave radiation gains observed at sites of differing slope orientation within the MCRB underscore the important control of snow albedo in determining snow radiation and melt in mountain environments. Snow albedo is a key factor in determining whether the presence of forest-cover acts to provide a net gain or net loss of radiation to snow. Across mountain landscapes, snow albedo controls the degree of shortwave variability produced by topography, and by result, the potential divergences in snowmelt timing from differences in slope orientation. However, accurate characterisation of snow albedo is challenging, especially in forests due to effects from litter deposition, canopy snow unloading and drip. Yet, detailed snow albedo measurements obtained at the MCRB field sites suggest that accurate determinations of snow albedo in mountain environments may be further complicated by the considerable spatial variation of energy-driven albedo decay rates caused by differences in forest-cover and topography. Consequently, better understanding of the factors controlling the spatial and temporal changes in snow albedo are expected to provide a critical improvement in the accurate representation of mountain snowmelt processes using physically-based simulation approaches such as CRHM.

As with any investigation of a physical hydrological problem, a major limitation of this work relates to the locality of field observations and model exercise applications from which its results are based. Although conclusions drawn from results are expected to be applicable for similar headwater basins in the eastern Canadian Rockies, uncertainly exists in their transfer to other locations such as coastal mountain environments where radiation may represent a less important factor controlling snowmelt. At the very least however, this work highlights the many involved and complex mechanisms by which needleleaf forest-cover impacts mountain snow hydrology. Findings clearly demonstrate that level terrain assumptions are unsuitable in assessing how forest-cover may influence radiation exchanges to snow and snowmelt processes across complex mountain terrain. Finally, from a water resource standpoint, results illustrate the considerable potential for altering the magnitude and timing of spring snowmelt runoff through targeted forest management practices.

REFERENCES

Andreadis, K., Storck, P., and D. Lettenmaier, 2009. Modeling snow accumulation and ablation processes in forested environments. *Water Resources Research*, 45, W05429, doi:10.1029/2008WR007042.

Analytical Spectral Devices, Inc. FieldSpec Pro FR Portable Spectroradiometer User's Guide. February 2000, 94 pp.

Anderson, E.A. 1976. A point energy and mass balance model of a snow cover. NWS Technical Report 19, National Oceanic and Atmospheric Administration, Washington, DC, 150 pp.

Arp, C. D., Gooseff, M. N., Baker, M. A., and W. Wartsbaugh. 2006. Surface-water hydrodynamics and regimes of small mountain steam-lake ecosystems. *J. Hydrol.*, 329 (3-4): 500-513.

Barclay, H. 2001. Distribution of leaf orientations in six conifer species. *Can. J. Bot.*, 79: 389-403.

Baret, F. and M. Weiss. 2004. CANEYE hemispherical photograph analysis software. Avignon, l' Institut national de la recherch agrinomique (INRA). <caneye@avignon.inra.fr.> (first accessed: 02/02/2006).

Beckstead, G.R.E. and W.M. Veldman. 1985. The Marmot Creek Experimental Watershed: Final Report. HydroCon Engineering (Continental) LTD. 119 pp.

Beke, G.J. 1969. Soils of three experimental watersheds in Alberta and their hydrological significance. Unpublished PhD thesis, University of Alberta, Edmonton.

Black, T. A., Chen, J., Lee, X., and R. Sagar. 1991. Characteristics of shortwave and longwave irradiances under a Douglas-fir Forest stand. *Can. J. For. Res.*, 21: 1020-1028.

Bohren, C.F. and D.B. Thorud. 1973. Two theoretical models of radiation heat transfer between forest trees and snowpacks. *Agric. Meteorol.*, 11: 3-16.

Brutsaert, W., 1982: *In*: Evaporation into the atmosphere, theory, history and applications. Kluwer, Dordrecht, 299 pp.

Campbell Scientific, Inc. Model HMP45C Temperature and Relative Humidity Probe: Instruction Manual. 2002.

Campbell Scientific, Inc. CM21 Pyranometer Instruction Manual. Copyright 2001, pp. 12-14.

Campbell Scientific, Inc. CG1 Pyrgeometer and CG2 Net Pyrgeometer Instruction Manual. (version 0204). Copyright 2003, pp. 15-16.

Campbell Scientific, Inc. Vaisala HMP45C212 Temperature and Relative Humidity Probe: Instruction Manual. Copyright May 2008, 3 pp.

Campbell Scientific, Inc. Met One 014a Wind Speed Sensor: Instruction Manual. Copyright May 1999/2009, 2 pp.

Campbell Scientific, Inc. 05103, 05106, 05305 RM Young Wind Monitors: Instruction Manual. Copyright May 2009, pp. 1-2.

Campbell Scientific, Inc. SR50 Sonic Ranging Sensor Operator's Manual: (revision 3/03). Copyright 2003, pp. 1-2.

Campbell Scientific, Inc. HFT3 Soil Heat Flux Plate (revision 10/03). Copyright 2003, 1 pp.

Campbell Scientific, Inc. CS616 and CS625 Water Content Reflectometers: (revision 8/06). Copyright 2006., 1 pp.

Campbell Scientific, Inc. Model 107 Temperature Probe: (revision 10/08). Copyright 2008, pp. 1-2.

Chen, J.M. and T.A. Black. 1992. Defining leaf area index for non flat leaves. *Plant Cell Environment*, 15: 421-429.

Church, J. E., 1912. The Conservation of Snow - Its Dependence on Forests and Mountains. *Scientific American Supplement*, 74(1914): 152-155.

Churchill, S. W. and M. Bernstein. 1977. A Correlation Equation for Forced Convection from Gases and Liquids to a Circular Cylinder in Cross Flow. *J. Heat Transfer*, *Trans. ASME*94: 300-306.

Cionco, R.M. 1965. A mathematical model for air flow in an idealized vegetative canopy. *J. Applied Meteorology*, 4: 517-522.

Cooper, D. J., Dickens, J., Hobbs, N. T., Christensen, L., and L. Landrum. 2006. Hydrologic, geomorphic and climactic processes controlling willow establishment in a montane ecosystem. *Hydrol. Process*., 20: 1845-1864.

Corbaud B., Coligny, F. and T. Cordonnier. 2003. Simulating radiation distribution in a heterogeneous Norway spruce forest on a slope. *Agric. For. Meteorol*., 116: 1-18.

Davis, R. E., Hardy, J. P., Ni, W., Woodcock, C., McKenzie, J. C., Jordan, R. and X. Li. 1997. Variation of snow cover ablation in the boreal forest: a sensitivity study on the effects of conifer canopy. *J. Geophysical Research*, 102: 29389-29395.

Duursma, R.A., Marshall, J.D. and A.P. Robinson. 2003. Leaf area index inferred from solar beam transmission in mixed conifer forests on complex terrain. *Agric. Forest Meteorol.*, 118(3-4): 221-236.

Eagleson, P.S. *In* Ecohydrology, Darwinian expression of vegetation form and function. Cambridge University Press, Cambridge, UK, 2002, 443 pp.

Eschner, A.R., Leonard, R.E. and A.L. Leaf. 1969. Soil Moisture priming, soil temperature and water available for snowmelt runoff. *Proc. Eastern Snow Conference*, 19-23.

Essery R., Bunting P., Hardy J., Link T., Marks D., Melloh R., Pomeroy J., Rowlands A., and N. Rutter. 2007. Radiative transfer modelling of a coniferous canopy characterized by airborne remote sensing. *J. Hydrometeorology*, 9: 228-241, doi:10.1175/2007JHM870.1

Essery R., Rutter N., Pomeroy J., Baxter R., Stähli R., Gustafsson D., Barr A., Bartlett P., and K. Elder. 2009. An evaluation of forest snow process simulations. *Bulletin of the American Meteorological Society*, 90(8): 1120-1135.

Essery, R.L.H., Pomeroy J.W., Ellis C., and T. Link. 2008. Modelling longwave radiation to snow beneath forest canopies using hemispherical photography and linear regression. *Hydrol. Process*., 22: 2788-2800, doi: 10.1002/hyp.6630.

Exergen Corporation. 2009. IRt/c.5 sensor: IRt/c Technical Specification Manual. http://www.exergen.com/industrl/specs/IRtc_5.html (accessed: 15/01/09).

Faria, D.A., Pomeroy, J.W. and R.L.H. Essery, 2000. Effect of covariance between ablation and snow water equivalent on depletion of snow-covered area in a forest. *Hydrol. Process.*, 14: 2683-2695.

Federer, C. A. 1968. Radiation and snowmelt on a clearcut watershed. *Proc. East. Snow Conf.*, *25th, Boston, 1968*, 28-42.

Federer, C. A. 1971. Solar radiation absorption by a leafless hardwood forest. *Agric. Meteorol.*, 9: 3-20.

Flerchinger, G.N. and K.E. Saxton. 1989. Simultaneous heat and water model of a freezing snow-residue-soil system I. Theory and development. *Trans. of ASAE*, 32(2): 565-571.

Frazer, G. W., Canham, C. D. and K. P. Lertzman. 2000. Gap Light Analyzer (GLA) (version 2.0. Technical Tools. *Bulletin of the Ecological Society of America*, 191-197.

Gary, H. L. 1980. Patch Clearcuts to Manage Snow in Lodgepole Pine. Symposium on Watershed Management, American Society of Civil Engineers, New York, New York (held in Boise, Idaho, July 1980), 335-346.

Gary, H. L. and C. A. Troendle, 1982. Snow Accumulation and Melt Under Various Stand Densities in Lodgepole Pine in Wyoming and Colorado. USDA Forest Service, Rocky Mountain Forest and Range Experiment Station, Fort Collins, Colorado, USDA Forest Service Research Note RM-417, June 1982, 7 pp.

Gelfan A., Pomeroy, J.W. and L. Kuchment. 2004. Modelling forest-cover influences on snow accumulation, sublimation and melt. *J. Hydrometeorology*, 5: 785-803.

Geonor Technical Inc. Geonor T-200B series Technical Specification Manual. All-weather precipitation gauges. http://www.geonor.com/precipitation_gauge.html (accessed: 09/09/2009).

Grant, L., Seyfried, M., and J. McNamara. 2004. Spatial variation and temporal stability of soil water in a snow-dominated mountain catchment. *Hydrol. Process*., 18: 3439-3511.

Gray, D.M. and D.H. Male (eds). 1981. *In* Handbook of Snow: Principles, Processes, Management and Use. Pergamon Press: Toronto, 776 pp.

Gray, D.M. and P.G. Landine. 1988. An energy budget snowmelt model for the Canadian Prairies. *Canadian Journal of Earth Sciences*, 22(3): 464-472.

Gryning, S. and E. Batchvarova. 2001. Energy balance of a sparse coniferous high–latitude forest under winter conditions. *Boundary Layer Meteorology*, 99: 465-488.

Harding, R. J. and J. W. Pomeroy. 1996. The energy balance of the winter boreal landscape.

Journal of Climate, 9: 2778-2787.

Hardy, J. P., Davis, R. E., Jordan, R., Ni, W., and C. Woodcock. 1998. Snow ablation modelling at the stand scale in a boreal jack pine forest. *Hydrol. Process.*, 12(10/11): 1763-1778.

Hardy, J., Melloh, R., Koenig, G., Marks, D., Winstral, A., Pomeroy, J. and T. Link. 2004. Shortwave radiation transmission through conifer canopies. *Agric. Forest Meteorol.*, 126: 257-270.

Hardy, J.P., Melloh, R., Robinson, P., and R. Jordan. 2000. Incorporating effects of forest litter in a snow process model. *Hydrol. Process*., 14: 3227-3237.

Haverd, V., Cuntz, M., Leuning, R. and H. Keith. 2007. Air and biomass heat storage fluxes in a forest canopy: Calculation within a soil vegetation atmosphere transfer model. *Agric. Forest Meteorology*, 147: 125-139, doi:10.1016/j.agrformet.2007.07.006.

Hedstrom, N.R. and J.W. Pomeroy. 1998. Measurements and modelling of snow interception in the boreal forest. *Hydrol. Process*., 12: 1611-1625.

Hellström, R. Å., 2000. Forest-cover algorithms for estimating meteorological forcing in a numerical snow model. *Hydrol. Process*., Special Issue: Eastern Snow Conference, 14(18): 3239-3256.

Iqbal, M., 1983. *In*: An Introduction to Solar Radiation Vol. xviii, Academic Press, New York, 1983, 390 pp.

Jeffery, W. W. 1965. Snow hydrology in the forest environment. *Proc. of the workshop seminar: Snow Hydrology*, University of New Brunswick, Canada, 1965, 1-19.

Jeffery, W. W. Hydrology of Land Use, *In* section XIII of Handbook on the Principles of Hydrology (Ed. D.M. Gray) National Research Council of Canada. 1970.

Jonckheere, I., Fleck, S., Nackaerts, K., Muysa, B., Coppin, P., Weiss, M., and F. Baret. 2004. Reviews of methods for in situ leaf area index determination. Part I. Theories, sensors, and hemispherical photography. *Agric. Forest Meteorol.*, 121: 19-35.

Jordan, R. 1991. Special Report 91–16. A one–dimensional temperature model for a snow cover, Technical documentation for SNTHERM.89. US Army Corps of Engineers Cold Regions Research and Engineering Laboratory, Hanover, New Hampshire, 49 pp.

Jost, G., Weiler, M., Gluns, D.R. and Y. Alila. 2007. The influence of forest and topography on snow accumulation and melt at the watershed-scale. *J. Hydrol.*, 347: 101-115, doi:10.1016/j.jhydrol.2007.09.006.

Kirby, C.L. and R.T. Ogilvy. 1969. The forest of Marmot Creek watershed research basin. Fisheries and Forestry Canada, Canadian Forest Service, Northern Forest Research Centre, Edmonton, information report NOR-X-51.

Koivusalo, H., and T. Kokkonen. 2002. Snow processes in a forest clearing and in a coniferous forest. *J. Hydrol.*, 262: 145-164.

Kondratyev, K.Y. 1969. *In* Irradiance in the Atmosphere. *Int. Geophys. Ser.*, Vol. 12, Academic Press, New York.

Lefsky, M. A., Cohen, W. B., Acker, S. A., Parker, G. G., Speies, T. A. and D. Harding. 1999. Lidar remote sensing of the canopy and biophysical properties of Douglas Fir-Western Hemlock forests. *Remote Sens. Environ.*, 70: 339-361.

Li, X., Strahler, A., and C. E. Woodcock. 1995. A hybrid geometric optical radiative transfer approach for modeling albedo and directional reflectance in discontinuous canopies. *IEEE Trans. Geosci. Remote Sens.*, 33: 466-480.

Link, T. and D. Marks. 1999. Point simulation of seasonal snow cover dynamics beneath boreal forest canopies. *J. Geophysical Research*, 104: 27841-27857.

Link, T. E., Marks, D., and J. Hardy. 2004. A deterministic method to characterize canopy radiative transfer properties. *Hydrol. Process.*, 18: 3583-3594.

Link, T. Radiation regimes in discontinuous forest canopies: evidence for incoming all–wave radiation paradoxes (*in preparation for submission*).

List, R. J., 1966. Smithsonian Meteorological Tables. Smithsonian Institution, Washington, D.C., 527 pp.

Liu, B.Y.H. and R.C. Jordan. 1960. The interrelationship and characteristic distribution of direct, diffuse and total solar radiation. *Sol. Energy*, 4: 1-19.

Lundberg, A. and S. Halldin. 1994. Evaporation of intercepted snow, analysis of governing factors. *Water Resources Research*, 30: 2587-2598.

Mazurkiewicz, A., J.J. McDonnell, D. Callery 2008. Assessing the controls of the snow energy balance and water available for runoff in a rain-on-snow environment. *J. Hydrology*, 354: 1-14.

MacDonald, J. 2010. Unloading of intercepted snow in conifer forests. MSc. Dissertation, Department of Geography and Planning, University of Saskatchewan.

Marks, D., Domingo, J., Susong, D., Link, T. and D, Garen. 1999. A spatially distributed energy balance snowmelt model for application in mountain basins *Hydrol. Process*., 13: 1935-1959.

Marks, D., Kimball, J., Tingey, D., and T. Link. 1998. The sensitivity of snowmelt processes to climate conditions and forest-cover during rain-on-snow: A study of the 1996 Pacific Northwest Flood. *Hydrol. Process.*, 12: 1569-1587.

Marks, D. and A. Winstral. 2001. Comparison of snow depositions, the snowcover energy balance, and snowmelt at two sites in a semi–arid mountain basin. *J. Hydrometeorology*, 2: 213-227.

Martz, L., Bruneau, J. and T. Rolfe. *In* Climate Change and Water. South Saskatchewan River Basin Final Technical Report, April 2007, 252 pp.

McNay, R.S., Petersen, L.D., and J.B. Nyberg. 1988. The influence of forest stand characteristics on snow interception in the coastal forests of British Columbia. *Can. J. For. Res.*, 18: 566-573.

Meesters, A. and H.F. Vugts. 1996. Calculation of heat storage in stems. *Agric. Forest Meteorology*, 78(3-4): 181-202.

Melloh, R., Ballard, J., Hardy, J., Woodcock, C., Liu, J., Smith, J., Koenig, G., and R. Davis. 2003. Spatial distribution of canopy gaps in lodgepole pine forest. *Proc. East. Snow Conf., 60th, Sherbrooke, Quebec, Canada, 2003*, pp. 111-123.

Melloh, R., Hardy J., Davis R., and P. Robinson. 2001. Spectral albedo/reflectance of littered forest during the melt season. *Hydrol. Process*., 15: 3409-3422, doi: 10.1002/hyp.1043.

Melloh, R.A., Hardy, J.P., Bailey, R.N., and T.J. Hall. 2002. An efficient snow albedo model for the open and sub-canopy. *Hydrol. Process.*, 16: 3571-3584.

Met one instruments, Inc. 2001. Technical manual for Met One 50.5 solid state anemometer. (version: 3/19/01).

Metcalfe, R.A. and J.M. Buttle. 1995. Controls of canopy structure on snowmelt rates in the boreal forest. *Proceedings of the 52nd Eastern Snow Conference*, 249-257.

Michaletz, S. T. And E.A. Johnson. 2006b. Foliage influences forced convection heat transfer in conifer branches and buds. *New Phytologist*, 170: 87-98.

Monteith, J.L. 1965. Evaporation and environment. *Symposia of the Society for Experimental Biology*, 19: 205-234.

Monteith, J.L. and M.H. Unsworth. 1990. *In* Principles of Environmental Physics, 2nd Ed., Edward Arnold. New York. pp. 53-54.

Mote, P., Hamlet, A., Clark, M., and D. Lettenmaier. 2005. Declining mountain snowpack in Western North America. *Bulletin of the American Meteorological Society*, January 2005, doi: 10.1175/BAMS-86-1-39.

Moore, R. D. and J. D. Rowland. 1990. Evaluation of model performance when observed data are subject to error. *Physical Geography*, 11(4): 379-392.

Moore, R.D. and D. Scott. 2005. Camp Creek revisited: Streamflow changes following salvage harvesting in a medium-sized, snowmelt-dominated catchment. *Canadian Water Resources Journal*, 30: 331-344.

Myneni, R.B. and G. Asrar. 1993. Radiative transfer in three-dimensional atmosphere/vegetation media. *J. Quant. Spectroscp. Radiat. Transfer.*, 49: 585-598.

Nijssen, B. and D. P. Lettenmaier. 1999. A simplified approach for predicting shortwave radiation through boreal forest canopies. *J. Geophysical Research*, 104: 27859-27868.

Nilson, T. 1971. A theoretical analysis of the frequencies of gaps in plant stands. *Agric. Meteorol.*, 8: 25-38.

Oke, T.R. *In* Boundary Layer Climates. Routledge: New York. 1987, 435 pp.

Omega Engineering Inc. 1994. Operator’s manual: IRt/c Series 0S36, OS37, 0S38 Infrared Thermocouples.

Parviainen, J. 2000. A multi-scale intercepted snow sublimation model, MSc Thesis, University of Saskatchewan, Saskatoon, Canada, 103 pp.

Parviainen, J. and J.W. Pomeroy. 2000. Multiple-scale modelling of forest snow sublimation, initial findings. *Hydrol. Process.*, 14: 2669-2681.

Pomeroy, J.W., Granger, R., Pietroniro, A., Elliott, J., Toth, B., Hedstrom, N.R., and J.R. Janowicz. 2002. Hydrological Pathways in the Prince Albert Model Forest: Final report, July 1997. National Hydrological Research Institute, Saskatoon, Saskatchewan, 233 pp.

Pomeroy, J.W., Gray, D.M., Hedstrom, N.R., and J.R. Janowicz. 2002. Prediction of seasonal snow accumulation in cold climate forests. *Hydrol. Process.*, 16: 3543-3558.

Pomeroy, J.W., Marks, D., Link, T., Ellis, C., Hardy, J., Rowlands, A., and R. Granger. 2009. The impact of coniferous forest temperature on incoming longwave radiation to melting snow. *Hydrol. Process*., 23(17): 2513-2525. doi: 10.1002/hyp.7325.

Plüuss, C., Ohmura, A. 1997. Longwave radiation on snow-covered mountainous surfaces. *J. Applied Meteorology*, 36: 818-824.

Pomeroy, J. W. and K. Dion. 1996. Winter irradiance extinction and reflection in a boreal pine canopy: measurements and modelling. *Hydrol. Process.*, 10: 1591-1608.

Pomeroy, J.W. and D.M. Gray. 1995. *In* Snowcover Accumulation, Relocation and Management. NHRI Science Report No. 7, National Hydrology Research Institute, Environment Canada, Saskatoon, SK, 134 pp.

Pomeroy, J.W., Gray, D.M., and P.G. Landine. 1993. The prairie blowing snow model: characteristics, validation, operation. *J. Hydrol.*, 144:165-192.

Pomeroy, J.W. and R.A. Schmidt. 1993. The Use of Fractal Geometry in Modelling Intercepted Snow Accumulation and Sublimation. *Proceedings of the Eastern Snow Conference*, 50: 1-10.

Pomeroy, J.W., Gray, D.M., Brown, T., Hedstrom, N.R., Quinton, W.L., Granger, R.J., and S.K. Carey. 2007. The cold regions hydrological model, a platform for basing process representation and model structure on physical evidence. *Hydrol. Process*., 21(19): 2650-2667.

Pomeroy, J.W., Gray, D.M., Hedstrom, N.R., and J.R. Janowicz. 2002. Prediction of seasonal snow accumulation in cold climate forests. *Hydrol. Process*., 16: 3543-3558.

Pomeroy, J.W., Parviainen, J., Hedstrom, N., and D.M. Gray. 1998a. Coupled modelling of forest snow interception and sublimation. *Hydrol. Process*., 12: 2317-2337.

Pomeroy, J.W., Rowlands, A. Hardy, J., Link, T., Marks, D., Essery, R., Sicart, J.E., and C. Ellis. 2008. Spatial Variability of Shortwave Irradiance for Snowmelt in Forests. *J. Hydrometeorology*, 9(6):1482-1490.

Pomeroy, J.W. and R.J .Granger. 1997. Sustainability of the western Canadian boreal forest under changing hydrological conditions - I - snow accumulation and ablation. Eds. D. Rosjberg, N. Boutayeb, A. Gustard, Z. Kundzewicz and P. Rasmussen) Sustainability of Water Resources under Increasing Uncertainty. IAHS Publ. No. 240. IAHS Press, Wallingford, UK., 237-242.

Pomeroy, J.W. and R.L.H. Essery. On the longwave radiant temperature of snow (in preparation for submission).

Reifsnyder, W.E., and H.W. Lull. 1965. Radiant energy in relation to forests. U.S. Department of Agriculture, Technical Bulletin No. 1344, 111 pp.

Roujean, J. L. 1999. Two-story equations of transmission of solar energy (TSETSE) in open boreal conifer tree stands. *J. Geophysical Research*, 104: 27869-27879.

Rowland, J. D., and R. D. Moore. 1992. Modelling solar irradiance on sloping surfaces under leafless deciduous forests. *Agric. Forest Meteorol.*, 60: 111-132.

Rutter, A.J., Kershaw, K.A., Robins, P.C., Morton, A.J. 1971. A predictive model of rainfall interception in forests. I. Derivation of the model from observations in a plantation of Corsian pine. *Agricultural Meteorology*, 9: 367-384.

Rutter, N., Essery, R., Pomeroy, J., Altimir, N., Andreadis, K., Baker, I., Barr, A., Bartlett, P., Boone, A., Deng, H., Douville, H., Dutra, E., Elder, K., Ellis, C., Feng, X., Gelfan, A., Goodbody, A., Gusev, Y., Gustafsson, D., Hellström, R., Hirabayashi, Y., Hirota, T., Jonas, T., Koren, V., Kuragina, A., Lettenmaier, D., Li, W-P, Martin, E., Nasanova, O., Pumpanen, J., Pyles, R., Samuelsson, P., Sandells, M., Schadler, G., Shmakin, A., Smirnova, T., Stahli, M., Stockli, R., Strasser, U., Su, H., Suzuki, K., Takata, K., Tanaka, K., Thompson, E., Vesala, T., Viterbo, P., Wiltshire, A., Xia, K., Xue, Y., and T. Yamazaki. 2009. Evaluation of forest snow process models (SnowMip2). *Journal of Geophysical Research - Atmospheres*, 114, D06111, doi:10.1029/2008JD011063.

Satterlund, D. R. 1983. Forest shadows: How much shelter in a shelterwood? *Forest Ecology and Management*, 5: 23-37.

Schmidt, R.A., Jairell, R.L., and J.W. Pomeroy. 1988. Measuring snow interception and loss from an artificial conifer. *Proceedings of the Western Snow Conference*, 56: 166-169.

Schmidt, R. A. 1991. Sublimation of snow intercepted by an artificial conifer, *Agric. Forest Meteorol.*, 54: 1-27.

Schmidt, R. A. and D.R. Gluns 1991. Snowfall interception on branches of three conifer species', *Can. J. For. Res*., 21: 1262-1269.

Schmidt, R.A. 1991. Sublimation of snow by an artificial conifer. *Agric. Forest Meteorol.*, 54: 1-27.

Sicart, J.E., Pomeroy, J.W., Essery, R.L.H., Hardy, J.E., Link, T., and D. Marks. 2004. A sensitivity study of daytime net radiation during snowmelt to forest canopy and atmospheric conditions. *J. Hydrometeorology*, 5: 744-784.

Silberstein, R.P., Sivapalan, M., Viney, N.R., Held, A., and T.J. Hatton. 2003. Modelling the energy balance of a natural jarrah (Eucalyptus marginata) forest. *Agric. Forest Meteorol.*, 115(3-4): 203-232.

Stadt, K. J. and V. J. Leiffers. 2000. MIXLIGHT: a flexible light transmission model for mixed species forest stands. *Agric. Forest Meteorol*., 102: 235-252.

Stadt, K.J., Lieffers, V.J., Hall, R.J. and C. Messier. 2005. Spatially explicit modeling of PAR transmission and growth of *Picea glauca* and *Abies balsamea* in the boreal forests of Alberta and Quebec. *Can. J. For. Res*., 35: 1-12, doi: 10.1139/X04-141.

Stork, P., Bowling, L,. Wetherbee, P., and D. Lettenmaier. 1998. Application of a GIS-based distributed hydrology model for prediction of forest harvest effects on peak stream flow in the Pacific Northwest. *Hydrol. Process*., 12(6): 889-904, doi: 10.1002/(SICI)1099-1085.

Storr, D. 1967. Precipitation variation in a small forested watershed. Proc. 35th Western Snow Conference.

Thorpe, A. and B. Mason. 1966. The evaporation of ice spheres and crystals. *J. Appl. Phys*., 17: 541-548.

Tian, Y.Q., Davies-Colley, R.J., Gonga, P. and B.W. Thorrold. 2001. Estimating shortwave radiation on slopes of arbitrary aspect. *Agric. Forest. Meteorol.*, 109: 67-74.

Troendle, C. A. and C.F. Leaf. 1981. Effects of Timber Harvest in the Snow Zone on Volume and Timing of Water Yield. *In* Interior West Watershed Management. Cooperative Extension, Washington State University, Pullman, Washington (Symposium, Spokane, Washington, April 8-10, 1980), pp. 231-243.

Troendle, C.A. and R.M. King. 1985. The effect of timber harvest on the Fool Creek watershed: 30 years later. *Water Resources Research*, 21: 1915-1922.

Tuller, S. E. 1976. The relationship between diffuse, total and extraterrestrial solar radiation. *Solar Energy*, 18: 259-263.

Unites States Army Corps of Engineers, 1956. *Snow Hydrology*. U.S. Army Corps Eng., 437 pp.

Vaisala Inc. HMP45A and HMP45C humidity and temperature probes. Reference: A599en, 2008.

Valente, F., David, J.S. and J.H.C. Gash. 1997. Modelling interception loss for two sparse eucalypt and pine forests in central Portugal using reformulated Rutter and Gash analytical models. *J. Hydrology*, 190: 141-162.

Wang, Q., Tenhunen, J., Schmidt, M., Kolcun, O., and M. Droesler. 2006. A model to estimate shortwave irradiance in complex terrain. *Boundary-Layer Meteorology*, 119: 409-429.

Weiss, M., Baret, F., Smith, G.J., and I. Jonckheere. 2004. Methods for in situ leaf area index measurement, part II: from gap fraction to leaf area index: retrieval methods and sampling strategies. *Agric. For. Meteorol.*, 121: 17-53.

Williams, L. D., Barry, R. G., and J. T. Andrews. 1972. Application of computed shortwave irradiance for areas of high relief. *J. Applied Meteorology*, 11: 526-533.

Yamazaki, T. and J. Kondo. 1992: The snowmelt and heat balance in snow covered forested areas. *J. Applied Meteorology*, 31: 1322-1327.

Appendix A. Topographical adjustment of shortwave irradiance

Estimates of shortwave irradiance to the sloped sites (K_o(S)) are made via separate adjustment of direct-beam and diffuse shortwave irradiance observed at a nearby level clearing site (K_o(L)) (e.g. Tian et al., 2001), i.e.

$$K_\mathrm{o}(\mathrm{S}) = (1 - k_\mathrm{d})\, K_\mathrm{o}(\mathrm{L})\omega + K_\mathrm{o}(\mathrm{L}) k_\mathrm{d} v \qquad \text{(A1)}$$

where ω is the geometric slope correction factor for direct-beam irradiance and k_d is the diffuse fraction of shortwave irradiance. Determination of k_d is made through a semi-empirical relation to the atmosphere transmittance index (k_t) [] of the linear form:

$$k_\mathrm{d} = a k_\mathrm{t} + b \qquad \text{(A2)}$$

where the a and b denote empirical coefficients which were determined as those providing the highest ME index for adjustment of daily shortwave irradiance observed at the LPC to the SPC for the period extending from March to June, 2005. From this, the optimal adjustment is given by the following form of Eq. A2

$$k_\mathrm{d} = 1.1 - 1.09\, k_\mathrm{t} \qquad \text{(A3)}$$

where k_t is the atmosphere transmittance index [] (Chapter 3, Eq. 3.5). Although this relation was developed by an indirect approach, Figure A1 shows it compares well with those provided from direct measurements of separate direct-beam and diffuse irradiance at various Canadian locations by Tuller (1976) and at a northern Alberta site by Stadl et al. (2005). In Eq. A3, the geometric correction factor for direct-beam irradiance, ω is given by

$$\omega = \frac{\cos(S \wedge \Theta)}{\cos(H \wedge \Theta)} \qquad \text{(A4)}$$

where H and S denote the vector of the normal angle respective to horizontal and sloped surfaces, and Θ is the directional vector of direct-beam irradiance [radians]. Here, the cosine of the angle between either H (or S) to that of Θ is calculated using Williams' et al. (1972) expression:

$$\cos((S(H)^\wedge \Theta) = [c_1 \sin(h) + c_2 \cos(h) + c_3]\,dh \qquad \text{(A5)}$$

where:

$c_1 = -\sin(\varphi)\sin(\Lambda)\cos(\delta)$

$c_2 = [(\cos(\Phi)\cos(\Lambda) - \sin(\Phi)\cos(\varphi)\sin(\theta)]\cos(\delta)$

$c_3 = [(\sin(\Phi)\cos(\Lambda) + \cos(\Phi)\cos(\varphi)\sin(\theta)]\sin(\delta)$.

Similarly, calculation of exo-atmospheric shortwave irradiance (K_{ex}) is made by

$$K_{ex} = I_o \cos(S(H)^\wedge \Theta) \qquad \text{(A6)}$$

where I_o is the solar constant, equal to 4.921 MJ m^{-2} h^{-1}.

Using this approach, daily K_o observed at the SPC is shown compared to corrected LPC irradiance for topography and uncorrected LPC irradiance in Figure A2, with a statistical comparison between each in Table A1.

Table A1. Statistical comparison between observed daily shortwave irradiance (K_o) at the Southeast-facing Pine Clearing site (SPC) to that observed (i.e. uncorrected) and corrected at the Level Pine Clearing (LPC) site.

	SPC (observed)	**LPC (uncorrected)**	**LPC (corrected)**
Mean daily K_o [MJ m^{-2}]	17.1	13.8	17.7
ME []	–	0.59	0.80
RMSE [MJ m^{-2} d^{-1}]	–	4.68	3.24

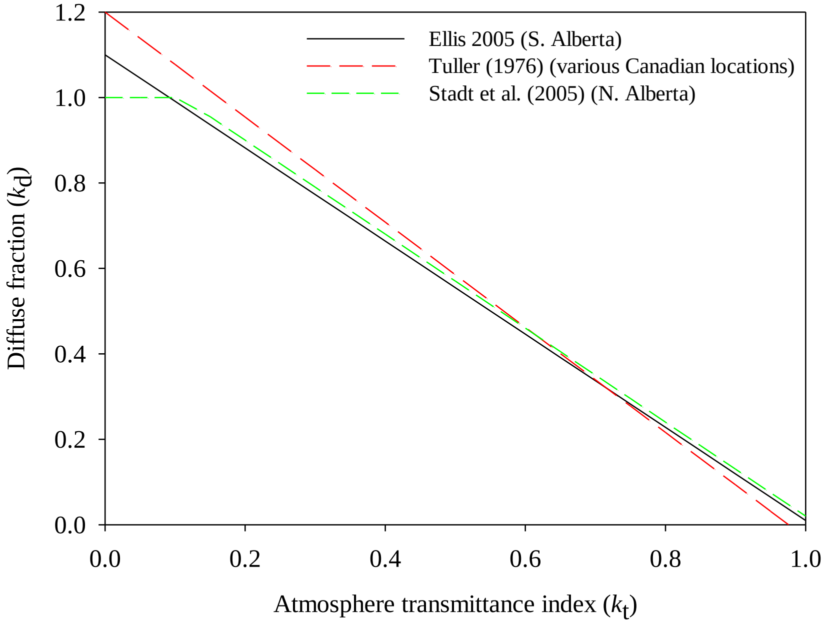

Figure A1. Relation between the diffuse fraction of shortwave irradiance (k_d) and atmosphere transmittance index (k_t) developed from irradiance observations between the SPC and LPC sites at the MCRB (Ellis 2005 (S. Alberta)) compared to those specified by Tuller (1976) and Stadt et al. (2005).

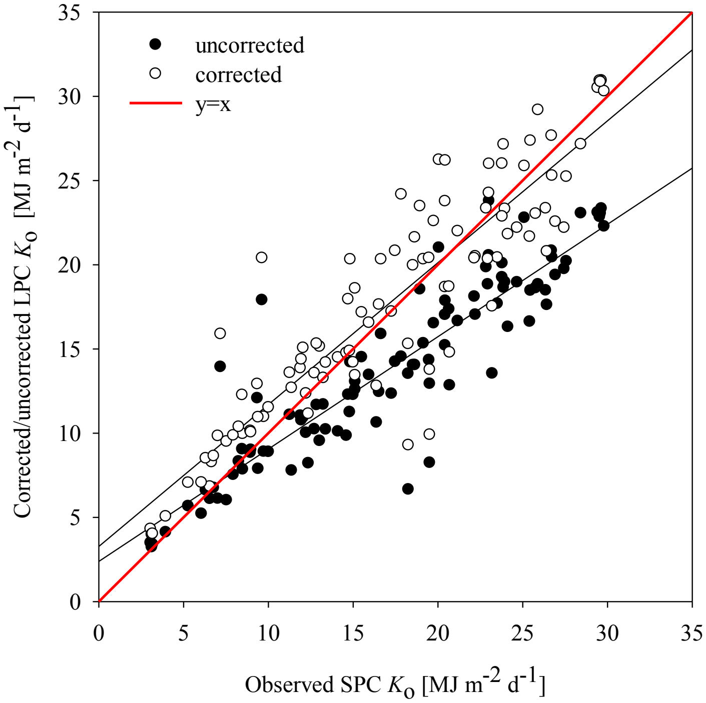

Figure A2. Comparison of daily shortwave irradiance (K_o) observed at the Southeast-facing Pine Clearing slope site (SPC) compared to corrected and uncorrected irradiance from the Level Pine Clearing site (LPC). The best fit linear relations for both uncorrected and corrected irradiance are also shown.

Appendix B. Optimisation of the active biomass layer depth (b_d)

As described in for Eq. 5.15 (Section 5.7.1.2., Chapter 5), the change in the canopy temperature brought about by Q^*_f is closely related to the thermal capacitance of the b_d outer biomass layer of the forest, as a function of the depth of the layer. Optimisation of the depth of the b_d layer was made following an empirical approach utilizing observations of surface temperature, shortwave irradiance, and longwave irradiance to a single south-exposed trunk surface at the SPF (Figure B1). Approximation of shortwave irradiance incident to the trunk surface was made through geometric adjustment of pyranometer observations at the trunk base, with the determinations of other energy terms in Eq. 5.16 made using meteorological data collected at an observation tower located approximately 6 m from the trunk. Through rearrangement of Eq. 5.15 and Eq. 5.16, optimization of the depth of the b_d layer was made according to the highest ME value for the determination of hourly trunk surface temperature as compared to observations. As shown in Figure B2, best results were obtained for a b_d depth of approximately 4.2×10^{-3} m, with ME values decreasing from this value for both smaller and larger b_d depths.

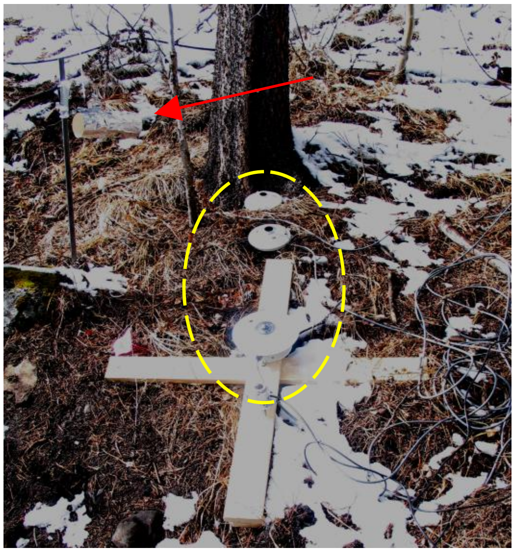

Figure B1. Picture showing the instrumentation set-up used in the empirical optimization of the b_d biomass depth used to approximate the thermal capacity of the outer biomass layer of the forest stand (infrared thermocouple measuring trunk surface temperature indicated by arrow, with pyranometers and pyrgeometers indicated by yellow dashed line).

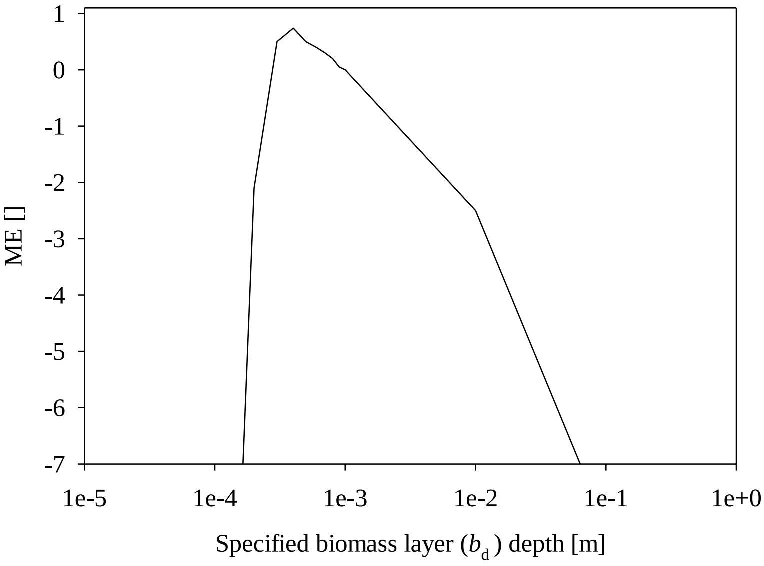

Figure B2. Model Efficiency (ME) of trunk surface temperature as determined as a function of the specified b_d biomass depth in Eq. 5.15 and Eq. 5.16, at the Southeast-facing Pine Forest slope site (SPF) (note that the x-axis is logarithmic).

Appendix C. Determination of individual energy terms of the canopy energy balance

In calculating the net energy available for heating and cooling of the canopy (Q^*_f), all energy terms in Eq. 5.16 are resolved on a per second time step. Here, determination of K^*_f to the active b_d biomass layer with account for additional shortwave gains from multiple reflections between the forest and snow layers is made by:

$$K^*_f = K_\mathrm{o}\left[(1-\alpha_f) + \frac{\tau}{1-\alpha_\mathrm{s}\alpha_f(1-v)}\right] \tag{C1}$$

where α_f is the albedo of the forest canopy []. Although longwave exchanges to b_d are expected to occur with various environmental surroundings (i.e. terrain, sub-canopy snow), the majority of thermal exchanges are considered to be with that of shaded canopy foliage, which assumes the within-canopy air temperature (T_a). Accordingly, the L^*_f is determined by:

$$\begin{aligned} L^*_f &= -\varepsilon_f\sigma(T_f^{\,4} - T_\mathrm{a}^{\,4}) \\ &\cong -4\varepsilon_f\sigma T_\mathrm{a}^{\,3}(T_f - T_\mathrm{a}) \end{aligned} \tag{C2}$$

Determination of sensible heat transfer (H^*_f) is given by the following expression

$$H^*_f = -\rho_\mathrm{a} c_\mathrm{a} D_\mathrm{h} Nu(T_f - T_\mathrm{a})/d \tag{C3}$$

where ρ_a is the air density [kg m^{-3}], c_a specific heat capacity of air [MJ kg^{-1} K^{-1}], D_h is the thermal diffusivity of air [m^2 s^{-1}], Nu is the dimensionless Nusselt number for turbulent heat transfer, and d denotes the characteristic dimension, equal to the representative diameter of foliage, branches, and trunks (Monteith and Unsworth, 1990). Considering the dominance of forced convection observed in pine forests (Michaletz and Johnson, 2006b) separate treatment for mixed or free convection is not made. However, due to the markedly different vegetative morphologies of trunks and crowns, separate determination of Nu are made for each in Eq. C3, which for the crown foliage fraction of the canopy (f_C) is given by Michaletz and Johnson's (2006) empirical relation developed from investigations of turbulent transfer characteristics of lodgepole pine crowns in the Canadian Rocky Mountains:

$$Nu\ (f_\mathrm{C}) = 0.044Re^{0.714} \tag{C4}$$

where *Re*, the Reynolds number, is given by

$$Re = \frac{u_f\, d}{k_\mathrm{v}} \tag{C5}$$

in which u_f is the observed within-canopy wind speed [m s^{-1}], and k_v is the kinematic viscosity of air [m^2 s^{-1}], which may be obtained from meteorological tables (e.g. List, 1966). Alternatively, for the trunk foliage fraction of the canopy (f_T), which is abstracted in the model as an array of upright cylinders of a representative dimensions (of which are approximated from forest survey data provided in Chapter 4), the surface averaged *Nu* is estimated by the Churchill-Bernstein (1977) equation describing turbulent flow across cylinders surfaces:

$$Nu(f_\mathrm{T}) = 0.3 + \frac{0.62 + Re^{1/2}Pr^{1/3}}{[1+(0.4/Pr)^{2/3}]^{1/4}}\left[1+\left(\frac{Re}{282000}\right)^{5/8}\right]^{4/5} \tag{C6}$$

where μ_v is the dynamic viscosity of air [kg m^{-1} s^{-1}], and *Pr*, the Prandtl number, is given by

$$Pr = \frac{k_\mathrm{v}}{D_\mathrm{h}} \tag{C7}$$

Although energy to a surface brought about by advection through rainfall may be substantial, this energy term is not considered in Eq. 5.16 (Chapter 5), as data restrictions prevent the reliable approximation of rainfall temperature. However, energy losses by evaporation of intercepted rainfall (E^*_f) may provide substantial cooling of the canopy, which are approximated by the Penman-Monteith combination equation for the case of no stomatal resistance (Monteith, 1965):

$$E^*_f = -\frac{C}{S_{\max}} \frac{\Delta(K^*_f + L^*_f) + \rho_{\mathrm{a}} c_{\mathrm{a}} vdd g_{\mathrm{a}}}{\Delta + \gamma} \tag{C8}$$

Where C/S_{max} is the fraction of canopy saturation [], Δ is the slope of the saturation vapour pressure curve [Pa K^{-1}], γ is the psychrometeric constant [Pa K^{-1}], *vdd* is the vapour pressure deficit [Pa], and r_{a} is the aerodynamic conductance [m s^{-1}].

Appendix D. Determination of shortwave heating of crown and trunk foliage layers

As stated in Chapter 5 (Section 5.7.1.2.) and Appendix C, separate determinations of H^*_f are made for the crown fraction (f_C) and trunk fraction (f_T) of the canopy, leading to a divergence in the calculated crown and trunk temperatures. As such, separate determinations are also required describing the probability of longwave transfer from heating foliage to the sub-canopy (p_f) from each the f_C and f_T, which for the f_C, the p_f is given by the following modification of Eq. 5.23 (Chapter 5)

$$p_f(f_\mathrm{C}) = \frac{e^{-L`}(1 - e^{-(L`\xi_\mathrm{S} - L`)\, f_\mathrm{C}})}{(L`\xi_\mathrm{S} - L`)\, f_\mathrm{C}} \qquad \textbf{(D1)}$$

Alternatively, determination of p_f for the trunk fraction ($p_f(f_\mathrm{T})$) may be made by the subtraction of $p_f(f_\mathrm{C})$ (Eq. D1) from the p_f (Eq. 5.23), i.e.

$$p_f(f_\mathrm{T}) = p_f - p_f(f_\mathrm{C}) \qquad \textbf{(D2)}$$

Thus, the T_{eff} of the entire forest layer is given by the sum of the determined temperatures of the crown fraction ($T(f_\mathrm{C})$) and trunk fraction ($T(f_\mathrm{T})$), weighed by their respective fractional composition of total forest foliage and their longwave transfer probabilities as determined in Eq. D1 and Eq. D2:

$$T_{eff} = f_\mathrm{C}\, T(f_\mathrm{C})\, p_f(f_\mathrm{C}) + f_\mathrm{T}\, T(f_\mathrm{T})\, p_f(f_\mathrm{T}) \qquad \textbf{(D3)}$$

Appendix E. C++ source code for the forest snow accumulation and energy balance module ‘canopy’ within the Cold Regions Hydrological Model (CRHM)

(version: 5/25/2010)

```
ClassCRHMEllis* ClassCRHMEllis::klone(string name) const{
  return new ClassCRHMEllis(name);
}

void ClassCRHMEllis::decl(void) {

  Description = "'All season canopy module.'";

// forest rain interception:

  declvar("intcp_evap", NHRU, "canopy evaporation", "(kg/m^2)", &intcp_evap);
  declvar("Cpy_evapC", NHRU, "cumulative canopy evaporation", "(kg/m^2)",
&Cpy_evapC);
  declvar("Cpy_rainStore", NHRU, "canopy storage at timestep start",
"(kg/m^2)", &Cpy_rainStore);
  declvar("drip_cpy", NHRU, "canopy drip", "(kg/m^2)", &Cpy_drip);
  declvar("Cpy_thrufall", NHRU, "direct rainfall through canopy", "(kg/m^2)",
&Cpy_thrufall);
  declvar("Cpy_netRain", NHRU, " direct rainfall + drip", "(kg/m^2)",
&Cpy_netRain);
  declvar("Cpy_netRainC", NHRU, " cumulative direct rainfall + drip",
"(kg/m^2)", &Cpy_netRainC);

  declvar("cum_net_rain", NHRU, "daily net rain", "(kg/m^2*d)",
&Cpy_netRainD);

// coupled snow interception and sublimation (Is_*):

  decllocal("Is_RhoS", NHRU, "density of falling snow", "(kg/m^3)",
&Is_RhoS);
  declvar("Is_LStar", NHRU, "maximum canopy snow load", "(kg/m^2)",
&Is_LStar);
  declvar("Is_SLoad", NHRU, "canopy snow load (timetep start)", "(kg/m^2)",
&Is_SLoad);
  declvar("Is_SThru", NHRU, "snow 'direct' throughfall", "(kg/m^2)",
&Is_SThru);
  declvar("Is_cpySubl", NHRU, "canopy snow sublimation", "(kg/m^2)",
&Is_cpySubl);
  decldiag("Is_cpySublC", NHRU, "cumulative canopy snow sublimation",
"(kg/m^2)", &Is_cpySublC);
  decldiag("Is_SThruC", NHRU, "cumulative snow throughfall", "(kg/m^2)",
&Is_SThruC);
  declvar("Is_SUnload", NHRU, "unloaded canopy snow", "(kg/m^2)",
&Is_SUnload);
  decldiag("Is_SUnloadC", NHRU, "cumulative canopy snow unload", "(kg/m^2)",
&Is_SUnloadC);
  decllocal("Is_uVent", NHRU, "wind speed at Zvent", "(m/s)", &Is_uVent);
  declvar("Is_SnowBal", NHRU, "snow balance (sublimation + throughfall +
unloading)", "(kg/m^2)", &Is_SnowBal);
```

```
  decldiag("Is_SnowBalC", NHRU, "cumulative snow balance", "(kg/m^2)",
&Is_SnowBalC);
  declvar("Is_netsnow", NHRU, "sub-canopy swe (throughfall + unload)",
"(kg/m^2)", &Is_netsnow);
  decldiag("Is_netsnowC", NHRU, "cumulative sub-canopy swe", "(kg/m^2)",
&Is_netsnowC);
  declvar("Is_netsnowD", NHRU, "daily sub-canopy swe", "(kg/m^2*d)",
&Is_netsnowD);

  decllocal("fvel0", NHRU, "u* over ground", "()", &fvel0);
  decldiag("uRef", NHRU, "above-canopy reference wind speed", "(m/s)",
&uRef);
  declvar("uFHt", NHRU, "wind speed at forest top (z = FHt)", "(m/s)",
&uFHt);
  declvar("uForest", NHRU, "wind speed in forest", "(m/s)", &uForest);
  decllocal("vdd_airToSnow", NHRU, "snow vapour density deficit (relative to
air)", "(g/m^3)", &vdd_airToSnow);

  declvar("Pevap", NHRU, "'potential' evaporation", "(mm)", &Pevap);

// CRHM outputs:

  decldiag("Ab_t", NHRU, "timesteps since albedo refresh", "()", &Ab_t);
  declstatvar("winter", NHRU, "winter", "()", &winter);
  declstatvar("meltflag", NHRU, "meltflag", "()", &meltflag);
  declstatvar("Albedo", NHRU, "Snow Albedo", "()", &Albedo);
  decllocal("Cc", NHRU, "Canopy coverage", "()", &Cc);
  declvar("net_rain", NHRU, "sub-canopy rainfall", "(mm/int)", &net_rain);
  declvar("net_snow", NHRU, "sub-canopy snowfall", "(mm/int)", &net_snow);
  declvar("intcp_evap", NHRU, "HRU Evaporation from interception",
"(mm/int)", &intcp_evap);

  decllocal("Qh_snow_W", NHRU, "sensible heat to snow", "(W/m^2)",
&Qh_snow_W);
  decllocal("Qh_snow_MJ", NHRU, "sensible heat to snow", "(MJ/m^2)",
&Qh_snow_MJ);

  decllocal("Qe_snow_W", NHRU, "latent heat to snow", "(W/m^2)", &Qe_snow_W);
  decllocal("Qe_snow_MJ", NHRU, "latent heat to snow", "(MJ/m^2)",
&Qe_snow_MJ);

  decllocal("ga", NHRU, "aerodynamic conductance", "(m/s)", &ga);

// parameters:

  declparam("basin_area", BASIN, "1", "1e-6", "1e+09", "total basin area",
"(km^2)", &basin_area);
  declparam("hru_area", NHRU, "[1]", "1e-6", "1e+09", "hru area", "(km^2)",
&hru_area);
  declparam("LAI", NHRU, "[2.2]", "0.1", "10.0", "leaf-area-index", "()",
&LAI);
  declparam("FHt", NHRU, "[25.0]", "0.0", "100.0", "forest height", "(m)",
&FHt);
  declparam("smax", NHRU, "[2.0]", "0.0", "10.0", "maximum canopy rain
storage", "(kg/m^2)", &smax);
  declparam("windz", NHRU, "[10]", "0.01", "100.0", "wind measurement
height", "(m)", &windz);
```

```
  declparam("Sbar", NHRU, "[6.6]", "0.0", "100.0", "maximum canopy snow
interception load", "(kg/m^2)", &Sbar);
  declparam("Zvent", NHRU, "[0.75]", "0.0", "1.0", "ventilation wind speed
height (z/FHt)", "()", &Zvent);
  declparam("refresh", NHRU, "[3.0]", "0.0", "50.0", "minimum sub-canopy
snowfall to refresh albedo", "(mm)", &refresh);
  declparam("hru_elev", NHRU, "[637]", "-0.0", "1e4.0", "elevation m.a.s.l.",
"()", &hru_elev);
  declparam("hru_GSL", NHRU, "[0.0]", "0.0", "90.0", "slope gradient", "(°)",
&hru_GSL);
  declparam("hru_ASL", NHRU, "[0.0]", "0.0", "360.0", "slope aspect", "(°)",
&hru_ASL);
  declparam("hru_lat", NHRU, "[51.317]", "0.0", "90.0", "latitude", "(°)",
&hru_lat);
  declparam("unload_t", NHRU, "[1.0]", "-10.0", "10.0", "if ice-bulb temp >=
unload temp: canopy snow is unloaded ", "(°C)", &unload_t);

  declparam("WindLoc", BASIN, "0", "0", "2", "wind observation location: 0 =
clearing, 1 = above-canopy, 2 = within canopy", "()", &WindLoc);

// Observations

  obs_QsiCnt = declreadobs("Qsi", NOBS, "above-canopy shortwave irradiance",
"(W/m^2)", &Qsi);
  obs_TsCnt = declreadobs("Ts", NOBS, "snow surface temperature", "(°C)",
&Ts);

// get variables:

  declgetvar("*", "hru_snow", "(mm/int)", &hru_snow);
  declgetvar("*", "hru_rain", "(mm/int)", &hru_rain);
  declgetvar("*", "hru_ea", "(kPa)", &hru_ea);
  declgetvar("*", "hru_rh", "(%)", &hru_rh);
  declgetvar("*", "hru_u", "(m/s)", &hru_u);
  declgetvar("*", "hru_t", "(°C)", &hru_t);
  declgetvar("*", "hru_tmin", "(°C)", &hru_tmin);
  declgetvar("*", "hru_tmax", "(°C)", &hru_tmax);
  declgetvar("*", "SWE", "(mm)", &SWE);
  declgetvar("*", "snowdepth", "(m)", &snowdepth);
  declgetvar("*", "hru_evap", "(mm/int)", &hru_evap);
}

void ClassCRHMEllis::init(void) {

nhru = getdim(NHRU);
nobs = getdim(NOBS);

for (hh = 0; hh < nhru; ++hh) {

      Is_cpySublC[hh] = 0.0;
      Is_SThruC[hh] = 0.0;
      Is_SLoad[hh] = 0.0;
      Is_SnowBalC[hh]= 0.0;
      Is_netsnow[hh] = 0.0;
      Is_netsnowC[hh] = 0.0;
      Is_SUnloadC[hh] = 0.0;
      Cpy_evapC[hh] = 0.0;
```

```
      Cpy_netRainC[hh] = 0.0;
      Ab_t[hh] = 0.0;
      Albedo[hh] = 0.0;
      intcp_evap[hh] = 0.0;
      net_rain[hh] = 0.0;
      net_snow[hh] = 0.0;
  }
}

void ClassCRHMEllis::run(void) {

//=============================================================================
==

  const float AlbedoIce = 0.8;       // albedo of ideal ice sphere
  const float Radius = 5.0e-4;       // radii of single 'ideal' ice sphere
in, m)
  const float M = 18.01;             // molecular weight of water*/
  const float R = 8313.0;            // universal gas constant, J/(mole*K)
  const float KinVisc = 1.88e-5;     // kinematic viscosity of air (Sask.
avg. value)
  const float RhoI = 900;            // 'typical' density of ice, kg/m3)
  const float ks = 0.0114;           // snow shape coefficient for jack pine
  const float Fract = 0.37;          // fractal dimension of intercepted snow
  const float psyC = 0.483;          // psychronmetric constant (g/m^2/K)
  const float Rv = 0.4615;           // specific gas constant for H20 (J/g/K)
  const float Lv = 2.47;             // latent heat of vapourization (MJ/kg)
  const float ci = 2.102e-3;         // heat capacity of ice (MJ/kg/K)
  const float Press = 101.3;         // 'typical' near-ground atmospheric
pressure (kPa)
  const float vonK = 0.4;            // von Karmon canstant
  const float Hs = 2.838e6;          // heat of sublimation (MJ/kg)
  const float cp = 1.005;            // 'typical' specific heat of air
(KJ/g/K)
  const float pa = 1.275;            // typical air denity (kg/m^3)

//=============================================================================
===


 float A1, B1, J, D, m, Nu, SStar, Nr, I1;
 float dis, q, For_vent, PQeMJ, Ir_netrainPM;
 long nstep;

 nstep = getstep()%Global::Freq;
 float tstep = 86400/Global::Freq;  // no. seconds/timestep

 for(hh = 0; chkStruct(); ++hh) {
   net_snow[hh] = 0.0;
   net_rain[hh] = 0.0;
   Is_SThru[hh] = 0.0;

// calculate horizontal canopy-coverage (Cc):

  Cc[hh] = 0.29 * log(LAI[hh]) + 0.55;
```

```
//  Forest rain interception and evaporation model. 'sparse' Rutter
interception model (i.e. Valente 1997):

// calculate rain accumulation on canopy before evap loss:

 if (((Cpy_rainStore[hh]/Cc[hh]) + hru_rain[hh]) > smax[hh]){
       Cpy_rainStore[hh] = smax[hh] * Cc[hh];
       Cpy_drip[hh] = (((Cpy_rainStore[hh]/Cc[hh]) + hru_rain[hh])-
smax[hh])* Cc[hh];
 }
 else{
       Cpy_rainStore[hh] = (hru_rain[hh] + Cpy_rainStore[hh]/Cc[hh])* Cc[hh];
       Cpy_drip[hh] = 0;
 }

// calculate direct throughfall:

  Cpy_thrufall[hh] = hru_rain[hh] * (1-Cc[hh]);

// calcualte net throughfall (direct + drip)

  Cpy_netRain[hh] = Cpy_thrufall[hh] + Cpy_drip[hh];

// calculate wind speed at forest top:

  float zo_snow = 1e-3;

  fvel0[hh] = (hru_u[hh]*vonK) / log(windz[hh]/zo_snow);    // u* (ground)

  float HtRef = FHt[hh]+ 1;

  if(WindLoc[0]<= 0.5)
     uRef[hh] = fvel0[hh] / vonK * log(HtRef/zo_snow);  // u at reference
height
  else
     uRef[hh] = hru_u[hh]; // u at reference height (if wind obs is above-
canopy)

// calculate aerodynamic resistance:
// Boundary-layer parameters 'dis' and 'zoF' set according to average for a
variety of needle-leaf canopies (Eagleson, p. 107)*/

 dis = 0.78 * FHt[hh];       // vegetation displacement height (/FHt)
 float zoF = 0.08 * FHt[hh];     // forest roughness length (/FHt)

 float fvelM0, fvelM1;

 if (WindLoc[0] <= 0.5){
    fvelM0 = (uRef[hh] * vonK)/ (log((HtRef-dis)/(zoF)));  // u* (above-
canopy)
    fvelM1 = 0.0;
    }
 else {
   fvelM1 = (uRef[hh] * vonK)/(log((windz[hh]-dis)/(zoF))); // u* (above-
canopy)
   fvelM0 = 0.0;
    }
```

```
// calculate wind speed at forest top (z = FHt):

 if(WindLoc[0] <= 0.5)
  uFHt[hh]= fvelM0 / vonK * log((FHt[hh]-dis)/zoF);
  else
  uFHt[hh]= fvelM1 / vonK * log((FHt[hh]-dis)/zoF);

// calculate wind speed 0.5 metre above snow:

float xi = 1-((snowdepth[hh]+ 0.5)/FHt[hh]);
if (xi <= 0.0)
    xi = 0.0;

float gamma = 1.15;
double windExt = (gamma * LAI[hh] * xi);     // wind extinction coefficient

   if (WindLoc[0] >= 2)
      uForest[hh] = hru_u[hh];
   else
      uForest[hh] = uFHt[hh] * exp(-1 * windExt);

float uforestHt = snowdepth[hh] + 0.5;

// calculate conductance:

  ga[hh] = pow(vonK, 2.0f) * uForest[hh] / pow(log(uforestHt/zo_snow), 2.0f);

// calculate sensible heat fluz to snow

  Qh_snow_W[hh] = pa*cp* ga[hh]*(hru_t[hh]-Ts[hh])*tstep/1e3;
  Qh_snow_MJ[hh] = Qh_snow_W[hh]*tstep/1e6;

float Ir_raM;  // calculate aerodynamic resistance above-canopy

  if (WindLoc[0] <= 0.5)
      Ir_raM = log((HtRef-dis)/zoF)/(vonK * fvelM0);
  else
      Ir_raM = log((windz[hh] - dis)/zoF)/(vonK * fvelM1);

  if (fvelM0 <= 0.0 || fvelM1 <= 0.0)
      Ir_raM = 1e2;

// calculate 'actual evap' of water from canopy:

 if(Cpy_rainStore[hh] >= smax[hh]){  // (evaporation in mm)
     intcp_evap[hh] = hru_evap[hh] * Cc[hh];  // if cpy saturated: actEvp =
potEvp
     Cpy_rainStore[hh] -= intcp_evap[hh];
 }
 else
     intcp_evap[hh] = Cpy_rainStore[hh];

// sum evaporation and net (sub-canopy) rainfall (mass-balance check):
// cumulative amounts:

  Cpy_evapC[hh]+= intcp_evap[hh];               // cumulative canopy evap
```

```
  Cpy_netRainC[hh]+= Cpy_netRain[hh];         // cumulative net rain (sub-
canopy)

  if (nstep == 1)
      Ir_netrainPM = Cpy_netRain[hh];
 else
      Ir_netrainPM += Cpy_netRain[hh];

 if (nstep == 0)
     Cpy_netRainD[hh] = Ir_netrainPM;          // daily 'net' (sub-canopy)
rainfall

//===========================================================================
===
// coupled forest snow interception and sublimation routine:
// after Hedstom & Pomeroy / Parviainen & Pomeroy:

// calculate intercepted snow load by canopy:

// density of falling snow (kg/m^2):

 if (hru_t[hh] < 4.0)
    Is_RhoS[hh] = 67.92 + 51.25* exp(hru_t[hh]/2.59);
 else
    Is_RhoS[hh] = 1e3;

// calculate maximum canopy snow load (L*):

  float Is_IStar = Sbar[hh]* (0.27 + 46.0/Is_RhoS[hh])* LAI[hh];   // I*
  Is_LStar[hh] = Is_IStar * LAI[hh];                // L*

// calculate intercepted snowload at timestep start:
if(hru_snow[hh] > 0.0 && Is_LStar[hh] > 0.0){
 if (uFHt[hh] <= 1.0)  // if wind speed at canopy top > 1 m/s
     I1 = (Is_LStar[hh]-Is_SLoad[hh])*(1-exp(-
Cc[hh]*hru_snow[hh]/Is_LStar[hh]));
 else
     I1 = (Is_LStar[hh]-Is_SLoad[hh])*(1-exp(-1*hru_snow[hh]/Is_LStar[hh]));
// calculate canopy snow throughfall before unloading:

 Is_SLoad[hh] += I1;

 Is_SThru[hh] += hru_snow[hh] - I1;

 if (Is_SThru[hh] <= 0.0)
     Is_SThru[hh] = 0.0;

}

// calculate snow ventilation windspeed:

  float xi2 = 1-Zvent[hh];
  float windExt2 = (gamma * LAI[hh] * xi2);

  Is_uVent[hh] = uFHt[hh] * exp(-1 * windExt2);

  if(Is_uVent[hh] <= 0.0)
```

```
     Is_uVent[hh] = 0.0;

// calculate sublimation of intercepted snow:

// calculate sublimation of ideal intercepted ice sphere (500 microns
diameter):

  float Es = 611.15f * exp(22.452f*hru_t[hh]/(hru_t[hh] + 273.0f));  // {sat
pressure}

  float SvDens = Es*PBSM_constants::M/(PBSM_constants::R*(hru_t[hh] +
273.0f)); // {sat density}

  float Lamb = 6.3e-4*(hru_t[hh]+273.0) + 0.0673;  // thermal conductivity of
atmosphere
  Nr = 2.0 * Radius * Is_uVent[hh] / KinVisc;  // Reynolds number
  Nu = 1.79 + 0.606 * sqrt((float) Nr); // Nusselt number
  SStar = M_PI * sqr(Radius) * (1.0f - AlbedoIce) * Qsi[min <long> (hh,
obs_QsiCnt)];  // SW to snow particle !!!! changed
  A1 = Lamb * (hru_t[hh] + 273) * Nu;
  B1 = Hs * M /(R * (hru_t[hh] + 273.0f))- 1.0;
  J = B1/A1;
  float Sigma2 = hru_rh[hh]/100 -1;
  D = 2.06e-5* pow((hru_t[hh]+273.0f)/273.0f, -1.75f); // diffusivity of
water vapour
  float C1 = 1.0/(D*SvDens*Nu);
  m = (4.0f/3.0f* M_PI* pow(Radius, 3.0f)* RhoI); // mass of single ice
sphere

  float Alpha = 5.0;
  float Mpm = 4.0/3.0 * M_PI * PBSM_constants::DICE * Radius*Radius*Radius
*(1.0 + 3.0/Alpha + 2.0/sqr(Alpha));

// sublimation rate of single 'ideal' ice sphere:

 float Is_Vs = (2.0* M_PI* Radius*Sigma2 - SStar* J)/(Hs* J + C1)/Mpm;

// snow exposure coefficient (Ce):

 float Is_Ce;
 if ((Is_SLoad[hh]/Is_IStar) <= 0.0)
      Is_Ce = 0.07;
 else
      Is_Ce = ks* pow((Is_SLoad[hh]/Is_IStar), -Fract);

// calculate 'potential' canopy sublimation:

 float Is_Vi = Is_Vs* Is_Ce;

// calculate 'ice-bulb' temperature of intercepted snow:

 float Is_IceBulbT = hru_t[hh] - (Is_Vi* Hs/1e6/ci);

// determine whether canopy snow is unloaded:

 if(Is_IceBulbT >= unload_t[hh])
    Is_SUnload[hh] = Is_SLoad[hh];
```

```
 else
    Is_SUnload[hh] = 0.0;

// calculate 'actual' canopy sublimation (positive!):

  Is_cpySubl[hh] = Is_SLoad[hh]*Is_Vi*Hs;

// limit sublimation to canopy snow available and take sublimated snow away
from canopy snow at timestep start
  float wtsubl = -Is_cpySubl[hh]*86400*Global::Interval/Hs;
  if (wtsubl > Is_SLoad[hh]){
     Is_cpySubl[hh] = -Is_SLoad[hh]/(86400*Global::Interval/Hs);
     wtsubl = Is_SLoad[hh];
     Is_SLoad[hh] = 0.0;
  }
  else
    Is_SLoad[hh] -= wtsubl;

 if(Is_SLoad[hh] <= 0.0)
    Is_SLoad[hh] = 0.0;

// calculate total sub-canopy snow:

 net_snow[hh] = Is_SThru[hh] + Is_SUnload[hh];

 if (net_snow[hh] <= 0.0)
     net_snow[hh] = 0.0;

// sum throughfall, sublimation and unloading (mass-balance check):

 Is_SnowBal[hh] = net_snow[hh] + Is_cpySubl[hh];

// cumulative amounts....

 Is_cpySublC[hh]+= Is_cpySubl[hh]; // cumulative snow sublimation
 Is_SThruC[hh] += Is_SThru[hh];   // cumulative 'direct' snow throughfall
 Is_netsnowC[hh] += net_snow[hh]; // cumulative sub-canopy snow
 Is_SUnloadC[hh] += Is_SUnload[hh]; // cumulative snow unloading
 Is_SnowBalC[hh] += Is_SnowBal[hh]; // cumulative snow balance

 // calculate daily net snowfall...

 if (nstep == 1)
     Is_netsnow[hh] = net_snow[hh];
 else
     Is_netsnow[hh] += net_snow[hh];  // cumulate sub-canopy swe throughout
day

 if (nstep == 0)
     Is_netsnowD[hh] = Is_netsnow[hh];  // daily 'net' (sub-canopy) snowfall

//=============================================================================
===
// albedo routine:

  if(Is_netsnowD[hh] >= refresh[hh])
   Ab_t[hh] = 0;
```

```
 else
   Ab_t[hh] = Ab_t[hh] + 1;

// albedo decay formulation after (Baker et al., 1990):

  Albedo[hh] = 0.9 - 0.0473 * pow(Ab_t[hh]/Global::Freq, 0.1f);

//  Baker, D.G., Ruschy, D.L., Wall, D.B., 1990.
//  The albedo decay of prairie snows. J. Appl. Meteor. 29 _2, 179-187

// if albedo < 0.16 or no snow albedo = 0.16:

 if(Albedo[hh] < 0.16 || SWE[hh] <= 0.0)
   Albedo[hh] = 0.16;

//============================================================================
===
// Melt Flag and Winter (put in to satisfy other modules in CRHM):

  if (SWE[hh] > 50.0)
     winter[hh] = 1;
  else
     winter[hh] = 0;

  if(hru_tmin[hh] > -2.0 && hru_tmax[hh] > 0.0)
    meltflag[hh] = 1;

  else
    meltflag[hh] = 0;

    net_rain[hh] = Cpy_netRain[hh];
    intcp_evap[hh] = intcp_evap[hh];

  }
}
//=====================================END=====================================
===

void ClassCRHMEllis::finish(bool good) {
  for(hh = 0; chkStruct(); ++hh) {
    LogMessageA(hh, string("'" + Name + " (trees)'  cumintcp_evap  (mm)
(mm*hru) (mm*hru/basin): ").c_str(), Cpy_evapC[hh], hru_area[hh],
basin_area[0]);
    LogMessageA(hh, string("'" + Name + " (trees)'  cumcpy_subl  (mm)
(mm*hru) (mm*hru/basin): ").c_str(), Is_cpySublC[hh], hru_area[hh],
basin_area[0]);
    LogDebug(" ");
  }
}
```

Appendix F. Adjustment of wind speed for forest sheltering effects

In order to approximate turbulent energy exchanges to forest snow, as well as evaporation of rain and sublimation of snow from the canopy, suitable estimations of within–canopy wind speed are required. This often is accomplished through a proportional reduction of wind speeds observed in open environments (Link and Marks, 1999; Hellström, 2001), or that observed at some height above the canopy. This latter approach in describing wind speed reductions from the canopy top often appeal to exponential decay expressions, in which wind speeds decrease proportionately with the vertical depth of the canopy. One such approach follows that of Cionco's (1965) exponential canopy wind flow model which approximates the wind speed at a penetration depth of ξ within the canopy (u_ξ) (in terms of the fraction of total canopy height (h)) as a function of wind speed at the top of the canopy (u_h) [m s^{-1}] as expressed in Figure 6.8 (Chapter 6)

$$u_\xi = u_\mathrm{h} e^{-a\xi} \tag{F1}$$

where a is a dimensionless canopy flow index. Application of Eq. F1 for the estimation of sub–canopy wind speeds in cold regions needleleaf forests was provided by Parviainen and Pomeroy (2000), in which a was approximated by

$$a = n + m e^{-u_\xi} \tag{F2}$$

where n and m are constants which may be optimized for a particular forest stand by wind speeds observations along a vertical forest profile. This was performed by Parviainen and Pomeroy (2000) in both a (i) regenerating pine forest stand of a measured LAI of 2.5 m^2 m^{-2} and a (ii) mature pine forest stand of measured LAI equal to 2.2 m^2 m^{-2} located in Central Saskatchewan, Canada. For Eq. F2, optimal n and m values for describing the forest wind profile corresponded to 2.97 and 3.20 in the regenerating forest and 2.43 and 3.46 in the mature forest stand (Parviainen, MSc Thesis).

Alternative approaches in prescribing a in Eq. F1 have been made through appeal to the similarity between wind speed extinction and shortwave irradiance extinction in needleleaf forest canopies. Here, analytical studies of the wind flow characteristics in needleleaf forest canopies have shown a to be well approximated by the shortwave extinction coefficient (L`) (otherwise refereed to the optical depth of the forest vertical profile in Chapter 5), with $a = 1$ for clustered needleleaf canopies and $a = 1.15$ for individual needleleaf trees (Eagleson, 2002). Evaluation of both methods of specifying a is made by comparison of simulated sub–canopy wind speed via Eq. F1 wind speed observations collected at the aforementioned regenerating and mature pine forest sites. Here, L` is related to the measured LAI at both sites by

$$L` = G(\theta)\Omega \mathrm{LAI} \tag{F3}$$

where Ω represents the clumping index [] and $G(\theta)$ is the describes the distribution of vertical inclination of needleleaf foliage (Chen and Black, 1992). Typically, needleleaf forest canopies may be described as having near spherical (i.e. random) vertical leaf orientation distributions , giving a $G(\theta) = 0.5$, and a typical Ω value for needleleaf foliage equal to 0.61 (Chen and Black, 1992). Using these approximations gives corresponding L` values of 0.76 and 0.67 for the regenerating and mature pine stands, from which the estimation of sub–canopy wind speed by Eq. F1, as well as that estimated by the optimized a approach are shown compared to observations at both sites in Figure F1, with a statistical evaluation of both in Table F1. Here, although superior estimation of sub–canopy wind speeds are made by the optimised (i.e. calibrated a value) method for both sites, satisfactory results are also obtained through the direct relating of forest wind speed reductions to L`(and LAI). As such, results from this evaluation demonstrates are encouraging toward representing forest wind speed reductions directly from information of the density of the physical stand, thus allowing for its flexible application among differing forest stands.

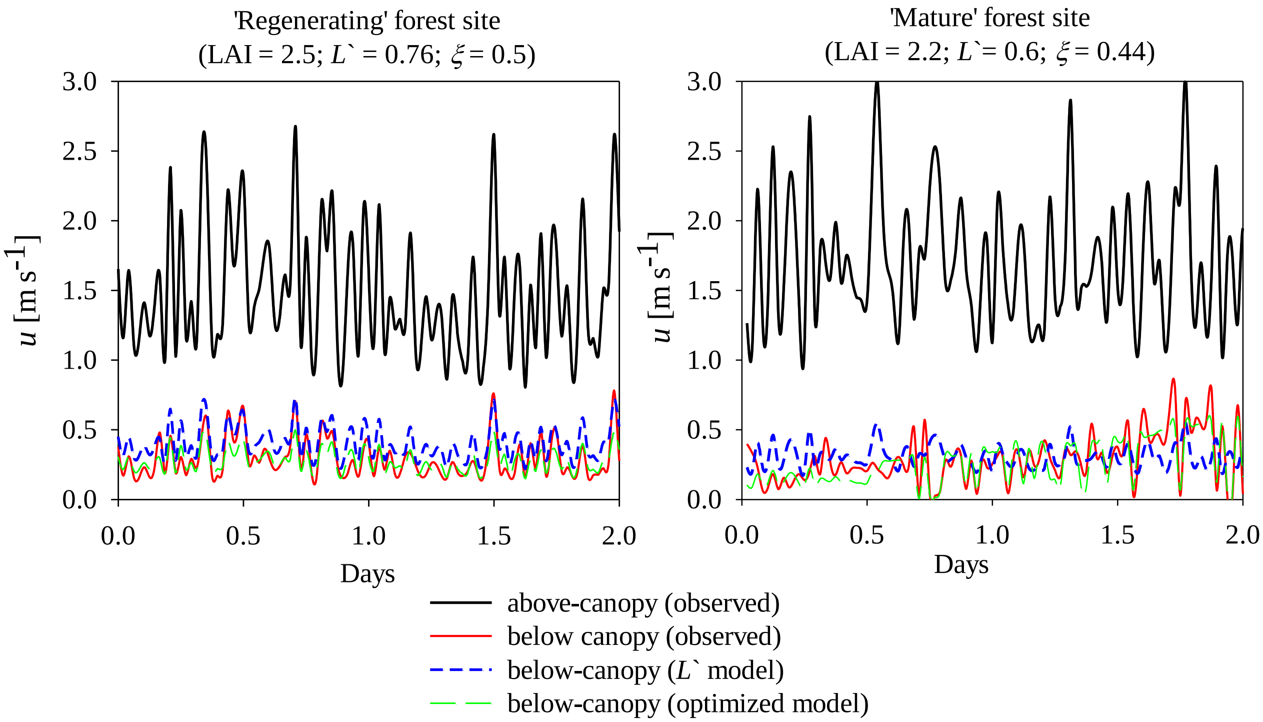

Figure F1. Comparison of within–canopy wind speed estimates provided by (i) empirical optimization of *a* in Eq. F1 (optimized model) and (ii) the specification of *a* by *L*` as determined by LAI measurements (*L*` model).

Table F1. Mean above–canopy wind speed (*u*), and comparison between observed sub–canopy wind speed (*u*) to that estimated via the (i) optimisation of *a* in Eq. F1. (optimized model) and (ii) specification of *a* in Eq. F1 by *L*` (*L*` model) simulation approaches in terms of the model efficiency (ME) and the RMSE for mean daily values.

	Regenerating forest site				**Mature forest site**			
	Observed above–canopy *u*	Observed sub–canopy *u*	estimated sub–canopy *u* (optimized model)	estimated sub–canopy *u* (*L*` model)	Observed above–canopy *u*	Observed sub–canopy *u*	estimated sub–canopy *u* (optimized model)	estimated sub–canopy *u* (*L*` model)
Mean daily *u* [m s^{-1}]	1.52	0.30	0.41	0.28	1.68	0.26	0.31	0.30
ME []	–	–	0.62	0.23	–	–	0.56	0.37
RMSE [m s^{-1}]	–	–	0.08	0.14	–	–	0.07	0.15

END